

UNCLASSIFIED

AD NUMBER

**AD127419**

NEW LIMITATION CHANGE

TO

**Approved for public release, distribution  
unlimited**

FROM

**Distribution authorized to U.S. Gov't.  
agencies and their contractors;  
Administrative/Operational Use; MAR 1957.  
Other requests shall be referred to Bureau  
of Aeronautics [Navy], Washington, DC.**

AUTHORITY

**USNASC ltr dtd 13 Apr 1973**

THIS PAGE IS UNCLASSIFIED

~~UNCLASSIFIED~~

AD 27419

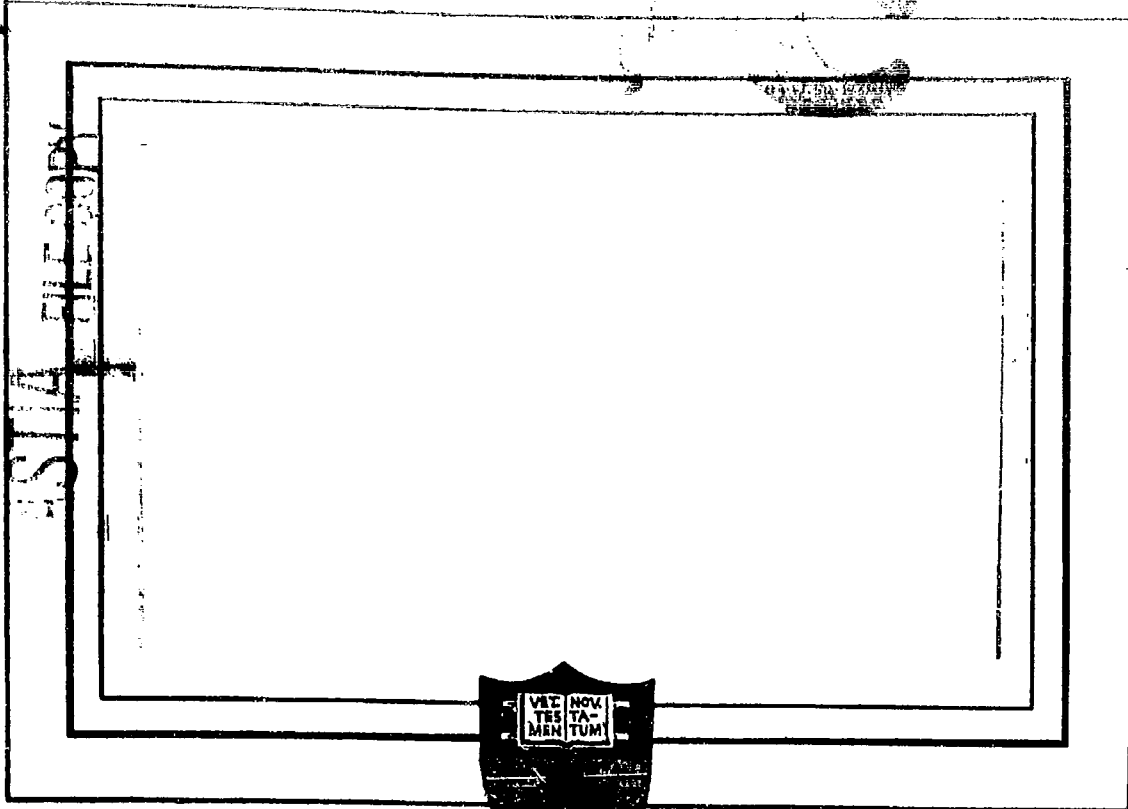
Armed Services Technical Information Agency

Reproduced by  
DOCUMENT SERVICE CENTER  
KNOTT BUILDING, DAYTON, 2, OHIO

This document is the property of the United States Government. It is furnished for the duration of the contract and shall be returned when no longer required, or upon recall by ASTIA to the following address: Armed Services Technical Information Agency, Document Service Center, Knott Building, Dayton 2, Ohio.

NOTICE: WHEN GOVERNMENT OR OTHER DRAWINGS, SPECIFICATIONS OR OTHER DATA ARE USED FOR ANY PURPOSE OTHER THAN IN CONNECTION WITH A DEFINITELY RELATED GOVERNMENT PROCUREMENT OPERATION, THE U. S. GOVERNMENT THEREBY INCURS NO RESPONSIBILITY, NOR ANY OBLIGATION WHATSOEVER; AND THE FACT THAT THE GOVERNMENT MAY HAVE FORMULATED, FURNISHED, OR IN ANY WAY SUPPLIED THE SAID DRAWINGS, SPECIFICATIONS, OR OTHER DATA IS NOT TO BE REGARDED BY IMPLICATION OR OTHERWISE AS IN ANY MANNER LICENSING THE HOLDER OR ANY OTHER PERSON OR CORPORATION, OR CONVEYING ANY RIGHTS OR PERMISSION TO MANUFACTURE, USE OR SELL ANY PATENTED INVENTION THAT MAY IN ANY WAY BE RELATED THEREETO.

~~UNCLASSIFIED~~



PRINCETON UNIVERSITY  
DEPARTMENT OF AERONAUTICAL ENGINEERING

Department of the Navy  
Bureau of Aeronautics  
Contract N0as 53-817-C

COMBUSTION INSTABILITY

IN

LIQUID PROPELLANT ROCKET MOTORS

TECHNICAL REPORT:

DETERMINATION OF COMBUSTION TIME LAG PARAMETERS

IN A LIQUID BIPROPELLANT ROCKET MOTOR

Aeronautical Engineering Report No. 372

Prepared by

*George R. Matthews*  
George B. Matthews

Approved by

Endorsed by

*Henry G. Drey*  
*Henry G. Drey*  
*Luigi Cucco*

1 March 1957

Princeton University  
Department of Aeronautical Engineering

#### ACKNOWLEDGEMENTS

The work described herein was carried out with the assistance and encouragement of a number of people associated with the James Forrestal Research Center of Princeton University.

First and foremost, my gratitude is extended to my principal thesis advisor and professor-in-charge of the project under which the test program was conducted, Professor Luigi Crocco, who originated the basic ideas for the entire investigation and whose suggestions and guidance in the development of the theoretical framework and methods of analysis made this program possible.

Also, I offer my deepest appreciation to Professor Jerry Grey who, acting as secondary advisor and project engineer, offered continued encouragement and constructive advice during the execution of the experimental testing and data reduction.

Special thanks are due to many of the members of the staff of the Jet Propulsion Research Program whose contributions of time and effort were indispensable. Among these are: the project technicians, who were responsible for maintenance, repair, and actual operation of the rocket motor; the instrumentation and recording room personnel, who patiently recorded operational data and assisted in its playback; the graduate assistants and research aide, who acted as test engineers and also aided in primary data reduction; the computing staff, who programmed and operated digital procedures, carried out many laborious hand computations, and helped construct plots of the results; the draftsmen, who carefully prepared these plots for publication; and the secretarial staff, who typed the entire manuscript.

Finally, I wish to acknowledge gratefully the lasting interest and patient support of the United States Navy Bureau of Aeronautics who so

ii.

generously sponsored the experimental and computational work under Contract NOas-53-817-c. This continuing sponsorship over a long and trying period of method and equipment development has been encouraging indeed to all those affiliated with the Program.

DETERMINATION OF COMBUSTION TIME LAG PARAMETERS  
IN A LIQUID BIPROPELLANT ROCKET MOTOR

SUMMARY

The importance of time lag parameters in a systematic study of combustion instability in liquid bipropellant rocket motors is emphasized in a review of early treatments of this phenomenon. Useful application of any such treatment is dependent upon the ability to determine reliable values for these time lag parameters. It is the purpose of this study to develop a theoretical model of the combustion process amenable to experimental verification and to evaluate the parameters defined therein by laboratory measurements under actual rocket motor operating conditions.

Crocco's concept of such a combustion time lag and its dependence upon chamber conditions is discussed, and complex equations are derived by one-dimensional analysis for two theoretical models of a rocket combustion chamber having such a time lag. Both models represent low-frequency, small-amplitude oscillations in chamber pressure and injection flow rates. The exit boundary condition is given by "nozzle impedance" relations for flow through a conical exhaust nozzle with non-isentropic oscillations in gas properties at the entrance. Changes in flame temperature resulting from small variations in instantaneous mixture ratio are considered, but the effects of such variations on the time lag, the position of combustion front, and the generation of reflected waves at the nozzle are neglected in both analyses.

The simplified model approximates the actual combustion distribution by a discontinuous front at a fraction ( $1-f$ ) of chamber length. Derivation of the combustion equation is based upon the mass conservation rule applied collectively to the gas produced, contained in, and exhausted from the chamber as a whole. The refined model is developed from an extension of Crocco's

analysis to include the condition of oscillating injection flows. An arbitrary form of combustion distribution is introduced, and the equations for chamber pressure and gas velocity are derived for the case of moderate frequency, neutral oscillations. These derivations are based upon principles of mass, momentum, and energy conservation, the perfect gas law, a droplet dynamics equation, and a burning rate equation involving the aforementioned time lag concepts. An order of magnitude analysis and an iterative scheme are employed to extrapolate these equations to low frequencies. Final solutions for the time lag and the interaction index between chamber pressure and time lag are obtained by the application of the aforementioned nozzle boundary condition. The final combustion chamber equations resulting from both theoretical analyses are compared term-by-term, and a combined model is formed from both equations, following the form of the simplified model and embodying correction factors derived from the refined treatment.

The quantities to be determined experimentally as inputs for the theoretical analysis and the methods for obtaining these data are discussed. The design and operation of a modulating unit producing sinusoidal injection flow oscillations are described, and the experimental implications of near-constant instantaneous mixture ratio restrictions are noted. The actual measuring vehicle and its auxiliary equipment are mentioned, along with detailed accounts of the sensing, transducing, and recording instrumentation utilized in the measurements.

Calculation procedures employed in the reduction of primary data and in their application to the complex combustion chamber equation are outlined. Measured values of chamber and injector pressure oscillations, steady state gas velocity distributions, and steady state combustion and flow parameters are presented for motor operation at three chamber pressure levels of 300, 450, and 600 psia over a range of modulating frequencies from 60 to 250 cycles

per second. The results of two calculation procedures are presented in tabular and graphical form as values of rocket chamber transfer function, mean chamber gas residence time, average position of the combustion "front", mean total combustion time lag, sensitive portion of this time lag, and index of interaction between time lag and chamber pressure. Finally, these results are criticized with regard to their validity and accuracy, and conclusions are drawn regarding the general applicability of the theoretical model and experimental methods.

TABLE OF CONTENTS

TITLE PAGE	<u>PAGE</u>
ACKNOWLEDGMENTS	i
SUMMARY	iii
TABLE OF CONTENTS	vi
INTRODUCTION	1
CONCEPTS AND THEORY	6
Theoretical Background	6
Fundamental Concepts	8
Combustion Chamber Equations	13
Solution by Iteration for Small $\omega$	54
Comparison of Equations	64
Combined Theoretical Model	67
EXPERIMENTAL METHODS AND EQUIPMENT	77
Experimental Requirements	77
Measuring Vehicle	80
Sensing and Transducing Instrumentation	84
Recording Instrumentation	89
Calibration Methods	91
ANALYSIS OF EXPERIMENTAL DATA	93
Reduction of Primary Data	93
Calculation Procedures	96
Experimental Accuracies and Errors	107
PRESENTATION AND DISCUSSION OF RESULTS	111
Experimental Results	111
Alternate Calculation Procedures	130
Conclusions	141

	<u>PAGE</u>
REFERENCES	148
LIST OF TABLES AND FIGURES	152
TABLES (I through VII)	
FIGURES (1 through 80)	
APPENDIX A: Derivation of Nozzle Boundary Equation for Non- Isentropic Oscillations at Entrance	
APPENDIX B: Method of Solution of Velocity Perturbation Integral Equation	
APPENDIX C: Theoretical Calculation of Pressure-Flow Phase Lag in the Bipropellant Rocket Motor Injectors	
APPENDIX D: Sample Calculations	

DETERMINATION OF COMBUSTION TIME LAG PARAMETERS  
IN A LIQUID BIPROPELLANT ROCKET MOTOR

INTRODUCTION

The extensive occurrence during recent years of destructive pressure oscillations in large rocket motors has led to considerable interest and activity in the field of combustion instability. Endeavors to scale the designs of small test motors up to large operational sizes, attempts to improve rocket performance through concentration or intensification of the combustion processes, and efforts to reduce component weights by lowering the pressure levels in propellant supply equipment have resulted in the incidence of such instabilities in a surprisingly large number of rocket development projects. Elimination of these troublesome vibrations through blind "cut-and-try" methods has eventually proved successful in some of these cases; but these methods suffer from their lack of general applicability to engines other than the particular ones for which they were devised and thus merely emphasize the lack of basic understanding associated with the appearance of such instabilities. The demand for more rational procedures for overcoming these vibrations and the desire for reliable generalized design criteria to prevent their occurrence have necessitated fundamental studies of the nature and causes of the phenomena from theoretical as well as experimental viewpoints.

A common annoyance at the outset of any relatively new research effort is the question of definition, and rocket combustion instability is certainly not excepted from this problem. A multitude of terms (including rough burning, screech, squeal, scream, whistle, chug, groan, hum, buzz, and others) have been employed to describe the acoustic quality of pressure oscillations in rockets. However, the essential differences between stable

and unstable oscillations as well as the distinctions between various types of instabilities must be expressed in subjective terms if they are to be widely accepted and applied. Perhaps the most comprehensive treatment of this matter is that given by Crocco and Cheng (1) in a recent publication. The essence of their discussion will be summarized briefly. In normal combustion the presence of turbulence, inhomogeneity of mixture, and other effects may cause the appearance of fluctuations in the gas and liquid properties within the rocket chamber. These are purely random perturbations, however; and if they are observed at points in the chamber sufficiently distant from one another there will be no time-wise correlation in the variation of any one quantity between the two points. On the other hand, if the fluctuations exhibit definite coordination in the frequencies and amplitudes with which they occur at any two points of the chamber, no matter how distant, then they lose their random character and become organized oscillations representative of abnormal combustion. An examination of the amplitudes of these coordinated perturbations then determines whether combustion is stable, neutrally-stable, or unstable according as they die out, remain constant, or increase with time.

The second consideration in terminology is that of identifying the various types of unstable behavior encountered by different investigators. The most widely accepted classification scheme is based upon differences in the underlying mechanisms causing instabilities; and the general breakdown places unstable oscillations into one of three major groups, characterized primarily by their frequency ranges; (a) low frequency instabilities, commonly referred to as "chugging", with frequencies from as low as thirty to as high as two hundred cycles per second; (b) high frequency, or "screaming", oscillations occurring at frequencies between several hundred and several thousand cycles per second; and (c) intermediate frequency instabilities lying in a range between the other two types.

The destructive phenomena associated with these types of unstable

oscillations may be quite different, and in the case of the first two are easily identified. Low frequency instability usually arises from an interaction between the feeding system and the combustion process (although theoretical studies (2) have shown that an "intrinsic" instability in which there is no feed system coupling is still possible), and the characteristic time associated with the period of this "chugging" instability is the "charging time" or emptying time of the rocket chamber (3, 4). The damage incurred by the action of this type of oscillation is usually associated with structural failures resulting from large amplitude mechanical vibrations of the rocket components or the entire propulsion system. One common "cure" for this problem is simply an increase in pressure drop across the injection system of the liquid propellants, a conclusion which is easily deduced from the theory.

Screaming type oscillations, however, occur at frequencies much too high for any serious interaction with the feeding system and are considered to be of the nature of acoustic oscillations deriving their energy from the combustion process. For such oscillations, therefore, the characteristic time giving the order of magnitude of their period is the wave-travel time between the boundaries of the chamber associated with the particular mode of vibration encountered. The amplitudes of such waves may reach as high as a hundred percent of steady rocket chamber pressure, and the extreme increase in heat transfer to the chamber and injector in such circumstances is very often sufficient to destroy the motor. No generally acceptable mechanical artifice or change in geometric design has yet been developed to completely subdue or prevent the existence of such waves, and it is this perplexity which has been primarily responsible for the increased attention placed on combustion instability studies.

The third, or intermediate frequency, instability has only recently been satisfactorily identified as a separate phenomenon with causes and manifestations distinct from the other two. Berman and Cheney (5)

associated its appearance with the existence of an "off mixture-ratio" zone or "temperature discontinuity" which has been interpreted by Crocco (6) and Scaln (7) as an "entropy wave". This wave travels downstream with the fluid particle velocity and reflects a pressure disturbance from the nozzle which moves upstream with the wave velocity, producing a characteristic period of oscillation shorter than that of the chugging vibration and longer than the screaming one, hence the descriptive term "intermediate-frequency".

Until very recently experimental work in the field of rocket combustion instability consisted primarily of two major efforts: observation of the physical characteristics of the oscillations, e.g., their frequencies, amplitudes, and starting transients; and attempts to control or eliminate the vibrations through the introduction of stabilizers of various types. Both these attacks have been thoroughly reviewed in a survey paper by Ross and Datner (8) and it will suffice here to mention them only briefly. The initial task of identification was performed chiefly through visual or optical means by the application of photographic techniques to transparent motors or observation slits cut into conventional motors (5, 9, 10, 11). This restriction to optical methods was primarily due to the unreliability of existing pressure instrumentation, and of late, data of a more quantitative nature have been reported (12, 13, 14, 15) on the basis of more precise pressure measurements. Meanwhile, the work on stabilizers reported in the unclassified literature has progressed from basic studies of the characteristics and possible applications of servo-controls in the feed system (16, 17) to the conception of a particular design for such a control and a detailed analysis of its behavior (18).

During this same period, theoretical studies of instabilities continued to progress in dealing with more realistic models of the combustion chamber and in extending the range of their applicability to more general and more interesting cases. Of course these improvements were not

attained without additional mathematical complications, so it is perhaps not surprising that so very little experimental work has been directed toward the evaluation of hypotheses or conclusions of the theory. However, in all existing theoretical treatments a number of combustion parameters arise from both physical and mathematical considerations which are of primary importance in describing the stability behavior of any liquid rocket motor. The work reported in this paper was conducted with the aim of evaluating some of these parameters, and to this end it embodies a three-fold approach: (a) extension of existing theory involving important combustion stability parameters to a range of physical variables amenable to empirical examination, (b) determination of typical values for these parameters by application of the derived equations to experimental measurements, and (c) an estimation of the range of application and validity of the relationships expressed by the theory.

CONCEPTS AND THEORYTheoretical Background

Attempts to analyze mathematically the behavior of a rocket motor under conditions of oscillating chamber pressure have a historical background almost as extensive as the existence of the phenomenon itself. Perhaps the earliest efforts in this direction were carried out by Von Karman and his group at the Jet Propulsion Laboratory of the California Institute of Technology shortly after the first appearance of "chugging" in a rocket under test there in 1941. However, the first published theory appeared in a paper by Gunder and Friant (19) and a subsequent discussion of this paper by Yachter (20). Probably the most important contribution of these early treatments was the introduction of the concept of a combustion time lag (conceived independently by Von Karman's group) between the instant of injection of a particle of liquid propellant and the succeeding instant of burning in which that particle is transformed into hot gas capable of exerting chamber pressure. The influence of this time lag on the theory is evident when one notes that it has been the single parameter common to all succeeding analytical papers describing combustion instabilities in any of the various regimes previously mentioned. Its mathematical significance is obvious, since it produces one or more terms in the combustion chamber equation which must be evaluated at a time different from the remaining terms. This time delay produces a sort of "response time" for the rocket motor and hence provides a feedback mechanism essential for unstable oscillations in the chamber-injector system.

Primarily because of the lack of information concerning its magnitude or physical variation, this time lag was originally treated as a constant for all propellant elements under a particular set of operating conditions and was assumed to be insensitive to small variations in these conditions.

Neglecting the effects of small oscillations upon the time lag was considered compatible with the overall assumption of linearization, common to all theoretical analyses reported herein, in which each time-dependent variable is treated as the sum of a steady state quantity plus a small perturbation. On this basis Gunder and Friant derived equations for response of the rocket chamber to oscillations in propellant flow rates for both monopropellant and bipropellant systems. They assumed that the chamber pressure was directly proportional to the injection rates and considered only the effects of inertia and friction of the propellants in the feed lines of a pressurized supply system. Yachter, in a discussion of their paper, indicated the importance of the chamber itself as a capacitance in which the product gases could be stored; and he derived an expression for the critical injector pressure drop for stable operation, without regard to the inertia of the liquids in the feed system. Following these two analyses, Summerfield (4) combined the effects of feed system and chamber capacitance to obtain an equation from which he calculated values for the limits of stable operation in terms of the frequency of oscillation and the magnitude of the time lag.

These theoretical contributions provided a satisfactory explanation for the presence of low frequency instabilities in cases where the injector flow rates responded to fluctuations in chamber pressure. However, the existence of observed instabilities, in a range of frequencies sufficiently high so as to preclude the possibility of injection coupling, could not be explained on the basis of a constant combustion time lag. The theoretical analysis of this "screaming" phenomenon, as well as the so-called "intrinsic" case of constant injection, low frequency instability, was accomplished by Crocco (2, 21) through the introduction of the concept of a sensitive time lag. Originally this sensitivity was treated as a purely environmental activity in which the processes contributing to the total combustion time lag were considered to be affected by thermodynamic and gas dynamic conditions

such as pressure, temperature, density, or gas velocity. Any one of these parameters could then be related to the others by means of the equation of state or compressible flow equations. Of these several properties, pressure is probably the most amenable to experimental measurement; hence this was treated as the primary variable on which to base the correlation of all the others. Crocco then postulated an index,  $n$ , to express the interaction between chamber pressure and the time lag.<sup>1</sup>

#### Fundamental Concepts

In any liquid propellant rocket motor, a number of physical and chemical processes take place during the transformation from raw propellants to hot gases. These preparation processes are extremely complicated individually, and their mutual interactions are almost totally undetermined. However, the gross effects of pressure, temperature, density, and gas velocity may be discussed in a qualitative manner and may help to provide a physical basis for the ensuing mathematical derivation of a burning-rate equation. First, the liquid streams issuing from the injector are broken up into droplets by capillarity and by the relative velocity between liquid and gas velocities. The rate at which this breakup occurs as well as the final droplet size distribution for a particular injector will depend to a large extent upon the density and velocity of the combustion gases and, thus, upon chamber pressure. In general, an increase in pressure produces smaller droplets and speeds up the atomization process, thereby decreasing the time con-

---

<sup>1</sup> Very recently, a second interaction index has been introduced by Scala (7) to express the dependence of time lag upon mixture ratio. This has been of considerable importance in predicting the appearance of intermediate-frequency instabilities; but it does not appear in the present treatment, which is based primarily upon the high-frequency and intrinsic low-frequency analyses.

sumed in this phase of propellant preparation. Following and during atomization, evaporation at the droplet surface occurs. The rate of this vaporization is influenced by the droplet size and by a sort of film coefficient. The result of increased chamber pressure acting through both of these parameters is an increase in the overall evaporation rate, decreasing this contribution to the total time lag. Similarly the increase in temperature of both liquid and unburned gas by diffusion and convection will be accelerated by an increase in gas pressure. Also, the kinetics of most of the combustion reactions encountered in rocket motors is speeded up by increasing the pressure within the medium, particularly when the reaction occurs in the vapor state. In fact, the only process occurring during the time lag which might conceivably be totally independent of the thermodynamic conditions within the chamber is that of liquid-liquid mixing, in a bipropellant motor. Certain other processes will take place which may be nearly unaffected by chamber pressure; but these, along with liquid phase mixing, are likely to take place in a time and space very close to injection. Therefore, a graphical representation of an index of interaction as described would probably show a very small value close to the injector, with increasing values during the later phases of the preparation. This distribution of an interaction function may be schematized as having zero magnitude for a portion of the total time lag and a constant magnitude for the remaining portion.

As a consequence of these considerations, one concludes that the total combustion time lag in a liquid propellant rocket may be represented in an approximate fashion as the sum of an insensitive portion and a sensitive portion, the former being independent of the temperature and pressure of the chamber gases and the latter generally decreasing with an increase in chamber pressure through the action of a constant interaction index. Thus:

$$\tau_T = \tau_i + \tau_s \quad (1)$$

where the subscript T is used to denote the total value and i indicates the insensitive portion. This schematic time lag is shown in Figure 1.

Following the method of Crocco (1, 6) in expressing the above ideas mathematically, one may state that the transformation of propellants into hot gases will be complete after sufficient transfer of energy has taken place to raise each particle to a certain energy level,  $E_a$ , which may be considered similar in concept to an activation energy for the overall preparation and combustion processes. Since the equilibrium flame temperature varies primarily with mixture ratio of the incoming propellants and only in a secondary manner with chamber pressure, this final energy level may be considered to have a constant value, provided the mixture ratio is constant and pressure oscillations remain small in comparison to the average chamber pressure. If one represents the combined rates of all the preparation and combustion processes as a function,  $f(P, T, U, \dots)$ , of the various aero-thermodynamic parameters, then the time lag will be ended only when the integrated value of this rate function has reached the final energy level,  $E_a$ ; thus, for a particle injected at time  $t = t_0$  and burning at time  $t$ :

$$\int_{t-t_0}^t f(t') dt' = E_a - \text{CONSTANT.} \quad (2)$$

Under the restriction of small perturbations, the rate function may be written as:

$$f(P, T, U, \dots) = f(\bar{P}, \bar{T}, \bar{U}, \dots) + \left( \frac{\partial f}{\partial P} \right)_{P=\bar{P}} P' + \left( \frac{\partial f}{\partial T} \right)_{T=\bar{T}} T' + \left( \frac{\partial f}{\partial U} \right)_{U=\bar{U}} U' + \dots \quad (3)$$

where the superscript bar indicates mean values of the oscillating quantities and the prime designates the perturbed portion.

Introducing the correlating functions between pressure and the remaining parameters, this equation becomes:

$$f(P, T, U, \dots) - f(\bar{P}, \bar{T}, \bar{U}, \dots) = f - \bar{f} = f' = P \left[ \frac{\partial f}{\partial P} + \frac{\partial f}{\partial T} \frac{dT}{dP} + \frac{\partial f}{\partial U} \frac{dU}{dP} + \dots \right]_{P=\bar{P}} \quad (4)$$

from which an expression for the interaction index, defined here as the influence of small fractional changes in pressure on the rate function, takes the form:

$$\eta = \left( \frac{f - \bar{f}}{f} \right) / \left( \frac{P - \bar{P}}{P} \right) = \left( \frac{f'}{f} \right) \left( \frac{\bar{P}}{P} \right) = \frac{\bar{P}}{f} \left[ \frac{\partial f}{\partial P} + \frac{\partial f}{\partial T} \frac{dT}{dP} + \frac{\partial f}{\partial U} \frac{dU}{dP} + \dots \right]_{P=\bar{P}} \quad (5)$$

The instantaneous rate of the preparation processes is then:

$$f(P, T, U, \dots) - \bar{f}(\bar{P}, \bar{T}, \bar{U}, \dots) \left[ 1 + \frac{n P'}{P} \right] \quad (6)$$

and Equation 2 becomes:

$$\int_{t-\bar{T}_T}^t \bar{f} \left[ 1 + \frac{n P'(t')}{P} \right] dt' = E_a \quad (7)$$

The value of  $\bar{f}(\bar{P}, \bar{T}, \bar{U}, \dots)$  will change only through spatial non-uniformities of  $\bar{P}$ ,  $\bar{T}$ , etc.; and since the velocities of liquids and gases in the chamber are usually small compared to the sound velocity, the steady state values of pressure and temperature are practically uniform throughout the chamber. Then, since  $n$  and  $E_a$  are treated as constants,

$$\int_{t-\bar{T}_T}^t \bar{f} \left[ 1 + \frac{n P'(t')}{P} \right] dt' = E_a = \int_{t-\bar{T}_T}^t \bar{f}(t') dt' \quad (8)$$

from which one may easily obtain a relation for the variation in time lag around its average value as:

$$\tau_T - \bar{\tau}_T = - \frac{n}{P} \int_{t-\bar{T}_T}^t P'(t') dt' = \tau - \bar{\tau} \quad (9)$$

the latter part of this equation having been deduced from the assumed constancy of the insensitive portion of the time lag.

A number of possibilities exist for the application of the time lag concept to the overall physical model of combustion described. In the actual case, if one follows two propellant elements from the instant of injection to their final reacted gaseous state, their volumes are small at first, increasing rapidly as exothermic chemical reactions take place, and reaching a final value when combustion becomes complete. The schematization introduced by the above time lag concept is the replacement of this gradual complex volume change by a step-wise transition from droplet volume to final gaseous volume. In the most general case, this approximation is made individually for each element of combustion gas, resulting in a time lag and a corresponding space lag (the distance traveled during these preparation and reaction processes) for each pair of propellant elements destined to react together. The combined picture for all propellant elements is then one of continuous combustion in both space and time, since these lags vary continuously over a finite range between individual particles injected at the same instant but a different location in the injector pattern. Further simplifying assumptions were made in a series of papers by Crocco (2, 21) and Cheng (22, 23) which have been well summarized in a monograph on the subject of combustion instability in liquid rocket motors (1). In these additional cases the steady state combustion pattern takes one of the following forms: (a) all burning takes place at a single spatial location, but the particles require different times to reach this location, resulting in distributed time lags and a concentrated space lag; (b) all particles require the same preparation time, but their different velocities carry them to various locations, producing a concentrated time lag with distributed space lags; and (c) the more drastic simplification in which combustion is considered completely concentrated at a given position

in both time and space. The present paper includes only the two extreme cases, i.e., distribution of both time and space lags and complete concentration of both lags.

Another refinement to the original instability theories was the introduction by Crocco and Cheng (24) of the influence of the exhaust nozzle geometry. This effect had been observed by Berman, Logan, and Cheney (5, 9) in an experimental motor; and the gasdynamic relations involved in oscillating flow through a supersonic nozzle were derived by Tsien (25) for the isothermal case. Crocco (26) extended the theory to several additional cases and applied the so-called "nozzle impedance" relations as a boundary condition for the equations of the combustion chamber. The further extension of the nozzle equations to include low frequency, non-isentropic oscillations at the entrance section for both linear and non-linear velocity distributions is contained in Appendix A of this paper.

#### Combustion Chamber Equations

In developing a usable combustion equation for application to experimental data, the same general scheme of analysis is employed regardless of the model chosen to represent the actual combustion process. Equations are obtained for the variations in pressure, velocities of gas and liquid, and gas density or entropy. These are then related by a burning rate equation containing the desired time lag parameters and reduced to a final single equation involving chamber pressure and time lag by the application of boundary conditions at the nozzle and injector ends of the chamber. This overall method has been applied to several combustion models by Crocco and Cheng (1); and the analysis contained herein is intended as an extension of their work to include the condition of oscillating injection flow rates, which is the actual situation encountered in the laboratory work described later.

Two distinct physical models of the combustion process are treated. The simplified model deals with the chamber as a whole, approaching the flow field from a macroscopic point of view; while the more refined model is derived from an analysis of differential increments of mass, volume, and length. The framework for both models is furnished by the one-dimensional equations of conservation of mass, momentum, and energy in unsteady flow. Perturbations of all physical quantities are limited to small fractions of their average or steady state values; hence the treatment is linearized throughout, with squares and products of perturbations considered negligibly small. A number of other assumptions are common to both theoretical models. These are:

1. Oscillations in fluid properties are neutrally stable with time and are of a sinusoidal nature.
2. In keeping with the assumption of one-dimensionality, the time lag is assumed uniform across any axial section of the motor.
3. Instantaneous variations in mixture ratio are sufficiently small so as to have negligible effects upon the combustion time lag or upon the generation of reflected waves at the nozzle.
4. Combustion is completed within the chamber length; the flow of burned gas through the exhaust nozzle is isentropic following a fluid particle.
5. The velocity gradient along the axis of the subsonic portion of the nozzle is that corresponding to a conical geometry.

A schematic representation of the two models is illustrated in Figure 2.

The model assumed in the simplified analysis is the result of a series of alterations to an original representation by Crocco (2) of low frequency oscillations in a monopropellant rocket motor. This was extended to a bipropellant motor with combustion occurring at the injector face and with quasi-steady flow through the nozzle. Further modifications included relocation of the combustion at a fixed front downstream from the injector and

oscillating exhaust flow occurring in accord with a linear velocity gradient along the subsonic portion of the nozzle. The present model is one in which the actual combustion distribution is replaced by a discontinuous "front", or burning zone, at an arbitrary fraction ( $1-f$ ) of chamber length, the position of this front being permitted to oscillate with chamber gas properties. Upstream of this front the gases are assumed to have zero velocity, while downstream they have a uniform velocity that is constant under steady-state conditions. Also, in this representation the velocity gradient along the axis of the exhaust nozzle is arbitrary, and calculations for nozzle impedance parameters are based upon the special, non-linear case of a conical geometry.

The basic equation governing this model is simply the mass conservation equation stated in the form, "The rate of increase of the mass of gas within the chamber is equal to the difference between the rate of production of hot gases and the rate of discharge of these gases." Stated mathematically this becomes:

$$\frac{d}{dt} (M_g) = \dot{m}_b - \dot{m}_e, \quad (10)$$

where:

$M_g$  = total mass of gas within the chamber at any instant.

$\dot{m}_b$  = instantaneous mass rate of production of burned gas.

$\dot{m}_e$  = instantaneous mass flow rate into the exhaust nozzle.

Before continuing with the derivation, it might be well to point out several heretofore unmentioned assumptions and approximations which are implicit in a "black-box" treatment of this sort. Perhaps the most evident of these is the omission of any effects of the presence of liquid droplets or streams. This simplification is based upon the premise that the volume occupied by the liquid is quite small in comparison to the total chamber volume; therefore the

presence of such droplets cannot seriously effect the volumetric changes in hot gases resulting from pressure and temperature oscillations. However, the existence of a finite droplet velocity throughout a portion of the chamber may have a noticeable effect upon the magnitudes of both time and space lags, since it may enter into momentum and energy equations in a primary way. Then, too, these droplets will certainly be sensitive to fluctuations in gas velocity and may thus contribute to oscillation in the position, distribution, and time histories of the sources of hot gas production. Such considerations are included in the more refined analysis which is presented later.

Another restriction inherent in this simplified mass conservation equation is its validity only at very low frequencies of pulsation. This is exhibited by the tacit assumption that the mass of gas within the chamber oscillates as a whole and, therefore, that the entire chamber experiences the same gas pressure at any one instant of time. The physical basis for this approximation lies in the fact that at extremely low frequencies the period of one oscillation is much longer than the time required for a pressure wave to travel the length of the chamber and return; thus, any small change in pressure will be transmitted essentially instantaneously throughout the chamber, and a new equilibrium level will be reached before another small change has taken place. This is strictly true only in the limit of zero frequency oscillations, i.e., a continuous succession of steady state conditions, and hence represents a quasi-steady flow restriction which is also removed in the refined analysis.

Returning to Equation 10, one must express each of the three mass rates in terms of quantities amenable to experimental measurement. If one defines a fractional variation in mass flow rate around an average value by:

$$\mu = \frac{\dot{m} - \bar{\dot{m}}}{\bar{\dot{m}}}$$

and an average gas residence time for the full chamber by:

$$\theta_g = \bar{M}_g / \dot{m}$$

where the superscript bar is used to denote average or steady-state conditions, then Equation 10 may be written in a fractional form as:

$$\theta_g \frac{d}{dt} \left( \frac{\dot{m}_g}{\bar{M}_g} \right) + \mu_e = \mu_b \quad (11)$$

with all terms to be evaluated at the same instant of time,  $t$ .

Consider the third term, representing hot gas generation. From the concept of a combustion time lag described previously, it is apparent that an element of mixed propellants burning at time  $t$  and contributing to  $\dot{m}_b(t)$  must have been injected at a previous instant  $t - \bar{T}_T$ , where  $\bar{T}_T$  represents the total combustion time lag of this element. Then, those elements which burn over the incremental time  $dt$  required a corresponding, but not equal, time interval  $d(t - \bar{T}_T)$  for injection. Equating these two expressions for the same mass at different times in its history gives:

$$\dot{m}_b^{(t)} dt = \dot{m}_i^{(t - \bar{T}_T)} d(t - \bar{T}_T), \quad (12)$$

Where  $\dot{m}_i$  symbolizes the mass rate of injection of the total propellants, and the superscript parentheses indicate the times at which the terms are to be evaluated.

This equation may be re-written as:

$$\dot{m}_b^{(t)} = \dot{m}_i^{(t - \bar{T}_T)} \left( 1 - \frac{dt}{d(t - \bar{T}_T)} \right), \quad (13)$$

where the injection rate is delayed in time by the average value of the total time lag (introducing only second order errors), and the sensitive time lag has been substituted in the derivative expression, since the insensitive portion of the total lag does not vary with time.

The variation of the time lag around its steady-state value has been derived in Equation 9, and differentiation of this expression with respect to time, again evaluating the delayed term at its average time and neglecting higher order quantities, gives:

$$\frac{dt}{dt} = -\frac{n}{P} \frac{d}{dt} \int_{t-\bar{\tau}}^t [P(t') - \bar{P}] dt' = -n \left\{ \left[ \frac{P(t) - \bar{P}}{\bar{P}} \right] - \left[ \frac{P(t-\bar{\tau}) - \bar{P}}{\bar{P}} \right] \right\} \quad (14)$$

If one now defines a fractional variation in chamber pressure by:

$$\phi^{(t)} = \frac{P(t) - \bar{P}}{P},$$

Equation 14 may be written in the desired form:

$$\left( 1 - \frac{dt}{dt} \right) = 1 + n \left[ \phi^{(t)} - \phi^{(t-\bar{\tau})} \right]. \quad (15)$$

Substituting this expression in Equation 13, introducing the previous definitions of fractional mass flow oscillations, and neglecting products of perturbations, one obtains:

$$\mu_b^{(t)} = \mu_i^{(t-\bar{\tau}_T)} + n \left[ \phi^{(t)} - \phi^{(t-\bar{\tau})} \right] \quad (16)$$

The injection flow rate oscillation for a bipropellant rocket may be broken up into its two components. Performing this separation and introducing a mixture ratio parameter,  $H$ , defined by:

$$H = \frac{1}{2} \left( \frac{\bar{r}-1}{\bar{r}+1} \right)$$

where:

$$\bar{r} = \bar{m}_o / \bar{m}_F$$

with the subscripts O and F indicating oxidizer and fuel, respectively, gives

$$\mu_i = \frac{\dot{m}_o + \dot{m}_F - \bar{m}}{\bar{m}} = \left( \frac{1}{2} + H \right) \mu_o + \left( \frac{1}{2} - H \right) \mu_F \quad (17)$$

Substitution of these terms into Equation 16 yields the final expression for the fractional variation in rate of gas production. Thus:

$$\mu_b^{(t)} = \left(\frac{1}{2} + H\right) \mu_o^{(t - \bar{T}_T)} + \left(\frac{1}{2} - H\right) \mu_F^{(t - \bar{T}_T)} + n \left[ \phi^{(t)} - \phi^{(t - \bar{T})} \right] \quad (18)$$

The next term to be examined and amplified is the exhaust rate,  $\mu_e$ . The results of the derivation of Appendix A indicate the following relation between mass flow, pressure, and entropy fluctuations at the entrance to the nozzle:

$$\mu_e = \phi_e \left[ \frac{r+1}{2\tau} + \frac{i\omega l}{rc^*} \left( W_1 - \frac{r-1}{2} W_2 \right) \right] - \frac{\epsilon_e}{2\tau} \left( 1 + \frac{i\omega l}{c^*} W_1 \right) \quad (19)$$

where:

$$\epsilon = (S/C_v) - (\overline{S}/\overline{C}_v)/(\overline{S}/\overline{C}_v) = \text{fractional entropy perturbation.}$$

$l$  = length of subsonic portion of nozzle.

$c^*$  = velocity of sound at nozzle throat.

$W_1, W_2$  = integrated nozzle velocity parameters.

$\omega$  = frequency of oscillation.

$\gamma$  = ratio of specific heats of gas.

Some additional conditions must be specified in order to evaluate the fractional variation in entropy. First, the discontinuous combustion "front" is arbitrarily located at a fraction  $(1-f)$  of the chamber length downstream from the injector. Second, it is assumed that after burning and throughout the remainder of its stay within the chamber, each particle preserves the entropy with which it was formed, although its temperature and pressure may both oscillate. Thus, a particle which burns at a time  $t$  will reach the nozzle entrance at a time  $t + f\theta_g$  with the particular value of  $\epsilon$  which it had at the time  $t$ . Conversely, the entropy of gas particles entering the nozzle at time  $t$  is precisely the entropy given to them during burning at time  $t - f\theta_g$ .

20.

Thus:

$$\epsilon_e^{(t)} = \epsilon_b^{(t-f\theta_g)}$$

(20)

The oscillations in entropy taking place at the burning station can be expressed in terms of measurable quantities through the first law of thermodynamics, yielding:

$$\epsilon_b^{(t-f\theta_g)} = \gamma \left( \frac{T_{g_b} - \bar{T}_g}{\bar{T}_g} \right)^{(t-f\theta_g)} - (\gamma-1) \phi^{(t-f\theta_g)}, \quad (21)$$

where  $T_{g_b}$  is the instantaneous equilibrium gas temperature at the end of combustion. If one neglects the variation of this adiabatic flame temperature with small pressure oscillations,  $T_{g_b}$  for any element of mixture is uniquely determined by the mixture ratio of that element at the time of burning, which is precisely the mixture ratio at the instant of injection of that element a time lag earlier. Employing a correlation factor, K, defined by:

$$K = \frac{1}{2} \frac{\bar{T}}{\bar{T}_g} \left( \frac{d\bar{T}_g}{dr} \right) r = \bar{F}$$

the gas temperature oscillation at the burning station is written as:

$$\left( \frac{T_{g_b} - \bar{T}_g}{\bar{T}_g} \right)^{(t-f\theta_g)} = 2K \left( \frac{r_b - \bar{F}}{\bar{F}} \right)^{(t-f\theta_g)} = 2K \left( \frac{r_i - \bar{F}}{\bar{F}} \right)^{(t-f\theta_g - \bar{T}_T)}, \quad (22)$$

where the subscripts b and i have again been used to designate burning and injection, respectively. Substitution of the fractional flow rate oscillations at the injector and introduction of the resultant equation, along with Equation 21, into Equation 20 produces for the entropy oscillations,

$$\epsilon_e^{(t)} = 2\gamma K (\mu_o - \mu_F) \left( \frac{r_i - \bar{F}}{\bar{F}} \right)^{(t-f\theta_g - \bar{T}_T)} - (\gamma-1) \phi^{(t-f\theta_g)}, \quad (23)$$

which results in a final evaluation for the exit mass flow fluctuations as follows:

$$\mu_e^{(t)} = \phi^{(t)} \left[ \frac{\sigma+1}{2\sigma} + \frac{i\omega l}{\gamma c^*} \left( W_1 - \frac{\sigma-1}{2} W_2 \right) \right] + \\ + \left( \frac{\sigma-1}{2\sigma} \right) \left( 1 + \frac{i\omega l}{c^*} W_1 \right) \phi^{(t-f\theta_g)} - K \left( 1 + \frac{L\omega l}{c^*} W_1 \right) (\mu_o - \mu_F)^{(t-f\theta_g - \bar{T}_T)} \quad (24)$$

The remaining term in the original mass balance equation is that which expresses the rate of accumulation of mass in the combustion chamber. Since the volume of the chamber is fixed, any perturbations in the mass contained therein must arise from density changes only. Expressing the total mass as an integrated density function and applying the perfect gas law gives:

$$\frac{M_g}{M_g} = \frac{1}{\int_g V_C} \int_{V_C} f_g(x,t) dV' = \frac{P(t) \bar{T}_g}{P V_C} \int_{V_C} \frac{dV'}{T_g(x,t)}, \quad (25)$$

where, as previously stated, pressure is assumed uniform throughout the chamber. For a cylindrical chamber with combustion concentrated in the aforementioned location, the time rate of change of this mass becomes:

$$\Theta_g \frac{d}{dt} \left( \frac{M_g}{M_g} \right) = \Theta_g \frac{d}{dt} \left\{ \left( 1 + \phi^{(t)} \right) \left[ \int_0^{(1-f)L} \frac{\bar{T}_g}{T_g(x,t)} dx + \int_{(1-f)L}^L \frac{\bar{T}_g}{T_g(x,t)} dx \right] \right\} \quad (26)$$

The integral involving temperature changes within the chamber is thus broken into two parts. The gas in the zone upstream of the combustion front is treated as a stagnant mass in which turbulent eddy velocities may exist, but which has no net velocity along the chamber. Under such conditions of recirculation, mixing should be sufficiently thorough as to warrant the assumption of uniform temperature throughout the zone, in which case the contribution to the time rate of change of mass from this term will become:

$$\Theta_g \frac{d}{dt} \left[ \left( 1 + \phi^{(t)} \right) \int_0^{(1-f)L} \frac{\bar{T}_g}{T_g(x,t)} dx \right] = \Theta_g \frac{d}{dt} \left[ \left( 1 + \phi^{(t)} \right) \frac{\bar{T}_g}{T_{g_s}^{(t)}} (1-f) \right] \quad (27)$$

Neglecting heat transfer from the chamber walls, the oscillations in pressure and temperature within this region may be considered isentropic, so

that:

$$\frac{T_g^{(t)} - \bar{T}_g}{\bar{T}_g} = \frac{\gamma-1}{\gamma} \left[ \frac{P^{(t)} - \bar{P}}{\bar{P}} \right] = \frac{\gamma-1}{\gamma} \phi^{(t)}$$

or:

$$\frac{\bar{T}_g}{T_{gS}} = 1 - \frac{\gamma-1}{\gamma} \phi^{(t)}, \quad (28)$$

neglecting squares of small perturbations. Substitution of this function into Equation 27 gives:

$$\Theta_g \frac{d}{dt} \left[ (1+\phi^{(t)}) \int_{0}^{(1-f)L} \frac{\bar{T}_g}{T_g(x,t)} dx \right] = \Theta_g \frac{d}{dt} \left[ (1 + \frac{\phi^{(t)}}{\gamma})(1-f) \right] \quad (29)$$

If, now, one specifies that the gas within this recirculation zone remains stagnant, then there can be no flow across the combustion front; and the position of this front will oscillate in such a way as to retain a constant upstream mass. Therefore, the mass represented by the bracketed term of Equation 29 must remain constant with time and will be equal to the mass under average, or steady state, conditions when  $f = \bar{f}$  and  $\phi = 0$ . Thus:

$$(J^V)_{o \rightarrow (1-f)} = \bar{f} L A_c (1-f) \left( 1 + \frac{\phi^{(t)}}{\gamma} \right) = (J^V)_{o \rightarrow (1-\bar{f})} = \bar{f} L A_c (1-\bar{f}) \quad (30)$$

and:

$$(1-f) = (1-\bar{f})(1 - \frac{\phi}{\gamma}) \quad (31)$$

where squares of perturbations have again been neglected.

In the remainder of the chamber downstream of the front, temperature is varying with distance as well as time because of the small fluctuations in mixture ratio occurring at the combustion location. Each element of burned gas produced at this location has its own particular temperature and entropy determined by its mixture ratio at the time of burning. In the analysis of

the exhaust flow term, it was pointed out that the entropy of such an element remains constant as it progresses down the chamber at nearly constant velocity. This constancy of entropy may be expressed mathematically by the use of the "streaming", or Lagrangian, derivative, which states:

$$\frac{D\epsilon}{Dt} = \frac{\partial \epsilon}{\partial t} + u \frac{\partial \epsilon}{\partial x} = 0 , \quad (32)$$

for which the familiar traveling wave solution may be written, employing the first law of thermodynamics:

$$\epsilon(x,t) = \frac{T_g(x,t) - \bar{T}_g}{\bar{T}_g} - \frac{\gamma-1}{\gamma} \phi^{(t)} = g \left[ t - \int_{(1-f)L}^L \frac{dx'}{u(x')} \right] \quad (33)$$

where the integral represents the time required for a particle to traverse the distance from the burning station to the point  $x$ , a time designated as  $\Theta_b(x)$ . The form of the function  $g$  may be obtained from conditions at the burning station, where the value of this integral is zero. Thus:

$$g(t) = \frac{\bar{T}_g - \bar{T}_b}{\bar{T}_g} - \frac{\gamma-1}{\gamma} \phi^{(t)} = 2K(\mu_0 - \mu_F)^{(t-\bar{T}_T)} - \frac{\gamma-1}{\gamma} \phi^{(t)} . \quad (34)$$

From this expression, neglecting products and squares of perturbations, one obtains:

$$\frac{\bar{T}_g}{T_g(x,t)} = 1 - \frac{\gamma-1}{\gamma} \left[ \phi^{(t)} - \phi^{(t-\Theta_b(x))} \right] - 2K(\mu_0 - \mu_F)^{(t-\bar{T}_T-\Theta_b(x))} \quad (35)$$

Returning to Equation 26, expressing the contributions of each of the portions of the chamber to the overall rate of accumulation of gas and noting that by assumption the mass within the recirculation zone is constant, one may substitute the results of Equation 35 to derive:

$$\begin{aligned} \Theta_g \frac{d}{dt} \left( \frac{M_g}{M_g} \right) &= \Theta_g \frac{d}{dt} \left[ (1+\phi) \int_{(1-f)L}^L \frac{\bar{T}_g}{T_g(x,t)} dx \right] \\ &= \Theta_g \frac{d}{dt} \int_{(1-f)L}^L \left\{ 1 + \phi^{(t)} - \frac{\gamma-1}{\gamma} \left[ \phi^{(t)} - \phi^{(t-\Theta_b(x))} \right] - 2K(\mu_0 - \mu_F)^{(t-\Theta_b(x)-\bar{T}_T)} \right\} dx \quad (36) \end{aligned}$$

It is now expedient to introduce the condition of sinusoidal oscillations in perturbed quantities, in which case all variables are written in the general form:

$$G(t) = \tilde{G} e^{i\omega t} \quad (37)$$

so that the time and distance variables under the integral sign in Equation 36 may be separated, yielding:

$$\Theta_g \frac{d}{dt} \left( \frac{M_g}{M_g} \right) = \Theta_g \frac{d}{dt} \left\{ f_L \left[ 1 + \phi^{(t)} \right] - \frac{\gamma-1}{\gamma} \phi^{(t)} \int_{(1-f)L}^L \left[ 1 - e^{-i\omega\theta_b(x)} \right] dx - \right. \\ \left. - 2K(\mu_o - \mu_F)^{(t-\tau_T)} \int_{(1-f)L}^L e^{-i\omega\theta_b(x)} dx \right\} \quad (38)$$

For essentially constant gas velocity,  $\theta_b$  is easily evaluated as:

$$\theta_b(x) = \int_x^L \frac{dx'}{U(x')} = \frac{x - (1-f)L}{U} \quad (39)$$

enabling one to perform the indicated integrations of Equation 38 to produce the time-dependent relations:

$$\Theta_g \frac{d}{dt} \left( \frac{M_g}{M_g} \right) = \Theta_g \frac{d}{dt} \left\{ f \left[ 1 + \frac{\phi^{(t)}}{\gamma} \right] + \right. \\ \left. + \frac{L}{\omega} \frac{d}{dt} \left\{ \left[ \frac{(\gamma-1)}{\gamma} \phi^{(t)} - 2K(\mu_o - \mu_F)^{(t-\tau_T)} \right] \left( e^{-i\omega f \theta_g} - 1 \right) \right\} \right\} \quad (40)$$

where use has been made of the definition of a gas residence time for the whole chamber length:

$$\Theta_g = L/U$$

Carrying out the differentiations indicated, with the expression for instantaneous location of the combustion front given by Equation 31, the mass accumulation term becomes:

$$\Theta_g \frac{d}{dt} \left( \frac{M_g}{M_g} \right) = \Theta_g \frac{d}{dt} \left\{ \frac{1}{\gamma} + \frac{2(1-f)}{\gamma^2} \phi^{(t)} + \frac{(1-f)}{\gamma} e^{-Lw f \theta_g} \left[ \frac{\gamma-1}{\gamma} \phi^{(t)} - 2K(\mu_o - \mu_F)^{(t-\tau_T)} \right] \right\} + \quad (41) \\ + \frac{i}{\omega} (e^{-i\omega f \theta_g} - 1) \left[ \frac{\gamma-1}{\gamma} \frac{d\phi^{(t)}}{dt} - 2K \frac{d}{dt} (\mu_o - \mu_F)^{(t-\tau_T)} \right]$$

Substituting the exponential form for  $\phi$ ,  $\mu_o$ , and  $\mu_f$ , and evaluating these derivatives, again neglecting squares and products of perturbations, gives the final expression for the mass accumulation term. Thus:

$$\Theta_g \frac{d}{dt} \left( \frac{M_g}{M_0} \right) = \frac{i\omega \Theta_g}{\sigma} \phi + \left[ \frac{\sigma-1}{\sigma} \phi - 2K(\mu_o - \mu_f) e^{-i\omega \bar{\tau}_T} \right] (1 - e^{-i\omega \bar{\tau}_T \Theta_g}) \quad (42)$$

where evaluation of the exponential terms at their average values can be shown to introduce only second order inaccuracies.

Substitution of the sinusoidal form for the oscillating quantities in Equations 18 and 24 and subsequent replacement of these expressions into the original mass balance relation as expressed by Equation 11 results in a complete combustion chamber equation which, after combining terms, has the form:

$$\begin{aligned} \phi & \left[ \frac{i\omega \Theta_g + \frac{3\sigma-1}{2\sigma} + i\omega \frac{2}{\sigma C^*}}{\sigma} (W_1 - \frac{\sigma-1}{2} W_2) - \left( \frac{\sigma-1}{2\sigma} \right) \left( 1 - \frac{i\omega \ell}{C^*} W_1 \right) e^{-i\omega \bar{\tau}_T \Theta_g} - \right. \\ & \left. - n(1 - e^{-i\omega \bar{\tau}_T}) \right] = e^{-i\omega \bar{\tau}_T} \left[ \left( \frac{1}{2} + H + 2K \right) \mu_o + \left( \frac{1}{2} - H - 2K \right) \mu_f - K(\mu_o - \mu_f) \left( 1 - \frac{i\omega \ell}{C^*} W_1 \right) \times \right. \\ & \left. \times e^{-i\omega \bar{\tau}_T \Theta_g} \right] \end{aligned} \quad (43)$$

Average values of the four essential parameters, e.g., gas residence time, total combustion time lag, sensitive time lag, and interaction index, are thus exhibited in a relationship involving experimentally measurable steady state and perturbed quantities.

A few additional modifications may be made to express the perturbations in a more conventional form; thus, if one forms an instantaneous fractional mixture ratio variation:

$$\frac{\mu_o}{\mu_f} = M e^{i\delta}$$

combines the two steady state mixture ratio parameters in the form:

$$H + 2K = R$$

and defines the ratio of fractional variations in one propellant injection rate to those of chamber pressure as the inverse transfer function of the

rocket motor, expressed in a complex form as:

$$\frac{M_F}{\Phi} = \frac{\tilde{M}_F e^{i\omega t}}{\Phi e^{i(\omega t - \beta_F)}} = R_F e^{i\beta_F}$$

Then the final combustion chamber equation for the simplified model becomes:

$$R_F e^{i\beta_F} \left\{ 1 + (\eta e^{i\delta} - 1) \left[ \left( \frac{1}{2} + \bar{r} \right) - K \left( 1 - \frac{i\omega l}{c^*} W_1 \right) e^{-i\omega \bar{t} \theta_g} \right] \right\} = \\ = e^{i\omega \bar{t}_T} \left[ \frac{i\omega \theta_g + 3\bar{r} - 1}{2\bar{r}} + \frac{i\omega l}{\bar{r} c^*} \left( W_1 - \frac{\bar{r}-1}{2} W_2 \right) - \left( \frac{r-1}{2\bar{r}} \right) \left( 1 - \frac{i\omega l}{c^*} W_1 \right) e^{-i\omega \bar{t} \theta_g} - \eta \left( 1 - e^{-i\omega \bar{t}} \right) \right] \quad (44)$$

Limitations of such a "black-box" approach have been pointed out earlier in the discussion. Their essential effect is to restrict the range of validity of the final equation to very low frequencies of oscillation. The following derivation, performed from a differential standpoint, represents a more refined physical model and is applicable over a higher frequency range. This treatment parallels that of Crocco and Cheng in the high frequency, so-called "intrinsic" case of oscillations in chamber pressure with constant injection flows. However, the present work extends the previous theories to include the derivation of a combustion chamber equation in the presence of small perturbations in both propellant flow rates. In a later step the frequency of oscillation is extrapolated from values in the vicinity of acoustic modes of vibration to a range an order of magnitude smaller and consistent with the scope of artificially produced flow rate fluctuations.

This refined theoretical model embodies substantial gains in generality over the simplified model, although it still retains the encumbrance of considering variations in instantaneous mixture ratio sufficiently small so as to have negligible effects on combustion distribution, time lags, and the generation of reflected waves at the nozzle. The major innovations of this model are: arbitrary distribution of the combustion process along the length of the chamber; introduction of liquid droplet mass, velocity, and

energy into the conservation equations; and the incorporation of acoustic wave travel considerations which admit the variation in both amplitude and phase of pressure and velocity perturbations along the chamber.

Certain restraining assumptions are introduced in order that the equations may be made amenable to reasonable analytical treatment. In addition to those of one-dimensionality and linearization of perturbations, the refined model contains two simplifications concerning the motion of liquid droplets in a streaming gas atmosphere. First, in describing the momentum of these droplets, a simple drag-type expression is employed in which an overall coefficient exists inversely proportional to a Reynolds' number based on droplet diameter. Effects of evaporation on the droplet dynamics are neglected; hence the droplet drag coefficient is considered constant. Second, the complicated transfer of energy to and from the liquid as a result of drag, evaporation, and thermal radiation and convection is treated by assuming that the loss in droplet kinetic energy is balanced by the gain in thermal energy in such a way that the stagnation enthalpy, per unit mass, of a particular droplet remains constant until the total mass of this droplet has been transformed into burned gas.

Operating under this framework of assumptions and following the notation of Crocco and Cheng (1), the equations for one-dimensional motion of the gas-liquid mixture within the combustion chamber may be written in a non-dimensional form as:

Conservation of mass:

$$\frac{\partial P}{\partial t} + \frac{\partial (Pw)}{\partial x} = \frac{\partial w}{\partial x} > - \frac{\partial P_g}{\partial t} - \frac{\partial (P_g u_g)}{\partial x} \quad ; \quad (45)$$

Conservation of momentum (neglecting wall friction):

$$\frac{\partial (Pw)}{\partial t} + \frac{\partial (Pw^2)}{\partial x} = - \frac{1}{T} \frac{\partial P}{\partial x} - \frac{\partial (P_g u_g)}{\partial t} - \frac{\partial (P_g u_g^2)}{\partial x} \quad (46)$$

Conservation of energy (neglecting wall heat transfer):

$$\rho \left( \frac{\partial h_s}{\partial t} + u \frac{\partial h_s}{\partial x} \right) = \frac{\gamma - 1}{\gamma} \frac{\partial P}{\partial t} - (h_s - h_{P_s}) \frac{\partial w}{\partial x} \quad (47)$$

Gas phase equation of state:

$$P = \rho R T \quad (48)$$

Droplet dynamics relation:

$$\frac{\partial u_s}{\partial t} + u_s \frac{\partial u_s}{\partial x} = k(u - u_e) \quad (49)$$

Droplet energy balance:

$$\frac{\partial h_{P_s}}{\partial t} + u_e \frac{\partial h_{P_s}}{\partial x} = 0 \quad (50)$$

The various quantities involved are defined by:

$x$  = axial distance from injector face

$t$  = dimensionless time

$\rho$  = density

$u$  = velocity

$w$  = rate of production of burned gas in the total volume  
between the injector face ( $x = 0$ ) and the station  $x$

$p$  = pressure

$\gamma$  = specific heat ratio of combustion gases (51)

$e$  = internal energy

$h$  = enthalpy

$T$  = temperature

$k$  = droplet drag coefficient,

and the subscripts are to be interpreted as follows:

$s$  = stagnation conditions

$l, p$  = liquid propellant properties

Reference values chosen for non-dimensionalization are those of the properties existing at the injector face, along with chamber length and the speed of sound,  $c_0$ , at the injector face. Enthalpies have been non-dimensionalized

by the quantity  $\frac{\gamma-1}{C_p^2} = \frac{\gamma-1}{\gamma RT_0}$ , so that under the assumptions of constant  $\gamma$  and  $C_p$  throughout the variations of gas temperatures involved, one may write:

$$dh = dT \quad \text{and} \quad \Delta h = \Delta T \quad (52)$$

Also, the quantity  $h_p$  represents a common value of the internal energy and enthalpy of the liquid phase, including the chemical energy of the propellants; and in expressing the gas phase stagnation enthalpy, use has been made of the energy-enthalpy relation in non-dimensional form:

$$\int \rho e_s = \int h_s - \frac{\gamma-1}{\gamma} p$$

In steady flow all time derivations are suppressed, and corresponding equations may be written subject to the boundary conditions at the injector,  $x = 0$ :

$$\begin{aligned} u &= 0; \rho = 1; p = 1; T = 1; u_i = \bar{u}_{i_0}; \\ w(0) &= 0; \bar{s}_{i_0} \bar{u}_{i_0} = w_i; h_p = h_{p_0} \end{aligned} \quad (53)$$

where  $w_i$  is the injection flow rate per unit cross-sectional area of the chamber. These steady-state quantities, indicated by a superscript bar, are related by:

$$\bar{\rho} \bar{u} = \bar{w} \quad \text{and} \quad \bar{s}_2 \bar{u}_2 = \bar{w}_i - \bar{w} \quad (54)$$

$$\bar{p} = 1 - \gamma (\bar{\rho} \bar{u}^2 + \bar{s}_2 \bar{u}_2^2 - \bar{s}_{i_0} \bar{u}_{i_0}^2) = 1 - \gamma \left[ \bar{w} (\bar{u} - \bar{u}_2) + \bar{w}_i (\bar{u}_2 - \bar{u}_{i_0}) \right] \quad (55)$$

$$\bar{h}_s = \bar{h} + \frac{\gamma-1}{2} \bar{u}^2 = \bar{h}_{p_{s_0}} = \bar{h}_o; \bar{\rho} = \bar{p} \bar{T} \quad (56)$$

$$\bar{u}_2 \frac{du}{dx} = K(\bar{u} - \bar{u}_2) \quad (57)$$

Rewriting Equation 56 with the help of Equation 52:

$$\bar{T} = 1 - \frac{\gamma-1}{2} \bar{u}^2 \quad (56a)$$

Employing this result, a relation between the steady-state burning rate and gas velocity is obtained (using the perfect gas law) in the form:

$$\bar{\rho} = \frac{P}{1 - \frac{\gamma-1}{2} \bar{u}^2} = \frac{\bar{w}}{\bar{u}} = \frac{1 - \gamma \bar{w}_i (\bar{u}_f - \bar{u}_{x_0})}{1 + \frac{\gamma+1}{2} \bar{u}^2 - \gamma \bar{u} \bar{u}_e} \quad (58)$$

Combustion will be restricted to the length of the chamber, with all burning complete at  $x = 1$ , the gas velocity having reached a final value  $\bar{u}_1$ .

From Equation 58, then:

$$\bar{w}_i = \bar{w}_i = \frac{\bar{u}_i}{1 + \frac{\gamma-1}{2} \bar{u}_i^2 - \gamma \bar{u}_i \bar{u}_{x_0}} \quad (59)$$

Sufficient relationships now exist in Equations 54 through 59 so that by specifying the distribution of steady gas velocity  $\bar{u}(x)$  only, the burning rate, temperature, pressure, density, and liquid velocity distributions may be calculated for any given injection flow rate and droplet drag coefficient.

Before proceeding to the unsteady equations of motion, one may determine some simplifying conditions from an analysis of the order of magnitude of the fundamental variables involved in the steady state framework. As a result of the choice of reference quantities for non-dimensionalization, the gas velocity  $\bar{u}_1$  at the end of the chamber is very nearly the Mach number,  $M$ , at that section and is therefore determined by the area ratio of the nozzle. For all practical motors, excluding throatless varieties, the value of  $M$  at the nozzle entrance is of the order 0.1; and this quantity may be used as an order of magnitude reference to which all other quantities will be compared. In such a range of values  $\bar{u}_1$  is approximately equal to  $M$ ; and for combustion gases in which the speed of sound is of the order of 3000 ft./sec.,  $\bar{u}_1^*$  will be approximately 300 ft./sec. From these rough figures and from the droplet dynamics Equation 57, one may deduce that within the scope of operational injector designs, the liquid velocity,  $\bar{u}_d$ , must also be at most of order  $M$

not only near injection but throughout the chamber. Figure 3 shows schematically the variation in  $\bar{u}_f$  to be expected from a typical  $\bar{u}(x)$ . The magnitude of the drag coefficient  $k$  may be deduced if one considers the extreme case  $\bar{u} = 0$ . Under such conditions, the droplets would come to rest at some distance down the chamber which may be called the "penetration distance" of the droplets. Taking half the chamber length as a safe estimate for this distance, the value of  $k$  becomes  $2\bar{u}_f$ , from Equation 57, which indicates that the actual range of values of  $k$  must be of order  $M$ .

With this information in mind, one finds from Equations 55 through 59 that, correct to terms of order  $M^2$ , indicated by the symbol  $O(M^2)$ :

$$\bar{T} = \bar{P} = \bar{f} = 1$$

and:

$$\bar{w} = \bar{u}$$

Also, from Equation 54,

$$\bar{f}_e \bar{u}_f = \bar{u}_f - \bar{u} + O(M^2)$$

Therefore,

$$\bar{f}_e = O(1) \quad (61)$$

An additional approximation may be made in the droplet enthalpy equation. So little information is available concerning the interaction between droplet velocity, droplet diameter, evaporation, and the combustion process in a two-phase system that the effects of non-uniformities of droplet size and perturbations of injection velocity on the droplet energy balance will be neglected, and the liquid stagnation enthalpy will be considered constant throughout the flow field. Thus:

$$h_{p_s} = h_p + \frac{\gamma-1}{2} u_f^2 - h_{p_{s_0}} = \text{constant} \quad (62)$$

Proceeding now to the derivation of perturbation equations, one treats each physical variable as the sum of a steady state component and a linear perturbation, sufficiently small so as to make terms of second or higher

order in these perturbations negligible. Considering only neutral oscillations and indicating perturbations by a superscript prime, one may write:

$$\frac{P'}{\phi(x)} = \frac{P'}{\sigma(x)} = \frac{P'_L}{\xi(x)} = \frac{U'}{\nu(x)} = \frac{W'}{g(x)} e^{st} \quad (63)$$

where  $s = i\omega$

Replacing the instantaneous values of Equations 45 and 46 with their linearized forms, subtracting the steady state equations, and introducing the notation of Equation 63, one obtains:

$$s\sigma + \frac{d}{dx}(\bar{P}\nu + \bar{U}\sigma) = \frac{d\phi}{dx} = -s\zeta - \frac{d}{dx}(\bar{P}_L\eta + \bar{U}_L\zeta) \quad (64)$$

$$s(\bar{P}\nu + \bar{U}\sigma) + \frac{d}{dx}(2\bar{P}\bar{U}\nu + \bar{U}^2\sigma) = \frac{1}{\gamma} \frac{d\phi}{dx} - s(\bar{P}_L\eta + \bar{U}_L\zeta) - \frac{d}{dx}(2\bar{P}_L\bar{U}_L\eta + \bar{U}_L^2\zeta) \quad (65)$$

The droplet energy Equations 47, 56, and 62, combine to give:

$$\frac{\partial}{\partial t}(\bar{P}h_s' - \frac{\gamma-1}{\gamma}P') = -\frac{\partial}{\partial x}(\bar{P}\bar{U}h_s) \quad (66)$$

$$\text{where the value of } h_s' = h' + (\gamma-1)\bar{U}U' = T' + (\gamma-1)\bar{U}U' \quad (67)$$

However:

$$T' = \frac{P' - \bar{T}\zeta'}{\bar{P}} \quad , \text{ from the equation of state,}$$

so:

$$\bar{P}h_s' = \bar{P}' - \bar{T}\zeta' + (\gamma-1)\bar{P}\bar{U}U' , \text{ from which Equation 66 becomes:}$$

$$s \left[ \frac{\phi}{\bar{P}} - \bar{T}\sigma + (\gamma-1)\bar{P}\bar{U}\nu \right] = -\frac{d}{dx} \left\{ \bar{U} \left[ \frac{\phi}{\bar{P}} - \bar{T}\sigma + (\gamma-1)\bar{P}\bar{U}\nu \right] \right\} \quad (68)$$

The droplet motion Equation 49 becomes:

$$\bar{U}_L \frac{d\eta}{dx} + \left( s + \frac{d\bar{U}_L}{dx} + k \right) \eta = k\nu \quad (69)$$

Boundary conditions at the injector end of the chamber ( $x = 0$ ) are as follows:

(a)  $u(0,t) = \bar{u}_0 = u'_0 = 0; \gamma(0) = 0$  for all  $t$ .

(b) Since no burning has yet occurred,  $\bar{w}(0) = w'(0) = g(0) = 0$

(c) For constant liquid bulk density  $\rho_{li}$  in the injector passages:

$$\rho_{li} A_i = \rho_{li} A_c \quad (70)$$

where  $A_i$  and  $A_c$  represent the areas of the total injector ports and the chamber, respectively.

Then:

$$\rho_{li} = \rho_{li} (A_i/A_c) = \text{constant, and } \xi(0) = 0.$$

(d)  $u'_e(0,t) = \eta(0) \neq 0$

At the nozzle end of the chamber ( $x = 1$ ), burning is complete, and:

$$\bar{\rho}_e = \rho'_e = 0; \frac{dg}{dx} = 0. \quad (71)$$

Five ordinary linear differential equations, e.g., 64, 65, 67, 68, 69, have thus been derived for the six perturbations,  $\phi, \sigma, \eta, \nu, \xi$ , and  $g$ . A sixth relation will be furnished by the burning rate equation in which the important time lag parameters are introduced. However, before proceeding to this final derivation, the existing equations are put into a form suitable for iterative solution by combining the variables into groups defined as follows:

$$X = (\gamma - 1) \bar{F} \bar{u} \frac{\nu}{\phi_0} + (1 - \bar{T}) \frac{\sigma}{\phi_0}$$

$$Y = \frac{g}{\phi_0} - \bar{u} \frac{\phi}{\phi_0} + (1 - \bar{F}) \frac{\nu}{\phi} - \bar{u} (1 - \bar{T}) \frac{\sigma}{\phi_0} - (\gamma - 1) \bar{F} \bar{u}^2 \frac{\nu}{\phi_0}$$

$$Z = \bar{u} \frac{\sigma}{\phi_0} - (1 - \bar{F}) \frac{\nu}{\phi_0} + \bar{F}_e \frac{\eta}{\phi_0} + \bar{u}_e \frac{\zeta}{\phi_0}$$

$$T = 2 \bar{F} \bar{u} \frac{\nu}{\phi_0} + 2 \bar{F}_e \bar{u}_e \frac{\eta}{\phi_0} + \bar{u}^2 \frac{\sigma}{\phi_0} + \bar{u}_e^2 \frac{\zeta}{\phi_0}$$

(72)

34.

where all perturbed quantities are compared to a reference value of the pressure fluctuations at the injector. In terms of these grouped variables, Equations 64 and 65 becomes:

$$\begin{aligned}\frac{d}{dx} \left( \frac{\nu}{\phi_0} \right) + s \frac{\phi}{\gamma \phi_0} &= -s X + \frac{dy}{dx} \\ \frac{d}{dx} \left( \frac{\phi}{\gamma \phi_0} \right) + s \frac{\nu}{\phi_0} &= -s Z - \frac{dT}{dx}\end{aligned}\quad (73)$$

which can be rewritten, with the addition of two new combined terms, E and F, in the more nearly symmetrical form:

$$\begin{aligned}\frac{d}{dx} \left( \frac{\nu}{\phi_0} - Y \right) + s \left( \frac{\phi}{\gamma \phi_0} + T \right) &= s(T - X) = SE \\ \frac{d}{dx} \left( \frac{\phi}{\gamma \phi_0} + T \right) + s \left( \frac{\nu}{\phi_0} - Y \right) &= -s(Y + Z) = -SF\end{aligned}\quad (74)$$

Treating E and F as if they were known functions of x, these equations are integrated directly to give:

$$\begin{aligned}\frac{\phi}{\gamma \phi_0} + T &= C_1 \sinh sx + C_2 \cosh sx - s \int_{x_0}^x [F(x') \cosh h(x-x') + E(x') \sinh s(x-x')] dx' \\ \frac{\nu}{\phi_0} - Y &= C_1 \cosh sx - C_2 \sinh sx + s \int_{x_0}^x [F(x') \sinh s(x-x') + E(x') \cosh s(x-x')] dx'\end{aligned}\quad (75)$$

The constants  $C_1$  and  $C_2$  are determined by evaluation of the various quantities at the injector boundary, where these conditions are given by Equation 70. Substituting these values into Equation 75 gives:

$$\frac{\phi}{\phi_0} = \left( 1 + 2 \bar{w}_L \frac{\gamma \eta_0}{\phi_0} \right) \cosh sx - \bar{\sigma} T(x) - \bar{\sigma} s \int_{x_0}^x [F(x') \cosh s(x-x') + E(x') \sinh s(x-x')] dx' \quad (76)$$

$$\frac{\nu}{\phi_0} = - \left( 1 + 2 \bar{w}_L \frac{\gamma \eta_0}{\phi_0} \right) \sinh sx + \bar{\sigma} Y(x) + \bar{\sigma} s \int_{x_0}^x [F(x') \sinh s(x-x') + E(x') \cosh s(x-x')] dx'$$

The additional relation between  $q(x)$  and the other variables arises from the burning rate equation, which is based upon the combustion time lag concepts discussed earlier. Consider the fraction of injected propellants burning in steady state between stations  $\bar{x}$  and  $\bar{x} + dx$ . Call this fraction  $\delta \bar{m}_b$  and assume that the time lag  $\bar{\tau}_T(\bar{x})$  which this fraction experienced in reaching  $\bar{x}$  is the same for all particles or elements within the fraction  $\delta \bar{m}_b$ , although it may differ for different fractions burning at stations other than  $\bar{x}$ . This fraction, then, was injected at time  $(t - \bar{\tau}_T)$  as a fraction  $\delta \bar{m}_i$  of the injector mass flow rate  $\bar{m}_i$ .

In the unsteady case, define a new fraction of injection mass flow rate,  $\delta \dot{m}_i$ , such that  $\delta \dot{m}_i$  is the same geometrical fraction of  $\dot{m}_i$  as  $\delta \bar{m}_i$  is of  $\bar{m}_i$ . Thus, the fraction of unsteady flow rate and the fraction of steady flow rate are considered as existing at geometrically similar positions within corresponding propellant streams in the injection pattern. This fraction  $\delta \dot{m}_i$  now experiences a time lag  $\tau_T(x)$  (in general different from  $\bar{\tau}_T(\bar{x})$ ) and finally burns between stations  $x$  and  $x + dx$ , producing a fractional burning rate  $\delta \dot{m}_b$ .

Having defined the relationship between  $\delta \dot{m}_i$  and  $\delta \bar{m}_i$  one must then express some relation between  $\tau_T(x)$  and  $\bar{\tau}_T(\bar{x})$ . For this purpose suppose that chamber and throat geometry are instantaneously varied in such a way that during the combustion of  $\delta \dot{m}_i$  the steady-state thermodynamic conditions exist, i.e.,  $p = \bar{p}$ ,  $T = \bar{T}$ , etc. Then  $\delta \dot{m}_i$  (which is shielded by other propellant elements in the same way as  $\delta \bar{m}_i$  and which experiences the same break-up of droplets and jet-spreading from hydraulic influences as does  $\delta \bar{m}_i$ ) is flowing through a gas atmosphere in the same thermodynamic state as that through which  $\delta \bar{m}_i$  flowed. The final transformation of propellant elements into hot gases can only take place after these elements have reached a well-determined energy level,  $E_a$ ; and the time required to

reach this level depends directly on the rates at which the energy transfer processes take place. These rates are primarily functions of pressure, temperature, mixture ratio, and relative velocities between fluid particles and gas. Since the relative velocity ( $u_g - u$ ) is determined by the burning rate distribution itself (which produces  $u$ ), its variation with changes in injection flow rate will probably be a second order quantity. Therefore, postulating constant mixture ratio even with varying injection flow, the rates of energy transfer to the droplets are all approximately the same for  $\bar{\delta}\dot{m}_i$  as for  $\bar{\delta}\dot{m}_i'$ , under the aforesaid hypothetical restriction of the same pressure and temperature in the two cases. This implies that under similar conditions the time required to transform the droplets into hot gases will be the same for  $\bar{\delta}\dot{m}_i$  as for  $\bar{\delta}\dot{m}_i'$ . That is,  $\tau_T(x) = \bar{\tau}_T(\bar{x})$ . It must be emphasized that even under these imposed conditions of similarity,  $x$  will not in general be equal to  $\bar{x}$ . Thus, if the velocity  $u_g$  of the droplets in  $\bar{\delta}\dot{m}_i$  is greater or less than the velocity  $\bar{u}_g$  of the droplets in  $\bar{\delta}\dot{m}_i'$ , the station  $x$  at which they burn will be correspondingly greater or less than  $\bar{x}$ , since the same time elapsed in both cases.

This assumption can be expressed mathematically by saying:

$$\text{when: } P = \bar{P}, T = \bar{T}, \rho = \bar{\rho}, \dot{m}_o / \dot{m}_F = \bar{\dot{m}}_o / \bar{\dot{m}}_F$$

$$\text{and: } \bar{\delta}\dot{m}_i / \dot{m}_i = \bar{\delta}\dot{m}_i' / \dot{m}_i' \quad (\text{both quantitatively and geometrically})$$

$$\text{then: } \tau_T(x) = \bar{\tau}_T(\bar{x})$$

where:  $\bar{\delta}\dot{m}_i$  burns at station  $x$ , and (77)

$$\bar{\delta}\dot{m}_i' \quad " \quad " \quad \bar{x}$$

and, in general:  $x \neq \bar{x}$

Proceeding to the derivation of a relation for  $q(x)$  from  $w(x,t)$  and  $\bar{w}(\bar{x})$ , one obtains from the definition of  $\bar{w}(\bar{x})$  as the rate of gas generation in all the volume between  $x = 0$  and  $x = \bar{x}$ ,

$$\delta \bar{m}_b = \frac{d\bar{w}(\bar{x})}{d\bar{x}} d\bar{x} \quad (78)$$

Similarly:

$$\delta \dot{m}_b = \frac{\partial w(x,t)}{\partial x} dx$$

However,  $\delta \bar{m}_b$  is the fraction of propellants injected at time  $(t - \bar{\tau}_T)(x)$ , hence:

$$\delta \bar{m}_b dt = \delta \dot{m}_i d(t - \bar{\tau}_T) = \delta \dot{m}_i dt \quad (79)$$

Now,  $\delta \dot{m}_b(t)$  was injected as  $\delta \dot{m}_i$  at time  $(t - \bar{\tau}_T)$ ; but the short interval of time  $dt$  during which  $\delta \dot{m}_b$  burns is not, in general, equal to the interval of time in which  $\delta \dot{m}_i$  was injected. Rather, as shown previously in Equation 12:

$$\delta \dot{m}_b(t) dt = \delta \dot{m}_i(t - \bar{\tau}_T) d(t - \bar{\tau}_T) \quad (80)$$

or:

$$\delta \dot{m}_b(t) = \delta \dot{m}_i(t - \bar{\tau}_T) \left(1 - \frac{dt}{d(t - \bar{\tau}_T)}\right)$$

Then, from the definition of  $\delta \dot{m}_i$  of Equations 77:

$$\delta \dot{m}_b(t) = \delta \bar{m}_i \frac{\dot{m}_i(t - \bar{\tau}_T)}{\bar{m}_i} \left(1 - \frac{dt}{d(t - \bar{\tau}_T)}\right)$$

or, substituting:

$$\dot{m}_i = \bar{m} + \dot{m}'$$

$$\delta \dot{m}_b(t) = \delta \bar{m}_i \left[ 1 + \frac{\dot{m}'(t - \bar{\tau}_T)}{\bar{m}_i} - \frac{dt}{d(t - \bar{\tau}_T)} \right] \quad (81)$$

which, employing the relations of Equations 78, becomes:

$$\frac{\partial w(x,t)}{\partial x} dx = \frac{d\bar{w}(\bar{x})}{d\bar{x}} d\bar{x} \left[ 1 + \frac{\dot{m}'(t - \bar{\tau}_T)}{\bar{m}_i} - \frac{dt}{d(t - \bar{\tau}_T)} \right] \quad (82)$$

In order to integrate both sides of this equation over the same total mass of propellants, one must integrate the right side over those fractions which burn

38.

in steady-state between 0 and  $\bar{x}$  and the left side over those fractions burning in unsteady-state between 0 and  $x$  ( $\bar{x}, t$ ), noting that  $\bar{w}(0) = w(0, t) = 0$  for all fractions. Then:

$$w(x, t) = \bar{w}(\bar{x}) - \int_0^{\bar{x}} \frac{dt}{dt} \frac{d\bar{w}(x')}{dx} dx' + \int_0^{\bar{x}} \frac{m_i'(t-t_T)}{m_i} \frac{d\bar{w}(x')}{dx'} dx' \quad (83)$$

From the time lag assumptions previously expressed by Equation 14:

$$\frac{dt}{dt} = -\frac{n}{P} \left\{ p'(x', t) - p' \left[ \xi(x'), t - \bar{\tau}(x') \right] \right\} \quad (84)$$

where  $\bar{\xi}(x)$  is the station at which an element burning in steady state at  $x$  begins the portion of its time lag which is sensitive to chamber conditions.

From this definition  $\bar{\xi}(x)$  and  $\bar{\tau}(x)$  are related by:

$$\int_{\xi(x)}^x \frac{dx'}{u_2(x')} = \bar{\tau}(x) \quad (85)$$

Now since  $w(x, t) = \bar{w}(x) + w'(x, t)$ , Equation 83 becomes:

$$w'(x, t) = \bar{w}(\bar{x}) - \bar{w}(x) - \int_0^{\bar{x}} \frac{dt}{dt} \frac{d\bar{w}(x')}{dx'} dx' + \int_0^{\bar{x}} \frac{m_i'(t-t_T)}{m_i} \frac{d\bar{w}(x')}{dx'} dx' \quad (86)$$

In order to find the relation between  $x$  and  $\bar{x}$ , the insensitive time lag is expressed as:

$$\bar{\tau}_i = \int_0^{\bar{\xi}} \frac{dx'}{u_2(x', t')} \quad (87)$$

, where  $t'$  is the time when

the element was at station  $x'$ .

That is:

$$u_e(x') = u_e \left[ x', t'(x') \right] = \bar{u}_e(x') + u'_e \left[ x', t'(x') \right]$$

However, since  $T_i = \frac{1}{U_i}$  constant,

$$\int_0^{\xi} \frac{dx'}{U_e(x')} = \int_0^{\xi} \frac{dx'}{U_e(\bar{x})} = \int_0^{\xi} \frac{dx'}{U_e(x')} + \int_{\xi}^{\bar{x}} \frac{dx'}{U_e(x')} \quad (88)$$

Neglecting higher order terms, since  $|\xi - \bar{x}| \ll 1$ ,

$$\int_{\xi}^{\bar{x}} \frac{dx'}{U_e(x')} = \frac{\bar{x} - \xi}{U_e(\bar{x})}$$

Then, Equation 88 becomes:

$$\frac{\xi}{\bar{x}} - \frac{\xi}{\bar{x}} = U_e(\bar{x}) \int_0^{\bar{x}} \frac{u'_e(x', t')}{U_e^2(x')} dx' \quad (89)$$

In the unsteady case, Equation 2 representing transfer of energy to the propellants by a rate function  $f$ , is expressed as:

$$\int_{\xi(x)}^x \frac{dx'}{U_e(x')} f(x') = E_a = \int_{\xi}^{\bar{x}} \frac{dx'}{U_e(x')} \bar{f}(x') - \bar{f} \int_{\xi}^{\bar{x}} \frac{dx'}{U_e(x')} \quad (90)$$

where:  $dt' = \frac{dx'}{U_e(x')}$  in the unsteady case.

The function  $f$  may be written as in Equation 4:

$$f(x') = f[x', t'(x')] = \bar{f}[1 + np'(x', t')] \quad (91)$$

where use has been made of Equation 60 for evaluation of  $\bar{p}$ . Splitting the integration of Equation 90 from  $\xi$  to  $\bar{x}$  into three parts and neglecting higher order terms, one obtains, as before:

$$\int_{\xi}^{\bar{x}} \frac{dx'}{U_e(x')} = \frac{\bar{x} - \xi}{U_e(\bar{x})} \quad \text{and} \quad \int_x^{\bar{x}} \frac{dx'}{U_e(x')} = \frac{\bar{x} - x}{U_e(x)}$$

so that after substitution of Equation 89, Equation 90 becomes:

40.

$$\int_{\xi}^x \frac{dx'}{u_2(x')} f(x') = \bar{f} \left[ \int_{\xi}^x \frac{1 + n p'(x', t')}{u_2(x', t')} dx' \right] \\ = \bar{f} \left[ \int_0^{\bar{x}} \frac{u'_2(x', t')}{\bar{u}'_2(x')} dx' + \frac{\bar{x} - x}{\bar{u}_2(x)} + \int_{\xi}^x \frac{dx'}{u_2(x')} \right] \quad (92)$$

from which the desired relation is derived:

$$x - \bar{x} = \bar{u}_2(x) \left[ \int_0^x \frac{u'_2(x', t')}{\bar{u}'_2(x')} dx' - n \int_{\xi}^x \frac{p'(x', t')}{\bar{u}_2(x')} dx' \right] \quad (93)$$

The first term in Equation 93 represents a shift in the instantaneous burning station due to a change in droplet velocity from that experienced in steady state, and the second term is the contribution of a changing time lag arising from fluctuations of the pressure around its steady value. Considering only terms of first order in the perturbations, one can evaluate the integrals in Equation 93 at  $\bar{x}$  and  $\xi$  instead of at  $x$  and  $\xi$ . Also, to this order of approximation:

$$\bar{w}(x) - \bar{w}(\bar{x}) = \frac{d\bar{w}(\bar{x})}{dx} (x - \bar{x}) \quad (94)$$

Substituting for  $(x - \bar{x})$  from Equation 93, replacing  $\bar{w}$  by its equivalent  $\bar{u}$  (from Equation 60), and inserting these terms plus the value of  $\frac{dt}{dt}$  into Equation 86 gives:

$$w'(x, t) = n \left\{ p'(x', t) - p' \left[ \xi(x'), t - \bar{T}(x') \right] \right\} \frac{d\bar{u}(x')}{dx'} dx' + \\ + \int_0^x \frac{m'_1[x', t - \bar{T}_1(x')]}{m'_1} \frac{d\bar{u}(x')}{dx'} dx' + \\ + \bar{u}_2 \frac{d\bar{u}(x)}{dx} \left\{ n \int_{\xi(x)}^x \frac{p[x', t'(x')]}{\bar{u}_2(x')} dx' - \int_0^x \frac{u'_2[x', t'(x')]}{\bar{u}'_2(x')} dx' \right\} \quad (95)$$

where the time  $t'$  is related to  $t$  by the equation

$$t'(x') = t - \int_{x'}^x \frac{dx''}{u_2[\bar{x}'', t''(x'')]} \quad (96)$$

which can be approximated by:

$$t'(x') = t - \int_{x'}^x \frac{dx''}{\bar{u}_e(x'')}, \quad (96)$$

since it is

only used in computations of the perturbations.

The expression for  $w'(x,t)$  given in Equation 95 consists of a first term due to time variations in the local burning rate, a term due to the variation in injection flow rate, and two terms due to the variation in locality of the burning station, one contributed by time lag variations and the other by a kinematic displacement, i.e., a change in "penetration" of the droplets.

In terms of the transformed perturbation variables of Equation 63, for exponential oscillations, this burning rate equation is:

$$\begin{aligned} \frac{\eta(x)}{\Phi_0} = & \eta \left[ \frac{\phi(x) - \phi(\tilde{x}) e^{-s\bar{T}(x')}}{\Phi_0} \right] \frac{d\bar{u}(x')}{dx'} dx' + \int_{x'}^x \frac{\eta_0 e^{-s\bar{T}(x')}}{\bar{u}_{e_0} \Phi_0} \frac{d\bar{u}(x')}{dx'} dx' + \\ & + \bar{u}_e(x) \frac{d\bar{u}(x)}{dx} \left\{ \eta \int_{\tilde{x}}^{x'} \frac{\phi(x')}{\tilde{x}\Phi_0 \bar{u}_e(x')} e^{\int_{\tilde{x}}^{x'} \frac{dx''}{\bar{u}_e(x'')}} dx' - \int_0^x \frac{\eta(x')}{\phi \bar{u}_e^2(x')} e^{\int_x^{x'} \frac{dx''}{\bar{u}_e(x'')}} dx' \right\} \end{aligned} \quad (97)$$

The required six equations in terms of the six perturbation variables have now been derived. Substitution and evaluation of the combined unknowns  $\bar{Y}(x)$ ,  $\bar{T}(x)$ ,  $\bar{E}(x)$ , and  $\bar{F}(x)$ , must be accomplished in order to reduce Equation 76 to a pair of simultaneous equations in two unknowns. The first step in this process might logically be solution of the droplet dynamics relation. This linear differential Equation 69 may be rewritten in the form:

$$\frac{d}{dx} (\bar{u}_e \eta) + \left( \frac{s+k}{\bar{u}_e} \right) (\bar{u}_e \eta) = k \nu \quad (98)$$

Multiplying both sides of the equation by an integrating factor,

$$e^{(s+k) \int_0^x \frac{dx'}{\bar{u}_e(x')}}$$

the left-hand side becomes an exact differential; and the equation is immediately integrable. The boundary condition expressing oscillation of injector flow rates is simply: at  $x = 0, \eta = \eta_0, \bar{u}_e = \bar{u}_{e_0}$ , from which the solution of Equation 98 is:

$$\eta(x) = \frac{k}{\bar{u}_e(x)} \int_0^x \nu(x') e^{(s+k) \int_{x'}^x \frac{dx''}{\bar{u}_e(x'')}} dx' + \frac{\eta_0 \bar{u}_{e_0}}{\bar{u}_e(x)} e^{-(s+k) \int_0^x \frac{dx'}{\bar{u}_e(x')}} \quad (99)$$

Substituting this result into Equation 97, making use of the definition of average total time lag of a particle burning at location  $x$ , namely:

$$\bar{\tau}_T(x) = \int_0^x \frac{dx'}{\bar{u}_e(x')}$$

the burning rate equation becomes:

$$\begin{aligned} \frac{f(x)}{\phi_0} &= \eta Q(x) + \frac{\eta_0}{\phi_0 \bar{u}_{e_0}} \int_0^x e^{-s\bar{\tau}_T(x')} \frac{d\bar{u}_e(x')}{dx'} dx' + \eta \bar{u}_e(x) \frac{d\bar{u}_e(x)}{dx} \int_0^x \frac{\phi(x')}{\bar{u}_e(x')} e^{s \int_{x'}^x \frac{dx''}{\bar{u}_e(x'')}} dx' - \\ &- k \bar{u}_e(x) \frac{d\bar{u}_e(x)}{dx} e^{-s\bar{\tau}_T(x)} \int_0^x \frac{e^{-k\bar{\tau}_T(x')}}{\bar{u}_e^3(x')} dx' \int_0^{x'} \frac{\nu(x'')}{\phi} e^{(s+k)\bar{\tau}_T(x'')} dx'' - \\ &- \frac{\eta_0 \bar{u}_{e_0}}{\phi_0} \bar{u}_e(x) \frac{d\bar{u}_e(x)}{dx} e^{-s\bar{\tau}_T(x)} D(x) \end{aligned} \quad (100)$$

whereas

$$Q(x) = \int_0^x \left\{ \frac{\phi(x') - \phi[\bar{\tau}_T(x')] e^{-s\bar{\tau}_T(x')}}{\phi_0} \right\} \frac{d\bar{u}_e(x')}{dx'} dx' \quad (101)$$

is a quantity directly related to the pressure sensitivity of the burning rate, and:

$$D(x) = \int_0^x \frac{e^{-k\bar{\tau}_T(x')}}{\bar{u}_e^3(x')} dx' \quad (102)$$

is a term involving the effects of droplet drag on the oscillation in burning station of a propellant element.

A number of terms in the burning rate equation as well as in the combined Equations 76 become considerably simplified if one performs an order of magnitude analysis on the quantities contained therein.

For this purpose, it is assumed that steady state combustion is sufficiently distributed so that maximum local values of  $\frac{d\bar{u}}{dx}$  are of order unity; that the dimensional sensitive time lag,  $\bar{\tau}^*$ , is of the order of the wave propagation time, hence  $\bar{\tau}$  is of order unity; and, furthermore, that:

$$\frac{\phi}{\phi_0}, \frac{\sigma}{\phi_0}, \frac{1}{\phi_0}, \frac{1}{\phi_0} \frac{d\phi}{dx}, \frac{1}{\phi_0} \frac{d\nu}{dx} = O(1). \quad (103)$$

For  $\bar{\tau}(x) = O(1)$  Equation 85 shows:

$$\frac{x - \bar{\xi}(x)}{\bar{\tau}_*(x)} = \bar{\tau}(x) + O(M)$$

or:

$$x - \bar{\xi}(x) = \bar{\tau}_*(x) \bar{\tau}(x) + O(M) = O(M)$$

The pressure oscillation at a particular burning station,  $x$ , can differ from that at the beginning of the corresponding sensitive time lag by a quantity at most of  $O(M)$ , since (by virtue of 103):

$$\begin{aligned} \frac{\phi(x)}{\phi_0} &= \frac{\phi[\bar{\xi}(x)]}{\phi_0} + \frac{1}{\phi_0} \left( \frac{d\phi}{dx} \right)_{x=\bar{\xi}} (x - \bar{\xi}) + O(M^2) \\ \text{or: } \frac{\phi(x) - \phi[\bar{\xi}(x)]}{\phi_0} &= \frac{1}{\phi_0} \left( \frac{d\phi}{dx} \right)_{x=\bar{\xi}} (x - \bar{\xi}) = E(x) = O(M), \end{aligned} \quad (104)$$

Insertion of this relation into Equation 101 then gives:

$$Q(x) = \int_0^x \frac{\phi(x')}{\phi_0} \left[ 1 - e^{-s\bar{\tau}(x')} \right] \frac{d\bar{u}(x')}{dx'} dx' + \int_0^x E(x') e^{-s\bar{\tau}(x')} \frac{d\bar{u}(x')}{dx'} dx' \quad (105)$$

---

<sup>1</sup> Crocco (1) has shown this to be true for moderate  $\omega$  when  $\rho$  is not too large.

For the neutral oscillation condition specified, where  $s = i\omega$ :

$$e^{-s\bar{\tau}(x')} = O(1)$$

Hence, because  $\frac{d\bar{u}(x')}{dx'}$  integrates to a quantity of  $O(M)$ , the second integral in 105 is of  $O(M^2)$  and may be neglected, giving:

$$Q(x) = \int_0^x \frac{\phi(x')}{\phi_0} \left[ 1 - e^{-s\bar{\tau}(x')} \right] \frac{d\bar{u}(x')}{dx'} dx' = O(M) \quad (106)$$

A similar simplification is applied to the third term of Equation 100.

In this term, the variable of integration,  $x'$ , lies between  $x$  and  $\xi(x)$ . Then:

$$(x-x') \leq x - \xi(x) = O(M)$$

and:

$$\phi(x) = \phi(x') + \left( \frac{d\phi}{dx} \right)_{x=x'} (x-x') + O(M^2)$$

from which the term in question is written:

$$\eta \bar{u}_e \frac{d\bar{u}}{dx} \int_{\xi(x)}^{x'} \frac{\phi(x')}{\phi_0 \bar{u}_e(x')} e^{\int_{\bar{u}_e(x')}^{x'} \frac{dx''}{\bar{u}_e(x'')}} dx' = \eta \bar{u}_e \frac{d\bar{u}}{dx} \frac{\phi(x)}{\phi_0} \int_{\xi(x)}^x \left[ 1 - \frac{1}{\phi_0} \left( \frac{d\phi}{dx} \right)_{x'} (x-x') \right] e^{\int_{\bar{u}_e(x')}^x \frac{dx''}{\bar{u}_e(x'')}} \frac{s \int_{\bar{u}_e(x')}^{x'} \frac{dx''}{\bar{u}_e(x'')}}{\bar{u}_e(x')} dx'$$

The first portion of this integration may be performed directly; and for the purpose of order of magnitude determination a proper mean value of the integrand will be removed from the integral, yielding:

$$\begin{aligned} \eta \bar{u}_e \frac{d\bar{u}}{dx} \int_{\xi(x)}^{x'} \frac{\phi(x')}{\phi_0 \bar{u}_e(x')} e^{\int_{\bar{u}_e(x')}^{x'} \frac{dx''}{\bar{u}_e(x'')}} dx' &= \frac{\eta \bar{u}_e(x)}{s} \frac{\phi(x)}{\phi_0} \left[ 1 - e^{-s \int_{\xi(x)}^x \frac{dx'}{\bar{u}_e(x')}} \right] \frac{d\bar{u}(x)}{dx} - \\ - \eta \bar{u}_e \frac{d\bar{u}}{dx} \frac{\phi(x)}{\phi_0} \left[ \frac{1}{\bar{u}_e \phi_0} \frac{d\phi}{dx} \right] &\int_{\xi(x)}^x (x-x') e^{\int_{\bar{u}_e(x')}^x \frac{dx''}{\bar{u}_e(x'')}} dx' \end{aligned} \quad (107)$$

The barred, bracketed quantity represents the mean value chosen and is of  $O(1/M)$ . Since the exponential interior integral is at most of  $O(1)$ , the maximum value of the second term of 107 is:

$$\bar{n} \bar{u}_e(x) \frac{d\bar{u}(x)}{dx} \frac{\phi(x)}{\phi_0} \left[ \frac{1}{\bar{u}_e \phi_0} \frac{d\phi}{dx} \right] \frac{[x - \bar{x}(x)]^2}{2},$$

which, from Equation 103 and the discussion immediately following it, is of  $O(M^2)$ . Thus:

$$\begin{aligned} & \bar{n} \bar{u}_e(x) \frac{d\bar{u}(x)}{dx} \int_{\bar{x}(x)}^x \frac{\phi(x')}{\phi_0} \frac{1}{\bar{u}_e(x')} e^{\int_x^{x'} \frac{dx''}{\bar{u}_e(x'')}} dx' = \\ & = \bar{n} \bar{u}_e(x) \frac{d\bar{u}(x)}{dx} \frac{\phi(x)}{\phi_0} \left[ 1 - e^{-s \bar{x}(x)} \right] + O(M^2) \end{aligned} \quad (108)$$

The order of magnitude of injection velocity perturbations is determined by the size of mass flow oscillations as follows:

$$\dot{m}_0 = \bar{m} + \dot{m}'_0 = \bar{P}_{e_0} \bar{u}_{e_0} A_c = (\bar{P}_{e_0} + \dot{P}'_{e_0})(\bar{u}_{e_0} + u'_{e_0}) A_c$$

$$\text{so that: } \dot{m}'_0 = (\dot{P}_{e_0} u'_{e_0} + \bar{m}_{e_0} \dot{P}'_{e_0}) A_c$$

or, if:  $\dot{m}'_0 = m_0 e^{st}$ , then the fractional perturbation of injected mass flow becomes:

$$\frac{\dot{m}_c}{\bar{m}} = \frac{\eta_1}{\bar{u}_{e_0}} + \frac{\zeta_0}{\bar{P}_{e_0}}$$

However, from Equations 70,

$$\zeta_0 = 0$$

Hence:

$$\frac{\dot{m}_c}{\bar{m}} = \frac{\eta_1}{\bar{u}_{e_0}} \quad (109)$$

The actual magnitude of mass flow fluctuations in the injected streams is arbitrary, since these are to be artificially produced in the laboratory. In the present program, the fractional flow rate oscillations will be limited to the same order of magnitude as the fractional pressure perturbations. Then:

$$\frac{m}{\dot{m}} = O\left(\frac{\phi_0}{P}\right)$$

or, since

$$\bar{P} = 1 + O(M^2), \quad \frac{\eta_0}{\bar{U}_0 \phi_0} = O(1), \quad (110)$$

and:

$$\frac{\eta_0}{\phi_0} = O(M)$$

An inspection of Equation 102 shows that the droplet drag integral  $D(x) = O(1/M^3)$ , so that the final term of Equation 100 is of  $O(1)$ .

Combining the results of Equations 104 through 110, the burning rate equation becomes:

$$\begin{aligned} \frac{g(x)}{\phi_0} = & n Q(x) + \frac{\eta_0}{\phi_0 \bar{U}_0} \int_0^x e^{-s\bar{E}_T(x')} \frac{d\bar{U}(x')}{dx'} dx' + \\ & + \bar{U}_0(x) \frac{d\bar{U}}{dx} \left\{ \frac{n}{s} \frac{\phi(x)}{\phi_0} \left[ 1 - e^{-s\bar{E}_T(x)} \right] - \frac{\eta_0 \bar{U}_0}{\phi_0} D(x) e^{-s\bar{E}_T(x)} \right. - \\ & \left. - k e^{-s\bar{E}_T(x)} \int_0^x \frac{dD(x')}{dx'} dx' \int_0^{x'} \frac{v_{C(x'')}}{\phi_0} e^{(s+k)\bar{E}_T(x'')} dx'' \right\} \end{aligned} \quad (111)$$

where:

$$Q(x) = \int_0^x \frac{\phi(x')}{\phi_0} \left[ 1 - e^{-s\bar{E}_T(x')} \right] \frac{d\bar{U}(x')}{dx'} dx'$$

and  $D(x)$  is given by Equation 102.

The order of magnitude of the first two terms and the initial expression within the brackets is  $O(M)$ ; the second contribution inside the brackets is  $O(1)$ ; and the final expression is of an order not yet determined, but which is shown by inspection to be not greater than  $O(1/M)$ .

The order of magnitude analysis may now be extended to treat the combined variables  $E(x)$  and  $F(x)$  appearing in the two basic Equations 76. From the definitions in Equations 72 and 74 and the order of magnitude assumptions and determinations of the preceding pages, these may be written:

$$E(x) = \frac{\gamma(x)}{\phi_0} \bar{J}(x) \frac{\psi(x)}{\phi_0} + \bar{J}_2(x) \frac{\eta(x)}{\phi_0} + \bar{u}_2(x) \frac{\varphi(x)}{\phi_0} + O(M^2) \quad (112)$$

$$E(x) = (3-\gamma) \bar{u}(x) \frac{\psi(x)}{\phi_0} + \bar{J}_2(x) \bar{u}_2(x) \frac{\eta(x)}{\phi_0} + \bar{u}_2(x) \frac{\varphi(x)}{\phi_0} + O(M^2) \quad (113)$$

For the case of neutral oscillations of moderate frequencies,

$s = i\omega = O(1)$ , the final terms in Equations 76 are of the form:

$$\int_0^x \gamma s F(x') e^{\pm s(x-x')} dx' ; \int_0^x \gamma s E(x') e^{\pm s(x-x')} dx' ,$$

so that the orders of magnitude of the unknowns will be analyzed in this integral context. The initial quantity of interest is, then:

$$\int_0^x \gamma s \frac{q(x)}{\phi_0} e^{\pm s(x-x')} dx'$$

which is broken up into five contributing terms by Equation 111. The first of these is:

$$\int_0^x \gamma s \eta Q(x) e^{\pm s(x-x')} dx' = \gamma n \int_0^x e^{\pm s(x-x')} dx' \int_0^{x'} \left[ \frac{\psi(x')}{\phi_0} \left[ 1 - e^{-s\bar{\tau}_0} \right] \right] \frac{d\bar{u}(x')}{dx'} dx' \quad (114)$$

The interior integral produces an expression of maximum  $O(M)$ ; and for  $n$  of  $O(1)$ , as may be expected for most of the physical processes involved, the entire term is of  $O(M)$ . The second term is also  $O(n)$ , appearing in the form:

$$\frac{\gamma s \eta_0}{\bar{u}_2 \phi_0} \int_0^x e^{\pm s(x-x')} dx' \int_0^x e^{-s\bar{\tau}_T(x')} \frac{d\bar{u}(x')}{dx'} dx' \quad (115)$$

The third term becomes:

$$\gamma n \int_0^x \bar{u}_2(x) \frac{d\bar{u}(x')}{\phi_0} \left[ 1 - e^{-s\bar{\tau}(x')} \right] e^{\pm s(x-x')} \frac{d\bar{u}(x')}{dx'} dx' = O(M^2) \quad (116)$$

since the maximum value of both exponential terms appearing in the integrand is 1.0.

$$\frac{rs\eta_0\bar{\eta}_L}{\phi_0} \int_0^x D(x') \bar{\eta}_L(x') \frac{d\bar{\eta}(x')}{dx'} e^{-s[\bar{\tau}_T(x')\bar{\tau}(x-x')]} dx'$$

The fourth term of this burning rate contribution is:

$$\text{Here } D(x') = O(1/M^3), \bar{\eta}_L(x') = O(M), \frac{\eta_0\bar{\eta}_L}{\phi_0} = O(M^2), \text{ and the}$$

maximum value of the exponential factor is again 1.0. Therefore:

$$\frac{rs\eta_0\bar{\eta}_L}{\phi_0} \int_0^x D(x') \bar{\eta}_L(x') \frac{d\bar{\eta}(x)}{dx'} e^{-s[\bar{\tau}_T(x')\bar{\tau}(x-x')]} dx' \leq \frac{rs\eta_0\bar{\eta}_L}{\phi_0} \left[ D(x') \bar{\eta}_L(x') \right]_{\text{MAX}} \bar{\tau}(x) = O(M)$$

where the maximum value of the first three factors of the integrand has been removed from beneath the integral for the purpose of order of magnitude evaluation.

The final term will be retained in its original form for the

present, resulting in:

$$rk \int_0^x \bar{\eta}_L(x') \frac{d\bar{\eta}(x')}{dx'} e^{-s[\bar{\tau}_T(x')\bar{\tau}(x-x')]} dx' \int_0^{x''} \frac{dD(x'')}{dx''} dx'' \int_0^{x'''} \bar{\eta}_L(x'') \frac{2V(x''')}{\phi_0} e^{k\bar{\tau}_T(x''')} d \left[ e^{s\bar{\tau}_T(x''')} \right] \quad (118)$$

which is at most of  $O(M)$ , depending upon the integrated value of  $\frac{2V(x)}{\phi_0}$ .

Collecting all the terms from the burning rate relation as expressed by Equations 114 through 118, one obtains:

$$\begin{aligned} & \int_0^x \frac{rs\beta(x)}{\phi_0} e^{\pm s(x-x')} dx' = rs \int_0^y e^{\pm s(x-x')} dx' \int_0^{x'} \frac{d(x'')}{\phi_0} \left[ 1 - e^{-s\bar{\tau}(x'')} \right] \frac{d\bar{\eta}(x'')}{dx''} dx'' + \\ & \frac{rs\eta_0}{\bar{\eta}_L \phi_0} \int_0^x e^{\pm s(x-x')} dx' \int_0^{x'} \frac{-s\bar{\tau}_T(x'') \frac{d\bar{\eta}(x'')}{dx''}}{D(x'')} dx'' - \frac{rs\eta_0\bar{\eta}_L}{\phi_0} \int_0^x D(x') \bar{\eta}_L(x') \frac{d\bar{\eta}(x')}{dx'} e^{-s[\bar{\tau}_T(x')\bar{\tau}(x-x')]} dx' - \\ & - rk \int_0^x \bar{\eta}_L(x') \frac{d\bar{\eta}(x')}{dx'} e^{-s[\bar{\tau}_T(x')\bar{\tau}(x-x')]} dx' \int_0^{x''} \frac{dD(x'')}{dx''} dx'' \int_0^{x'''} \bar{\eta}_L(x''') \frac{2V(x''')}{\phi_0} e^{k\bar{\tau}_T(x''')} d \left[ e^{s\bar{\tau}_T(x''')} \right]. \end{aligned} \quad (119)$$

The next term of Equation 112 to be evaluated is:

$$\int_0^x \gamma s \bar{u}(x') \left[ \frac{\phi(x') - \sigma(x')}{\phi_0} \right] e^{\pm s(x-x')} dx'$$

Rewriting Equation 68, neglecting terms of  $O(M^2)$ :

$$\frac{\phi - \sigma}{\phi_0} = \frac{\gamma-1}{\gamma} \left( \frac{\phi}{\phi_0} + \bar{u} \frac{\gamma \nu}{\phi_0} \right) - \frac{1}{S} \frac{d}{dx} \left[ \bar{u} \left( \frac{\phi - \sigma}{\phi_0} + \frac{\gamma-1}{\gamma} \bar{u} \frac{\gamma \nu}{\phi_0} \right) \right]$$

Multiplying by the factors  $\gamma s \bar{u}(x') e^{\pm s(x-x')}$  and integrating gives:

$$\begin{aligned} & \int_0^x \gamma s \bar{u}(x') \left[ \frac{\phi(x') - \sigma(x')}{\phi_0} \right] e^{\pm s(x-x')} dx' = (\gamma-1) S \int_0^x \bar{u}(x') \frac{\phi(x')}{\phi_0} e^{\pm s(x-x')} dx' + \\ & + (\gamma-1) S \int_0^x \frac{\gamma \nu(x')}{\phi_0} \bar{u}'(x') e^{\pm s(x-x')} dx' - S \int_0^x \bar{u}(x') e^{\pm s(x-x')} \frac{d}{dx'} \left[ \bar{u} \left( \frac{\phi - \sigma}{\phi_0} + \frac{\gamma-1}{\gamma} \bar{u} \frac{\gamma \nu}{\phi_0} \right) \right] dx' \end{aligned}$$

The quantities  $\frac{\nu}{\phi_0}$ ,  $\frac{\phi}{\phi_0}$ , and  $\frac{\sigma}{\phi_0}$  have been assumed of  $O(1)$  in Equation 103.

Therefore, the last two terms are of  $O(M^2)$ , since integration produces at most the product of  $\bar{u}^2(x)$  times a quantity of  $O(1)$ . Then:

$$\int_0^x \gamma s \bar{u}(x') \left[ \frac{\phi(x') - \sigma(x')}{\phi_0} \right] e^{\pm s(x-x')} dx' = (\gamma-1) S \int_0^x \bar{u}(x') \frac{\phi(x')}{\phi_0} e^{\pm s(x-x')} dx' + O(M^2) \quad (120)$$

The third term of  $F(x)$  contributes an integral expression of the form:

$$\int_0^x \gamma s \bar{P}_L(x') \frac{\eta(x')}{\phi_0} e^{\pm s(x-x')} dx'$$

Substituting for the perturbation  $\frac{\eta(x')}{\phi_0}$  from Equation 99, this contribution becomes:

$$\gamma s k \int_0^x \frac{\bar{P}_L(x')}{\bar{u}_L(x')} e^{\pm s(x-x') - (s+k) \bar{\tau}_T(x')} dx' \int_0^{x'} \frac{\gamma \nu(x'')}{\phi_0} e^{(s+k) \bar{\tau}_T(x'')} dx'' + \frac{\gamma s \eta_0 \bar{u}_{L0}}{\phi_0} \int_0^x \frac{\bar{P}_L(x')}{\bar{u}_L(x')} e^{\pm s(x-x') - (s+k) \bar{\tau}_T(x')} dx'$$

Since  $\bar{\rho}_L(x) = 0(1)$  by Equation 61, and since the drag coefficient,  $k$ , is always positive,

$$\bar{\rho}_L(x') e^{\pm s(x-x')} - k \bar{\tau}_T(x') \leq O(1)$$

Therefore:

$$\begin{aligned} \left\{ \int_0^x \gamma s \bar{\rho}_L(x') \frac{\eta(x'')}{\phi_0} e^{\pm s(x-x'')} dx' \right\} &\leq O \left\{ -k \int_0^x \frac{d}{dx'} \left[ e^{-s \bar{\tau}_T(x')} \right] dx' \int_0^{x''} \frac{\gamma(x'')}{\phi_0} e^{(s+k) \bar{\tau}_T(x'')} dx'' + \right. \\ &\quad \left. + \frac{\gamma \eta_0 \bar{u}_L \phi_0}{\phi_0} \int_0^x \frac{d}{dx'} \left[ e^{-s \bar{\tau}_T(x')} \right] dx' \right\} \end{aligned} \quad (121)$$

From Equation 103,  $\frac{\nu(x'')}{\phi_0} = O(1)$ , and the first term of 121 is at most of  $O(M)$ .

The second term, based on Equation 110, is of  $O(M^2)$ ; and the resulting expression may be written:

$$\begin{aligned} &\int_0^x \gamma s \bar{\rho}_L(x') \frac{\eta(x')}{\phi_0} e^{\pm s(x-x')} dx' = \\ &= \gamma k s \int_0^x \frac{\bar{\rho}_L(x')}{\bar{u}_L(x')} e^{\pm s(x-x')} dx' \int_0^x \frac{\gamma(x'')}{\phi_0} e^{-(s+k)} \left[ \bar{\tau}_T(x'') - \bar{\tau}_T(x') \right] dx'' + O(M^2) = O(M) \end{aligned} \quad (122)$$

The final term contributing to the integrated form of  $F(x)$  is:

$$\int_0^x \gamma s \bar{u}_L(x') \frac{\xi(x')}{\phi_0} e^{\pm s(x-x')} dx'$$

The order of magnitude of the perturbation variable  $\xi(x')/\phi_0$  is determined from the right-hand side of Equation 64, rewritten as:

$$\frac{d}{dx} \left( \bar{u}_L \frac{\xi}{\phi_0} \right) + \frac{s}{\bar{u}_L} \left( \bar{u}_L \frac{\xi}{\phi_0} \right) = -\frac{1}{\phi_0} \frac{dq}{dx} - \frac{d}{dx} \left( \bar{\rho}_L \frac{\eta}{\phi_0} \right)$$

Direct integration of this differential equation subject to the boundary condition  $\xi(0)=0$ , produces the result:

$$\frac{\bar{u}_\ell \bar{s}(x)}{\phi_0} = -e^{-s\bar{\tau}_T(x)} \int_0^x \left[ \frac{1}{\phi_0} \frac{d q_\ell(x')}{dx'} + \frac{d}{dx'} \left( \bar{\beta}(x') \frac{\eta(x')}{\phi_0} \right) \right] e^{s\bar{\tau}_T(x')} dx'$$

or:

$$\frac{s \bar{u}_\ell \bar{s}(x)}{\phi_0} = -e^{-s\bar{\tau}_T(x)} \int_0^x \frac{\bar{u}_\ell(x')}{\phi_0} \frac{d q_\ell(x')}{dx'} - \frac{d}{dx'} \left[ e^{s\bar{\tau}_T(x')} \right] dx - s e^{-s\bar{\tau}_T(x)} \int_0^x e^{s\bar{\tau}_T(x')} \frac{d}{dx'} \left[ \bar{\beta} \frac{\eta(x')}{\phi_0} \right] dx \quad (123)$$

The order of magnitude of  $\frac{1}{\phi_0} \frac{d q_\ell}{dx}$  is found from the left-hand side of Equation 64 to be:

$$\frac{1}{\phi_0} \frac{d q_\ell(x)}{dx} = \frac{s \sigma(x)}{\phi_0} + \frac{1}{\phi_0} \frac{d u(x)}{dx} + \frac{d}{dx} \left[ \bar{u}(x) \frac{\sigma(x)}{\phi_0} \right] = O(1)$$

where the magnitude of the final term is determined from Equation 68 as  $O(1)$ .

Then, by virtue of Equation 103, all terms in the expression for  $\frac{1}{\phi_0} \frac{d q_\ell}{dx} = O(1)$ , and the contribution of the first integral of Equation 123 is  $O(M)$ .

The value of the second integral in this equation is obtained from an integration by parts of 99. Thus:

$$\begin{aligned} \frac{\eta(x)}{\phi_0} \cdot \frac{k}{5} \left\{ \frac{z(x)}{\phi_0} - \frac{e^{-(s+k)\bar{\tau}_T(x)}}{\bar{u}_\ell(x)} \int_0^x \frac{(s+k)\bar{\tau}_T(x')}{dx'} \left[ \frac{\nu(x')}{\phi_0} \left( k + \frac{d \bar{u}_\ell}{dx} \right) + \frac{\bar{u}_\ell(x')}{\phi_0} \frac{d \nu(x')}{dx'} \right] \right\} + \\ + \frac{\gamma_0 \bar{u}_{L0}}{\phi_0 \bar{u}_\ell(x)} e^{-(s+k)\bar{\tau}_T(x)} \end{aligned} \quad (124)$$

In this relation, all terms are of  $O(M)$ , for moderate values of  $s$ ; hence the second integral of 123 will also be  $O(M)$ . Then:

$$\bar{u}_\ell(x) \frac{\bar{s}(x)}{\phi_0} = O(M) \text{ for } s = O(1)$$

and:

$$\frac{\bar{s}(x)}{\phi_0} = O(1)$$

(125)

With this order of magnitude in mind, Equation 64 will be multiplied

52.

by  $\gamma \bar{u}_L(x') e^{\pm s(x-x')}$

and integrated to give:

$$\int_0^x \gamma s \bar{u}_L(x') \frac{5(x')}{\phi_0} e^{\pm s(x-x')} dx' = -\gamma \int_0^x \frac{\bar{u}_L(x')}{\phi_0} \frac{d\eta(x)}{dx'} e^{\pm s(x-x')} dx' - \\ - \gamma \int_0^x \bar{u}_L(x') e^{\pm s(x-x')} \frac{d}{dx'} \left[ \bar{p}_L(x') \frac{\eta(x')}{\phi_0} \right] dx' - \gamma \int_0^x \bar{u}_L(x') e^{\pm s(x-x')} \frac{d}{dx'} \left[ \bar{u}_L(x') \frac{5(x')}{\phi_0} \right] dx' \quad (126)$$

With the orders of magnitude of both  $\bar{p}_L(x) \eta(x)/\phi_0$  and  $\bar{u}_L(x) 5(x)/\phi_0$  given by Equations 124 and 125 as  $O(M)$ , integration by parts of the last two terms in 126 indicates their contributions will be  $O(M^2)$  and may be neglected. Similarly, any terms of  $O(M)$  contributing to  $\frac{\eta(x)}{\phi_0}$  will produce negligibly small terms when integrated as a part of the first term of 126. Employing Equation 111 and retaining only terms of  $O(1)$ , one obtains:

$$\int_0^x \gamma s \bar{u}_L(x') \frac{5(x')}{\phi_0} e^{\pm s(x-x')} dx' = \frac{\gamma \eta_0 \bar{u}_{L0}}{\phi_0} \bar{u}_L^2(x) \frac{d\bar{u}(x)}{dx} D(x) e^{-s\bar{u}_T(x)} + \\ + \gamma \int_0^x \frac{\eta(x')}{\phi_0} e^{\pm s(x-x')} \left[ \frac{d\bar{u}_L(x')}{dx'} \mp s\bar{u}_L(x') \right] dx' \quad (127)$$

An examination of Equation 119 shows that:

$$\int_0^x \gamma s \frac{\eta(x')}{\phi_0} e^{\pm s(x-x')} dx' = O(M)$$

so that the final integration of 127 will produce only terms of  $O(M^2)$ .

Then:

$$\int_0^x \gamma s \bar{u}_L(x') \frac{5(x')}{\phi_0} e^{\pm s(x-x')} dx' = \frac{\gamma \eta_0 \bar{u}_{L0}}{\phi_0} \bar{u}_L^2(x) \frac{d\bar{u}(x)}{dx} D(x) e^{-s\bar{u}_T(x)} + O(M^2) \quad (128)$$

and is of  $O(M)$  for all moderate values of  $s$ .

Collecting all the terms contributing to  $F(x)$  from Equations 114

through 128, one writes:

$$\begin{aligned}
 & \int_0^x \gamma S F(x') e^{\pm s(x-x')} dx' = \gamma S \int_0^x e^{\pm s(x-x')} dx' \int_0^{x'} \frac{\phi(x'')}{\phi_0} \left[ 1 - e^{-s\bar{\tau}_T(x'')} \right] \frac{d\bar{u}(x'')}{dx''} dx'' + \\
 & + \frac{\gamma S \eta_0}{\bar{u}_{k_0} \phi_0} \int_0^x e^{\pm s(x-x')} dx' \int_0^{x'} e^{-s\bar{\tau}_T(x'')} \frac{d\bar{u}(x'')}{dx''} dx'' + \\
 & + \frac{\gamma S \eta_0 \bar{u}_{k_0}}{\phi_0} \int_0^x \bar{u}_k(x') D(x) \frac{d\bar{u}(x')}{dx} e^{-s\bar{\tau}_T(x') \pm s(x-x')} dx' - \\
 & - \gamma S k \int_0^x \bar{u}_k(x') \frac{d\bar{u}(x')}{dx'} e^{\pm s(x-x') - s\bar{\tau}_T(x')} dx' \int_0^{x'} \frac{dD(x'')}{dx''} dx'' \int_0^{x''} \frac{\gamma(x'')}{\phi_0} e^{(s+k)\bar{\tau}_T(x'')} dx''' - \\
 & - (\gamma-1) S \int_0^x \bar{u}_k(x') \frac{\phi(x')}{\phi_0} e^{\pm s(x-x')} dx' + \frac{\gamma \eta_0 \bar{u}_{k_0}}{\phi_0} \bar{u}_k(x) D(x) \frac{d\bar{u}(x)}{dx} e^{-s\bar{\tau}_T(x)} \quad (129)
 \end{aligned}$$

where all terms have been shown to be of  $O(M)$  when integrated.

The corresponding evaluation of

$$\int_0^x \gamma S E(x') e^{\pm s(x-x')} dx'$$

is considerably simplified by employing the results obtained for order of magnitude of the terms:  $\bar{\rho}_k(x) \frac{\eta(x)}{\phi_0}$  AND  $\bar{u}_k(x) \frac{\gamma(x)}{\phi_0}$ , both of which are of  $O(M)$ .

Thus, Equation 113 becomes:

$$E(x) \cdot (\beta - \gamma) \bar{u} \frac{\gamma(x)}{\phi_0} + O(M^3) = O(M)$$

Then:

$$\int_0^x \gamma S E(x') e^{\pm s(x-x')} dx' = \gamma(\beta - \gamma) S \int_0^x \bar{u}(x') \frac{\gamma(x')}{\phi_0} e^{\pm s(x-x')} dx' = O(M) \quad (130)$$

All the terms in the original complex set of Equations 76 have now been examined for their orders of magnitude and have been related to two primary perturbation variables,  $\frac{\gamma(x)}{\phi_0}$  and  $\frac{\phi(x)}{\phi_0}$ .

54.

$$\text{Now, noting that: } \bar{\omega}_c \frac{\eta_c}{\Phi_0} = \bar{\rho}_{L_0} \bar{\tau}_{L_0} \frac{\eta_c}{\Phi_0} = O(M^2)$$

and:

$$\begin{aligned} T(x) &= 2\bar{\rho}(x)\bar{U}(x) \frac{\gamma(x)}{\Phi_0} + 2\bar{\rho}_{L_0}\bar{U}_{L_0} \frac{\eta(x)}{\Phi_0} + \bar{U}^2(x) \frac{\sigma(x)}{\Phi_0} + \bar{U}_{L_0}^2(x) \frac{\tau(x)}{\Phi_0} \\ &= R\bar{U}(x) \frac{\gamma(x)}{\Phi_0} + O(M^2) \end{aligned}$$

$$\begin{aligned} Y(x) &= \frac{\gamma(x)}{\Phi_0} - \bar{U}(x) \frac{\Phi(x)}{\Phi_0} + (1-\bar{\rho}) \frac{\gamma(x)}{\Phi_0} - \bar{U}(x)(1-\bar{\rho}) \frac{\sigma(x)}{\Phi_0} - (1-\bar{\rho}) \bar{U}^2(x) \frac{\gamma(x)}{\Phi_0} \quad (131) \\ &= \frac{\gamma(x)}{\Phi_0} - \bar{U}(x) \frac{\Phi(x)}{\Phi_0} + O(M^2) \end{aligned}$$

Equations 76 become:

$$\frac{\dot{U}(x)}{\Phi_0} = \cosh s x \cdot 2\bar{U}(x) \frac{\gamma\gamma(x)}{\Phi_0} - RS \int_s^x [F(x') \cosh s(x-x') + E(x') \sinh s(x-x')] dx' + O(M^2)$$

$$\frac{\dot{\gamma}(x)}{\Phi_0} = \sinh s x + \frac{\gamma\gamma(x)}{\Phi_0} \cdot R\bar{U}(x) \frac{\Phi(x)}{\Phi_0} + RS \int_s^x [F(x') \sinh s(x-x') + E(x') \cosh s(x-x')] dx' + O(M^2) \quad (132)$$

### Solution by Iteration for Small $\omega$

Since the integral Equations 132 are not amenable to direct analytical solution, a procedure is adopted in which successive iterations are performed, each including terms of a smaller order of magnitude than the preceding one. Considering terms of order  $M^2$  negligibly small, two iteration steps are required, the first including only terms of order 1.0 and the second, terms of order  $M$ . Thus:

$$\begin{aligned} \frac{\Phi(x)}{\Phi_0} &= \cos \omega x + O(M) \\ \frac{\gamma\gamma(x)}{\Phi_0} &= -L \sin \omega x + \frac{\gamma\gamma(x)}{\Phi_0} + O(M) \quad (133) \end{aligned}$$

Because the results of these equations are to be applied to mechanically-produced oscillations of low frequencies, it is necessary to examine the contributions of the various terms of  $O(1)$  and  $O(M)$  for the case of small  $\omega$ . Thus, if  $\omega = O(M)$ , then all terms of  $O(\omega M)$  or  $O(\omega^2)$  become negligibly small in keeping with the assumptions to date.

For this range of frequencies:

$$\sin \omega x = \omega x + O(\omega^3) = O(M),$$

from which the zeroth iteration of Equation 133 may be expressed as:

$$\begin{aligned} \frac{\phi^{(0)}}{\phi_0} &= \cos \omega x \\ \frac{\gamma_2^{(0)}}{\phi_0} &= \frac{\gamma q^{(0)}}{\phi_0} \end{aligned} \quad (134)$$

where the superscript zero indicates the order of the iteration, and only terms of  $O(1)$  have been included.

Substituting possible  $O(1)$  terms from Equation 131 for the zeroth iteration of  $q(x)/\phi_0$ , the second of the above equations becomes:

$$\begin{aligned} \frac{\gamma_2^{(0)}}{\phi_0} &= -\gamma k \bar{u}_L(x) \frac{d\bar{u}(x)}{dx} e^{-s\bar{\tau}_T(x)} \int_0^x \frac{dD(x')}{dx'} dx' \int_0^x \frac{J^{(0)}(x'')}{\phi_0} e^{(s+k)\bar{\tau}_T(x'')} dx'' - \\ &\quad - \frac{\gamma \eta_0 \bar{u}_{L0}}{\phi_0} \bar{u}_L(x) \frac{d\bar{u}(x)}{dx} e^{-s\bar{\tau}_T(x)} D(x) \end{aligned} \quad (135)$$

where:

$$D(x) = \int_0^x \frac{e^{-k\bar{\tau}_T(x')}}{\bar{u}_L^3(x')} dx'$$

Two new integral values may be defined by:

$$I_2(x) = \int_0^x \frac{J^{(0)}(x')}{\phi_0} e^{(s+k)\bar{\tau}_T(x')} dx'$$

and:

$$J_2(x) = \int_0^x \frac{e^{-k\bar{\tau}_T(x')}}{\bar{u}_L^3(x')} I_2(x') dx'$$

by whose substitution Equation 135 is reduced to a second order differential equation in  $J_2(x)$ , the solution of which yields the result:

$$\frac{\gamma_2^{(0)}}{\phi_0} = \frac{\gamma \eta_0}{K \phi_0} \frac{d\bar{u}(x)}{dx} e^{-s\bar{\tau}_T(x)} \left[ e^{-k\bar{\tau}_T(x)} - 1 \right] \quad (136)$$

The details of this solution are given in Appendix B.

This result furnishes some very useful information for additional order of magnitude evaluations. The presence of the factor  $\frac{d\bar{u}}{dx}$ , which may

56.

be of  $O(1)$ , shows that although  $\omega$  may locally be of  $O(1)$ , it can only remain of that order for a short distance and will be of  $O(M)$  when integrated over any portion of the chamber. (This variation is schematically indicated by Figure 4). As Equation 134 indicates, the same conclusions may be drawn for the burning rate perturbation.

The only remaining term whose order of magnitude may be increased by  $\omega = O(M)$  is  $\bar{u}_\ell \frac{\zeta}{\Phi_0}$ , which, from Equation 123 will be expressed as:

$$\frac{\bar{u}_\ell(x) \zeta(x)}{\Phi_0} = \bar{\rho}_\ell \frac{\eta_0}{\Phi_0} e^{-S\bar{\tau}_T(x)} \frac{\zeta(x)}{\Phi_0} - \bar{\rho}_\ell(x) \frac{\eta(x)}{\Phi_0} + \int_0^x \left[ \frac{\eta(x')}{\Phi_0} + \bar{\rho}_\ell \frac{\eta(x')}{\Phi_0} \right] \frac{d}{dx'} \left[ e^{S(\bar{\tau}_T(x') - \bar{\tau}_T(x))} \right] dx' \quad (137)$$

This result shows that in the evaluation of  $T(x)$  and  $I(x)$ , the quantity  $\bar{u}_\ell \frac{\zeta}{\Phi_0}$  must be considered of  $O(1)$  because of the presence of the term  $\frac{\zeta(x)}{\Phi_0}$ .

However, the contribution to  $\int_0^x S F(x') e^{\pm S(x-x')} dx'$

of this term will be negligible, since the largest integral involved will be:

$$S \int_0^x \frac{\zeta(x')}{\Phi_0} e^{\pm S(x-x')} dx' = O(\omega M)$$

An inspection of the remaining terms in Equations 129 and 130 indicate that, for  $\omega = O(M)$ ,

$$\int_0^x S F(x') e^{\pm S(x-x')} dx' = O(\omega M) + O(\omega M^2) = \int_0^x S E(x') e^{\pm S(x-x')} dx'$$

From this expression, the first order iterations for Equations 133, containing terms of  $O(M)$  and larger become:

$$\frac{\Phi^{(1)}}{\Phi_0} = \cos \omega x - S T^{(1)}(x); \quad \frac{S \omega^{(1)}}{\Phi_0} = -i \omega x + S Y^{(1)}(x) \quad (138)$$

whereas  $\gamma T^{(1)}(x) = \gamma \bar{u}(x) \frac{\gamma \varphi^{(0)}}{\phi_0} + \bar{u}_x^2(x) \frac{\gamma \eta^{(0)}}{\phi_0} + O(M^2)$

$$\gamma Y^{(1)}(x) = \frac{\gamma \varphi^{(1)}(x)}{\phi_0} - \gamma \bar{u}(x) \frac{\phi^{(0)}}{\phi_0} + O(M^2) \quad (139)$$

The value of  $\frac{\eta^{(1)}(x)}{\phi_0}$ , correct to terms of  $O(M)$  will be, from III:

$$\frac{\eta^{(1)}(x)}{\phi_0} = n \int_0^x \left[ 1 - e^{-i\omega \bar{\tau}(x')} \right] \frac{d\bar{u}(x')}{dx'} dx' + \frac{\eta_0}{\bar{u}_{k_0} \phi_0} \int_0^x e^{-i\omega \bar{\tau}_T(x')} \frac{d\bar{u}(x')}{dx'} dx' -$$

$$- \frac{i\eta_0}{\omega} \bar{u}_x(x) \frac{d\bar{u}(x)}{dx} \frac{\phi^{(0)}(x)}{\phi_0} \left[ 1 - e^{-i\omega \bar{\tau}(x)} \right] + \frac{\eta^{(0)}(x)}{\phi_0}$$

Substituting the values for  $\frac{\phi^{(0)}}{\phi_0}$  and  $\frac{\eta^{(0)}}{\phi_0}$  from Equations 134 and 136 gives:

$$\frac{\eta^{(1)}(x)}{\phi_0} = n \int_0^x \cos \omega x' \left[ 1 - e^{-i\omega \bar{\tau}(x')} \right] \frac{d\bar{u}(x')}{dx'} dx' + \frac{\eta_0}{\bar{u}_{k_0} \phi_0} \int_0^x e^{-i\omega \bar{\tau}_T(x')} \frac{d\bar{u}(x')}{dx'} dx' -$$

$$- \frac{i\eta_0}{\omega} \bar{u}_x(x) \cos \omega x \frac{d\bar{u}(x)}{dx} \left[ 1 - e^{-i\omega \bar{\tau}(x)} \right] + \frac{\eta_0}{k \phi_0} \frac{d\bar{u}(x)}{dx} e^{-i\omega \bar{\tau}_T(x)} \left[ e^{-k \bar{\tau}_T(x)} - 1 \right].$$

The first term of this equation may be integrated by parts. Performing this integration and neglecting terms of  $O(\omega M)$ , one obtains:

$$\frac{\eta^{(1)}(x)}{\phi_0} = n \bar{u}(x) \cos \omega x - n \int_0^x e^{-i\omega \bar{\tau}(x')} \cos \omega x' \frac{d\bar{u}(x')}{dx'} -$$

$$- \frac{i\eta_0}{\omega} \bar{u}_x(x) \cos \omega x \frac{d\bar{u}(x)}{dx} \left[ 1 - e^{-i\omega \bar{\tau}(x)} \right] + \frac{\eta_0}{\phi_0 \bar{u}_{k_0}} \left[ \int_0^x e^{-i\omega \bar{\tau}_T(x')} \frac{d\bar{u}(x')}{dx'} dx' + \right. \quad (140)$$

$$\left. + \frac{\bar{u}_{k_0}}{k} \frac{d\bar{u}(x)}{dx} e^{-i\omega \bar{\tau}_T(x)} \left( e^{-k \bar{\tau}_T(x)} - 1 \right) \right].$$

With this result, Equations 139 are evaluated as:

$$\gamma T^{(1)}(x) = \frac{\alpha \bar{u}(x)}{k} \frac{\eta_0}{\phi_0} \frac{d\bar{u}(x)}{dx} e^{-i\omega \bar{\tau}_T(x)} \left[ e^{-k \bar{\tau}_T(x)} - 1 \right] - \bar{u}_x \frac{\gamma \varphi^{(0)}}{\phi_0}$$

$$\gamma Y^{(1)}(x) = \gamma n \bar{u}(x) \cos \omega x - \gamma n \int_0^x e^{-i\omega \bar{\tau}_T(x')} \cos \omega x' \frac{d\bar{u}(x')}{dx'} dx' - \frac{i\eta_0}{\omega} \bar{u}_x(x) \cos \omega x \frac{d\bar{u}(x)}{dx} \left[ 1 - e^{-i\omega \bar{\tau}(x)} \right] + \frac{\gamma \eta_0}{\bar{u}_{k_0} \phi_0} \left[ \int_0^x e^{-i\omega \bar{\tau}_T(x')} \frac{d\bar{u}(x')}{dx'} dx' + \frac{\bar{u}_{k_0}}{k} \frac{d\bar{u}(x)}{dx} e^{-i\omega \bar{\tau}_T(x)} \left( e^{-k \bar{\tau}_T(x)} - 1 \right) \right] - \gamma \bar{u} \cos \omega x$$

Substituting for  $\frac{\phi^{(e)}}{\phi_0}$  and combining terms, one derives:

$$\gamma T^{(1)}(x) = \frac{\gamma}{k} \frac{\eta_0}{\phi_0} \frac{d\bar{u}(x)}{dx} e^{-i\omega\bar{\tau}_T(x)} \left[ e^{-k\bar{\tau}_T(x)-1} \right] \left[ 2\bar{u}(x) - \bar{u}_L(x) \right] + \\ + \frac{i\gamma n}{\omega} \bar{u}_L^2(x) \frac{d\bar{u}(x)}{dx} \cos \omega x \left[ 1 - e^{-i\omega\bar{\tau}(x)} \right] \quad (141)$$

$$\gamma Y^{(1)}(x) = \gamma(n-1) \bar{u}(x) \cos \omega x - \gamma n \int_0^y e^{-i\omega\bar{\tau}(x')} \cos \omega x' \frac{d\bar{u}(x')}{dx'} dx' - \\ - \frac{i\gamma n}{\omega} \bar{u}_L(x) \frac{d\bar{u}(x)}{dx} \cos \omega x \left[ 1 - e^{-i\omega\bar{\tau}(x)} \right] + \\ + \frac{\gamma\eta_0}{\bar{u}_L\phi_0} \left[ \int_0^x e^{-i\omega\bar{\tau}_T(x')} \frac{d\bar{u}(x')}{dx'} dx' + \frac{\bar{u}_L}{k} \frac{d\bar{u}(x)}{dx} e^{-i\omega\bar{\tau}_T(x)} \left( e^{-k\bar{\tau}_T(x)-1} \right) \right].$$

One additional simplification may profitably be made by expanding

the second term of  $\gamma T^{(1)}(x)$  and the third term of  $\gamma Y^{(1)}(x)$ . Thus:

$$-\frac{i}{\omega} \left[ 1 - e^{-i\omega\bar{\tau}(x)} \right] = 1 - \frac{[1 - i\omega\bar{\tau}(x) - \omega^2/2\bar{\tau}^2(x) + \dots]}{\omega} \\ = \bar{\tau}(x) + O(M),$$

since  $\bar{\tau}(x)$  has been assumed of order 1.0. Then, the second term of  $\gamma T^{(1)}(x)$  is of  $O(M^2)$ , and the third term of  $\gamma Y^{(1)}(x)$  becomes:

$$-\frac{i\gamma n}{\omega} \bar{u}_L(x) \frac{d\bar{u}(x)}{dx} \cos \omega x \left[ 1 - e^{-i\omega\bar{\tau}(x)} \right] = \gamma n \bar{u}_L(x) \bar{\tau}(x) \frac{d\bar{u}(x)}{dx} \cos \omega x$$

Introducing this change into 141 and substituting the resulting two equations into 138, one arrives at the final values of the perturbation quantities correct to terms of  $O(M)$ :

$$\frac{\phi^{(1)}(x)}{\phi_0} = \cos \omega x - \frac{\gamma \eta_0}{k \phi_0} \frac{d\bar{u}(x)}{dx} e^{-i\omega\bar{\tau}_T(x)} \left[ e^{-k\bar{\tau}_T(x)-1} \right] \left[ 2\bar{u}(x) - \bar{u}_L(x) \right] \quad (142)$$

$$\frac{\gamma Y^{(1)}(x)}{\phi_0} = -i\omega x + \gamma \bar{u}(x) \cos \omega x \left[ (n-1) + n \frac{\bar{u}_L(x)}{\bar{u}(x)} \frac{d\bar{u}(x)}{dx} \bar{\tau}(x) \right] - \\ - \gamma n \int_0^y e^{-i\omega\bar{\tau}(x')} \cos \omega x' \frac{d\bar{u}(x')}{dx'} dx' + \frac{\gamma\eta_0}{\bar{u}_L\phi_0} \left[ \int_0^x e^{-i\omega\bar{\tau}_T(x')} \frac{d\bar{u}(x')}{dx'} dx' + \right. \quad (143)$$

$$\left. + \frac{\bar{u}_L}{k} \frac{d\bar{u}(x)}{dx} e^{-i\omega\bar{\tau}_T(x)} \left( e^{-k\bar{\tau}_T(x)-1} \right) \right].$$

The pressure and velocity perturbations represented by these two equations are related through the boundary conditions at the nozzle entrance. For a conical geometry in the subsonic portion of the exhaust nozzle, the derivation of Appendix A shows that the variations in pressure, velocity, and entropy at the entrance section may be expressed in the form:

$$\nu_{eN} = \frac{\Phi_{eN}}{\gamma} \left[ \frac{r-1}{2} + \frac{i\beta_N}{(1-w_e^2)} \left( \int_0^1 \frac{d\xi}{w} - \frac{r-1}{2} \int_0^1 w d\xi \right) \right] + \frac{E_{eN}}{2\gamma} \left[ 1 - \frac{i\beta_N}{(1-w_e^2)} \int_0^1 \frac{d\xi}{w} \right] \quad (144)$$

where the subscript  $e$  denotes properties evaluated at the entrance section and  $N$  indicates that non-dimensionalization is based on nozzle reference parameters. Comparison of the two non-dimensionalizing procedures leads to the following conversion from nozzle to chamber variables:

$$\begin{aligned} \nu_{eN} &= \frac{u'_1}{u_1} = \frac{u'^{*}}{u_1^{*}} = \left( \frac{c_0^{*}}{c_0^{**}} \right) \left( \frac{u_1^{**}}{u_1^{*}} \right) = \nu_1 \left( \frac{c_0^{**}}{u_1^{*}} \right) = \frac{\nu_1}{u_1} \\ \Phi_{eN} &= \frac{p'_1}{p_1} = \frac{p'^{*}}{p_1^{*}} = \left( \frac{p_1^{**}}{p_1^{*}} \right) \left( \frac{p_1^{*}}{p_1^{**}} \right) = \Phi_1 \left( \frac{p_1^{**}}{p_1^{*}} \right) = \Phi_1 + O(M^2) \\ E_{eN} &= \frac{s'_1}{c_v} = \frac{p_1^{**}}{p_1^{*}} - \gamma \frac{p_1^{*}}{p_1^{**}} = \frac{\Phi_1}{p_1} - \gamma \frac{\sigma_1}{p_1} = \Phi_1 - \gamma \sigma_1 + O(M^2) \end{aligned} \quad (145)$$

The frequency of oscillation, expressed in terms of chamber parameters, becomes:

$$\beta_N = \frac{\omega^* c}{c_t^{**}} = \left( \frac{\omega^* L}{c_0^{**}} \right) \left( \frac{c_0^{**}}{c_t^{**}} \right) \left( \frac{\ell}{L} \right) = \omega \sqrt{\frac{r+1}{2}} \frac{\ell}{L}, \quad (146)$$

where:

$\ell$  = length of the subsonic portion of the nozzle.

$c_t^{**}$  = velocity of sound at the nozzle throat.

The integrated nozzle velocity parameters:

$$\left( \frac{1}{1-w_e^2} \right) \int_0^1 \frac{d\xi}{w} \text{ AND } \left( \frac{1}{1-w_e^2} \right) \int_0^1 w d\xi$$

are defined in Appendix A and are functions only of the nozzle geometry.

Introducing Equations 145 and 146 into Equation 144 and defining:

$$\frac{1}{(1-\omega e^{\xi})} \int_0^1 \frac{d\xi}{w} = w_1; \quad \frac{1}{(1-\omega e^{\xi})} \int_0^1 w d\xi = w_2; \quad \sqrt{\frac{\gamma+1}{2}} \frac{\ell}{L} = \Gamma,$$

one obtains for the nozzle boundary equation the following:

$$\frac{\gamma z(1)}{\bar{u}_1 \phi_0} - \frac{\phi(1)}{\phi_0} \left[ \frac{\gamma-1}{2} + \omega \Gamma \left( w_1 - \frac{\gamma-1}{2} w_2 \right) \right] + \frac{\epsilon(1)}{2 \phi_0} (1 - \omega \Gamma w_1) \quad (147)$$

The entropy perturbation  $\epsilon(x)$  is derived from Equation 68, re-

written in the form:

$$\frac{s}{\bar{u}(x)} \left\{ \bar{u}(x) \left[ \frac{\phi(x) - \gamma \sigma(x)}{\phi_0} + (\gamma-1) \bar{u}(x) \frac{\gamma z(x)}{\phi_0} \right] + \frac{d}{dx} \left\{ \bar{u}(x) \left[ \frac{\phi(x) - \gamma \sigma(x)}{\phi_0} + (\gamma-1) \bar{u}(x) \frac{\gamma z(x)}{\phi_0} \right] \right\} \right. \\ \left. = -(\gamma-1) \frac{d}{dx} \left[ \bar{u}(x) \frac{\phi(x)}{\phi_0} \right] \right.$$

Integrating this linear differential equation and retaining terms

of  $O(M)$  and greater gives:

$$\frac{\epsilon(x)}{\phi_0} = \frac{\phi(x) - \gamma \sigma(x)}{\phi_0} = -(\gamma-1) \left[ \bar{u}(x) \frac{\gamma z^{(0)}(x)}{\phi_0} + \frac{\phi^{(1)}(x)}{\phi_0} - \frac{\omega}{\bar{u}(x)} \int_{\phi_0}^{\phi(x)} e^{i\omega \int_{\bar{u}(x')}^{\bar{u}(x)} dx''} \right] \quad (148)$$

Substitution of the expressions for  $\frac{\gamma^{(0)}(x)}{\phi_0}$  and  $\frac{\phi^{(1)}(x)}{\phi_0}$  from Equations 136 and 142 into 148 produces:

$$\frac{\epsilon(x)}{\phi_0} = (\gamma-1) \left\{ \frac{r \eta_0}{k \phi_0} \bar{u}(x) \frac{d\bar{u}(x)}{dx} e^{-i\omega \bar{\tau}_T(x)} \left[ e^{-k \bar{\tau}_T(x)} - 1 \right] \left[ \bar{u}(x) - \bar{u}_L(x) \right] - \right. \\ \left. - \cos \omega x + \frac{\omega}{\bar{u}(x)} \int_x^{\infty} e^{i\omega \int_{\bar{u}(x')}^{\bar{u}(x)} dx''} \cos \omega x' dx' \right\} + O(\omega M) + O(M^2),$$

or, after integrating the final term in the brackets by parts,

$$\frac{\epsilon(x)}{\phi_0} = (\gamma-1) \left\{ \frac{r \eta_0}{k \phi_0} \bar{u}(x) \frac{d\bar{u}(x)}{dx} e^{-i\omega \bar{\tau}_T(x)} \left[ e^{-k \bar{\tau}_T(x)} - 1 \right] \left[ \bar{u}(x) - \bar{u}_L(x) \right] - \right. \\ \left. - \frac{1}{\bar{u}(x)} \int_x^{\infty} e^{i\omega \int_{\bar{u}(x')}^{\bar{u}(x)} dx''} \cos \omega x' \frac{d\bar{u}(x')}{dx'} dx' \right\} + O(\omega^2). \quad (149)$$

The three thermodynamic properties must be evaluated at the nozzle entrance before insertion in the boundary equation. This evaluation is con-

siderably simplified by the condition that all combustion must be complete within the chamber. Then, at  $x = 1$ ,

$$\left(\frac{d\phi}{dx}\right)_1 = \left(\frac{du}{dx}\right)_1 = 0,$$

so that Equations 142, 143, and 149 reduce to:

$$\begin{aligned} \frac{\phi_1}{\phi_0} &= \cos \omega \\ \frac{\gamma \bar{u}_1}{\phi_0} &= -i\omega + \gamma \bar{u}_1(n-1) \cos \omega - \gamma n \int e^{-i\omega \bar{\tau}(x)} \cos \omega x \frac{d\bar{u}(x)}{dx} dx + \\ &\quad + \frac{\gamma \eta_0}{\bar{u}_1 \phi_0} \int e^{-i\omega \bar{\tau}(x)} \frac{d\bar{u}(x)}{dx} dx \\ \frac{e_1}{\phi_0} &= -\frac{(n-1)}{\bar{u}_1} \int e^{-i\omega \theta g(x)} \cos \omega x \frac{d\bar{u}(x)}{dx} dx \end{aligned} \quad (150)$$

where:

$$\theta g(x) = \int_x^1 \frac{dx'}{\bar{u}(x')}$$

is a gas residence parameter denoting the time required for a particle of combustion gas produced at station  $x$  to reach the nozzle entrance.

The three relations 150 are introduced into the boundary condition

Equation 147, yielding:

$$\begin{aligned} \frac{\gamma \eta_0}{\bar{u}_1 \phi_0} \int e^{-i\omega \bar{\tau}(x)} \frac{d\bar{u}(x)}{dx} dx + \gamma(n-1) \cos \omega - \frac{\gamma n}{\bar{u}_1} \int e^{-i\omega \bar{\tau}(x)} \cos \omega x \frac{d\bar{u}(x)}{dx} dx = \\ = \frac{i\omega}{\bar{u}_1} + \cos \omega \left[ \frac{\gamma-1}{\bar{z}} + i\omega \Gamma(W_1 - \frac{\gamma-1}{\bar{z}} W_2) \right] - \end{aligned} \quad (151)$$

$$-\frac{1}{\bar{u}_1} \left( \frac{\gamma-1}{\bar{z}} \right) \left( 1 - i\omega \Gamma W_1 \right) \int e^{-i\omega \theta g(x)} \cos \omega x \frac{d\bar{u}(x)}{dx} dx$$

as a combustion chamber equation for the refined theoretical model.

The initial velocity fluctuation is transformed into the form of a transfer function for the injector-chamber combination (as in the simplified model derivation) by noting that:

$$\frac{\eta_0}{\bar{u}_1} = \frac{u'_0 e^{-st}}{\bar{u}_0} \cdot \frac{\rho_{e_0} u'_0 e^{-st}}{\rho_0 \bar{u}_0} = \frac{m' e^{-st}}{\bar{m}}$$

$$= M_i e^{-st} = M_i, \quad (152)$$

62.

which is the amplitude of the fractional injection mass flow perturbation as defined for the simplified model. Also:

$$\phi_0 = \frac{P_0 e^{-\gamma t}}{P_0} = \tilde{\phi}_0 e^{-i\beta_F}$$

is the amplitude of fractional chamber pressure oscillation at the injector face with a phase angle indicating a time based on the fuel injection perturbation. In the simplified model, the pressure is assumed uniform over the entire chamber. Thus, in terms of amplitude at an average position,  $x = \frac{1}{2}$ ,

$$\phi_0 = \left( \frac{\phi_0}{\bar{u}_1 \tilde{\phi}_0} \right) \tilde{\phi} e^{-i\beta_F} = \frac{\tilde{\phi}}{\cos(\omega/2)} e^{-i\beta_F} \quad (153)$$

Then, from 152 and 153,

$$\frac{\eta_0}{\bar{u}_1 \phi_0} = \frac{\tilde{\mu}_1}{\tilde{\phi}} \cos(\omega/2) e^{i\beta_F}$$

or, employing the mixture ratio parameters defined previously in the derivations of Equations 17 and 34:

$$\begin{aligned} \frac{\eta_0}{\bar{u}_1 \phi_0} &= \frac{\tilde{\mu}_F}{\tilde{\phi}} \left[ (\gamma_2 + H) r e^{i\delta} + (\gamma_2 - H) \right] \cos(\omega/2) e^{i\beta_F} \\ &= R_F e^{i\beta_F} \cos(\omega/2) \left[ (\gamma_2 + H) (r e^{i\delta} - 1) + 1 \right] \end{aligned} \quad (162)$$

Replacing the term in Equation 151 by its modified form as expressed in 154 results in a combustion chamber equation as follows:

$$\begin{aligned} &R_F e^{i\beta_F} \cos(\omega/2) \left[ 1 + (r e^{i\delta} - 1)(\gamma_2 + H) \right] \frac{1}{\bar{u}_1} \int_0^1 e^{-i\omega \bar{\tau}_T(x)} \frac{d\bar{u}_1(x)}{dx} dx = \\ &= \frac{i\omega}{8\bar{u}_1} - n \left[ \cos \omega - \frac{1}{\bar{u}_1} \int_0^1 e^{-i\omega \bar{\tau}(x)} \cos \omega x \frac{d\bar{u}_1(x)}{dx} dx \right] + \\ &+ \cos \omega \left[ \frac{3\gamma-1}{2\gamma} + \frac{i\omega}{\gamma} \Gamma \left( W_1 - \frac{\gamma-1}{2} W_2 \right) \right] - \left( \frac{\gamma-1}{2\gamma} \right) \left( 1 - i\omega \Gamma W_1 \right) \frac{1}{\bar{u}_1} \int_0^1 e^{-i\omega \theta_0(x)} \cos \omega x \frac{d\bar{u}_1(x)}{dx} dx \end{aligned}$$

In keeping with the assumptions of small  $\omega$  and consistent with the neglect, heretofore, of terms of order  $\omega^2$  and  $\omega M$ , a further simplification may be made. The factors  $\cos \omega$  and  $\cos \omega x$  may be expanded in series form to yield:

$$\cos \omega = 1 - \frac{\omega^2}{2} + \frac{\omega^4}{4!} + \dots = 1 - O(\omega^2)$$

$$\cos \omega x = 1 - \frac{\omega^2 x^2}{2} + \frac{\omega^4 x^4}{4!} + \dots = 1 - O(\omega^2)$$

since  $x \ll 0(1)$ .

Thus, the variation in amplitude of pressure perturbations along the length of the chamber is seen to be negligibly small when the frequency of oscillation is of  $O(M)$ , and  $\cos \omega$  and  $\cos \omega x$  may be replaced everywhere by 1.0 to the order of accuracy considered.

Two of the time lag parameters,  $\bar{\tau}_T(x)$  and  $\Theta_9(x)$ , appearing in the combustion chamber equation may be calculated from velocity distributions. However, the distributed sensitive time lag,  $\bar{\tau}_T(x)$ , is totally undetermined, since the position  $\xi(x)$  where a particle enters the sensitive portion of its preparation processes is a completely unknown and somewhat artificial quantity. Hence it will be considered sufficient to determine a mean value of this sensitive time lag, and the exponential factor  $e^{-i\omega \bar{\tau}(x)}$  may be represented by a proper average and removed from beneath the integral in the third term of Equation 151. Thus, if one defines an average  $\bar{\tau}(x)$  by:

$$\bar{\tau}_{AVG} = \frac{1}{\bar{u}_1} \int_0^1 \bar{\tau}(x) \frac{d\bar{u}(x)}{dx} dx \quad (156)$$

then a series expansion of the integral expression containing  $\bar{\tau}(x)$  shows that:

$$\begin{aligned} & \frac{1}{\bar{u}_1} \int_0^1 e^{-i\omega \bar{\tau}(x)} \frac{d\bar{u}(x)}{dx} = 1 - i\omega \bar{\tau}_{AVG} - \frac{\omega^2}{2\bar{u}_1} \int_0^1 \bar{\tau}^2(x) \frac{d\bar{u}(x)}{dx} dx + \\ & + \frac{i\omega^3}{6\bar{u}_1} \int_0^1 \bar{\tau}^3(x) \frac{d\bar{u}(x)}{dx} dx + \dots \end{aligned} \quad (157)$$

Now, as previously postulated,

$$\bar{\tau}(x) = O(1)$$

then:

$$\frac{1}{\bar{\tau}_1} \int_0^1 e^{-i\omega \bar{\tau}(x)} \frac{d\bar{\tau}(x)}{dx} dx = 1 - i\omega \bar{\tau}_{AVG} + O(\omega^2) \quad (158)$$

Correspondingly, an exponential variation involving the average time lag may be written as:

$$\begin{aligned} e^{-i\omega \bar{\tau}_{AVG}} &= (1 - i\omega \bar{\tau}_{AVG} - \frac{\omega^2}{2} (\bar{\tau}_{AVG})^2 + \dots \\ &= 1 - i\omega \bar{\tau}_{AVG} + O(\omega^2) \end{aligned} \quad (159)$$

Hence, correct to terms of order ( $\omega$ ), one may equate the expressions in Equations 158 and 159 to yield:

$$\frac{1}{\bar{\tau}_1} \int_0^1 e^{-i\omega \bar{\tau}(x)} \frac{d\bar{\tau}(x)}{dx} dx = e^{-i\omega \bar{\tau}_{AVG}} + O(\omega^2) \quad (160)$$

where the averaging process for  $\bar{\tau}$  is given by Equation 156.

These simplifications result in a final combustion chamber equation for the refined theoretical model of the form:

$$\begin{aligned} R_F e^{i\beta_F} \left[ 1 + (k e^{i\delta} - 1)(Y_R + W) \right] \frac{1}{\bar{\tau}_1} \int_0^1 e^{-i\omega \bar{\tau}_T(x)} \frac{d\bar{\tau}_T(x)}{dx} dx &= \\ = \frac{i\omega}{Y \bar{\tau}_1} - n (1 - e^{-i\omega \bar{\tau}_{AVG}}) + \left( \frac{3Y-1}{2Y} \right) + \frac{i\omega}{Y} \Gamma \left( W_1 - \frac{Y-1}{2} W_R \right) - \\ - \left( \frac{Y-1}{2Y} \right) (1 - i\omega \Gamma W_1) \frac{1}{\bar{\tau}_1} \int_0^1 e^{-i\omega \theta_g(x)} \frac{d\bar{\tau}(x)}{dx} dx. \end{aligned} \quad (161)$$

#### Comparison of Equations

The final combustion chamber equations from both simplified (Equation 44) and refined (Equation 161) theoretical models are presented in Figure 5 in a form slightly modified for comparison purposes. The general corres-

pondence of terms is immediately evident.

The left-hand side of both equations consists of the product of the chamber transfer function times a phase-shifting total time lag exponential factor. In the simplified model, since all combustion is assumed to occur in a concentrated location, this exponential factor is a constant,  $\bar{\tau}_T$ , representing the mean time required by the droplets to reach the combustion front. In the refined model the exponential is an integrated function of the distributed steady-state time lag variable  $\bar{\tau}_T(x)$  weighted by the steady gas velocity  $\bar{u}(x)$ , which is equivalent to the combustion distribution.

The right-hand side of each equation has been written in fractional form with all mixture ratio parameters included in the denominator. If the fuel and oxidizer flow rates oscillate in phase and with equal amplitudes, there will be no fluctuations of instantaneous mixture ratio, and the denominators of both equations reduce to unity. In the refined model no attempt has been made to account for effects of mixture ratio variations on the combustion process. Therefore, only the injection mass flow oscillations contribute to the denominator. The simplified model, however, contains two additional quantities, which are the result of considerations of gross mixture ratio effects on the temperature and density of chamber gases. These terms are identified by the presence of  $K$ , a factor correlating mixture ratio and chamber gas temperature. The quantity with exponential time reduction ( $\omega \bar{f} \theta_0$ ) is the contribution from temperature oscillations at the nozzle entrance referred to mixture ratio fluctuations which existed at burning, a time  $\bar{f} \theta_0$  earlier; and the constant term  $2K$  is the temperature contribution at the burning station to oscillations of gas density within the chamber.

In the refined model such gross effects would be inconsistent with the distributed form derived for pressure, velocity, and density perturbations; and it would be necessary to postulate some interaction between mixture ratio

and the combustion process in order to express these effects in the functional character desired for a differential treatment. Scala (7) has performed such an analysis by introducing two additional interaction indices relating mixture ratio variations to variations in combustion time lag and in energy required for the propellant preparation processes. However, analytical solution of the complex combustion chamber equation resulting from incorporation of these unknown indices requires additional knowledge of the time lag or interaction function expressed in the present treatment.

The numerators of the right-hand sides of the two equations in Figure 5 contain terms which show direct correspondence. Under the non-dimensionalizing scheme of the refined analysis, ( $1/\bar{u}_1$ ) is precisely the gas residence time if the velocity of all particles is  $\bar{u}_1$ ; and since variations in steady-state gas density are of  $O(M^2)$ , this fraction is equivalent to the quantity  $\theta_g$  as defined for the simplified model, correct to terms of a negligibly small order.

The second term in each numerator arises from the contributions of pressure oscillations to the fluctuations of the mass of gas within the chamber.

The third term originates from the "nozzle impedance" analysis and represents the phase shift caused by the presence of the exhaust nozzle on pressure perturbations at its entrance.

Similarly, the fourth term arises from variations in entropy at the nozzle entrance produced by pressure perturbations occurring during combustion. Thus, an exponential time-depressing factor multiplies this term in each equation. In the simplified model, this factor is merely  $\bar{F}\theta_g$ , the time required for a particle at constant velocity,  $\bar{u}_1$ , to travel the distance from the combustion front to the nozzle. In the refined model, the exponential is again an integrated quantity weighted by the steady combustion distribution.

The final term in the numerator of each is the expression of pressure

effects upon the sensitive combustion time lag, and here the correspondence between models is exact, by virtue of the averaging process defined for the refined model.

A final comparison check on the two models is possible by considering the velocity  $\bar{u}(x)$  in the refined model as a step function of zero magnitude from  $x = 0$  to  $x = 1 - \bar{f}$ , and of constant magnitude  $\bar{u}_1$  for the remainder of chamber length. Under these conditions, except for the mixture ratio variations discussed earlier, the two models reduce to exactly the same equation.

#### Combined Theoretical Model

Each of the combustion chamber equations of the previous derivations has certain advantages when applied to experimental data for the purpose of obtaining reliable time lag information. One method of evaluating these advantages is by analysis of the measurable and unknown quantities in both and comparison of the relative difficulties of obtaining values for each.

The primary unknown quantities of both equations are the average sensitive time lag and the interaction index, i.e.,  $\bar{T}_{AVG}$  and  $n$ . These two variables occur in the same form, regardless of the choice of equation. However, they are, in essence, the only items appearing in the refined analysis which are totally undetermined, while the simplified analysis contains three other quantities which are either unknown or sufficiently in doubt as to require treatment as unknowns. These are the mean total time lag,  $\bar{T}_T$ , the gas residence time  $\theta_g$ , and the location of the combustion front,  $1 - \bar{f}$ . This implies that solution of the refined model may be accomplished by direct analytical methods; but the simplified model requires approximate, iterative, or asymptotic solution. (The actual methods employed for treatment of the simplified equation include an asymptotic one which is explained later in some detail.) However, the direct solution of the refined equation involves the use of intermediate, derived quantities whose

determination from fundamental measurements may be cumbersome and of questionable accuracy. Hence, the apparent advantage of direct analytical solution is somewhat misleading in this case.

The primary measured quantity in either equation is the transfer function parameter,  $R_F e^{-\Delta F}$ , whose evaluation is totally independent of the physical model chosen to describe the combustion process. Since measurements of oxidizer and fuel flow oscillations are obtained simultaneously, the transfer function may be based upon either propellant; and comparison of the two fluctuations then results in a second parameter, the instantaneous mixture ratio,  $\mu_O/\mu_F$ , which is required in both equations.

The major disadvantages in solution of the refined equation appear through another experimental measurement which enters in a prominent manner, namely the steady-state gas velocity distribution along the length of the rocket chamber. This is an extremely difficult quantity to determine with any reasonable degree of accuracy, since it depends upon a pressure difference which, for the usual contraction ratios of practical motors, is at most of the order of a few percent of nominal chamber pressure. Once this velocity distribution is known, it must be used in a numerical integration to determine  $\Theta_g(x)$  and  $\bar{u}_L(x)$ . The latter also necessitates the choice of a droplet drag coefficient, the value of which is, at best, an extrapolation of existing data from separate experimental work dealing with injection sprays, droplet dispersion, or single droplet studies under conditions which may be quite dissimilar from those encountered in the particular motor under consideration. This derived liquid velocity, as determined from the droplet dynamics equation in steady state, is then involved in a second numerical integration to obtain the distributed total time lag,  $\bar{\tau}_T(x)$ . Finally the three derived variables  $\bar{u}$ ,  $\Theta_g$ , and  $\bar{\tau}_T$  are introduced into two further numerical integrations to evaluate the exponential factors appearing in the refined equation. Thus it is seen that a combination of five

numerical integrations from data of a rather poor degree of precision are required before an analytical solution of the final refined equation can be performed.

Considerations of this sort indicate the desirability of combining some of the best features of each analysis into a composite equation for the combustion chamber. This combined relation is derived based on the format of the simplified model, with correction terms obtained from the refined model. Small variations in instantaneous mixture ratio of  $O(M)$  are permitted and are included in the same manner as in the simplified equation. The secondary unknowns  $\bar{\tau}_T$ ,  $\theta_g$ , and  $\bar{f}$  are introduced as exponential functions of average values, with the averaging process again defined by the steady-state velocity distribution, as in the refined model, through the determination of liquid velocity and a distributed total time lag. However, these relatively inaccurate distributions are applied only as correction terms to the average value employed for  $\bar{\tau}_T$  and  $\bar{f} \theta_g$ . Hence their uncertainties are much less pronounced in the final equation, since errors in the measurement of  $\bar{u}(x)$  and the choice of a drag coefficient  $k$  are of first order in the corrections only, not in the exponential terms themselves. These distributions also furnish a basis for the initial choice of the average space lag ( $1-\bar{f}$ ) as well as a check on the final iterated value of this parameter. Thus, the refined model contributes corrections to account, at least in part, for the two major limitations of the simplified model, namely, restriction to very low frequencies of oscillation and discontinuous representation of combustion distribution.

Under this framework of revisions, the combustion chamber equation is rewritten in the form:

$$R_F e^{i\omega F} e^{-i\omega \bar{\tau}_{AVG}} F(\omega, \bar{u}) \left\{ 1 + (re^{i\delta}) \left[ (\gamma_2 + k) - K \left( 1 - \frac{i\omega l}{c^* w_1} \right) e^{-i\omega \bar{f} \theta_g} g(\omega, \bar{u}) \right] \right\} =$$

$$= \frac{i\omega \theta_g}{\gamma} + \left( \frac{\gamma-1}{\alpha \gamma} \right) + \frac{i\omega l}{\gamma c^*} \left( w_1 - \frac{\gamma-1}{\gamma} w_2 \right) - n \left( 1 - e^{-i\omega \bar{\tau}_{AVG}} \right) -$$

$$- \left( \frac{\gamma-1}{\alpha \gamma} \right) \left( 1 - \frac{i\omega l}{c^* w_1} \right) e^{-i\omega \bar{f} \theta_g} g(\omega, \bar{u}). \quad (162)$$

where the time lag parameters  $\bar{\tau}_T$  and  $\bar{\tau}_{\bar{T}}$ , as well as the space lag parameter  $\bar{\theta}_g$ , appear as average values, in the manner of the simplified model. Correction factors  $F(\omega, \bar{u})$  and  $G(\omega, \bar{u})$  have been introduced in functional form to indicate that these corrections are based upon frequency considerations and upon actual combustion distribution.

The average sensitive time lag,  $\bar{\tau}_{avg.}$ , has been defined in Equation 156 from the integral form of the refined model, weighted by the combustion distribution (or gas velocity),  $\bar{u}(x)$ . The same procedure may be followed to define an average total time lag as:

$$\bar{\tau}_{T_{AVG.}} = \frac{1}{\bar{u}_1} \int_0^1 \bar{\tau}_T(x) \frac{d\bar{u}(x)}{dx} dx \quad (163)$$

The correction function  $F(\omega, \bar{u})$  must now be derived to equate (to terms of  $O(M^2)$ ) the exponential factor involving this average time lag to the integral expression of the refined model. Thus:

$$F(\omega, \bar{u}) e^{-i\omega \bar{\tau}_{T_{AVG.}}} = \frac{1}{\bar{u}_1} \int_0^1 e^{-i\omega \bar{\tau}_T(x)} \frac{d\bar{u}(x)}{dx} dx + O(M^2) \quad (164)$$

As in the derivation of Equations 157 to 160, one may expand both sides of 164 in a power series, yielding:

$$F(\omega, \bar{u}) \left[ 1 - i\omega \bar{\tau}_{T_{AVG.}} - \frac{(i\omega \bar{\tau}_{T_{AVG.}})^2}{2!} + \left( \frac{(i\omega \bar{\tau}_{T_{AVG.}})^3}{3!} + \frac{(i\omega \bar{\tau}_{T_{AVG.}})^4}{4!} + \dots \right) \right] = (165)$$

$$= 1 - i\omega \bar{\tau}_{T_{AVG.}} - \frac{\omega^2}{2\bar{u}_1} \int_0^1 \bar{\tau}_T^2(x) \frac{d\bar{u}}{dx} dx + \frac{i\omega^3}{3!\bar{u}_1} \int_0^1 \bar{\tau}_T^3(x) \frac{d\bar{u}}{dx} dx + \frac{\omega^4}{4!\bar{u}_1} \int_0^1 \bar{\tau}_T^4(x) \frac{d\bar{u}}{dx} dx + \dots$$

where use has been made of the definition of Equation 163.

This total time lag results from the integration of  $1/\bar{u}_g(x)$ , and hence must be considered of order  $1/M$ . Therefore,  $(\omega \bar{\tau}_{T_{AVG.}})$  and  $(\omega \bar{\tau}_T)(x)$  may both be of  $O(1)$ ; and the expansion of these may furnish contributions of  $O(M)$  for terms as high as the third power of the variable. Terms in the fourth power of  $(\omega \bar{\tau}_T)$  are reduced sufficiently by the factorial divisor as to

be considered negligible. Thus:

$$\frac{(\omega \bar{\tau}_T)^4}{4!} = \frac{O(1)}{2^4} = O(0.04) = O(M^2)$$

With this in mind, one may specify the form of the correction function  $F(\omega, \bar{u})$  also as a series expansion including terms of the third power in frequency, i.e.,

$$F(\omega, \bar{u}) = 1 - L\omega \Delta_1 - \frac{\omega^2}{2} \Delta_2 + \frac{L\omega^3}{6} \Delta_3, \quad (166)$$

where  $\Delta_1$ ,  $\Delta_2$ , and  $\Delta_3$  will show the dependence of the correction functions on velocity distributions. Rewriting Equation 165 then gives:

$$(1 - L\omega \Delta_1 - \frac{\omega^2}{2} \Delta_2 + \frac{L\omega^3}{6} \Delta_3) \left[ 1 - L\omega \bar{\tau}_{T \text{ AVG}} - \frac{\omega^2}{2} (\bar{\tau}_{T \text{ AVG}})^2 + \frac{L\omega^3}{6} (\bar{\tau}_{T \text{ AVG}})^3 \right] = \\ -1 - L\omega \bar{\tau}_{T \text{ AVG}} - \frac{\omega^2}{2 \bar{u}_1} \int_0^1 \bar{\tau}_T^2(x) \frac{d\bar{u}}{dx} dx + \frac{L\omega^3}{6 \bar{u}_1} \int_0^1 \bar{\tau}_T^3(x) \frac{d\bar{u}}{dx} dx + O(M^2) \quad (167)$$

Expanding this equation and equating the coefficients of like powers of  $M$  in a direct term-by-term comparison produces the following expressions for the correction factors:  $\Delta_1 = 0$

$$\Delta_2 = (\bar{\tau}_T^2)_{\text{AVG}} - (\bar{\tau}_{T \text{ AVG}})^2$$

$$\Delta_3 = (\bar{\tau}_T^3)_{\text{AVG}} + 2(\bar{\tau}_{T \text{ AVG}})^3 - 3\bar{\tau}_{T \text{ AVG}} (\bar{\tau}_T^2)_{\text{AVG}}, \quad (168)$$

where the higher power averages are arbitrarily defined from the relations:

$$(\bar{\tau}_T^n)_{\text{AVG}} = \frac{1}{\bar{u}_1} \int_0^1 \bar{\tau}_T^n(x) \frac{d\bar{u}(x)}{dx} dx$$

For evaluation of these correction terms, it is necessary to return to the original definition of  $\bar{\tau}_T(x)$  and perform the integrations numerically. These calculations are considerably simplified if one integrates the terms in 168 by parts, substituting relations from the steady-state droplet dynamics equation (57) wherever necessary. Performing this analysis gives:

72.

$$\Delta z = \frac{z}{k \bar{u}_1} \left[ 1 + k \int_0^x \frac{dx}{\bar{u}_1(x)} - \bar{u}_{L0} \bar{\tau}_{T1} \right] - \frac{1}{\bar{u}_1^2} \left[ 1 + \frac{(\bar{u}_{L1} - \bar{u}_{L0})}{k} \right]^2$$

(169)

and:

$$\begin{aligned} \Delta z = & \frac{3\bar{u}_{L0}\bar{\tau}_{T1}}{k\bar{u}_1} + \frac{c}{k\bar{u}_1^2} (1 - \bar{u}_{L0}\bar{\tau}_{T1}) \left[ 1 + \frac{(\bar{u}_{L1} - \bar{u}_{L0})}{k} \right] + \frac{c}{\bar{u}_1} \int_0^x \frac{\bar{\tau}_T(x)}{\bar{u}_1(x)} dx + \\ & + \frac{c}{\bar{u}_1^2} \left[ 1 + \frac{(\bar{u}_{L1} - \bar{u}_{L0})}{k} - \bar{u}_1 (\bar{\tau}_{T1} + \frac{1}{k}) \right] \int_0^x \frac{dx}{\bar{u}_1(x)} - \frac{z}{\bar{u}_1^3} \left[ 1 + \frac{(\bar{u}_{L1} - \bar{u}_{L0})}{k} \right]^3, \end{aligned} \quad (170)$$

where, as previously defined,

$$\bar{\tau}_T(x) = \int_0^x \frac{dx'}{\bar{u}_1(x')}$$

Because this form of correction term is easily applied to the combustion chamber equation and is not too difficult to evaluate numerically, it would be desirable to express the integral containing gas residence time in a similar series expansion. However, by definition,

$$\Theta_g(x) = \int_x^\infty \frac{dx'}{\bar{u}_1(x')}$$

and because the steady gas velocity must reduce to zero at the injector face, the gas residence time of a particle burning at this position ( $x = 0$ ) will be infinite. For all realistic distributions of combustion in the presence of some finite time lag, the velocity  $\bar{u}(x)$  approaches zero at this point as a flat curve, i.e., with small slope; and inspection of the integrated  $\Theta_g(x)$  shows that if the approach of the function is in the manner of a polynomial of first order or larger, this factor becomes infinitely large. Then, a series expansion of the form:

$$\int_0^\infty e^{-i\omega\Theta_g(x)} \cos \omega x \frac{d\bar{u}(x)}{dx} dx = \int_0^\infty \left[ 1 - i\omega\Theta_g(x) - \frac{\omega^2}{2!} \Theta_g^2(x) + \dots + \frac{(i\omega)^n}{n!} \Theta_g^n(x) + \dots \right] \cos \omega x \frac{d\bar{u}(x)}{dx} dx$$

considered as a function of  $\omega$   $\Theta_g$  has an essential singularity in the derivatives at  $\omega = 0$ .

For this reason it is impossible to express correction terms for this variable in the same power series form as was done for the  $\bar{U}_1(x)$  integral.

However, for certain discrete forms of the velocity distribution  $\bar{u}(x)$ , it is possible to evaluate the integral expression directly, without recourse to a series expansion. In particular, if  $\bar{u}(x)$  is made up of a number of straight line segments with  $\frac{d\bar{u}}{dx}$  zero at the injector face, such that:

$$\begin{array}{ll} \bar{u} = 0 & \text{for } 0 \leq x \leq x_0 \\ \bar{u} = a_1 x + b_1 & x_0 \leq x \leq x_1 \\ \bar{u} = a_2 x + b_2 & x_1 \leq x \leq x_2 \\ \bar{u} = a_m x + b_m & x_{m-1} \leq x \leq x_m \end{array} \quad (171)$$

then the integral:

$$I(\omega) = \frac{1}{\bar{u}_1} \int_0^1 e^{-i\omega \theta g(x)} \frac{d\bar{u}(x)}{dx} dx \quad (172)$$

may be evaluated as the sum of integrals over each defined range of linear  $\bar{u}(x)$ . Such a scheme may be used conveniently as an approximation to the actual velocity distribution. The degree of refinement desired will certainly direct the choice of the number of straight-line segments used to form the approximation; however, in most cases it should be sufficient to replace the actual curve of  $\bar{u}(x)$  with a single linear portion having as its slope the maximum slope of the true curve, as shown in Figure 6, since the largest contribution to the integral  $I(\omega)$  of Equation 172 must come from the area in which  $(\frac{d\bar{u}}{dx})$  is greatest.

In this case one may write:

$$\begin{array}{ll} \bar{u}(x) = 0 & \text{for } 0 \leq x \leq x_1 \\ \bar{u}(x) = mx + b & x_1 \leq x \leq x_2 \\ \bar{u}(x) = u_1 & x_2 \leq x \leq 1 \end{array}$$

and the integral  $I(\omega)$  is broken up into three parts:

$$I(\omega) = \frac{1}{\bar{u}_1} \int_0^{x_1} e^{-i\omega \theta g(x)} \left( \frac{d\bar{u}}{dx} \right)_{0 \rightarrow x_1} dx + \frac{1}{\bar{u}_1} \int_{x_1}^{x_2} e^{-i\omega \theta g(x)} \left( \frac{d\bar{u}}{dx} \right)_{x \rightarrow x_2} dx + \frac{1}{\bar{u}_1} \int_{x_2}^1 e^{-i\omega \theta g(x)} \left( \frac{d\bar{u}}{dx} \right)_{x_2 \rightarrow 1} dx$$

Here the only contribution to  $I(\omega)$  will come from the second interval ( $x_1$  to  $x_2$ ), since  $\frac{d\bar{u}}{dx} = 0$  for the other segments of the curve. Then:

$$I(\omega) = \frac{m}{\bar{u}_1} \int_{x_1}^{x_2} e^{-i\omega \int_{x_1}^x \frac{dx'}{\bar{u}(x')}} m dx$$

or, substituting the expressions for  $\bar{u}(x')$ ,

$$I(\omega) = \frac{m}{\bar{u}_1} \int_{x_1}^{x_2} e^{-i\omega \int_{x_1}^x \frac{mx' dx'}{mx'+b} - i\omega \int_{x_2}^x \frac{dx'}{\bar{u}_1}} dx \quad (173)$$

Performing the integrations indicated in Equation 173, one obtains for the value of the integral expression:

$$I(\omega) = \frac{e^{-i\omega \left( \frac{x_2-x_1}{\bar{u}_1} - i \tan^{-1} \frac{\omega(x_2-x_1)}{\bar{u}_1} \right)}}{\sqrt{1+\omega^2 \left( \frac{x_2-x_1}{\bar{u}_1} \right)^2}} \quad (174)$$

where  $m (= \frac{d\bar{u}}{dx})$  has been replaced by its equivalent form  $(x_2-x_1)/\bar{u}_1$ .

As pointed out previously, the quantity  $(\omega/\bar{u}_1)$  is equivalent to  $(\omega \theta_g)$  by the scheme of non-dimensionalization employed in the derivation of the refined model. Hence, one may write:

$$I(\omega) = \frac{e^{-i\omega \theta_g \left[ (x_2-x_1) + \frac{1}{\omega} \tan^{-1} (\omega a) \right]}}{\sqrt{1+\omega^2 a^2}} \quad (175)$$

where  $a = \frac{1}{m} = 1 / \left( \frac{d\bar{u}}{dx} \right)_{\text{MAX}}$ .

The similarity in form between this expression and the corrected exponential factor of the simplified model, e.g.,

$$e^{-i\omega \tilde{f} \theta_g} G(\omega, \bar{u})$$

allows for direct comparison between the two forms for evaluation of the average space lag and the correction factor. Thus, if:

$$a = \frac{1}{\omega} \left( \frac{d\bar{u}}{dx} \right)_{MAX}$$

$$\bar{f} = \left[ (1-x_2) + \frac{\bar{u}_1}{\omega} \tan^{-1}(\omega a) \right]$$

$$G(\omega, \bar{u}) = \frac{1}{\sqrt{1+\omega^2 a^2}}$$

(176)

then:

$$\text{as desired. } I(\omega) = G(\omega) e^{-i\omega \bar{f} \theta_g}$$

From the results of 176, one notes that the expressions for both  $\bar{f}$  and  $G(\omega, \bar{u})$  exhibit a harmonic behavior, a fact in keeping with the inability to express  $I(\omega)$  in a series expansion of ascending powers of frequency. Also, it is apparent that the space lag  $\bar{f}$ , which represents an effective average position for a concentrated combustion front replacing the actual distributed combustion, exists at a location between the beginning and end of the straight line segment approximating the maximum rate of rise of  $\bar{u}(x)$ . Thus:

$$(1-x_2) < (1-x_2) + \frac{\bar{u}_1}{\omega} \tan^{-1} \frac{\omega}{\bar{u}_1} (x_2 - x_1) < (1-x_1)$$

since:

$$\tan^{-1} \frac{\omega}{\bar{u}_1} (x_2 - x_1) < \frac{\omega}{\bar{u}_1} (x_2 - x_1)$$

In the particular case where the actual velocity  $\bar{u}(x)$  exhibits a relatively steep rise, the expression for  $\bar{f}$  may be considerably simplified.

Thus, when  $\left( \frac{d\bar{u}}{dx} \right)_{MAX} = O(1)$

then:  $\omega a = \frac{\omega}{\bar{u}_1} (x_2 - x_1) = O(\omega)$

and:  $\tan(\omega a) = \omega a + \frac{(\omega a)^3}{3} + \dots$

or:  $\tan^{-1} \frac{\omega}{\bar{u}_1} (x_2 - x_1) = \frac{\omega}{\bar{u}_1} (x_2 - x_1) + O(\omega^3)$

Hence:  $\bar{f} = (1-x_1) + O(\omega^3)$

$$G(\omega, \bar{u}) = 1 + O(\omega^2)$$

(177)

These results show that, as might be expected, the correction factor  $Q(\omega, \bar{u})$  approaches 1.0, and the location of the average space lag approaches the start of the rise in gas velocity as the velocity distribution becomes steeper and is thereby more closely approximated by a discontinuous combustion "front". (The approximation  $\tan \omega a = \omega a$  is a reasonable one for values of  $\omega a$  as great as 0.4 or 0.5. In the experiments described herein, the maximum  $\omega = 0.15$ , allowing the use of this simplification for  $a$  as large as 3.0, or  $(\frac{d\bar{u}}{dx})_{MAX}$  as small as 0.3.)

Returning to Equation 162 and substituting the derived values for the correction factors as expressed by Equations 166, 168, and 176, one obtains a final combustion chamber equation for the combined theoretical model as follows:

$$R_F e^{i(\beta_F \omega \bar{\tau}_{AVG})} \left( 1 - \frac{\omega^2}{2} \Delta_2 + \frac{i\omega^2}{6} \Delta_3 \right) \left\{ 1 + (n e^{i\delta} - 1) \left[ (\gamma_2 + h) - \frac{k(1 - \frac{i\omega^2}{cm} w_1)}{\sqrt{1 + \omega^2 a^2}} e^{-i\omega \bar{f} \theta_g} \right] \right\} = \\ + \frac{i\omega \theta_g}{\gamma} + \left( \frac{\partial \gamma - 1}{\partial \gamma} \right) + \frac{i\omega l}{\gamma cm} \left( w_1 - \frac{\gamma - 1}{2} w_2 \right) - \left( \frac{\gamma - 1}{\partial \gamma} \right) \left( 1 - \frac{i\omega^2}{cm} w_1 \right) \frac{e^{-i\omega \bar{f} \theta_g}}{\sqrt{1 + \omega^2 a^2}} n (1 - e^{-i\omega \bar{\tau}_{AVG}}) \quad (178)$$

with explicit definitions for  $\Delta_2$ ,  $\Delta_3$ ,  $a$ , and  $\bar{f}$  given by Equations 169, 170, and 176. This linearized, complex equation is the basis for analysis of the experimental data to obtain the four combustion time lag parameters,

$\bar{\tau}_{T AVG}$ ,  $\bar{f} \theta_g$ ,  $n$ , and  $\bar{\tau}_{AVG}$ . The exact method of application of the equation to the data is discussed in detail in a later section.

## EXPERIMENTAL METHODS AND EQUIPMENT

### Experimental Requirements

The experimental phase of this investigation is designed with the object of obtaining sufficient empirical data to determine combustion time lag parameters as described by the theory and to check the validity of the assumptions involved. Reference to the final combustion chamber equation (177) shows that primary experimental requirements consist of measurements of the rocket motor transfer function and the instantaneous propellant mixture ratio. These data must be obtained under conditions of stable combustion in the presence of small, controlled, sinusoidal oscillations in both propellant flow rates, since an exponential form of time variation for all perturbed quantities has been postulated throughout the theoretical analysis.

Initiation of a series of instantaneous step function or "square-wave" pulses in one or both propellant feed lines and subsequent detection of the chamber response to such sharp changes in conditions appears at first glance to be a more direct method of obtaining time lag parameter data than the production of sinusoidal perturbations. However, a number of latent complications in the single-pulse technique make it less desirable than the method chosen. These difficulties may be grouped into two major categories: indeterminacy of the input function and uncertainty in observation of the chamber response.

In the first category, the primary obstacle is the production of a true "step" change in flow rate by a practical, positive displacement method. The unavoidable presence of inertia in mechanical systems causes deviations from a truly instantaneous change from one operating level to another, and even minute values of compressibility and elasticity in liquid propellants and the feed lines containing them may be sufficient to cause serious wave-travel effects. In addition, determination of the precise shape of a pulse which is

acceptably close to a true step function requires extremely high frequency response instrumentation, a demand which is as yet unsatisfied in the realm of flow rate measurement.

From the viewpoint of observation of output from such a pulse input, the problems are chiefly those of analysis. Even an exact step change in flow rate must be smoothed out in the combustion chamber into a much less distinct shape by the action of turbulence, non-uniformities in liquid droplet size, deviations from purely one-dimensional flow conditions, and the existence of re-circulation patterns. Therefore, it becomes impossible to measure an exact time elapsed from the instant of injection of the pulse to a subsequent instant when this pulse has produced a similar change in chamber conditions. The only data immediately evident from an analysis of chamber pressure, temperature, or gas density records obtained with the optimum equipment available are those of a minimum and a maximum combustion time lag at operating conditions whose average is ill-defined. Even when both input and output wave shapes are considered known to an acceptable degree of precision, determination of a proper mean value of the time lag requires the use of complex Fourier methods in which the presence of random frequency combustion "noise" may contribute serious and indistinguishable effects.

These disadvantages indicate, in part, the desirability of producing some sort of continuous fluctuation in flow rates which would be amenable to analytical treatment. The method chosen for the investigation herein reported is merely the application of well-known mechanical techniques of simple harmonic motion for producing near-sinusoidal oscillations from pistons driven by a rotating, eccentric crankshaft. The obvious mechanical difficulties of such a system, e.g., complicated construction, eccentric balance problems, development of reliable dynamic seals, continuous lubrication of bearing surfaces, are compensated by a number of significant gains over the single-pulse technique.

Chief among these advantages is the ease of analysis of the fluctuating signals. Determination of the rocket chamber transfer function reduces to the measurement of the amplitudes and phase relationships of three sinusoidal signals of known frequency, free from transients and well within the response range of present sensing and recording instruments. These same amplitudes and phases also determine the value of instantaneous propellant mixture ratio, a quantity which must be closely controlled if the data are to be applied to the previously-derived theory. Also of importance in analysis is the fact that in such controlled variations the presence of random frequency combustion noise is easily detected and may be selectively filtered from the signals, if desired, without altering the characteristics of the fundamental oscillation of known frequency. In addition, this method of varying the input flow rates permits operation of the rocket motor at essentially stable conditions with well-defined average or steady-state values upon which small linearizable perturbations are superimposed. Thus, the restrictive assumptions of the theoretical treatment may be very closely approximated by the sinusoidal method of flow modulation with only minor sacrifices in mechanical simplicity.

In addition to these primary measurements of transfer function and instantaneous mixture ratio, the final combustion chamber equation indicates a number of secondary experimental requirements. First, in order to calculate fractional variations of all oscillating quantities, one must obtain average, or steady state, values of propellant flow rate, mixture ratio and chamber pressure. Also essential are injector pressures and rocket thrust for determination of the parameters  $\bar{r}$ ,  $H$ ,  $K$ , and  $c^*$ . The correction terms , , , and require a choice of droplet drag coefficient as well as a knowledge of steady-state gas velocity distribution along the chamber length, which may be obtained from an axial pressure survey and the application of one-dimensional flow equations.

Two further considerations contribute to the choice of experimental procedures and equipment: reliability and precision. The former is established primarily by performing repeatability tests at essentially constant operating conditions and observing the scatter of calculated results, while the latter influences the design of instrumentation and experimental methods by requiring that all measuring devices employed be amenable to straightforward observation and calibration. These demands are met by obtaining duplicate measurements from independent methods wherever possible and by comparing oscillating quantities observed during rocket runs with values produced electrically and calibrated from standard instruments.

#### Measuring Vehicle

Laboratory equipment required to obtain the desired experimental data includes a rocket motor suitable for easy instrumentation, a test stand relatively free from non-linear and two-dimensional effects, a propellant feed system isolated from interaction with the combustion process, flow-modulating equipment with adjustments available for altering amplitude and phase relationship, and the establishment of a standard test procedure for sensing and recording the desired phenomena.

The initial phases of the test program were conducted with the objects of establishing satisfactory procedures, testing the design features and power requirements of a flow-modulating unit, finalizing the choices of test stand and feed system components, and determining the range of application and operating characteristics of the instrumentation. For these purposes a simple monopropellant rocket motor and feed system were constructed to operate with ethylene oxide and small quantities of gaseous oxygen (14). The relatively low temperature of this combustion made possible the use of an uncooled motor which could be run with easily-installed pressure instrumentation for a duration of a half-minute or more. This stainless steel chamber with radial in-

jection is shown mounted on the thrust stand in Figure 7 in a configuration in which a total of 121 test runs were made. The flush-mounted pressure pickups are shown installed in injector and chamber in more detail in Figure 8.

Because the primary interest in combustion instability and the time lag parameters which contribute to its understanding lies in the field of liquid bipropellant rockets, the monopropellant system gave way, following the completion of the preliminary tests described above, to a bipropellant motor designed for obtaining valid time lag data at three operating chamber pressure levels.

The propellant combination chosen for these experiments, and currently in use on the test program, consists of liquid oxygen and ethyl alcohol (in a commercially-available form containing approximately 5% water and small quantities of gasoline, methyl alcohol, and ethyl acetate). This choice is based primarily upon the wealth of available information in the literature concerning reliable designs of rocket chambers, nozzles, injectors, and feed system elements for use with these propellants. Since the development of a high-performance rocket motor is not a primary objective of the program, it was felt that the adoption of a thoroughly tested propellant combination using proven component designs would represent a considerable saving in time in the experimental phase of the work.

The rocket combustion chamber itself is machined from solid copper bar stock as a thick-walled cylindrical shell of 3 - inch inside diameter, 6 - inch outside diameter, and a length of 4-1/64 - inches. A sectional view of the chamber, injector, and nozzle is shown in Figure 9. The motor is run uncooled for ease of installation and replacement of the flush-mounted pressure pickups (as illustrated in this figure) for a total run duration of 10 to 15 seconds. The L\* of the chamber-nozzle combination is approximately 47 inches; and the motor is designed to operate at 300, 450, and 600 psia chamber pressure levels, producing nominal thrusts of 250, 400, and 550 pounds,

respectively, at each of these pressures at a design mixture ratio of 1.35 (oxygen-to-fuel, by weight).

The injector configuration is based upon a Reaction Motors, Inc., design with two concentric manifolds leading fuel and oxidizer into a ring of paired injection orifices. This ring consists of twelve pairs of one-on-one, unlike, impinging streams with an impingement point zero distance from the injector face. The orifice angles are chosen to give net momentum of the mixed liquids in the axial direction, and the orifice diameters are designed to produce a pressure drop of approximately 120 psi under steady flow conditions. Thus, separate injectors, similar in all dimensions save the orifice diameter, are employed for operation at each chamber pressure level. The injector assembly is machined from solid brass stock in three parts, silver-soldered together, and bolted to the copper chamber, with "Flexatalllic" sealing gaskets at the interface.

The nozzle design is based upon a Purdue University prototype of a double-conical form with exit diameter chosen for correct expansion at 600 psia chamber pressure. The converging-diverging walls are 1/4 - inch thick copper with conical half angles of 30° and 15° at entrance and exit, respectively, and a throat diameter of 0.875 - inch. Spirally-wound copper wire and split filler blocks on the outside nozzle walls form helical passages for coolant water, which is pumped through this jacket at an inlet pressure of 400 psig and an outlet pressure of 100 psig.

The test stand on which the motor, flow-modulating unit, and some feed system components are mounted is illustrated in Figure 10. The stand is built on a concrete base with flat aluminum top, an arrangement which is simple, sturdy, and spacious enough for instrument installation and maintenance. The supports for this stand are of leaf-spring type, permitting only one degree of flexural freedom, with sandwich construction supplying rigidity.

Figure 10 also provides a view of the flow-modulating unit installation, details of which are shown in Figure 11. The design is based upon monopropellant experience and is a straightforward crank-piston arrangement with a 0.10 - inch crankshaft eccentricity. Connecting rods are aluminum, turning in roller bearings and attached with wrist pins to stainless steel pistons. These pistons are machined with two hardened bearing surfaces which ride in oil-filled, porous bronze bearings pressed into the surrounding stainless steel cylinders. Since the pistons have a fixed stroke of 0.20 - inches, desired amplitudes of modulation are achieved through the use of various sizes of piston-cylinder diameters, ranging from 0.195 - inch to 0.409 - inch. The seal at this cylinder head is obtained from cup-shaped, Teflon gaskets, impregnated with Fiberglas for additional strength and lubricated with an inert fluorocarbon grease. The cups are held in place by a removable piston cap. Power for the system is furnished by a 5 - HP, U. S. Motors Varidrive electric motor through a belt-pulley drive with 2:1 diameter ratio, providing modulating frequencies of from 59 to 248 cycles per second. The fuel and oxidizer halves of the crank shaft are joined by a split flywheel with 1° angular markings, which permits adjustment of the phase between the two modulations to any desired value before each rocket run.

The feed system, as seen in Figure 12, is a simple gas-pressurized one, employing nitrogen or helium as the inert gas. Fuel is supplied from a 20 - gallon, stainless steel tank, while the liquid oxygen is retained in a 40 - gallon, vacuum-jacketed, monel tank. Two sets of propellant valves are installed. The upstream "emergency" valves are pneumatically operated, while the main valves are hydraulically opened models obtained from a commercial design of a rocket motor. Both pairs of valves are controlled by solenoid operation of a pilot gas pressure, and both are spring-loaded for fail-safe closing. An extra by-pass needle valve is installed in the liquid oxygen line

for pre-cooling the oxygen system.

Multiple-hole cavitating venturis are placed in both feed lines between the main propellant valves and the flow-modulating unit for the purpose of isolating flow pulsations and combustion disturbances from the highly elastic feed system and storage tanks. Design details of these venturis are shown in Figure 13. Since the venturis continue to cavitate for downstream pressures as high as 0.8 of the upstream pressure, they permit the pre-run determination of constant average flow rates from the choice of tank pressures only, independent of small variations in downstream pressure. The multiple-hole configuration was chosen after some experience with single-hole venturis for the purpose of reducing the overall bubble volume and hence minimizing the effects of this capacitance upon the creation of near-sinusoidal flow oscillations.

Operation of the motor for these short duration tests has been reduced to a simple standard procedure involving remote firing from a console, observation through armored periscopes, and photographing of primary gauge readings within a reinforced concrete control room, illustrated in Figure 14. The procedure consists of five successive steps: pre-cool of the oxygen system through the by-pass needle valve; full flow of liquid oxygen for a period of 10 to 20 seconds; acceleration of the flow-modulating unit to full speed (5 to 35 seconds); electrical ignition of a solid propellant squib igniter; and initiation by opening the main fuel valve. The last step in this procedure is accomplished automatically when the squib igniter burns through a fuse circuit thereby operating relays which open the main fuel valve and furnish power to the timer circuit for the gauge panel clock and sequence camera.

#### Sensing and Transducing Instrumentation

The instruments required for measurement of time lag parameter data have been described in detail in several previous publications (15, 27), and it will suffice here merely to describe their principles of operation and the

reasoning behind their selection, grouping them according to application for sensing and recording either steady state or transient phenomena. Wherever possible, an attempt has been made to duplicate these measurements in two independent sensing elements.

The steady state data of interest consist of thrust, chamber and injector pressures, flow rates, axial pressure distributions, and heat transfer rates. The first of these, rocket motor thrust, is observed on a Bourdon-type gauge as the force derived from oil pressure in an Emery hydraulic load cell mounted on the concrete base of the test stand and receiving its input load from a bracket bolted to the test stand table top. Total deflection of the stand (and hence of the piston within the load cell) under the action of the maximum thrust load is approximately .002 - inch, eliminating the necessity of considerations of two-dimensional loading from the parallelogram-type stand. A separate electrical indication of thrust is obtained from an unbonded four-arm strain gauge pickup in the form of a tension member mounted on the same test stand bracket which, in turn, transmits the thrust force to the hydraulic load cell. This strain gauge pickup is used as a Wheatstone bridge circuit and is powered by a 90 - volt battery source.

Rocket chamber and injector pressures are also observed both pneumatically and electrically, the former appearing as indications on Heise-Bourdon gauges in the control room, receiving their input pressures direct from taps in the motor wall and injector manifolds. Electrical signals again originate in strain gauge pickups, each forming two active arms in a battery-powered bridge circuit. The pickups employed are Li-Liu, double-catenary-diaphragm, water-cooled models to be described in detail in a later section.

Propellant flow rates are measured from the output frequencies of Potter turbine-type flowmeters mounted directly in the lines just upstream of the main propellant valves. A secondary indication of flow rates is obtained from the individual injector pressure drops.

Axial pressure distribution along the length of the chamber is observed by two separate methods, neither of which is considered entirely satisfactory. The first method attempted involves the use of Statham strain gauge differential pressure meters powered by an alternating carrier current and providing an amplitude modulation as an output signal. The necessity for rather complex electrical equipment, including commutation for observing five separate pickup outputs in a 1/2 - second cycle, and the requirements for additional remotely-controlled valves for protection from overpressure during starting and shut-down transients make this system somewhat cumbersome and expensive. The alternate procedure of photographing armored manometers, although a more direct method for obtaining pressures, also suffers from the complication of protective valving as well as from the long response time of connecting tubing.

Heat transfer measurements are primarily intended for an associated investigation (28); however they also furnish correction data for performance calculations and are extremely reliable for indicating the existence of "screaming" oscillations in the motor. For this purpose, inlet and outlet thermocouples are embedded in the cooling-water tubes for the chamber pressure pickup and the nozzle.

The transient data requirements are fewer in number than those for steady state data but considerably greater in complexity. They consist of instantaneous flow rates, chamber and injector pressures, and frequency of flow modulation, of which the only relatively simple measurement is the last one. This frequency is determined directly from the rotation of the modulating unit crankshaft by embedding a two-pole permanent magnet in the shaft and observing the output frequency from a Potter flowmeter coil mounted on the thrust stand immediately above the magnet.

Of the two remaining measurements, the more difficult is certainly that of instantaneous flow rate. Previous attempts had been made to use the Li mass flowmeter and one model of an electromagnetic flowmeter. However,

the problems of fluid and electrical leakage, low natural frequency, electrical drift, and non-magnetic properties of organic fluids indicated a rather extensive development program with doubtful results before either of these methods could be considered satisfactory. This reasoning led to the choice of the present method, that of the application of a linearized form of the non-steady, incompressible, axially-symmetric equations of motion to the problem of pulsating liquid flow through an orifice. The application of this equation reduces the flow measurement problem to that of evaluation of inertial parameters from the geometry of the particular orifice configuration used and instantaneous measurement of the pressure drop across the orifice. The method was first applied to the radial injection system of the monopropellant motor and then for the simpler straight-orifice design of the bipropellant injector, the theoretical analysis of which is given in Appendix C. A more complete discussion of the method and its general applicability is given by Wick (29).

At the modulating frequencies encountered in the present operation departure of the flow rates from those calculated by the steady state Bernoulli equation are quite small; and a variance between actual flow-pressure drop relations and those predicted theoretically of as much as twenty percent would still have a negligibly small effect upon the total flow rate at any instant. Nevertheless, a study was initiated to attempt to evaluate the theory by experimental techniques (30, 31), with considerable effort spent on the development of a liquid hot-wire anemometer. It has been found that although this instrument has application in a few specialized cases, it is not generally acceptable for measurement of amplitudes of flow oscillations; and even in flow-pressure drop phase measurements, it suffers generally from restrictions of natural frequency and effects of vapor bubbles on the wire. These considerations have led to the present "momentum method" for evaluation of the theory, in which the instantaneous thrust of the injector manifold under

pulsating flow conditions is measured by mounting a mock-up of the injector on a cantilever beam containing bonded strain gauges.

The great importance of instantaneous pressure measurements in both rocket chamber and injector manifolds is thus emphasized, for these data are essential in the determination of both fractional perturbations in chamber pressure and instantaneous flow rate, the two primary parameters contributing to the rocket transfer function. Because of this emphasis on reliable pressure measurements, a great deal of effort has been expended in the development of the Li-Liu pressure pickup (27,32, 33). An exterior view of the model of this pickup used in the injector manifold is shown in Figure 15. The major advantage of this pickup is its ability to be flush mounted, by virtue of the existence of cooling water passages between its double diaphragm. This construction is indicated in the sectional view of Figure 16. The pressure-sensing diaphragm is formed from .004 - inch thick stainless steel of catenary cross-section, producing linear deformation with application of pressure. This pressure is transmitted through a spacer ring to a second, mirror-image diaphragm upon which rests the thin-walled aluminum strain tube. This tube is doubly-wound with special alloy strain wires for thermal and inductive compensation. Provision is made in the differential pressure models for the application of a reference pressure to the inner diaphragm, allowing for a more sensitive, but shorter-range, instrument. Safety stops are embodied in the spacer ring design to prevent overpressure damage in either direction. A series of thermal drift tests resulted in a recent design for an extremely stable chamber pressure pickup which is flange-mounted to the outer chamber wall and has double cooling jackets with separate inlets and outlets, providing drift-free operation at 600 psia chamber pressure. The two sets of strain gauge windings form two active arms of a battery-powered Wheatstone bridge, and the pickup output, at approximately 60 volts input, is of the

order 0.1 millivolt per psi.

The final problem in observation of data is that of time orientation, i.e., the coordination of all indicating and recording instruments from a starting point in time. This chosen start time is the opening of the fuel propellant valve, which marks the beginning of actual combustion in the rocket chamber. As previously mentioned, this operation takes place as the result of the opening of a relay in the igniter fuse circuit. This one circuit-breakage initiates three coincident indications of time during the run. The first of these is the transmission of power to an electric photo-timer clock with 10-second sweep which is mounted on the gauge panel of the operating control room. The same signal initiates a "pulse" circuit which operates the sequence camera photographing the entire gauge panel. Simultaneously, power is transmitted to the central recording room, remotely located, energizing a relay which conveys a 100-cps timer trace to a magnetic tape recorder for transient signals and a 1-cps signal to the steady state recording potentiometers. Thus, all gauges are photographed at times which appear directly on the photograph, and a reference time indication appears on all recorded data.

#### Recording Instrumentation

All electrical signals from which permanent records are desired are transmitted by shielded cables through an underground conduit from the test cell via the control room, to a central recording room which is isolated from extraneous outside electrical disturbances and shielded from the possible effects of test cell explosions. A schematic representation of the location of components and the instrumentation involved in pressure measurements is shown in Figure 17.

Records of all electrical steady state data are afforded by recording potentiometers of the Leeds and Northrup Speedomax type arranged

in the central recording room as illustrated in Figure 18. The bridge circuit output from the strain gauge thrust pickup is recorded directly on a 20-millivolt range instrument, while the frequency outputs of the Potter flowmeters are transmitted through integrator circuits whose d.c. outputs (directly proportional to frequency) are recorded on 10-millivolt potentiometers. A similar integrator circuit is used to transform the modulating frequency into a d.c. voltage which is recorded on an adjustable range potentiometer. Pressure pickup outputs must be simultaneously recorded on both steady state and transient instruments, which must be electrically matched to prevent interference and non-linear signal drainage. For this purpose battery-operated cathode follower circuits are employed which serve to isolate the steady state recorders from the transient instrumentation and also act as attenuators, reducing the pickup outputs to a range compatible with the 10-millivolt potentiometers on which steady state pressures are recorded. Thermocouple outputs are indicated as temperature differences on adjustable-range instruments. In the tests in which the Statham differential gauges are used to measure axial pressure distribution their outputs are obtained from demodulation of the alternating carrier voltage and are portrayed on a six-channel Hathaway light-beam galvanometer oscillograph.

Transient data are recorded simultaneously with, but independent from, steady state signals through a.c. equipment located in the central recording room as shown in Figure 19. The primary transient instrument is an Ampex 7-channel FM magnetic tape recorder with a flat frequency response from dc to 10,000 cps. Three channels are used for recording the oscillating portions of oxidizer and fuel injector pressures and rocket chamber pressure, while a fourth channel carries the 100-cps trace for time orientation. Since this recorder requires an input signal of approximately 1.0 volts for optimum fidelity, two stages of amplification are applied to the pickup output signals before introducing them to the tape. The first of

these stages is a d.c. powered pre-amplifier circuit with a gain of approximately 10, while the second consists of Technology Instrument Corporation multi-range constant-phase a.c. amplifiers with variable gain of from 10 to 1000. The Ampex tape recorder is the only instrument employed for obtaining quantitative transient records; however, for monitoring during rocket runs and for qualitative observations of data during playback from the magnetic tape, a 4-channel oscilloscope (with strip-film attachment available) and the aforementioned recording oscilloscope are both utilized.

#### Calibration Methods

Wherever possible, instrument calibrations are conducted with primary electrical, pressure and force standards in conditions simulating actual installations on the rocket test stand. The sensing elements are all calibrated by static methods, save in the case of the development of the Li-Liu pressure pickup, where some dynamic tests have been conducted (32). All calibrations are performed at regular intervals.

The thrust pickup and hydraulic load cell are calibrated coincidently by applying a thrust load to the test stand through a factory-calibrated proof ring and observing the deflection of this ring with a standard machinist's dial indicator gauge. Known pressures are applied to the Li-Liu pickups during calibrations with a dead-weight tester, and the pickup outputs are observed on a hand-balanced potentiometer with light-beam galvanometer. These tests determine the pickup output sensitivity under fixed voltage conditions, indicate the extent of the linear output range of the differential models, furnish a check on possible hysteresis or "back-lash" effects, and provide information on pickup repeatability through cycling tests. A typical output curve from such a cycling calibration test is reproduced from a previous publication (32) in Figure 20. Tests of "hot" sensitivity of differential pickups under actual firing conditions are

accomplished by applying successively two different values of reference pressure to a pickup during a rocket run and comparing the outputs from these two differential pressures at essentially constant chamber pressure. The Potter flowmeter sensing elements are factory-calibrated by direct time-weighing methods with fluid density and thermal contraction corrections applied. Calibration of the differential cells for axial pressure measurement is performed by applying pressure from a mercury manometer.

The steady state recording potentiometers are calibrated in a straightforward manner from hand-balanced potentiometer inputs. These tests, when conducted with the cathod follower circuits installed, constitute checks on the linearity, hysteresis, and output sensitivity of the complete steady state pressure recording system. All Bourdon gauges are checked by dead-weight gauge tester, and the frequency integrating circuits are calibrated with inputs from 60-cps and 120-cps regulated line voltage.

Calibration of the transient recording system is a somewhat more complex procedure and is performed in two separate operations, one before and one following a rocket run. Each involves the simulation of pressure fluctuations by an oscillating electrical signal which forms an input to the amplifier system, is played through the complete transient network at approximate run settings, and finally appears as a magnetic signal on the tape recorder. In the pre-run operation, individual recording channels are calibrated separately for amplitude sensitivity by choosing an electrical input of the size expected from the pressure pickup signal during the run and at the preset run frequency. Calibrations of phase differences between channels arising from the recording network are obtained in the post-run operation by simultaneously recording signals of the average run amplitude and the exact run frequency on all three transient pressure channels.

ANALYSIS OF EXPERIMENTAL DATAReduction Of Primary Data

A sample calculation for data points obtained during a typical rocket run is contained in Appendix D, with all steps in the data reduction procedure given in detail. The following discussion is therefore limited to a general explanation of the data handling operations involved and the calculation methods employed.

Primary steady state data are comprised of two major forms: gauge panel photographs and Speedomax recorder charts. The former are quickly reduced to corrected pressures and thrust by projecting the 70-mm strip film on a screen, reading the indicated gauge values, and correcting these readings from the dead-weight and proof-ring calibrations of pressures and thrust, respectively. At the same time, the instant at which each photograph was taken is noted from the gauge panel clock, and reliable points after the starting transient and before the release of pickup reference pressure preceding the end of the rocket run are selected. These photo times then determine the locations on the Speedomax charts at which data are to be read. The marker pen indications on these charts specify the instant of zero time from which the reading times of valid points are located as distances from the known recorder chart speed. Net chart readings at these points are then converted to numerical pressure, flow rate, frequency, and thrust measurements from their corresponding calibration curves. Corrections to the flow rate readings are calculated from thermal contraction at the liquid oxygen boiling point and from the fuel specific gravity at its measured temperature. Axial pressure distributions are either read directly from manometer photographs or reduced to pressure values from the oscilloscope charts and accompanying calibrations.

Having decided from the oscilloscope monitor of the run that the transient signals are of the desired order of magnitude for a constant mixture

ratio data point, one may then proceed at any convenient time to play back the permanent records of oscillating pressures from the tape recorder. The important data to be derived from these taped signals are the amplitudes of and phase angles between the chamber and injector pressure oscillations, and these may be played back at the recording speed of 60 inches per second for quantitative readings or 3 inches per second for display or investigation of the wave form of each cycle. The linearized perturbation analysis which produced the governing combustion chamber equation contains the inverse transfer function of the rocket motor in terms of the response of the chamber at the fundamental frequency of input oscillations, without the inclusion of second order effects of squared terms in the frequency or higher harmonics of this fundamental. For this reason, all three pressure signals are fed through passive, R-L-C element filters of constant inter-channel relative phase. These serve to eliminate small high-frequency oscillations and random combustion noise without distorting the fundamental wave shape.

The actual values of oscillating amplitudes and phases are determined by a method which has resulted from considerable development efforts. The original procedure consisted of direct measurements by linear scale of the peak amplitudes and peak-to-peak phase distances on playback records from the Hathaway oscillograph or from projected 35-mm strip films of the 4-channel oscilloscope face. This method was employed for reduction of monopropellant time lag data (14), but it proved too cumbersome and inaccurate for use in the bipropellant measurements, for which a system was adopted using a Ballantine vacuum-tube voltmeter for amplitude values and a Lissajous pattern on a two-beam oscilloscope for phase readings (15). The phase difference between any two signals was continuously nulled by hand during slow-speed playback by the variable resistance of an R-L-C phase-shift network. The required nulling resistance was noted, and the phase angle corresponding to this value was determined from previous calibrations of oscillator signals at run

frequencies in which the eccentricity of the Lissajous pattern was measured directly. Time orientation during playback was established by counting the 100-cps timer trace in a Berkeley electronic counter-timer and observing the tape footage at which photo values of time occurred.

Data reduction by these methods is extremely tedious and subject to considerable human error in the judgment of both reading times and observed values; hence a more reliable procedure of playback was developed which would furnish accurate time reference and permanent records of transient values. By this scheme, as seen in Figure 21, a signal amplitude is recorded as the output of a crystal diode half-wave rectifier on a recording potentiometer whose marker pen relay circuit is activated by playback of the taped timing trace, giving an accurate time reference. A sufficiently large driving signal for the diode is attained by the use of the aforementioned TIC amplifiers and a 10 - gain phantom repeater circuit, with the variable gain setting of the amplifier adjusted to prevent "clipping" of the diode input from saturation of the phantom repeater tubes. Linearity of the diode output is assured by passing two non-zero voltages through the diode circuit and presetting the adjustable-zero, adjustable-range recorder to place these signals in their proper linear relationship on the recorder scale. Careful choice of the values of these pre-set voltages insures that both calibration and run signals will lie within the known linear range, and both these taped signals are played back through this system to form a written amplitude record. Comparison between run and calibration levels and multiplication by the known calibration input produces the exact electrical value (in Millivolts) of the run signal, and division by the previously-determined pickup sensitivity (milli-volts per psi) transforms these readings into pressure units.

The final system evolved for phase measurement and recording warrants some individual discussion. A phasemeter-recorder developed as an experimental model by the Jones-Porter Instrument Company detects, by means

of a discriminator circuit, the phase difference between two of the filtered pressure signals and converts this angular difference to an electrical output which is used to drive a small servo motor attached to a Speedomax recording potentiometer. Movement of the potentiometer slidewire produces and opposing e.m.f. until the rotation of the servo shaft has completely balanced the input voltage. The resultant null position is then a linear function of the original phase difference. Velocity damping is added to stabilize the recorder operation, and frequency and amplitude compensations are made with variable resistances at the phasemeter input. Any phase shift inherent in the machine may be determined through a split oscillator signal which furnishes a third input to the meter. The recorder output is calibrated either from a commercially available phase standard or by Lissajous pattern eccentricities. Again the potentiometer marker pen relay is used with the taped 100-cps trace as a timing reference.

#### Calculation Procedures

Once these primary values have been obtained, the secondary data reduction processes are performed as a combination of hand computations and electronic operations on an IBM digital computer (Model 604) of the card program calculator type. These calculations are broken down into three successive stages, each of which depends upon outputs of the previous stage as inputs for the current stage. The overall calculation procedure is illustrated in block diagram form in Figure 22.

Calculations of the steady state parameters required as inputs to any of the stages may be performed at any point during the data reduction process. In addition to the primary values of propellant flow rates, injector pressures, chamber pressure, thrust and modulating frequency, steady state data furnish inputs for hand calculations of injector pressure drops, mixture ratio, total propellant flow, and axial pressure distribution. From these and measurements of the nozzle throat diameter, the characteristic

velocity,  $c^*$ , is computed. Plots are made of the variations of thrust with flow rate, chamber pressure with flowrate, and thrust with chamber pressure. These plots furnish a secondary source of total flow rate or chamber pressure if the primary source of either is not reliable because of instrument malfunction, and also act as a check on the validity of such primary readings. From calculations of adiabatic flame temperature and equilibrium composition, theoretical curves of various steady combustion parameters are constructed; and from these, at the observed rocket chamber pressure and mixture ratio of each valid point, one obtains theoretical values of flame temperature, characteristic velocity, specific heat ratio for both chamber and nozzle, combustion gas mean molecular weight, nozzle inlet Mach number, and the slope of the flame temperature-mixture ratio curve. From the ratio of actual-to-theoretical  $c^*$  and the theoretical temperature, one obtains the actual chamber temperature. Application of the perfect gas law and the theoretical molecular weight then produces a value of combustion gas density which, together with the total propellant flow rate, is sufficient for computing an average gas velocity assumed to exist at the combustion chamber exit. A second computation of this velocity arises from the application of one-dimensional incompressible flow theory to the axial pressure distribution. The speed of sound in the chamber is computed from the actual  $c^*$  and a theoretical value of chamber specific heat ratio, and both gas velocity figures are non-dimensionalized by this sound speed. Comparison between each of these calculated Mach numbers and the theoretical value for isentropic flow then reveals any order of magnitude discrepancies which may exist in the primary data or the intermediate computations.

Independent of these secondary steady state calculations or of the particular theoretical model chosen to define the combustion time lag parameters, the first stage of transient calculations requires only steady and transient pressure data as inputs. From these amplitudes and phases, together

with the theoretical injector inertial phase lags, this operation produces values of the transfer function and instantaneous mixture ratio in the form of the arguments and moduli of two complex numbers. Two intermediate complex quantities in addition to those already discussed arise during this calculation. The equations governing the various steps are as follows:

(a) Rocket transfer function:

$$R_F e^{i\beta_F} = \frac{\mu_E}{\phi} = \frac{\tilde{\mu}_F e^{i\beta_F}}{\phi}$$

(179)

(b) Instantaneous mixture ratio:

$$\eta e^{i\delta} = \frac{\mu_o}{\mu_F} = \frac{\tilde{\mu}_o}{\tilde{\mu}_F} e^{i\delta}$$

where the fractional variations  $\mu_o$ ,  $\mu_F$ , and  $\phi$  are defined prior to Equations 11 and 15. If one now defines two additional fractional oscillations by:

$$\psi_F = \frac{\Delta P_F - \bar{\Delta P}_F}{\bar{\Delta P}_F}, \quad \phi_F = \frac{P_F - \bar{P}_F}{\bar{P}_F}$$

where:

$P_F$  = instantaneous fuel injector pressure

$\Delta P_F$  = instantaneous fuel injector pressure drop,

then the transfer function may be written as:

$$\frac{\mu}{\phi} = \left( \frac{\mu_E}{\psi_F} \right) \left( \frac{\psi_F}{\phi_F} \right) \left( \frac{\phi_F}{\phi} \right) \quad (180)$$

These individual ratios are shown in vector form in Figure 23 and are calculated by the following relations:

$$\frac{\mu_F}{\psi_F} = \frac{\cos \alpha_F}{2} e^{-i\alpha_F}$$

$$\frac{\psi_F}{\phi_F} = \left( \frac{\Delta p_F^1}{p_F} \right) \left( \frac{\bar{p}_F}{\bar{p}_F} \right) = \left( \frac{\tilde{\Delta} p_F}{\bar{p}_F} \right) \left( \frac{\bar{p}_F}{\Delta p_F} \right) e^{i\gamma_F}$$

$$\tilde{\Delta} p_F = \sqrt{\tilde{p}_F^2 + \tilde{p}_c^2 - 2 \tilde{p}_F \tilde{p}_c \cos \lambda_F}$$

$$\tan \gamma_F = \frac{\sin \lambda_F}{(\tilde{p}_F / \tilde{p}_c) - \cos \lambda_F} \quad (181)$$

$$\frac{\phi_F}{\phi} = \left( \frac{\tilde{p}_F}{\tilde{p}_c} \right) \left( \frac{\bar{p}_c}{\bar{p}_F} \right) e^{i\lambda_F}$$

where:

$\alpha_F$  = fuel injector inertial phase lag

$\tilde{p}_F$  = fuel injector pressure amplitude

$\tilde{p}_c$  = chamber pressure amplitude

$\lambda_F$  = phase between fuel injector and chamber pressures.

Final expressions for the parameters of Equation 179 are then written as:

$$R_F = \frac{\cos \alpha_F}{z(p_F / \bar{p}_c - 1)} \sqrt{1 + \left( \frac{\tilde{p}_F}{\tilde{p}_c} \right)^2 - z \left( \frac{\tilde{p}_F}{\tilde{p}_c} \right) \cos \lambda_F}$$

$$\beta_F = \lambda_F - \alpha_F + \tan^{-1} \left( \frac{\sin \lambda_F}{\tilde{p}_F / \tilde{p}_c - \cos \lambda_F} \right)$$

$$\lambda = R_0 / R_F$$

$$\delta = \beta_0 - \beta_F \quad (182)$$

where  $R_0$  and  $\beta_0$  represent corresponding transfer function quantities based upon the oxidizer. The outputs of the first stage of calculations then consist of these mixture ratio and transfer values:  $R_0, R_F, \beta_0, \beta_F, \gamma_0, \gamma_F, \tilde{\Delta} p_0, \tilde{\Delta} p_F, \lambda$ , AND  $\delta$ .

Following this first stage of computation, one may proceed to a determination of the time lag parameters. Reference to the final combustion chamber equation, 178, shows that these variables are four in number: mean total time lag,  $\bar{T}_T$ ; average residence time of burned gases downstream from the combustion zone,  $\bar{f}\Theta_g$ ; time lag interaction index,  $\gamma$ ; and mean sensitive portion of the time lag,  $\bar{\tau}$ . Calculation of these four quantities is accomplished in two separate stages, the initial stage yielding values of  $\bar{T}_T$  and  $\bar{f}\Theta_g$  from an approximate form of the combustion chamber equation, and the subsequent stage furnishing quantitative indications of the remaining unknowns,  $\gamma$  and  $\bar{\tau}$ . An examination of 178 shows that the first term on the right-hand side of the equation contains the product of total gas residence time and modulating frequency. At very high values of frequency, this term may easily become a dominant one in the equation; and for a reasonable magnitude of  $\Theta_g$ , the term will reach values greater than  $O(1)$  as frequency increases. However, the final term on this side of the equation will always be of  $O(1)$  by virtue of its exponential form. Therefore, at values of the modulating frequency for which the product  $(\omega\Theta_g)$  is much greater than 1.0, the final term, containing two of the unknown time lag parameters, will become negligibly small in comparison with the first term (and others) on that side of the equation, reducing the number of unknown parameters by two. This is the approximate form of equation used in the second overall calculation stage.

Separation of the real and imaginary parts of this approximate equation produces two equations in two unknowns, from which a direct solution is possible for both  $\bar{f}\Theta_g$  and  $\bar{T}_T$  at each of the experimental values of modulating frequency. The behavior of each of these parameters as a function of frequency must be asymptotic, since the approximation on which the equation is based becomes more nearly valid as the frequency increases. The asymptotic value approached by each of the variables must then be the correct

value of the unknown, which theoretically will be independent of frequency. Hence, plots of  $\bar{\theta}_g$  and  $\bar{T}_T$  over the frequency spectrum should produce reliable results for these parameters at the high frequency end of the curve. The degree to which each variable approaches a true asymptote is then an indication of the maximum frequency required in the experiments.

Having determined these asymptotic values of  $\bar{\theta}_g$  and  $\bar{T}_T$ , one may then rewrite the original combustion chamber equation in its exact form, treating these quantities as known, and solving for the remaining unknown parameters,  $\eta$  and  $\bar{T}$ . Again separating real and imaginary parts of this complex equation, the third and final stage in the calculation procedure becomes a straightforward analytical solution in which the departure of the results of the approximation from the asymptote is an indication of the magnitude of the final unknowns.

The most difficult and intricate calculation in the three stages is obviously the second one, involving solutions of the approximate equation. Two approaches to this computation are taken, with the choice of method dependent upon the reliability of the measured distributions of axial velocity (pressure). One approach assumes that the position of major heat release  $\bar{F}$  is known from axial velocity distributions as expressed in Equation 176, but that the overall gas residence time,  $\Theta_g$  (which is equivalent to the inverse of the final chamber gas velocity), is unknown. Reduction of the approximate form of Equation 178 results in a solution for  $\Theta_g$  of the form:

$$(A\omega\Theta_g + B)^2 = C + (D + F\omega\Theta_g)\cos(\omega\bar{f}\Theta_g) + (E + G\omega\Theta_g)\sin(\omega\bar{f}\Theta_g) \quad (103)$$

where:

$$\omega = 2\pi \times \text{modulating frequency}$$

$A, B, C, D, E, F, G$  = constants at each point dependent upon steady state values and first stage outputs.

Solutions to this transcendental equation exist at points of intersection between the parabola of the left-hand side and the displaced sine curve of the right. These intersections are determined through convergence of a Newton-Rabson iterative computation performed on the IBM digital calculator.

The second approach to this calculation stage reverses the roles of known and unknown quantities. In this method, the chamber exit gas velocity,  $\bar{u}_1$ , and hence the overall gas residence time, is assumed known from calculations of the gas properties within the chamber and the total propellant flow rate, as previously described. The unknown then becomes the location of major heat release,  $\bar{f}$ , i.e., the average combustion "space lag". Under these conditions, the parabolic term of 183 is absorbed in the known constants, and the equation takes the form:

$$C_1 + C_2 \cos\left(\frac{\omega \bar{f}}{\bar{u}_1}\right) + C_3 \sin\left(\frac{\omega \bar{f}}{\bar{u}_1}\right) = 0 \quad (184)$$

where:

$C_1, C_2, C_3$  = constant terms at each point

$\omega$  = non-dimensional value of modulating frequency,  
based upon chamber length and speed of sound  
at the injector face.

Equation 184 is less complicated than 183 and is amenable to analytical solution for  $\sin \frac{\omega \bar{f}}{\bar{u}_1}$ ; however, the solutions obtained will in general be complex, involving hyperbolic as well as trigonometric terms. In this case, both real and imaginary parts of the solutions for  $\bar{f}$  must be plotted as functions of frequency. The requirements for validity of results are that the imaginary portion approach zero with increasing frequency, while the real part approaches a constant asymptotic value which may be considered the correct one. If these conditions are met within the available range of modulating frequency, this method offers an extremely attractive alternative to the determination of very precise axial velocity distributions.

Inputs which are common to both procedures in the second stage of calculation originate with the outputs from the first stage and a number of the steady state quantities whose determination has already been described. The first stage outputs of importance are  $R_p$ ,  $B$ ,  $\lambda_t$ , and  $\delta$ , while the steady state parameters used are mixture ratio, modulating frequency, characteristic velocity, specific heat ratio, chamber temperature, and slope of the temperature-mixture ratio curve. Two geometric lengths are also required, those of the cylindrical chamber and the subsonic portion of the nozzle. The integrated velocity parameters,  $W_1$ , and  $W_2$  (as described in Appendix A), are computed for the conical exhaust nozzle and included as inputs.

The correction terms appearing in the combustion chamber equation are calculated from the expressions given in Equations 169, 170, and 176. These depend primarily upon the axial velocity distribution and its straight-line segment approximation as previously discussed. In the first procedure for second stage calcuation in which the space lag, or  $F$ , is known, the approximation of Equation 177 is used, since the maximum non-dimensionalized value of experimental modulating frequency is of the order 0.15. Under these conditions,  $F = 1 - X$ , which is the distance to the first sharp rise in axial velocity. The second gas residence time correction factor, designated a in Equation 176, is treated as a known function of gas velocity, regardless of which stage procedure is employed.

The time lag distribution correction factors,  $\Delta_2$  and  $\Delta_3$ , depend heavily upon the choice of droplet drag coefficient, a quantity worthy of some detailed discussion. The actual experimental measurement and determination of statistical average of a droplet drag coefficient for a multiple-orifice, impinging-jet spray is an extremely difficult and exacting task and somewhat tedious for use in determining a relatively small theoretical correction factor. However, reference to the literature on droplet and spray analyses and experiments reveals the existence of a large number of

investigations of spray characteristics from which one might expect to glean sufficient information to make an order of magnitude estimate or calculation of the drag coefficient in this particular injector-motor configuration.

In the range of the droplet diameters and Reynolds' numbers anticipated for such a system, a great deal of empirical data (34, 35) is available which substantiates the assumption of the present theoretical analysis of a drag coefficient inversely proportional to Reynolds' number. On the basis of this premise, one must determine reasonable magnitudes for the several factors contributing to this Reynolds' number, e.g., droplet diameter, droplet velocity relative to gas velocity, gas density, and gas viscosity. Fairly accurate values of gas density and viscosity may be calculated from the measured, derived, and theoretical gas properties; and the gas velocity distribution is measured as a primary input exclusive of these correction factors. The only remaining properties are, then, liquid droplet diameter and velocity.

This latter quantity is established if one considers the assumption of the theory that drag coefficient may be considered a constant throughout the droplet stay time within the chamber. The magnitude of drag effects will certainly be greatest at the instant of injection into the chamber, since it is at this point that the greatest relative velocity between liquid and burned gas exists. Also, at this relatively early time in the combustion process, evaporation and surface burning effects are at a minimum, so that the purely hydro dynamic considerations of the droplet dynamics equation are likely to be most nearly valid. Therefore, rather than attempt to estimate an average drag coefficient during the entire history of the burning droplets, it will suffice (at least in the calculation of correction factors) to evaluate this quantity at the injector face. Here the gas velocity is zero, and the average liquid velocity may be computed from the known injector orifice area and total propellant flow rate, with an average

liquid density weighted by the known mixture ratio. In this manner the problem reduces completely to the determination of a reliable value of droplet diameter.

A great deal of empirical data is available in the published literature of the diameters of droplets resulting from single streams of liquid fuels sprayed into air or another oxidizing atmosphere, but relatively few quantitative data appear on the problem of impinging-stream sprays. Blair (36), in a Project Squid survey on combustion of fuel drops, cites a thesis by Simpson (37), saying "-- the size of drops in liquid propellant rockets ranged from about 20 to about 60 microns in diameter"; and in a theoretical study Penner (38) has chosen 50 microns as a representative diameter for such droplets. One might therefore expect a reasonable choice of droplet diameter for the injector orifices of the rocket motor employed in the present program to be within this order of magnitude. An early paper by Lee (39), published in 1932, in which impinging jets of diesel fuel issued from .028-inch orifices into air, shows measured mean droplet diameters of approximately 24 microns at very high jet velocities. Much more recently Schmidt (40) observed droplets of 33 to 77 microns diameter in the spray of a single fuel stream issuing at somewhat lower velocity into an air stream moving at speeds of 20 to 100 feet per second. The surprisingly close agreement in magnitude of results of experiments conducted over such a wide range of conditions indicates that the important parameters determining droplet diameter are -- as pointed out in a number of analyses -- liquid velocity, gas viscosity, and injector orifice diameter. In an attempt to correlate the data obtained from the two sources mentioned, the product  $d_o \sqrt{\Delta P / \rho_g}$  is calculated from values given in the references; and this orifice diameter - liquid velocity parameter is plotted as the abscissa against the droplet diameter ordinate in a log-log plot shown in Figure 24, assuming gas viscosities of the same order of magnitude in both experiments.

An approximate curve is drawn between the four points considered; and from the known values of injector orifice diameter, liquid density, and injector pressure drop at each of the three operating levels of the bipropellant motor described herein, the curve was consulted to obtain values for expected droplet diameters of 28, 30, and 32 microns, the diameters increasing with chamber pressure. A summary of this data is presented in Table I, with diameters derived for use in this analysis shown in parentheses. Although these values are certainly not precise, their order of magnitude is in agreement with the aforementioned data for bipropellant rockets, and they may be considered sufficiently accurate for calculation of correction factors.

A systematic computation of the average gas viscosity for use in the Reynolds' number determination may be performed from the known theoretical composition of the combustion gas at its equilibrium flame temperature. The effects of chamber pressure on viscosity are considered negligible on the basis of a comparison of the ratios of actual-to-critical pressures and temperatures with the evidence presented by Comings and Egly (41). Quantitative values of the viscosity of constituent gases at the existing flame temperature are determined from an extrapolation of recent National Bureau of Standards data (42) by the empirical equations presented with this data. The average viscosity for the mixture is then weighted by the molar fractions of each of the component gases.

From the above information, the final calculation of droplet drag coefficient is a simple matter. The Reynolds' number is determined; and from an empirical curve similar to that of Lapple and Shepherd (35) the product of Reynolds' number and drag coefficient is obtained, assuming a spherical shape for the droplets. Reference to the defining equation for the drag coefficient in the form to be applied to the correction factor, and non-dimensionalization by the length of the chamber and the sound speed at the injector face, results in values for this coefficient,  $k$ , of from .028 to

to .030. These are slightly smaller than the Mach number at the nozzle entrance, but still of the same order of magnitude, as assumed in the theory.

A series of integrations are then performed to obtain the final corrections  $\Delta_2$  and  $\Delta_3$ . Values of  $k$  and gas velocity give, by successive numerical integrations on the digital computer, liquid velocity distribution, total combustion time lag distribution, and the two combined velocity integrals exhibited in Equations 169 and 170. Performing the computations indicated by these two equations, one then acquires the values of  $\Delta_2$  and  $\Delta_3$ .

Having all the necessary inputs, one may then perform the second stage calculations by either procedure, select asymptotic values for  $\bar{f}\Theta_3$  and  $\bar{\zeta}_{T\text{ AVG}}$ , enter the exact combustion chamber equation with these quantities, and carry out the third stage computations to complete the determination of all four time lag parameters.

#### Experimental Accuracies and Errors

Before attempting to discuss the validity of results or the general applicability of experimental methods, it is expedient to consider the magnitudes of possible errors in the data which arise from inaccuracies in the measurements. To accomplish this, one must consider the inherent accuracies in each of the measured inputs as determined by calibrations of the sensing, transducing, and recording instrumentation. Each of the primary measurements is treated individually, with possible errors accumulated in the various steps leading to its final value noted in succession.

Steady state chamber pressure obtained from Heise gauge photographs is considered accurate to  $\pm 2$  psi. The gauge precision, based on the smallest unit of pressure detectable, is  $\pm 1$  psi, which is within the scatter of results of repeatability and hysteresis calibrations by dead-weight tester. However, uncertainties in observation of the photographs increases this to the larger

figure. Injector pressure Heise gauges are precise to  $\pm$  2 psi, with calibration accuracy again within these limits; but similar photographic uncertainties increase this possible error to  $\pm$  4 psi.

Determinations of these steady state pressures by Li-Liu strain gauge pickups are subject to errors primarily because of thermal zero drift of the pickup outputs. Although cold calibrations of the pickups through the cathode followers and Speedomax recorders show repeatability errors of only  $\pm$  2 psi, the uncertain location of zero points during a run may be as great as  $\pm$  .05 recorder divisions, which represents  $\pm$  5 psi. Therefore a cumulative error of  $\pm$  7 psi is conceivable. For this reason, photographed values of the three steady state pressures are used wherever possible.

The accuracy of steady state thrust readings is controlled by the calibration tests, since both photographed and recorded values may be read reliably with a precision of  $\pm$  1 pound. Proof-ring deflection under load is factory calibrated with a maximum error of  $\pm$  1/4 pound; however, load-cell and gauge hysteresis and strain gauge bridge current variations increase the possible error in thrust to  $\pm$  2 pounds.

Factory calibrations of the Potter steady state flowmeters are accurate to  $\pm$  .002 pounds per second, which is of the same order of magnitude as the precision with which the integrator circuit output may be read and is greater than observable departure of this output from linearity with frequency. Measurement of fuel specific gravity by hydrometer methods is considered accurate to  $\pm$  .0005 in an average value of 0.790; but corrections to the liquid oxygen flow rate for density and thermal contraction may be in error by as much as 1% of the measured value, which, at high pressure operation, results in an absolute error of  $\pm$  .010 pounds per second. Thus although fuel flow is measured reliably to  $\pm$  .001 pounds per second, the oxygen flow and total propellant flow must be considered possibly in error by as much as  $\pm$  .010 pounds

per second, resulting in a steady state mixture ratio accuracy of  $\pm .01$ .

The flow modulating frequency is measured by a Potter sensing coil and integrator circuit similar to that employed in flow rate measurements. Hence the integrator linearity and recorder precision and hysteresis determine the possible error, which varies with the range chosen for this adjustable recorder. At frequencies of 100 cps or less, the error is  $\pm .01$  cps; from 100 to 200 cps, it is  $\pm .02$  cps; above 200 cps, it is  $\pm .025$  cps.

The accuracy of transient pressure amplitudes is established by a number of factors. Dead-weight calibrations of the Li-Liu pickups, the signal-to-noise ratio of the transmitting circuit, amplitude distortion of the recording system, linearity of the amplifiers, accuracy of the vacuum-tube voltmeter for establishing calibration amplitude, linearity of the diode circuit output, and precision of the Speedomax potentiometer are all contributing components. Errors in the amplifying and recording systems are best expressed as a percentage accuracy figure of  $\pm 1\%$ , which represents a maximum error of  $\pm 0.3$  psi. Calibrations of the diode-Speedomax combination indicate linearity and repeatability of approximately 1/2%, while voltmeter comparisons with an a.c. voltage standard at periodic intervals show an error of  $\pm 1\%$ . Dead-weight test pickup calibrations exhibit an observation and hysteresis total error of  $\pm .05$  mv, which represents a pressure of  $\pm 0.5$  psi at average pickup sensitivities. The cumulative error from all these sources totals approximately  $\pm 1.5$  psi. The signal-to-noise ratio is retained at a value less than 0.1 millivolt; hence variations of this magnitude are definitely discernable and represent realistic values.

Because of the parallel-input calibration method employed, the accuracy of phase measurements is determined solely by the phase discriminating and recording device previously described. Calibration of this instrument by comparison with a TIC secondary phase standard shows a systematic error varying

110.

from zero at zero phase difference to 1.6 degrees at 45 degrees phase difference and returning to zero at 90 degrees. Comparison of the secondary standard with a Lissajous pattern calibration having an estimated observation error of  $\pm 1/2$  degree showed the same systematic error. By biasing the phase recorder 90 degrees and subtracting the output of the secondary standard, this 1.6 - degree error is reversed in sign, indicating that the error originates in the standard. For this reason it is felt that the phase meter-recorder system is more accurate than the available standard, and the error in transient pressure phase measurements is less than the value of  $\pm 0.5$  degrees obtained from Lissajous pattern calibrations.

The accuracy of time correlation for the various chart readings of steady state and transient playback data is determined by the errors in clock photograph observations and precision of distance measurements on the charts. These cumulative factors produce an overall reading time accuracy of  $\pm 0.1$  second.

PRESENTATION AND DISCUSSION OF RESULTSExperimental Results

Direct experimental measurements and calculated results are tabulated and plotted in graphical form for all acceptable data points in groups according to the stage of calculation in which they are derived in Tables I through VII and Figures 25 through 62. Data obtained over the full frequency spectrum are further arranged for each operating level of chamber pressure; and the test runs in these groups are presented in the chronological order in which they were performed, with each point identified by a run number and the time from start of the run at which the particular readings were observed. Figures pertinent to the discussion which are not a part of direct experimental measurements or calculations have been grouped in proper order following the presentation of results.

The most important measured and derived steady state values are listed for the complete survey of acceptable points in Tables II - A, B, and C, each table representing one chamber pressure level. Correlations between three of these variables; thrust, chamber pressure, and total propellant flow rate, are shown in Figures 25, 26, and 27. The slopes of these three curves represent, respectively, thrust coefficient, specific impulse, and characteristic velocity. The values of these slopes along with averages of steady state direct measurements and calculated or theoretical gas and liquid properties which contribute to the constant terms in the various stages of transient calculations are given in Table III. The scatter of these data around their average values not only gives an indication of repeatability of test runs but also acts as an initial standard of acceptability for each point. Thus, if the steady state conditions at one operating chamber pressure level are not predictable and repeatable over

a range of modulating frequencies at this level, then the time lag results at these varying frequencies are not considered comparable. The criterion for steady state data acceptability, chosen on the basis of overall instrument accuracy, is a deviation of no more than  $\pm 3\%$  from the average curve at each operating point. In addition to this acceptability function, the three correlation curves shown also provide a secondary source of thrust, chamber pressure, or total flow rate data in the event that one of these measurements is lost through instrument malfunction while all other direct readings appear satisfactory. Since these performance parameters are all functions of steady state mixture ratio, their use as acceptability criteria implies a certain restriction in mixture ratio. The design value of this quantity is 1.35, oxygen-to-fuel, by weight, and the nominal limits imposed by the aforementioned  $\pm 3\%$  allowable variation are from 1.31 to 1.39. This range has been arbitrarily extended in a few cases to include points from early rocket runs in which propellant specific gravity corrections could not be made because of the lack of temperature data. Point values of this steady state mixture ratio as well as the results of succeeding calculations of flame temperature and final chamber gas velocity are included in Tables II - A, B, and C.

Results of the first stage of transient calculation are shown in the three tables, IV - A, B, and C, and in graphical form in Figures 28 through 36. These are the values of the computed transfer function parameters and the instantaneous mixture ratio of fractional flow oscillations previously defined as the complex quantity  $\frac{1}{M} e^{i\phi}$ . By the terms of the theoretical analysis, the desired condition of constant instantaneous mixture ratio throughout all tests at one chamber pressure level are satisfied exactly only when this ratio of fractional oscillations has a value of 1.0 with a phase difference of  $0^\circ$  between the propellants. The degree to which

this exact condition is approximated forms the second acceptability criterion for data points. Since the maximum value of each propellant flow perturbation is limited by the linearized treatment of the theory to approximately 10% of its respective total flow rate, a deviation of  $\pm 0.1$  from exact equality of the two fractional oscillation amplitudes will represent a fluctuation in the overall instantaneous mixture ratio of only 1%, which is the order of magnitude of terms neglected in the theory. Similarly, a phase difference of  $\pm 10^\circ$  between these perturbations will introduce a sine component of order 0.1, which again represents approximately 1% of the total flow rate values. These two conditions, e.g.,  $\mu = 1.0 \pm 0.1$ ,  $\delta = 0^\circ \pm 10^\circ$ , then form the standards for judging the acceptability of transient data. Plots of the actual variation in these two mixture ratio perturbation parameters are shown in Figures 34, 35, and 36.

One notes from the tabulations that these limits have been relaxed for a small number of test points, particularly at high chamber pressure, with  $\mu$  values ranging from 0.8 to 1.3 and  $\delta$  as great as  $15^\circ$  included in the results. These runs have been accepted because equipment failures from fatigue after many cycles of flow pulsing or from excessive heat transfer rates at high chamber pressures precluded the possibility of obtaining additional data at more satisfactory conditions or because the resonance effects of feed system components prevented operation at the particular value of frequency which would produce the desired transient ratios.

It should be emphasized that this condition of equal, in-phase fractional flow oscillations is the most difficult experimental requirement to be fulfilled. Since the compressibilities of the two propellants are different and since each one varies with modulating frequency and line pressure in a manner different from the other, a particular pair of the fixed-stroke pistons installed in the flow-modulating unit will produce equal fractional

oscillations at only one value of frequency for each chamber pressure. The diameters of the discrete number of pistons available were therefore chosen on the basis of previous experience to achieve the desired constancy of mixture ratio somewhere within ranges of frequency of approximately 25 - cps width. The experimental procedure for producing acceptable transient data then consists of the selection of the proper pair of pistons for the desired frequency range and adjustments of frequency and split-flywheel settings in successive runs until the required conditions are met. This adjustment process is further complicated by the interaction between phase and amplitude of the two oscillations through the resultant chamber pressure fluctuation, which causes an interdependence of flywheel and frequency adjustments. Also, since one is able to monitor only pressure perturbations, he must perform a rough calculation similar to the first stage procedure after each rocket run to determine the approximate mixture ratio parameters from observed values of steady state and transient chamber and injector pressures as well as their relative phases. Differences between oxidizer and fuel injector pressure drops and variations with frequency of transient amplitudes and phases prohibit the establishment of overall pressure ratio limits prior to actual running; hence, this calculation must be performed following each run in order that acceptability may be established for that test. Because of these complexities and this inability to predict accurate settings, each acceptable rocket run is the result of approximately twelve attempts.

Calculated values of the transfer function parameters are presented in Figures 28 through 33 in the form of a modulus  $R$  and a phase angle  $\beta$  based on total injection flow oscillations. Although the combustion chamber equations have been derived in terms of a transfer function based on fuel oscillations only and multiplied by a correlating mixture ratio factor, the frequency variations of such fuel-based quantities are subject to the

random scatter of instantaneous mixture ratio and hence do not give a valid indication of actual behavior of the combustion chamber. The use of overall transfer function parameters based on total propellant fluctuations presents the data in the form of primary interest, namely the response of the chamber to small perturbations in injection flow rate (within specified mixture ratio limits) over a range of frequencies of oscillation. Such response curves may then be compared with those obtained at different average mixture ratios or with similar results from a monopropellant system.

One notes that the modulus and phase presented are actually the inverse of the transfer function as defined above, since they are the ratio of propellant flow perturbations to the resulting chamber pressure oscillations. The definitions of the two parameters and their derivations from previously-described quantities are as follows:

$$Re^{i\beta} = \frac{\mu_i}{\phi} = \frac{\tilde{\mu}_i}{\tilde{\phi}} e^{i\beta}$$

where:

$\tilde{\mu}_i$  = amplitude of injection flow oscillation

$\tilde{\phi}$  = amplitude of chamber pressure oscillation

$\beta$  = phase angle lag of chamber pressure

However, from earlier definitions and from the derivation of Equation 17,

$$\mu_i = (\frac{1}{2} + H)\mu_o + (\frac{1}{2} - H)\mu_f = \mu_F \left[ \left( \frac{1}{2} + H \right) (ke^{i\delta}) + \left( \frac{1}{2} - H \right) \right]$$

Hence:

$$Re^{i\beta} = \frac{\mu_i}{\phi} = \frac{\mu_F}{\phi} \left[ \left( \frac{1}{2} + H \right) (ke^{i\delta} - 1) + 1 \right]$$

116.

or  $R e^{i\beta} = R_F e^{i\beta_F} [(\frac{1}{2} + H)(k e^{i\delta} - 1) + 1]$

from which the overall parameters may be computed once those based on fuel oscillations alone are known.

Although the range of modulating frequencies obtainable with existing laboratory equipment does not extend below 60 cps, the curves of transfer function parameters have been extrapolated to zero frequency or steady state conditions. The behavior of both parameters at this point is easily determined by substituting  $\omega = 0$  in the combustion chamber equation for the combined theoretical model (178), which shows that the modulus  $R$  must approach a value 1.0, while the phase angle  $\beta$  approaches zero degrees.

Critical examination of the transfer function data at each chamber pressure shows noticeable scatter in two ranges: very low frequency (60 to 75 cps) and middle frequency (120 to 180 cps). The low frequency scatter arises from two major causes, e.g., poor signal-to-noise ratio in the electrical signals and a magnified effect of transients within the rocket motor. The electrical difficulties stem from the fact that the flow rate (and hence pressure) oscillations are directly proportional to frequency in a constant-displacement modulating system such as the one employed herein. Thus, even with the largest pistons consistent with the design features of the modulating unit, strain gauge pressure pickup outputs in the low frequency range are of the order of  $\frac{1}{2}$ -millivolt, r.m.s. Since the minimum noise level obtainable in the electrical transducing and transmitting networks is approximately 1/10 millivolt, the signal-to-noise ratio in this frequency range is no greater than 5, while at the highest modulating frequency it may be as large as 30. Also, because the majority of electrical "noise" disturbances are produced by 60 cps operational equipment in the

laboratory vicinity, distortion of the pickup signals is serious in this range and cannot be eliminated by filtering. The secondary source of low-frequency difficulties arises from the fact that small changes in flow modulating conditions resulting from piston heating and cooling or from seal leakage, which require a finite number of operating cycles to become stabilized, will extend over a longer period of time during low frequency operation than would be consumed at the higher frequencies. For this reason, the transient amplitude and phase playback records consistently show much longer stabilizing transients and more serious variations during running at low frequency conditions.

The scatter of these data and their departure from a smooth curve in the middle-frequency range is evidence of another serious complexity in the experimental program. A series of pre-run, cold flow tests with varying modulating frequency revealed the existence of certain "resonance" areas where interaction is thought to occur between the pulsations in pressure and the presence of cavitating venturis in the flow lines. Comparison tests using both single and multiple-hole venturis isolated the probable source of this resonance and stressed the importance of obtaining the minimum possible bubble size. However, even with the 7-hole venturi employed, two major areas are found where the existence of pulsations reduces the average, or steady state, flowrate by as much as 8%. These areas vary with line pressures and are different for the two propellants; but in general their effects are most predominant in two ranges, one from 100 to 150 cps, and the other from 160 to 200 cps. These two adjacent ranges overlap in the two feed lines at the 600 - psi chamber pressure level and hence necessitate a revision of the feed system configuration for obtaining reliable data in this area of frequency. Such a change has not been made in the present investigation, since data in this range are not essential for

construction of asymptotes in the calculation procedures anticipated at the time of testing.

Although the steady state flow rate deficiencies can be overcome by a simple increase in feed line pressures during middle-frequency operation, the resonance condition introduces serious effects in transient data which are not readily eliminated. These effects appear in either one or both injector pressure oscillations in the form of severe distortion of the wave shapes from their desired sinusoidal contours. The distortions are caused by the presence of large-amplitude harmonics of the fundamental flow-modulating frequency, as is evident from Figure 63, in which the fuel injector pressure fluctuation has been played back from the tape recorder through a sonic analyzer, and the oscilloscope face of the analyzer photographed during three separate sweeps of the cathode ray beam. In this figure both amplitude and frequency of the signal are shown on logarithmic scales, and the fundamental oscillation produced by the flow-modulating unit occurs with full-scale amplitude at a frequency of approximately 140 cps. The troublesome harmonic in this case appears at a frequency in the vicinity of 600 cps with an amplitude which is an appreciable fraction of the fundamental. This full-spectrum photograph also shows the presence of very high-frequency turbulence "noise" as well as the stray electrical noise in the range of 60 cps previously discussed. However, both these latter disturbances are relatively small random phenomena, while the large harmonic is repeated quite closely for the three separate sweeps photographed. A closer examination of the relations between fundamental and harmonic signals is possible from the "center frequency" photograph of the same fuel injector pressure trace shown in Figure 64. In this case, a central frequency of 350 cps has been used to locate the trace on the screen, and a linear frequency scale of  $\pm$  250 cps is employed on both sides of the center point. The fundamental frequency is

found to be 136 cps, and the harmonic is seen to be exactly a 4th multiple at 544 cps. The linear scale also employed herein for amplitude indicates that the harmonic is approximately one-fourth the size of the primary oscillation and again is shown by the presence of three distinct sweeps to be highly repeatable. The extreme distortion caused by this fourth harmonic is illustrated in Figure 65a by the oscillograph record of all three pressure perturbations during a portion of this run. In this case, the oxidizer injector pressure is undisturbed, and the fuel resonance condition is also reflected in a slight distortion of the chamber pressure trace. A number of examples also exist in which harmonic oscillations are present in the oxidizer trace singly, and a few in which both injector pressures are distorted. In all cases, however, the resonance effects appeared in the same ranges of frequency in which the aforementioned steady state flow rate decreases were observed, namely between 100 and 150 cps and between 160 and 200 cps.

The technique of selective electrical filtering is applied to all test data to eliminate the effects of high frequency combustion and turbulence noise (as previously mentioned in the discussion of data reduction methods), and it might be expected that such "low-pass" filtering might be employed to overcome the harmonic distortion so evident in this middle-frequency range. However, the validity of this filtering application is dependent upon two conditions: the perturbations must be small in comparison with the fundamental oscillation so as to be considered definitely second order quantities, and the frequency of occurrence of these random disturbances must be sufficiently high so that a large number of such oscillations will exist and hence effectively cancel each other over the space of one cycle of flow modulation. In the case of the harmonics described, neither of these conditions is satisfied. The amplitude is too large to be neglected in a linearized analysis, and the fourth harmonic frequency is too close

to the fundamental to be considered cancellatory over any appreciable portion of a modulating cycle. Thus, as shown in Figure 65b, although the filter action successfully removes the wave distortion caused by the presence of harmonics, in so doing it shifts the phase relationship between midpoints or peaks of the distorted and pure waves and alters the root mean square amplitude to such an extent that the resulting data are meaningless.

The alternative of analyzing the actual wave form by Fourier methods and including harmonic contributions to the fluctuating pressure is inconsistent with the fundamental premise of linearized oscillations of negligible second order or higher frequency terms, on which the entire analysis of the combustion chamber is based. It becomes evident, therefore, that test data in which such large harmonics exist are invalid, and one is obliged to attempt to obtain acceptable points in the narrow "borderline" range between 150 and 160 cps if a complete frequency spectrum is to be accomplished.

Several test runs within this range were performed at each chamber pressure level, and the resulting traces from one such run are shown in the "raw" and filtered oscillograph records of Figure 66. The appearance of the unfiltered pressure oscillations of Figure 66a indicates that only second order harmonic effects are present; and on the basis of these observations, all such runs in this frequency range which meet the aforementioned acceptability criteria have been considered reliable and employed for further calculations. The evident scatter of the transfer function data of even these carefully selected border points, however, emphasizes the severe effects of resonance interactions and leads one to a more careful examination of the filtering action. Comparison of the phase relationships between unfiltered and filtered traces in the border frequency test seen in Figure 66 with those of a typical valid high frequency run as presented by the oscillograph records

in Figure 67 show that the presence of even small harmonic components is sufficient to invalidate data points within this frequency band, since the filtering process increases the apparent value of  $\lambda_f$  by about 5 degrees. Such comparisons further stress the unreliability of visual observation of wave forms as a criterion for acceptability and demonstrate the necessity for more objective methods of selection, such as the use of a sonic analyzer, on all transient data.

It is evident, then, that valid results for transfer function parameters probably exist only at low and high frequencies and that the curve shapes, as presented, must be determined from data in these two ranges only. The choice of points in the low frequency range must be weighted by the known behavior of these curves at zero frequency, since their scatter is notably large. However, the large signal-to-noise ratio and freedom from harmonics of high frequency points produce a much higher degree of repeatability and hence a more reliable average value in this portion of the spectrum.

Pertinent data for calculation of drug coefficients and velocity correction factors required as inputs to the second and third computational stages are summarized in Table V, while the straight-line segmented curves of velocity distribution, determined from five-point axial pressure surveys with final velocity corrections, are shown graphically in Figures 37, 38, and 39. Results of numerical integrations of the droplet dynamics equation with pre-determined drag coefficient values are presented as liquid velocity distributions superimposed upon these figures. Subsequent integration of the inverse of liquid velocity yields a value of theoretical total time lag at each location representing the time spent by a droplet in reaching that point. These calculated total time lag distributions are plotted for all three

chamber pressure levels in Figure 40.

Values of the time lag parameters,  $\Theta_g$ ,  $\bar{f}$ ,  $\bar{\tau}_T$ , n, and  $\bar{\tau}'$ , calculated by the second and third procedural stages for both computation methods previously described are listed in Tables VI - A, B, and C, and are plotted as functions of frequency in Figures 41 through 58. The figures are grouped according to the parameter calculated, with curves for three chamber pressures resulting from one procedure followed by similar curves for the alternate procedure. The gas residence time parameter differs in the two procedures, since the overall residence time,  $\Theta_g$  is the unknown determined from the first procedure; and  $\bar{f}$ , the fractional length following the average space lag, is considered as the unknown in the second. Imaginary portions of the complex solutions for  $\bar{f}$  and  $\bar{\tau}_T$  obtained by the second procedure are observed to approach zero magnitude as the modulating frequency is increased, as may be verified by plotting the data of Table VI. However, since these imaginary quantities do not contribute to the selection of asymptotic values as inputs to the succeeding calculation stage, plots of their variation with frequency do not appear among the figures.

The overall gas residence time results ( $\Theta_g$ ), calculated from the approximate equation of procedure #1, appear as plots over the frequency spectrum in Figures 41, 42, and 43. Scatter in these values essentially reflects similar scatter in the transfer function modulus  $R$ , to which the calculation is primarily sensitive. Nevertheless, the more reliable data at high frequency approach nearly constant values of  $\Theta_g$ , and this parameter clearly reaches an asymptotic value within the available range of modulating frequency. Asymptotic values are noted on the curves as 0.958, 0.945, and 1.063 milliseconds, respectively, at the three mean chamber pressures of 301, 423, and 590 psia. Although these times are certainly of the order of magnitude to be expected on the basis of physical reasoning, they are consistently

smaller than the values of 1.6 to 2.0 milliseconds derived from calculated chamber gas velocities and employed in procedure #2, a discrepancy which casts some doubt upon the validity of the method of selecting these asymptotes.

Figures 44 through 46 present the variation with frequency of the real component of the space lag parameter  $\bar{f}$ , representing the fraction of chamber length downstream from the so-called combustion "front" as calculated by procedure #2. One notes that the scatter in these results is much less pronounced, even in the middle frequency range, than in the corresponding residence time values of procedure #1. Careful examination of the equations of this second procedure show that solutions for the real portion of the quantity  $\bar{f}$  are relatively insensitive to scatter in the transfer function modulus  $R$ , since variations in this real part merely change the angle of a complex vector whose length is primarily determined by the value of  $R$  and the chosen value of  $\theta_g$  in the dominant term  $\frac{\omega \theta_g}{Y}$ . Solutions for the imaginary portion of  $\bar{f}$ , however, must satisfy the length requirements of such a vector and hence are highly sensitive to scatter in  $R$  results. At high frequency, this scatter is much less pronounced, and the imaginary portion of  $\bar{f}$  becomes definitely smaller and more regular, enabling one to deal with only the real portion in choosing a reliable asymptote. The distributions presented for this parameter clearly indicate such an asymptotic behavior within the obtainable modulating frequency range, and values for the chosen asymptotes are noted on the curves as 0.715, 0.750, and 0.980, increasing with chamber pressure. These values agree closely with the estimates of 0.735, 0.835, and 1.000, selected from velocity distribution measurements and employed in procedure #1.

Values of the average total combustion time lag,  $\bar{T}_c$ , calculated from the approximate equation by both procedures are tabulated in Table VI -

A, B, and C. These solutions occur as phase angles in the product form  $\omega \bar{\zeta}$ , and are thus primarily sensitive to the magnitude of the transfer function phase angle  $\beta$ . Since the distributions of this parameter exhibit only slight scatter, the total time lag variations with modulating frequency form relatively smooth curves. However, these curves do not become sufficiently flat at higher modulating frequencies to enable one to choose asymptotic values with any degree of reliability. Although these straightforward frequency spectra have been used with some success in previous calculations to obtain values of total time lag which appeared well within expected physical and chemical orders of magnitude, their inadequacy in the present calculations is evident in Figures 47 through 52, in which the total time lag is plotted against the reciprocal of modulating frequency. In these graphs, the asymptotic values required for the third stage of calculations are represented by the intercept of the curve with the ordinate where  $1/f$  is zero, that is, where the frequency becomes infinitely large. It is obvious from these plots that the range of modulating frequency possible under the mechanical limitations of existing equipment is not sufficiently high to justify extrapolation of the calculated time lag values over the large space from the present minimum reciprocal frequency to zero, in spite of the fact that the curves are relatively flat in the range in which valid points have been determined.

These conditions lead one to a critical examination of existing results and underlying equations for some additional evidence of the behavior of the curves in their high frequency range. Initially, it is observed that because of the sine-cosine form of real and imaginary equations containing the angle  $\omega \bar{\zeta}$ , an indeterminacy of  $\pm 2n\pi$  ( $n = 0, 1, 2, \dots$ ) exists in the solution for this quantity. However, observation of the values of the transfer function phase angle  $\beta$  and a careful study of the behavior of the approximate combustion chamber equation at low and high frequencies in the form of

a vector diagram (this method of solution to be discussed later in more detail) indicates that the angle  $\omega \bar{Z}_T$  must begin with zero magnitude at zero frequency and cannot exceed  $\beta$ , which is less than  $\frac{\pi}{2}$  radians throughout the modulating range encountered herein. Hence solutions for  $\omega \bar{Z}_T$  are treated as positive and negative first quadrant angles only, with negative solutions arising from the approximate form of equation employed as well as from scatter in the first stage calculations for  $R$  and  $\beta$ . Values of  $\bar{Z}_T$  thus range from very small positive to equally small negative numbers, and the use of logarithmic plotting techniques to extrapolate to high frequency becomes meaningless. Further examination of the approximate equation shows that the slope of the curve of  $\beta$  with frequency approaches an asymptotic value which is numerically related directly to the desired value of  $\bar{Z}_T$ ; however, the existing scatter is too great and frequency range again too small to justify extrapolation for the measurement of such a slope.

These considerations indicate that in spite of its limited range of validity, the reciprocal frequency plot remains the most promising method for presentation of total time lag data for extrapolation to an asymptotic value. Rewriting the approximate equation in terms of this reciprocal value and investigating its behavior at very high frequency, one finds that the slope of the  $\bar{Z}_T$  versus  $1/f$  curve should approach a negative value of 0.25 as the frequency becomes infinitely large. Therefore, the extrapolated curve must be drawn in such a manner as to have this small positive slope at its intercept on the ordinate. Constructing such a smooth curve for each of the distributions presented, one obtains intercept values of the average total time lag as presented on the curves, e.g., 0.25, 0.17, and 0.11 milliseconds at mean chamber pressures of 301, 423, and 590 psia, respectively. Because of the similarity in distributions obtained from the two calculation procedures and the uncertainty of such large extrapolations, it

is impossible to distinguish between the two values at any one chamber pressure, and these choices represent the best possible average for both procedures. The unreliability of the asymptotic method is further emphasized by the difference in order of magnitude between these values and those reported in some previous investigations where the best choice of asymptotes from straightforward frequency plots are approximately 1/2 to 1 millisecond, which are of the order to be expected from purely physical and chemical reasoning.

Final time lag parameters, namely the pressure sensitive portion of the total time lag and the interaction index relating this sensitive portion to the pressure, are computed in the third stage of calculation from the complete combustion chamber equation, using asymptotic values of total time lag and the gas residence time or space lag parameter. Because of the uncertainty in the choice of asymptotes discussed above and the similarity of results from the two procedures in the second calculation stage, it will suffice here to present and discuss the third stage results from either procedure. More realistic values of gas residence time and relatively smooth variations in the space lag parameter dictate the choice of procedure #2; and the computed values of interaction index  $n$  and sensitive time lag  $\bar{\tau}$  for this procedure are presented over the modulating frequency spectrum at each chamber pressure in Figures 53 through 58.

These final calculations are extremely sensitive to scatter in the transfer function parameters  $R$  and  $\beta$ , and for this reason, the unreliable points throughout the middle frequency range have been omitted. Additional evidence of the importance of such scatter is given by the existence of negative solutions for one or both parameters, particularly in the low frequency range where both  $R$  and  $\beta$  exhibit considerable variations as previously discussed. Since negative time lags or sensitive time lags much greater than the total are both physically impossible, solutions in these

categories cannot be considered as valid results in themselves but only to the extent that they contribute to an average value. As has been pointed out, the transfer function data at higher frequency show the minimum of scatter; hence average values of interaction index and sensitive time lag are probably best determined in this frequency range. Such arithmetic averages have been computed and indicated on the curves and are tabulated, along with the asymptotic values employed in their solution from the results of the second stage calculations, in Table VII.

Additional doubts as to the validity of these results arise from the variation of both parameters with modulating frequency. Because the wave-travel time throughout the chamber is much shorter than the period of one cycle of flow modulation, conditions in the combustion chamber may be considered as quasi-steady with regard to chemical and thermal equilibrium, and variations of modulating frequency within the relatively small range possible may be expected to have no significant effect upon the values of these time lag parameters. The fact that such variations do, in fact, exist, is primarily due to the sensitivity of these calculations to the choice of asymptotes in the preceding calculation stage. This sensitivity has been investigated more closely for a particular data point by selecting a number of values for the  $\bar{C}_T$  asymptote and computing the magnitude of both  $\gamma$  and  $\bar{C}$  for each value. The extreme variation in interaction index for even modest changes in asymptotes is illustrated in Figure 68 for a high frequency point (241 cps) at 300 psia whose calculated values of  $R$  and  $\beta$  both appeared reliable.

Two additional attempts have been made to account for the frequency variation and scatter in these results on the basis of existing transfer function data. In the first of these attempts, the best possible smooth curve is constructed through the  $R$  and  $\beta$  points, and curve values at regular frequency intervals are observed and employed with asymptotic total

time lags to obtain  $\eta$  and  $\bar{\zeta}$  results. These calculations are simplified by neglecting mixture ratio variations which are seen from Figures 34, 35, and 36 to be small and essentially random in nature. The frequency spectrum resulting from the 600 psia calculation is shown in Figure 69, where it is seen that elimination of the scatter in  $R$  and  $\beta$  has led to consistently positive solutions for both  $\eta$  and  $\bar{\zeta}$ . However, with the chosen asymptote, both parameters vary over an order of magnitude range or greater within the span of available modulating frequencies.

The second attempt mentioned is based upon an inverse calculation in which average values of all four time lag parameters are treated as constants over the frequency range encountered, and the complete combustion chamber equation is employed to determine the distributions of  $R$  and  $\beta$  which would be required to produce such constant values. Figures 70 and 71 show the results of these calculations for all three chamber pressures. Note that in all cases the required values of both transfer function parameters are appreciably smaller than the values actually obtained and also that the required curves exhibit much less change throughout the frequency range than appears in the actual curves of Figures 28 through 33.

The pressure dependence of each of the parameters is indicated in the curves of Figures 59 through 62. Values of gas residence time calculated from the best available thermo-chemical data and measured pressures and mass flows which are employed in procedure #2 show a slight decrease with increasing chamber pressure, while those values obtained from the best possible choice of asymptotes in procedure #1 are essentially constant within experimental scatter. The space lag parameter  $f$  exhibits the expected increase with chamber pressure, indicating that combustion is concentrated closer to the injector face as chamber pressure rises. Correspondingly, the average total time lag of burning particles decreases as the combustion processes are

accelerated by higher chamber pressure. Behavior of the final two parameters, interaction index and sensitive time lag, is too uncertain in the present calculations to justify any authoritative statements concerning their changes with chamber pressure, and in both cases the best straight line average has been drawn. Both total and sensitive time lags are presented on log-log plots, the slopes of which represent gross values of interaction index over large variations in chamber pressure. These gross values are not expected to agree closely with the average calculated at any one chamber pressure because of the quasi-steady temperature conditions under which the instantaneous value of  $\eta$  is calculated for each pressure. Thus, the interaction index, defined herein as instantaneous rate of change of an energizing rate function with pressure, contains a contribution from the rate of change of the function with temperature multiplied by the ratio of small temperature changes to small pressure changes. In the case of oscillations in pressure around an average value, this ratio will be that of the adiabatic relations between temperature and pressure. However, between two different steady state values of chamber pressure, it will be merely the average slope of the equilibrium flame temperature curve drawn over the range of pressures encountered. Note that if the energizing rate function is not sensitive to temperature, that is, if the time lag "preparation" processes do not change their rates appreciably with temperature, then the contribution of this term to the interaction index will be negligibly small, and the gross and instantaneous values of  $\eta$  should agree very closely. This discussion of variations in the interaction index is presented in detail by Crocco and Cheng in Reference I.

From the above observations of (a) questionable distributions of transfer function data because of uncertainties in the middle frequency range, (b) existence of physically impossible solutions for two of the time

lag parameters, (c) large variations of these parameters with frequency, (d) discrepancies between required and actual transfer function distributions, and (e) the requirement of excessive extrapolations in a range in which mechanical limitations prevent obtaining data, one can only conclude that with the present theoretical framework and existing experimental equipment and techniques, the two-stage calculation procedure based on asymptotic behavior of an approximate form of the combustion chamber equation is not an adequate or satisfactory method for obtaining valid time lag parameter results. Since the entire procedure hinges upon the use of reliable distribution of transfer function data, one might naturally suggest that an obvious alternative to the asymptotic method is the use of a form of least-squares statistical fit of the unknown time lag parameters to existing transfer function calculations. However, such an analysis must logically begin with an attempt to normalize these data into the form of regular distributions by correlation of the rather scattered points with small variations in mixture ratio, chamber pressure, propellant temperature, etc., before the shape of such curves can be treated with the degree of certainty required for a meaningful statistical fit. The complexities of this involved treatment are too great to be justifiable in the present investigations; hence a number of simpler alternatives to the asymptotic method of solution are attempted.

#### Alternate Calculation Procedures

The methods selected herein as alternatives to the two-stage asymptotic solutions described previously all involve attempts to solve the complete combustion chamber equation directly with simplifications and iterative corrections derived from order of magnitude analyses. Basically the calculations are a much simplified form of the "best statistical fit" method in which modulating frequency is treated as an independent variable.

Then, following the general assumption of procedure #1 of the former analyses the position of major heat release, i.e., the average combustion space lag, is considered a known quantity from steady state gas velocity measurements, with the remaining four time lag parameters treated as unknowns. Separating real and imaginary parts of the single complex equation, one obtains two real equations in four unknowns, with the fifth variable, modulating frequency, to be chosen at one's discretion on the basis of reliability of transfer function data in the various frequency ranges. Assuming the time lag parameters to be constant over the available modulating frequency spectrum, one may then write the two real equations at each of two discrete frequencies, producing a system of four equations in four unknowns which can, in principle, be solved directly without recourse to asymptotic or approximate methods. However, these equations are not straightforward algebraic or trigonometric relations but are rather involved combinations of the two forms which are not amenable to direct analytical solutions. Therefore, an order of magnitude investigation of the various terms is performed for the purpose of simplifying the solutions.

The relative size of each of the terms in the combustion chamber equation and their phase relationships are illustrated by the vector diagram of Figure 72. Here the four unknown time lag parameters are assigned typical values which might be expected on the basis of physical reasoning in order to furnish an idea of the importance of the terms containing them. The velocity distribution correction term ( $\omega^3 \Delta g/6$ ) has been neglected, since its contribution is never greater than 1% of the value of R, even at maximum modulating frequency. Also the corrections for mixture ratio variations do not appear in the diagram, since they are comparatively small in all cases and essentially random in distribution over the frequency spectrum. The importance of modulating frequency in any order of magnitude observations is obvious

from the diagram, since frequency-dependent terms which are negligibly small at low frequency in comparison to constant terms may become sizeable and definitely not negligible at high frequency. For this reason, the vectors are constructed and identified at two typical frequencies, a low value of approximately 59.7 cps and a high value of four times that amount, or about 239 cps.

A great deal of information concerning the requirements for solutions and their sensitivity to distributions of  $R$  and  $\beta$  may be obtained from such a diagram. First, one notes that if physically real, i.e., positive, solutions for the total time lag and gas residence time are to exist, the value of  $R$  must always be greater than 1.0 and that of  $\beta$  must be greater than zero. Also, since the imaginary vector  $-\frac{\omega}{F}(\theta_g + E_2)$  and the angle  $\omega \bar{Z}_T$  both increase regularly and are directly proportional to frequency, the two transfer function parameters must also increase regularly and monotonically for the existence of solutions to even the approximate equation. One notes further that the angle  $(\beta - \omega \bar{Z}_T)$  increases monotonically with frequency in the diagram. Hence, the requirement of constant values of  $\theta_g$  and  $\bar{Z}_T$  implies that the angle  $\beta$  must always increase faster than  $\omega \bar{Z}_T$ ; that is, that the slope of a curve of  $\beta$  vs.  $\omega$  must always be greater than  $\bar{Z}_T$  within a finite range of modulating frequency. Following such reasoning further, it is apparent that if all four time lag parameters,  $\theta_g$ ,  $\bar{Z}_T$ ,  $n$ , and  $\bar{Z}$ , are to remain constant, then only one distribution of the transfer function quantities  $R$  and  $\beta$  is possible.

In the actual case, of course, one must deal with the inverse problem of treating experimental distributions of  $R$  and  $\beta$  to determine satisfactory values for the time lag parameters, and there is no certainty that constant values, or perhaps even real values, of these parameters will result. Thus, although a solution for a sort of average value of each of the

parameters can be obtained from the aforementioned treatment of two separate frequency points, the question of the constancy of these values over the frequency range can be answered in this method only by dealing with a number of such pairs of points at various intervals along the frequency spectrum. In the present investigation, valid data do not exist over this entire spectrum, and one is limited to obtaining only this sort of average values in two areas of frequency. However, the variation of these results with frequency is a very significant matter, since, in effect, it determines the validity and applicability of the theoretical representation of a total time lag made up from the sum of a sensitive and an insensitive portion as well as the linearized interaction function whose rate of change with pressure forms the index  $\gamma$ . Thus, it is essential in any future investigation that precise transfer function data be obtained over the full range of possible modulating frequencies.

Some additional useful information may be derived from the vector diagram. The indeterminacy of the quadrant of  $\omega \bar{Z}$  mentioned in the discussion of the asymptotic calculation method is resolved by referring to the diagram and noting that the angle  $\beta - \omega \bar{Z}$  always lies in the first quadrant for finite values of  $R$ . Then, since experimental values of  $\beta$  vary between 0 and  $\pi/2$  radians in the frequency range considered, the unknown angle  $\omega \bar{Z}$  must also lie within the first quadrant. A comparison of the sizes of the vectors  $n(1 - e^{-i\omega \bar{Z}})$  and  $\frac{i\omega}{\gamma} (\Theta_2 + \bar{\epsilon}_2)$  clearly shows that the basis of the approximate equation used previously is a valid one, since the length of the former is never greater than the magnitude of  $n$ , while the latter may increase without limit as  $\omega$  increases. It is also apparent that what has been termed the third stage calculation for the parameters  $\gamma$  and  $\bar{Z}$  will be extremely sensitive to scatter in the values of  $R$  and  $\beta$ , once  $\Theta_2$  and  $\bar{Z}$  asymptotes have been chosen, for relatively small changes in  $R$  and  $\beta$ .

will require corresponding changes in  $\eta$  and  $\bar{\Sigma}$  which represent much larger fractional values of these two parameters. Also, since the rotation of the vector  $\eta(1-e^{-i\omega t})$  is determined solely by the magnitude of  $\bar{\Sigma}$ , a change in the angle  $(\beta - \omega \bar{\Sigma}_T)$  will be reflected primarily in the value of  $\bar{\Sigma}$  required for a solution. Hence, the magnitude of  $\bar{\Sigma}$  and the distributions of both  $\eta$  and  $\bar{\Sigma}$  with frequency for given  $R$  and  $\beta$  curves depend heavily upon the choice of the asymptotic  $\bar{\Sigma}_T$ .

The influence of small mixture ratio fluctuations is not shown in the diagram, but their importance is obvious if one notes that the length of the R vector and its rotational angle  $\beta$  are directly affected through multiplication of the quantity  $Re^{i\beta}$  by a quantity equal to 1.0 plus the complex mixture ratio term

$$K \left[ \frac{ke^{i\delta} - 1}{(\frac{1}{2} + H)(ke^{i\delta} - 1) + 1} \right] \left[ 2 - \frac{(1-i\omega E_1)}{\sqrt{1+a^2\omega_c^2}} e^{-i\omega f \theta} \right]$$

which is proportional to fractional variations in mixture and to the slope of the mixture ratio-temperature curve. Because the effects of mixture ratio on the time lag parameters are unknown and unaccountable in the theoretical model, it is important that the contribution of this expression be kept small in comparison to 1.0 by controlling instantaneous mixture ratio within very narrow limits. The actual value of this correction term in existing data ranges from about  $\pm 0.02$  to  $\pm 0.12$  and is random in both size and direction over the frequency spectrum. Thus the influence of mixture ratio on solutions of the present combustion chamber equation is definitely of secondary importance. However, as yet no evaluation has been made to determine whether these small changes in mixture can appreciably alter the form of the time lag and gas residence terms contributing to the chamber response and, hence, the measured values of transfer function parameters. For this purpose a large

number of test data have been selected with mixture ratio variations both within and slightly exceeding the prescribed limits, and plots have been constructed of variations in  $R$  and  $\beta$  with steady state as well as fractional mixture ratio. The behavior of these plots appears to be completely random, and one may conclude that within the small range of mixtures considered acceptable for calculation purposes, there is no evident first order correlation between transfer function and mixture ratio scattering.

Having observed the behavior of the combustion chamber equation over the range of modulating frequency and having determined the relative importance of the various terms therein, one may now proceed to direct calculation of the aforementioned average values of all four time lag parameters by simultaneous solutions of the equation at two discrete frequencies. For this purpose the complete equation is re-written in a simplified functional form as:

$$Re^{i(\beta-\omega\bar{\epsilon}_T)}[P(\omega)+iQ(\omega)]/[1+C(\omega,\theta_g,\kappa,\delta,\bar{F})] = \frac{i\omega}{\gamma}(\theta_g+E_2) + \left(\frac{3\gamma-1}{2\gamma}\right) - \left(\frac{\gamma-1}{2\gamma}\right)F(\omega,\theta_g) - n(1-e^{-i\omega\bar{\epsilon}}) \quad (185)$$

where:

$$P(\omega) = 1 - \frac{\omega^2}{\gamma} \Delta_2 \quad = \text{velocity distribution correction}$$

$$Q(\omega) = \frac{\omega^3}{6} \Delta_3 \quad = \text{velocity distribution correction}$$

$$C(\omega,\theta_g,\kappa,\delta,\bar{F}) = \kappa \left[ \frac{\kappa e^{i\delta} - 1}{(\kappa + H)(\kappa e^{i\delta} - 1) + 1} \right] \left[ 2 - \frac{(1-i\omega E_1)}{\sqrt{1+\alpha^2\omega_g^2}} e^{-i\omega f\theta_g} \right] \quad = \text{mixture ratio correction}$$

$$F(\omega,\theta_g) = \frac{(1-i\omega E_1)}{\sqrt{1+\alpha^2\omega_g^2}} e^{-i\omega f\theta_g} \quad = \text{secondary gas residence contribution.}$$

If one now writes Equation 185 at each of two separate frequencies,  $\omega_1$  and  $\omega_2$ , transposes terms, and forms the ratio of the two equations,

then, assuming all time lag parameters independent of frequency, the interaction index is eliminated, and one obtains the following single complex equation in three unknowns:

$$\frac{R_1 e^{i(\beta_1 - \omega_1 \bar{\tau}_T)} (P_1 + iQ_1)(1+C_1) - \frac{i\omega_1}{\gamma} (\Theta_g + E_2) - \left(\frac{3\gamma-1}{2\gamma}\right) + \left(\frac{\gamma-1}{2\gamma}\right) F_1}{R_2 e^{i(\beta_2 - \omega_2 \bar{\tau}_T)} (P_2 + iQ_2)(1+C_2) - \frac{i\omega_2}{\gamma} (\Theta_g + E_2) - \left(\frac{3\gamma-1}{2\gamma}\right) + \left(\frac{\gamma-1}{2\gamma}\right) F_2} = \frac{1 - e^{-i\omega_1 \bar{\tau}}}{1 - e^{-i\omega_2 \bar{\tau}}} \quad (186)$$

From previous reasoning the order of magnitude of the sensitive time lag is expected to be approximately 0.2 milliseconds; hence, the angle  $\omega \bar{\tau}$  is at most of the order 0.3. As a first approximation, then, the exponential term  $e^{-i\omega \bar{\tau}}$  may be expressed as:

$$e^{-i\omega \bar{\tau}} = 1 - i\omega \bar{\tau} - \frac{(\omega \bar{\tau})^2}{2} + \dots$$

$$= 1 - i\omega \bar{\tau} - O(M^2)$$

and the right hand side of Equation 186 becomes:

$$\frac{1 - e^{-i\omega_1 \bar{\tau}}}{1 - e^{-i\omega_2 \bar{\tau}}} = \frac{\omega_1}{\omega_2} + O(M^2)$$

Defining a frequency ratio  $k = \omega_1/\omega_2$  and combining terms, one obtains, as a first approximate form of equation, the following:

$$k R_1 e^{i(\beta_1 - \omega_1 \bar{\tau}_T)} (P_1 + iQ_1)(1+C_1) - R_2 e^{i(\beta_2 - \omega_2 \bar{\tau}_T)} (P_2 + iQ_2)(1+C_2) =$$

$$= (k-1) \left( \frac{3\gamma-1}{2\gamma} \right) - \left( \frac{\gamma-1}{2\gamma} \right) (kF_1 - F_2) \quad (187)$$

which is considerably simplified over 186 by the disappearance of the term  $\frac{\omega}{\gamma} (\Theta_g + E_2)$  as a result of the approximation of the right-hand side exponential ratio. Nevertheless, the unknown  $\Theta_g$  still exists in the left-

hand side of the equation as a part of the expression  $C(\omega, \theta_g, k, \bar{\delta}, \bar{r})$ , defined following 185. An order of magnitude analysis in the discussion preceding this derivation has shown that a normal value of this function is about 0.05, which is of the order of terms neglected in the approximation of the exponentials. Thus, to the same order of accuracy, one may assume:

$$C_1 = C_2 = 0 + O(M^2)$$

It has also been pointed out previously that the term  $Q(\omega)$ , the cubic velocity correction term is always less than 0.01 and may therefore reasonably be neglected in this simplified analysis. Introducing these approximations into 187, one obtains a much simplified form of the original equation as follows:

$$kP_1R_1 e^{i(\beta_1 - \omega_1 \bar{\epsilon}_1)} - P_2 R_2 e^{i(\beta_2 - \omega_2 \bar{\epsilon}_2)} = (k-1) \left[ \frac{\beta_1}{2Y} \right] - \left( \frac{k-1}{2Y} \right) [kF(\omega, \theta_g) - f_2(\omega_2, \theta_g)] \quad (188)$$

in which the unknown  $\bar{\epsilon}_1$  occurs only on the left-hand side, and the second unknown,  $\theta_g$ , only on the right. In principle, this complex equation, which can be separated into real and imaginary parts to form two equations in two unknowns, can be solved directly for both unknowns. Actually, however, the existence of multiple angles  $\omega, \bar{\epsilon}_1, \omega_2 \bar{\epsilon}_2$ , and  $\omega, f\theta_g, \omega_2 f\theta_g$  prevents elimination of either one of the unknowns from the two equations, and graphical or numerical methods of solution are required. Even for the judicious selection of  $k = 2$  or  $4$ , in which the double-angle trigonometric relationships may be used, elimination of either unknown requires two successive squaring operations, resulting in a fourth-order trigonometric equation which again can be solved only by numerical or graphical methods. The choice of frequency ratio  $k$  is therefore arbitrary and is based solely upon the reliability of transfer function values at the points in question.

Such graphical solutions of Equation 188 have been attempted

for all three chamber pressures, and typical results are shown in Figures 73 and 74. For ease of calculation of the rather complex functions  $F(\omega, \beta)$ , the multiplying constant of the term containing these functions is normalized to a value of 1.0 by multiplying all terms by the quantity  $(2\pi f_1)$ . The left and right sides of the resulting equation are then treated as individual complex vectors, and their real and imaginary parts are computed from the available  $R$  and  $\beta$  data at the chosen frequency points for a series of trial values of  $\bar{\tau}_g$  and  $\theta_g$ . The end points of the vectors representing the two sides of the equation then form two curves which proceed in the directions indicated for increasing  $\bar{\tau}_g$  and  $\theta_g$ . Only positive values of these two parameters have been chosen for plotting purposes, since negative time lags or gas residence times are not physically possible. Two such graphical presentations are constructed at each chamber pressure with a single value of  $R_2$ ,  $\beta_2$ , and  $\omega_2$  and two different choices of  $R_1$ ,  $\beta_1$ ,  $\omega_1$ , and, hence,  $K$ . In all cases actual calculated values of the transfer function parameters were employed rather than average quantities from a smooth curve distribution. The existence of solutions to Equation 186 is shown on the graphical construction as intersections between the two curves, and in five of the six cases attempted, no intersection existed, as is seen for one such plot in Figure 73. The single case providing a solution is one of the two chosen from 600 psia chamber pressure data and is shown in Figure 74. The intersection is seen to occur for a value of  $\theta_g$  of 1.05 milliseconds and for a  $\bar{\tau}_g$  value of approximately 0.1 milliseconds, which is very nearly the value chosen from the asymptotic extrapolation of the second stage results in the original calculation method.

One is hardly justified in drawing any general conclusions concerning the existence of real solutions for time lag parameters on the basis of such a very rough approximation to the full combustion chamber equation.

Therefore, a second iteration in the graphical process is performed by inclusion of the mixture ratio and gas residence time function  $C(\omega, \theta_g, k, \delta, F)$  in the left side of the equation. Since the correct value of  $\theta_g$  is not known until solutions are actually obtained, it suffices to choose trial values of this parameter and calculate the correction to the left side for each of these. The values chosen cover the range of realistic magnitudes from zero to two milliseconds, and the revised curves including these correction terms are illustrated in Figure 75 for the aforementioned single case in which a solution to the uncorrected equation exists. In this figure the curves have been expanded in the neighborhood of possible solutions, but comparison of the values of  $\theta_g$  at the points of intersection with those corresponding to the corrected curves of the left side of the equation shows that agreement between these two values cannot be reached within the positive portions of the curves; hence, no solution to this corrected form of the equation is possible in the only case which provided an uncorrected intersection. Similar calculations performed on each of the other cases at values of  $\theta_g$  equal to zero and two milliseconds show that the inclusion of these corrections in all cases shifts the curves of the left side even farther from an intersection. Thus, no solutions at all exist to this second-approximation form of the equation.

The next logical step is a third iteration based on a correction to the exponential ratio on the right side of Equation 186. Consideration of second order terms in the series expansion of this expression produces:

$$\frac{1 - e^{-i\omega_1 \bar{\tau}}}{1 - e^{-i\omega_2 \bar{\tau}}} = \frac{\omega_1}{\omega_2} \left( \frac{1 - \omega_1 \bar{\tau}/2 + \dots}{1 - \omega_2 \bar{\tau}/2 + \dots} \right) = \frac{1}{K} (x + iy)$$

where:

$$x = \frac{1 + K/4(\omega, \bar{\tau})^2}{1 + (K/4)^2(\omega, \bar{\tau})^2}$$

$$y = \frac{(K-1)}{1 + (K/4)^2(\omega, \bar{\tau})^2} \omega, \bar{\tau}$$

and the third approximation to the exact equation has the form:

$$\begin{aligned} KR_1 R_2 e^{i(\beta_1 - \omega_1 \bar{\tau}_1)(1+C_1)} - (x+iy) R_2 R_2 e^{i(\beta_2 - \omega_2 \bar{\tau}_2)(1+C_2)} = \\ = (k-x-iy)\left(\frac{g-1}{28}\right) + i\frac{k\omega}{8}(1-x-iy)(g+E_2) - \left(\frac{g-1}{28}\right)[kF - (x+iy)E_2] \end{aligned} \quad (189)$$

One notes that departure of the exponential fraction from its original representation as a simple frequency ratio introduces an additional complication to the graphical solution in the form of a linear term in  $\theta_g$  on the right side of the equation. The effect of this term on the behavior of the curves is clearly shown in Figures 76 and 77, where the left side is again presented for trial  $\theta_g$  values of zero and two milliseconds, respectively. The size of the complex correction ( $x+iy$ ) is, of course, directly dependent upon the trial values chosen for the sensitive time lag  $\bar{\tau}$  in computing this correction. The three sets of curves presented for each  $\theta_g$  value are calculated for choices of  $\bar{\tau}$  of 0.1, 0.5, and 1.0 milliseconds. One observes that an increase in the value of  $\bar{\tau}$ , and hence in the importance of the correction term, increases the distance between the curves representing the two sides of the equation, thereby shifting them even further from a possible solution.

The results of one further investigation into the possibilities of graphical solutions are presented in Figures 78 and 79. As has been pointed out previously, calculations of all four time lag parameters are extremely sensitive to the values of the transfer function parameters  $R$  and  $\beta$ , and the figures illustrate graphically the very important effects of changes in these quantities. In Figure 78, the magnitude of  $R_1$  is varied from 1.0 to 1.25 around its experimental value of 1.086, with the value of  $\beta$ , fixed at its experimental value of 38.1 degrees. Although no inter-

sections exist in this case for the uncorrected curves presented, the obvious importance of  $R_1$  is shown by the large shift in the position of the curves for relatively small changes in this quantity. Similarly, the phase angle  $\beta$ , is varied from 35 to 45 degrees at fixed value of  $R_1 = 1.086$  in Figure 79. Again the existence of an intersection is heavily dependent upon the size of this transfer function parameter, and it is seen that a solution appears possible in the uncorrected case for a value of  $\beta$ , in the neighborhood of 35 degrees. Although this is not the measured value of  $\beta$ , the possibility of obtaining a real solution is deemed interesting enough to warrant the application of correction terms to this particular case. These corrected curves for  $\theta_g = 0$  and 2.0 milliseconds and for  $\bar{Z} = 0$  and 0.1 milliseconds are shown finally in Figure 80, where it is observed that an intersection appears possible for  $R_1 = 1.086$  and  $\beta = 35^\circ$ , with resulting approximate values at the intersection of  $\theta_g \approx 1.5$  milliseconds,  $\bar{Z}_T \approx 0.1$  milliseconds, and  $\bar{Z} \approx 0.05$  milliseconds. The fact that a realistic solution can be reached with only small changes in the angle  $\beta$ , suggests that the choice of a very low frequency point as one of the two for this calculation scheme may be an unfortunate one because of the extreme sensitivity of the computations to transfer function quantities in this frequency range.

### Conclusions

The foregoing discussion of experimental results and initial investigations into the possibilities of alternate calculation schemes leads one to certain obvious conclusions concerning the validity of results presented, the applicability of various calculation procedures, and the requirements for any more detailed future research.

Mechanical balance and lubrication problems of reciprocating or eccentric rotating machinery severely limit the possible range of modulating

frequency, and one cannot expect to extend this frequency much beyond its present scope with any reasonable modifications of existing equipment or with any practical alternate design of equipment at the existing scale. Then, since the two-stage asymptotic calculation procedure outlined herein demands an order of magnitude increase in modulating frequency before it can be legitimately applied and its results be extrapolated with any degree of confidence, it is apparent that one must abandon this method of analysis in favor of one which can better express the relationships of the theoretical model within the present frequency range. With the insight into the behavior of the equation gained from the above preliminary attempt at alternative solutions, one may conclude that the most promising method appears to be a detailed statistical analysis of the transfer function data with an eye toward correlation of the scatter in these data with variations in rocket motor operating conditions heretofore neglected, and the application of a least squares form of data reduction process to these correlated quantities to obtain the best possible values of four time lag parameters from two simultaneous equations. This least squares analysis might well take the form of a modification of the iterative "two-point" calculation procedure as presented above but applied to a series of pairs of points along the complete modulating frequency spectrum of the transfer function curves.

No matter what choice of calculation method is made, the evidence presented herein makes obvious the need for reliable transfer function data over the full scope of possible frequencies, not merely over short intervals at a few discrete points on the curve. Thus, in the two-point method discussed, the sensitivity of calculations to small changes in low frequency points suggests that similar computations should be performed with middle frequency quantities if the results are to be treated with any degree of confidence. Furthermore, the values obtained by any statistical means must be

treated as averages and should therefore be computed over the full range of the independent variable, in this case modulating frequency. Also, as has been pointed out, the only valid check of the theoretical model's representation of time lag parameters as linearized functions of the form described in deriving the combustion chamber equation is an observation of the constancy -- or departure therefrom -- of these parameters over the full frequency range.

This requirement of full frequency data suggests a number of experimental modifications and supporting analyses. Chief among these is the need for a detailed investigation of the interaction phenomenon between pulsating flow within the feed system and the two-phase vapor-liquid condition produced by the presence of cavitating venturis in the propellant lines. The aim of such an analysis is to either completely eliminate this interaction or to alter the design of the system in such a way as to shift the resonant frequency range of the modulating unit - venturi combination outside the limits available from existing equipment. A straightforward one-dimensional analysis of these quasi-steady flow oscillations, accompanied by relatively simple experimental observations with a liquid of known vapor pressure, density, and elastic properties, might be expected to yield sufficient insight into physical conditions within the present feed system to accomplish the desired aim through design changes of minimum complexity. In addition to the resonance problems, which are of primary concern only in the middle frequency area, one must also attempt to improve the accuracy and repeatability of data points in the low frequency range. The first step in this regard should logically consist of increased efforts to obtain appreciably higher signal-to-noise ratios for pressure pickup responses to flow modulations, and such increases are most likely to be the result of improved electrical shielding and isolation from "noise" disturbances throughout the entire

transducing, transmitting, amplifying, and recording system. One must also examine the response time characteristics of all data reduction instruments in this lower frequency range to ascertain whether corresponding times of readings on amplitude and phase playback records are actually comparable with regard to the instant at which the original phenomena occurred. Thus, if the response times of the two playback systems were widely different and if either one was of appreciable length, as may be the case with the servo-operated phase recorder, the return to electrical equilibrium following a small change in rocket operating conditions might appear at a much different time on the phase playback record than on the amplitude, even though both original signals were faithfully recorded on the magnetic tape. Since the production of a step function or other known change in phase of a pre-determined size and at a fixed, pre-selected frequency is not a straightforward matter with the relatively poor quality of existing phase measuring standards, this response determination is considerably more involved than might appear at first glance. An interesting alternative suggested by Crocco consists of obtaining average phase and amplitudes over a short time span by continuously replaying a single short loop of the magnetic tape occurring at any desired point during a run. Such continuous playback would obviate the need for any response determination.

Although these changes in amplitude and phase relationships during playback are of greatest importance at low frequencies, they nevertheless appear in varying degrees at all frequencies and may therefore reflect actual changes in pulsing flow conditions and their ensuing chamber responses during starting transients and at early reading times within runs. It is therefore very important to determine that flow and combustion equilibrium conditions have been reached at a time before data observations are made, or the calculations of transfer function parameters cannot be expected to be

repeatable over a number of runs at any fixed frequency. Establishment of this equilibrium condition at the earliest possible moment in the present limited-duration rocket runs is thus essential. The good repeatability of steady state data presented herein for a large number of runs indicates clearly that these values of chamber pressure, flow rates, and thrust are reached sufficiently early to guarantee the existence of equilibrium in average conditions at all reading times. Hence, one need concern himself only with the problem of achieving similar constancy of fluctuations in the two propellant flow rates at the prescribed values necessary to produce constant instantaneous mixture ratio, with the expectation that these conditions will result in more nearly constant amplitude and phase measurements. In the existing flow modulating unit, the creation of small flow leakage, particularly in the very low temperature liquid oxygen feed system, because of frictional wear of the sliding seals on the piston, causes a gradual change in capacitance of the system which often fails to reach an equilibrium condition within the run duration. This capacitance change cannot be controlled or compensated for during running and results in data of questionable value because of the inevitable variation in amplitude and phase and, consequently, mixture ratio. For this reason the major modifications in equipment presently planned for additional experimental tests center around the design of a flow modulating unit with improved piston seals and with servo-controlled piston stroke and phase relationships. It is expected that such a design will be capable of varying the amplitude of oscillations in one propellant line and the phase angle between the two propellants in a continuous fashion during rocket runs so as to produce very nearly constant values of these parameters, resulting in an order of magnitude smaller perturbations of instantaneous mixture ratio.

Notwithstanding the obvious shortcomings of the two-stage, asymptotic calculations procedure and the inability of present equipment to produce

reliable results over the full frequency range, the general experimental method for determining combustion chamber response and its associated transfer function parameters is seen to be a relatively simple and definitely practical one. The order of magnitude of present results for these parameters and the general shape of the curves describing their variation with frequency are shown to be valid merely by the existence of solutions for the time lag parameters from the approximate equation applied over the entire frequency range. Although sensitivity of the final calculations to low frequency data scattering and unfortunate resonance problems in the middle frequency interval prevent one from obtaining adequate verification of the validity of the theoretical model's representation of time lag parameters, it is seen that the experimental techniques for producing near-sinusoidal flow oscillations, the transducing, recording, and playback instrumentation for measuring these oscillations, and the methods for reducing these primary measurements to the form of useful transfer function parameters are all valid procedures capable of supplying data of sufficient accuracy in the present scale of operation to warrant at least preliminary time lag parameter computations. Also, it is apparent that with only minor modifications in analytical methods and laboratory equipment, satisfactory results may be obtained for the final time lag quantities to justify their use in a critical examination of the simplified representations of the theoretical model.

The calculation of transfer function parameters as an intermediate step in the overall determination of the more involved time lag phenomena offers an additional advantage in its range of applicability, for no matter how accurately the proposed theoretical model describes the actual complex combustion process, these transfer function data still represent reliable and useful experimental information to any rocket design engineer. Whether his problem be one of combustion chamber instability, feed system oscillations,

propellant line pressure fluctuations, mechanical structural vibrations, chamber and system recovery times after sharp changes in flow, analysis of servo controls in feed lines, or merely determination of starting and shutdown transients, the engineer must determine the response characteristics of the chamber-injector configuration; and the techniques described herein offer a practical, straightforward method for obtaining linearized transfer function data for just such applications.

REFERENCES

1. "Theory of Combustion Instability in Liquid Propellant Rocket Motors" by L. Crocco and Sin-I Cheng, AGARDograph No. 8, NATO, Butterworths, Ltd., London, 1956.
2. "Aspects of Combustion Stability in Liquid Propellant Rocket Motors; Part I" by L. Crocco, J. Amer. Rocket Soc., vol. 21, no. 6, November 1951.
3. "Combustion Instability in an Acid-Heptane Rocket with a Pressurized-Gas Propellant Pumping System" by A. O. Tischler and D. R. Bellman, NACA Tech. Note No. 2936, 1953.
4. "A Theory of Unstable Combustion in Liquid Propellant Rocket Systems" by M. Summerfield, J. Amer. Rocket Soc., vol. 21, no. 5, September 1951.
5. "Combustion Studies in Rocket Motors" by K. Berman and S. H. Cheney, Jr., ibid., vol. 23, no. 2, March, 1953.
6. "Appendix A: Introductory Remarks" by L. Crocco, Princeton University Aeronautical Engineering Report No. 216-n, "Combustion Instability in Liquid Propellant Rocket Motors", December, 1955.
7. "Appendix C: Combustion Instability in the Intermediate Frequency Range" by S. M. Scala, ibid.
8. "Combustion Instability in Liquid Propellant Rocket Motors - A Survey" by C. C. Ross and P. P. Datner, "AGARD: Selected Combustion Problems", NATO, Butterworths, Ltd., London, 1954.
9. "Rocket Motor Instability Studies" by K. Berman and S. H. Cheney, Jr., Jet Propulsion, vol. 25, no. 10, October, 1955.
10. "Photographic Techniques Applied to Combustion Studies - Two Dimensional Transparant Thrust Chamber" by J. H. Altseimer, J. Amer. Rocket Soc., vol. 22, no. 2, March, 1952.

11. "Experimental Investigation of Combustion Instability in Rocket Motors" by H. Ellis, I. Odgers, A. J. Stosick, N. Van de Verg, and R. S. Wick, Fourth Symposium on Combustion, Williams and Wilkins, Baltimore, 1953.
12. "Low-Frequency Combustion Instability in Bipropellant Rocket Motors - Experimental Study" by M. Barrere and A. Moutet, Jet Propulsion, vol. 26, no. 1, January, 1956.
13. "Experimental Aspects of Rocket System Stability" by Y. C. Lee, A. M. Pickles, and C. C. Miesse, *ibid.*
14. "Preliminary Measurements of the Combustion Time Lag in a Monopropellant Rocket Motor" by L. Crocco, J. Grey, and G. B. Matthews, Fifth Symposium on Combustion, Reinhold, New York, 1955.
15. "Measurements of the Combustion Time Lag in a Liquid Bipropellant Rocket Motor" by L. Crocco, J. Grey, and G. B. Matthews, Jet Propulsion, vol. 26, no. 1, January, 1956.
16. "Servo-Stabilization of Combustion in Rocket Motors" by H. S. Tsien, J. Amer. Rocket Society, vol. 22, no. 5, September, 1952.
17. "Servo-Stabilization of Low-Frequency Oscillations in a Liquid Bipropellant Rocket Motor" by F. E. Marble and D. W. Cox, Jr., *ibid.*, vol. 23, no. 2, March, 1953.
18. "Stabilization of Low-Frequency Oscillations of Liquid Propellant Rockets with Fuel Line Stabilizer" by Y. T. Li, Jet Propulsion, vol. 26, no. 1, January, 1956.
19. "Stability of Flow in a Rocket Motor" by D. F. Gundar and D. R. Friant, J. Applied Mech., vol. 17, p. 327, 1950.
20. Discussion of the paper of Gundar and Friant by M. Yachter, J. Applied Mech., vol. 18, p. 114, 1951.
21. "Aspects of Combustion Stability in Liquid Propellant Rocket Motors. Part II" by L. Crocco, J. Amer. Rocket Soc., vol. 22, no. 1, January, 1952.

22. "High Frequency Combustion Instability in Rocket Motors with Concentrated Combustion" by L. Crocco and Sin-I Cheng, *ibid* vol. 23, no. 5, September, 1953.
23. "High Frequency Combustion Instability in Rockets with Distributed Combustion" by L. Crocco and Sin-I Cheng, *Fourth Symposium on Combustion*, Williams and Wilkins, Baltimore, 1953.
24. "Low-Frequency Combustion Stability of Liquid Rocket Motor with Different Nozzles" by Sin-I Cheng, *Jet Propulsion*, vol. 25, no. 4, April, 1955.
25. "The Transfer Functions of Rocket Nozzles" by H. S. Tsien, *J. Amer. Rocket Soc.*, vol. 22, no. 3, May, 1952.
26. "Supercritical Gaseous Discharge with High-Frequency Oscillations" by L. Crocco, *L'Aerotechnica*, Roma, vol. 33, p. 46, 1953.
27. "Appendix B: Audio-Frequency Pressure Measurements in Rocket Testing" by H. B. Jones, Princeton University Aeronautical Engineering Report no. 216-k, "Combustion Instability in Liquid Propellant Rocket Motors", March, 1955.
28. "Appendix A: Investigation of Techniques for Measuring Local Heat Transfer Rates in an Uncooled Rocket Motor Wall" by P. V. Marrone, M.S.E. Thesis, Princeton University Aeronautical Engineering Department, published September, 1956.
29. Probable Title: "Instantaneous Flow Measurement in Liquids" by W. S. Davis, unpublished M.S.E. Thesis, Aeronautical Engineering Department, Princeton University, 1956 (Report in preparation).
30. "Appendix A: An Investigation into the Possibilities of Adapting the Hot-Wire Anemometer to Liquid Phase Measurement" by D. T. Harrje, Princeton University Aeronautical Engineering Report no. 216-d, *ibid.*, June, 1953.

31. "Some Aspects of the Measurement of Oscillatory Hydraulic Flow Including Non-Linear Effects" Robert S. Wick, Jet Propulsion, vol. 26, no. 12, December, 1956.
32. "Appendix C: Development of the Li-Liu Pressure Pickup" by G. B. Matthews, Princeton University Aeronautical Engineering Report no. 216-f, ibid., December, 1953.
33. "Dynamic Pressure Measuring System for Jet Propulsion Research" by Y. T. Li, J. American Rocket Society, vol. 23, no. 3, May, 1953.
34. "The Velocity of Free-Falling Droplets" by P. van der Leeden, L. D. Nio, and P. C. Suratman, Applied Scientific Research, Section A, vol. 5, no. 5, 1952.
35. "Calculation of Particle Trajectories" by C. E. Lapple and C. B. Shepherd, Ind. and Eng'g. Chem., vol. 32, no. 4, May, 1940.
36. "A Literature Survey on Some Physical Aspects of the Combustion of Falling Fuel Drops" by Phillip M. Blair, Project SQUID Tech. Note no. PUR-27-R, November, 1955.
37. "The Combustion of Droplets of Heavy Liquid Fuels" by D. S. Simpson, Sc. D. Thesis, Dept. of Chem. Eng'g., M. I. T., 1954.
38. "On Maximum Evaporation Rates of Liquid Droplets in Rocket Motors" by S. S. Penner, J. Amer. Rocket Soc., vol. 23, no. 2, March, 1953.
39. "The Effect of Nozzle Design and Operating Conditions on the Atomization and Distribution of Fuel Sprays" by Dana W. Lee, NACA Report No. 425, 1932.
40. "A Preliminary Investigation of the Atomization of Liquids Injected Into an Air Stream" by J. M. Schmidt, JPL Progress Report No. 4-101, May, 1949.
41. "Viscosities of Gases and Vapors at High Pressures" by E. W. Comings and R. S. Egly, Ind. and Eng'g. Chem., vol. 32, no. 4, May, 1940.
42. "Tables of Thermal Properties of Gases", National Bureau of Standards Circular #564, November, 1955.

LIST OF TABLES AND FIGURESTABLES

- I. Reference data for droplet diameter determination
- II. A. Steady state data for 300-psi operating level  
B. Steady state data for 450-psi operating level  
C. Steady state data for 600-psi operating level
- III. Summary of average steady state parameters
- IV. A. Transfer function and mixture ratio results for 300-psi level  
B. Transfer function and mixture ratio results for 450-psi level  
C. Transfer function and mixture ratio results for 600-psi level
- V. Summary of average data for velocity correction factors
- VI. A. Time lag parameter calculations for 300-psi level  
B. Time lag parameter calculations for 450-psi level  
C. Time lag parameter calculations for 600-psi level
- VII. Summary of time lag data at three operating pressures

FIGURES

1. Time lag schematization
2. Comparison of theoretical models
3. Typical velocity distributions for refined theoretical model
4. Typical variation of velocity perturbation
5. Comparison of combustion chamber equations
6. Velocity distribution approximation for correction calculations
7. Monopropellant rocket motor and test stand
8. Installation of monopropellant pressure instrumentation
9. Bipropellant rocket motor (liquid oxygen - alcohol)
10. View of bipropellant rocket test stand

11. Bipropellant flow modulating unit.
12. Schematic: bipropellant feed system
13. Detail of multiple cavitating venturis
14. View of operating control console and gauge panel
15. Exterior view of Li-Liu differential pressure pickup
16. Sectional diagram of Li-Liu pickup
17. Time lag instrumentation schematic diagram
18. Steady state recording instrumentation
19. Transient recording instrumentation
20. Cycling hysteresis check of Li-Liu differential pressure pickup No. 12
21. Transient playback instrumentation diagram
22. Schematic diagram of calculation procedure
23. Relationships of oscillating quantities (based on fuel)
24. Correlation of droplet diameter data
25. Steady state performance: thrust vs. chamber pressure
26. Steady state performance: thrust vs. total propellant flow
27. Steady state performance: chamber pressure vs. total propellant flow
28. Average chamber transfer function modulus ( $\bar{P}_c = 301$  psia)
29. Average chamber transfer function modulus ( $\bar{P}_c = 423$  psia)
30. Average chamber transfer function modulus ( $\bar{P}_c = 590$  psia)
31. Average chamber transfer function phase angle ( $\bar{P}_c = 301$  psia)
32. Average chamber transfer function phase angle ( $\bar{P}_c = 423$  psia)
33. Average chamber transfer function phase angle ( $\bar{P}_c = 590$  psia)
34. Fractional perturbation of mixture ratio ( $\bar{P}_c = 301$  psia)
35. Fractional perturbation of mixture ratio ( $\bar{P}_c = 423$  psia)
36. Fractional perturbation of mixture ratio ( $\bar{P}_c = 590$  psia)
37. Calculated velocity distributions (Nominal  $\bar{P}_c = 301$  psia)
38. Calculated velocity distributions (Nominal  $\bar{P}_c = 423$  psia)

154.

39. Calculated velocity distributions (Nominal  $\bar{P}_c = 590$  psia)

40. Calculated total time lag distributions

41. Overall gas residence time,  $\Theta_g$  (Procedure #1,  $\bar{P}_c = 301$  psia)

42. Overall gas residence time,  $\Theta_g$  (Procedure #1,  $\bar{P}_c = 423$  psia)

43. Overall gas residence time,  $\Theta_g$  (Procedure #1,  $\bar{P}_c = 590$  psia)

44. Real component of space lag,  $\mathcal{F}$  (Procedure #2,  $\bar{P}_c = 301$  psia)

45. Real component of space lag,  $\bar{\mathcal{F}}$  (Procedure #2,  $\bar{P}_c = 423$  psia)

46. Real component of space lag,  $\bar{\mathcal{F}}$  (Procedure #2,  $\bar{P}_c = 590$  psia)

47. Average total time lag,  $\bar{T}_T$  (Procedure #1,  $\bar{P}_c = 301$  psia)

48. Average total time lag,  $\bar{T}_T$  (Procedure #1,  $\bar{P}_c = 423$  psia)

49. Average total time lag,  $\bar{T}_T$  (Procedure #1,  $\bar{P}_c = 590$  psia)

50. Real component of total time lag,  $\bar{T}_T$  (Procedure #2,  $\bar{P}_c = 301$  psia)

51. Real component of total time lag,  $\bar{T}_T$  (Procedure #2,  $\bar{P}_c = 423$  psia)

52. Real component of total time lag,  $\bar{T}_T$  (Procedure #2,  $\bar{P}_c = 590$  psia)

53. Time lag interaction index,  $n$  (Procedure #2,  $\bar{P}_c = 301$  psia)

54. Time lag interaction index,  $n$  (Procedure #2,  $\bar{P}_c = 423$  psia)

55. Time lag interaction index,  $n$  (Procedure #2,  $\bar{P}_c = 590$  psia)

56. Average sensitive time lag,  $\bar{\tau}$  (Procedure #2,  $\bar{P}_c = 301$  psia)

57. Average sensitive time lag,  $\bar{\tau}$  (Procedure #2,  $\bar{P}_c = 423$  psia)

58. Average sensitive time lag,  $\bar{\tau}$  (Procedure #2,  $\bar{P}_c = 590$  psia)

59. Asymptotic gas residence time parameters,  $\Theta_{g, \text{Asy.}}, \bar{\mathcal{F}}_{\text{Asy.}}$

60. Asymptotic total combustion time lag,  $(\bar{T}_T)_{\text{Asy.}}$

61. Pressure variation of interaction index.

62. Pressure variation of sensitive time lag

63. Sonic analyzer spectrum of fuel pressure oscillation

64. Determination of resonant harmonic

65. Typical middle-frequency pressure oscillations

66. Typical border-frequency pressure oscillations

67. Typical high-frequency pressure oscillations
68. Typical variation of interaction index with total time lag asymptote
69. Calculated time lag parameters for average transfer function values
70. Required transfer function modulus for constant time lag parameters
71. Required transfer function phase angle for constant time lag parameters
72. Vector diagram of solutions to combustion chamber equation
73. Two-point calculation procedure: first iteration
74. Two-point calculation procedure: first iteration
75. Two-point calculation procedure: second iteration
76. Two-point calculation procedure: third iteration
77. Two-point calculation procedure: third iteration
78. Two-point calculation procedure: effect of  $R_1$  variation
79. Two-point calculation procedure: effect of  $\beta_1$  variation
80. Two-point calculation procedure: solution with modified  $\beta_1$

Appendix Figures

- C-1. Representation of bipropellant injector orifice
- C-2. Inertial phase lag between pressure drop and flow rate in bi-propellant oxidizer injector
- C-3. Inertial phase lag between pressure drop and flow rate in bi-propellant fuel injector

TABLE I  
REFERENCE DATA FOR DROPLET DIAMETER DETERMINATION

SOURCE OF DATA AND REFERENCE NO.	ORIFICE DIAM. (IN.)	Injector $\Delta P$ (PSI)	$\frac{S_e}{S_R}$ (LBS/FT <sup>3</sup> )	$d_o \sqrt{\frac{\Delta P}{S_R}}$	MEAN DROPLET DIAM. (MICRONS)
Schmidt (40 )	.018	75	62.4	.0198	73.2
Schmidt (40 )	.018	100	62.4	.0229	49.8
Schmidt (40 )	.018	125	62.4	.0256	46.5
Lee (39 )	.028	1730	54.7	.1576	24.4
Princeton Injector	.035	140	62.1	.0534	(28)
Princeton Injector	.042	140	62.0	.0643	(30)
Princeton Injector	.052	140	61.9	.0795	(32)

TABLE II - A  
STEADY STATE DATA FOR 300-PSI OPERATING LEVEL

RUN NO.	TIME OF READING (SECS)	$\bar{P}_c$ (PSIA)	$\bar{P}_o$ (PSIA)	$\bar{P}_f$ (PSIA)	THRUST (LBS)	$\bar{m}$ TOTAL (LBS/SEC)	$F = \frac{\bar{o}}{\bar{P}_f}$ (BY WT.)	CALC. $T_c$ (HR)	CALC. $\bar{v}_t$ (FT/SEC)
A-177	6.15	270	376	338	215	0.994	1.389	5108	207
A-187	11.80	279	377	346	214	1.021	1.305	5043	205
A-189	6.20	279	377	348	220	1.006	1.329	5233	202
A-189	8.20	279	377	348	220	1.015	1.350	5171	204
A-201	8.65	275	366	345	218	1.003	1.274	5023	203
A-201	10.80	275	366	345	218	1.003	1.274	5023	203
A-328	6.60	298	477	422	250	1.091	1.282	5232	204
A-328	8.90	298	477	422	250	1.083	1.280	5307	203
A-330	6.10	303	497	422	244	1.122	1.294	5351	207
A-330	8.35	303	497	422	245	1.124	1.289	5112	207
A-349	11.20	304	513	456	247	1.111	1.319	5077	205
A-352	10.62	306	510	447	254	1.099	1.303	5233	201
A-380	6.70	310	502	459	250	1.120	1.369	5518	203
A-380	8.80	308	500	459	250	1.120	1.359	5444	205
A-380	10.90	310	498	459	251	1.116	1.349	5525	202
A-385	6.20	308	495	444	255	1.103	1.311	5529	200
A-385	8.30	308	495	444	255	1.109	1.323	5491	202
A-385	10.50	303	485	439	255	1.103	1.320	5358	204
A-388	7.50	313	473	448	251	1.109	1.345	5697	199
A-388	9.50	314	474	449	252	1.112	1.339	5694	199
A-388	11.50	312	473	448	249	1.110	1.335	5635	200
A-392	7.18	308	485	444	253	1.127	1.342	5348	206
A-392	9.21	308	485	444	252	1.129	1.336	5320	206
A-392	11.30	303	476	439	248	1.121	1.329	5216	219
A-399	6.35	308	510	456	256	1.113	1.344	5488	203
A-399	8.50	308	510	457	257	1.113	1.344	5488	203
A-399	10.60	308	499	459	258	1.119	1.357	5448	206

TABLE II - B  
STEADY STATE DATA FOR 450-PSI OPERATING LEVEL

RUN NO.	TIME OF READING (SECS)	$\bar{P}_c$ (PSIA)	$\bar{P}_o$ (PSIA)	$\bar{P}_f$ (PSIA)	THRUST (LBS)	$\bar{m}$ TOTAL (LBS/SEC)	$\bar{r} = \frac{\rho}{F}$ (BY WT.)	CALC. $T_c$ (ft)	CALC. $\bar{u}$ , (FT/SEC)
A-231	4.39	389	532	515	341	1.467	1.132	4664	203
A-259	7.18	401	557	522	352	1.566	1.351	4701	221
A-259	9.82	406	557	522	353	1.564	1.355	4817	218
A-260	7.20	423	567	532	370	1.564	1.345	5213	209
A-260	9.87	415	567	532	370	1.561	1.340	5030	212
A-263	6.91	422	547	522	358	1.553	1.331	5238	209
A-263	9.56	401	547	522	358	1.551	1.336	4768	218
A-273	5.92	400	522	509	293	1.502	1.297	4994	211
A-273	8.52	400	522	509	316	1.494	1.295	5045	210
A-274	7.31	400	537	514	342	1.475	1.323	5262	208
A-274	9.62	400	537	514	342	1.473	1.327	5244	208
A-302	5.82	413	547	523	351	1.456	1.186	5449	193
A-440	6.92	430	581	540	385	1.562	1.351	5433	205
A-440	8.42	430	581	540	385	1.560	1.348	5440	206
A-440	9.92	430	581	540	385	1.558	1.345	5428	205
A-442	6.00	435	586	557	391	1.598	1.367	5339	208
A-442	8.00	435	586	557	391	1.600	1.370	5330	208
A-442	10.00	435	586	557	391	1.601	1.371	5324	208
A-449	6.85	435	581	547	387	1.603	1.371	5311	209
A-449	8.35	435	581	547	387	1.603	1.371	5311	209
A-449	9.85	435	581	547	386	1.603	1.371	5311	209
A-469	6.02	433	597	567	388	1.605	1.340	5215	209
A-469	8.10	429	587	565	390	1.611	1.335	5057	212
A-469	10.20	437	592	567	390	1.608	1.327	5252	208
A-472	5.90	434	597	562	386	1.606	1.358	5251	209
A-472	8.00	434	602	565	387	1.605	1.360	5256	209
A-474	7.25	422	609	557	375	1.627	1.358	4833	218
A-474	9.35	423	609	557	376	1.618	1.383	4946	217
A-474	11.45	423	609	557	376	1.618	1.383	4946	217
A-475	8.50	433	614	564	390	1.602	1.349	5235	215
A-475	10.50	433	614	564	391	1.602	1.342	5125	205
A-479	8.70	428	617	557	378	1.627	1.331	4929	214
A-479	10.90	428	617	557	379	1.624	1.343	4962	214

TABLE II - C  
STEADY STATE DATA FOR 600-PSI OPERATING LEVEL

RUN NO.	TIME OF READING (SECS)	$\bar{P}_2$ (PSIA)	$\bar{P}_3$ (PSIA)	$\bar{P}_F$ (PSIA)	THRUST (LBS)	$\dot{m}$ TOTAL (LBS/SEC)	$\bar{F} = \frac{\Omega}{\dot{m}}$ (BY WT.)	CALC. $T_C$ (OR)	CALC. $\bar{u}_1$ (FT/SEC)
A-411	8.36	622	770	744	551	2.233	1.351	5575	204
A-411	9.00	601	773	747	552	2.233	1.333	5175	211
A-419	4.90	586	725	705	545	2.235	1.365	4948	218
A-420	5.10	586	717	709	531	2.229	1.368	4993	216
A-420	7.23	597	732	709	532	2.227	1.362	5172	212
A-420	9.40	602	732	714	533	2.229	1.364	5263	211
A-432	6.31	574	727	734	520	2.220	1.366	4826	220
A-432	8.30	583	717	724	521	2.222	1.368	4973	217
A-432	10.30	579	727	719	521	2.224	1.365	4891	218
A-433	8.85	599	727	734	541	2.216	1.369	4516	228
A-433	10.50	601	730	727	538	2.216	1.365	5335	211
A-459	5.95	610	808	754	568	2.233	1.362	5381	208
A-459	7.65	610	808	754	569	2.233	1.362	5381	208
A-461	5.30	582	762	724	528	2.234	1.352	4877	218
A-461	7.00	581	752	714	527	2.231	1.356	4879	218
A-461	8.70	581	762	724	527	2.228	1.348	4882	218
A-488	6.72	577	728	708	528	2.172	1.382	5140	214
A-488	8.75	589	728	708	528	2.179	1.381	5321	211
A-488	9.90	589	728	708	528	2.179	1.381	5321	211
A-489	5.82	572	722	707	525	2.183	1.381	4999	217
A-489	7.88	582	722	707	525	2.185	1.378	5163	214
A-489	10.00	582	722	707	525	2.185	1.378	5163	214

TABLE III  
SUMMARY OF AVERAGE STEADY STATE PARAMETERS

	NOMINAL $\bar{P}_c = 300$	NOMINAL $\bar{T}_c = 450$	NOMINAL $\bar{P}_c = 600$
<u>PRESSURE DATA:</u>			
1. Rocket chamber pressure, $\bar{P}_c$ (psia)	301	423	590
2. Fuel injector pressure, $\bar{P}_f$ (psia)	423	541	722
3. Oxygen injector pressure, $\bar{P}_o$ (psia)	462	574	741
4. Fuel injector pressure drop, $\Delta\bar{P}_f$ (psi)	122	118	132
5. Oxygen injector pressure drop, $\Delta\bar{P}_o$ (psi)	161	151	151
<u>PROPELLANT DATA:</u>			
1. Fuel specific gravity	.798	.796	.788
2. Fuel flow rate, $\bar{w}_f$ (lbs/sec)	.467	.672	.939
3. Oxygen flow rate, $\bar{w}_o$ (lbs/sec)	.622	.900	1.276
4. Total propellant flow rate, $\bar{w}_T$ (lbs/sec)	1.089	1.572	2.215
5. Mixture ratio, $r = \bar{w}_o / \bar{w}_f$	1.33	1.34	1.36
6. Mean propellant density, $\bar{\rho}_{p0}$ (#/ft <sup>3</sup> )	62.1	62.0	61.9
7. Mean injection velocity, $\bar{u}_{e0}$ (ft/sec)	105	110	101
<u>PERFORMANCE DATA:</u>			
1. Rocket motor thrust, $\bar{F}$ (lbs)	238.2	368.7	534.6
2. Characteristic exhaust velocity, $c^*$ (ft/sec)	5490	5503	5530
3. Specific impulse, $I_{sp}$ (sec)	218.7	234.5	241.4
4. Thrust coefficient, $C_f$	1.316	1.417	1.473
<u>COMBUSTION PARAMETERS:</u>			
1. Combustion chamber temperature $T_c$ ( $^{\circ}R$ )	5450	5515	5625
2. Combustion gas density, $\bar{\rho}_c$ (#/ft <sup>3</sup> )	.1087	.1526	.2109
3. Combustion gas molecular weight, $M_c$	21.25	21.22	21.61
4. Combustion gas viscosity, $\bar{\mu}_c$ (poises)	$6.43 \times 10^{-4}$	$6.48 \times 10^{-4}$	$6.53 \times 10^{-4}$
5. Mean specific heat ratio, $\gamma$	1.213	1.211	1.210
6. Chamber sound velocity, $c_0$ (ft/sec)	3945	3945	3965
7. Temperature-mixture ratio slope $d\bar{T}_c/d\bar{R}$ ( $^{\circ}R$ )	2362	2482	2285
8. Chamber exit gas velocity, $\bar{u}_e$ , (ft/sec)	204.0	209.2	214.3
<u>MOTOR GEOMETRY:</u>			
1. Injector orifice diameter (inches)	.035	.042	.052
2. Nozzle throat diameter (inches)	.875	.885	.885
3. Combustion chamber length (inches)	4.016	4.016	4.016

TABLE IV - A  
TRANSFER FUNCTION AND MIXTURE RATIO RESULTS-300 PSIA

RUN NO.	TIME OF READING (SECS.)	MODULATING FREQUENCY (CPS)	$R = \frac{\tilde{U}_i}{\tilde{U}_f}$	$\beta$ (DEGREES)	$\mu = \frac{\tilde{U}_o}{\tilde{U}_f}$	$\delta = \beta_o - \beta_f$ (DEGREES)
A-177	6.15	99.2	2.134	58.1	1.002	8.2
A-187	11.80	99.5	2.031	54.5	0.890	1.2
A-189	6.20	148.8	2.857	70.3	1.064	-8.8
A-189	8.20	148.8	2.925	70.0	1.068	-12.4
A-201	8.65	174.5	2.653	76.2	0.905	8.4
A-201	10.80	174.5	2.561	77.6	0.923	9.6
A-328	6.60	65.5	1.130	37.1	1.076	0.4
A-328	8.90	65.5	2.424	30.4	0.861	0.6
A-330	6.10	65.5	1.975	18.5	1.050	-2.6
A-330	8.35	65.5	2.739	18.6	1.019	-2.3
A-349	11.20	162.0	1.241	78.6	0.956	-9.8
A-352	10.62	156.4	1.116	71.6	1.091	4.4
A-380	6.70	211.3	1.857	67.8	0.963	-4.4
A-380	8.80	211.3	1.813	67.5	1.000	-4.3
A-380	10.90	211.3	1.852	67.7	1.054	-4.3
A-385	6.20	219.0	1.844	72.6	0.933	-2.8
A-385	8.30	219.0	1.879	72.8	0.949	-0.8
A-385	10.50	219.3	1.927	72.7	1.061	0.6
A-388	7.50	242.5	2.046	77.1	0.934	-2.1
A-388	9.50	242.5	2.015	78.7	0.951	-4.3
A-388	11.50	242.7	1.872	79.3	0.932	-7.2
A-392	7.18	243.0	2.157	82.1	1.031	2.9
A-392	9.21	242.7	2.115	83.5	1.064	0.4
A-392	11.30	242.5	2.114	87.6	1.090	1.9
A-399	6.35	241.0	2.222	80.2	0.902	-8.9
A-399	8.50	241.0	2.155	77.3	0.952	-4.6
A-399	10.60	241.0	2.138	77.9	1.067	2.7

TABLE IV - B  
TRANSFER FUNCTION AND MIXTURE RATIO RESULTS-450 PSTA

RUN NO.	TIME OF READING (SECS.)	MODULATING FREQUENCY (CPS)	$R = \frac{\tilde{\mu}_i}{\tilde{\mu}}$	$\beta$ (DEGREES)	$\lambda = \frac{\tilde{\mu}_o}{\tilde{\mu} F}$	$\delta = \beta_o - \beta_F$ (DEGREES)
A-231	4.39	236.5	2.062	53.3	1.095	-8.6
A-259	7.18	154.4	2.321	45.4	1.007	0.3
A-259	9.82	154.4	2.517	45.5	1.026	2.0
A-260	7.20	150.2	3.907	38.7	1.072	-8.3
A-260	9.87	150.4	3.678	31.3	1.015	-3.8
A-263	6.91	155.4	3.521	42.4	0.979	1.1
A-263	9.56	155.4	3.219	42.9	1.003	4.6
A-273	5.92	198.7	1.783	72.2	0.927	14.4
A-273	8.52	199.1	1.574	67.8	1.089	1.7
A-274	7.31	198.9	1.701	68.7	1.015	10.0
A-274	9.62	198.9	1.696	69.4	1.013	3.3
A-302	5.82	84.7	3.996	23.8	1.131	5.8
A-440	6.92	244.8	2.003	75.1	1.006	-6.3
A-440	8.42	244.8	1.995	75.6	1.020	-5.5
A-440	9.92	244.8	2.039	74.5	1.001	-4.2
A-442	6.00	246.7	2.039	75.6	1.079	-2.6
A-442	8.00	246.7	2.042	75.0	1.113	-2.1
A-442	10.00	246.7	1.980	68.7	1.094	-15.0
A-449	6.85	221.1	1.748	76.7	1.170	6.9
A-449	8.35	221.1	1.690	79.3	1.273	0.5
A-449	9.85	221.1	1.628	78.9	1.263	2.5
A-469	6.02	68.1	0.961	37.9	1.040	3.0
A-469	8.10	68.1	0.911	38.8	1.082	-2.6
A-469	10.20	68.1	1.008	36.6	1.061	-4.8
A-472	5.90	121.4	1.356	53.8	1.092	-1.3
A-472	8.00	121.4	1.349	55.8	1.016	-1.5
A-474	7.25	174.2	1.765	66.5	0.947	-7.7
A-474	9.35	174.2	1.723	64.4	0.915	-7.4
A-474	11.45	174.2	1.715	66.5	0.954	-5.1
A-475	8.50	171.0	1.630	65.1	0.980	1.4
A-475	10.50	171.0	1.618	65.0	0.958	1.8
A-479	8.70	174.6	1.717	65.2	0.988	-12.2
A-479	10.90	174.6	1.710	66.1	0.975	-11.5

TABLE IV - C  
TRANSFER FUNCTION AND MIXTURE RATIO RESULTS-600 PSIA

RUN NO.	TIME OF READING (SECS.)	MODULATING FREQUENCY (CPS)	$R = \frac{\tilde{u}_o}{\tilde{\phi}}$	$\beta$ (DEGREES)	$\alpha = \frac{\tilde{u}_o}{\tilde{u}_r}$	$\delta = \beta_o - \beta_r$ (DEGREES)
A-411	8.36	76.7	1.174	61.2	1.377	-9.4
A-411	9.00	76.7	1.032	51.4	0.890	10.7
A-419	4.90	91.5	1.107	51.7	0.852	0.8
A-420	5.10	93.2	1.214	54.7	1.339	-8.5
A-420	7.23	93.2	1.199	56.3	1.127	-9.4
A-420	9.40	93.2	1.199	58.6	1.194	-8.4
A-432	6.31	205.6	2.115	79.9	0.910	-0.2
A-432	8.30	205.8	2.345	81.8	0.943	-2.0
A-432	10.30	205.8	2.365	81.2	1.025	-5.5
A-433	8.85	221.3	1.495	81.3	1.247	-1.7
A-433	10.50	221.3	2.178	77.9	1.147	-1.6
A-459	5.95	246.0	2.070	77.6	1.039	1.9
A-459	7.65	246.0	2.008	78.1	1.071	6.2
A-461	5.30	247.8	2.327	82.3	1.001	-10.4
A-461	7.00	247.6	2.325	82.4	1.068	-7.7
A-461	8.70	247.6	1.991	83.0	1.093	-7.9
A-488	6.72	68.8	0.973	39.3	1.102	6.1
A-488	8.75	68.8	1.093	42.8	1.112	8.7
A-488	9.90	68.8	1.024	43.3	1.166	9.7
A-489	5.82	67.8	1.011	37.5	0.989	3.8
A-489	7.88	67.8	1.086	38.1	0.965	5.0
A-489	10.00	67.8	1.117	36.2	1.009	6.8

TABLE V  
SUMMARY OF AVERAGE DATA FOR VELOCITY CORRECTION FACTORS

	$\bar{P}_c$ PSIA	$\bar{P}_e$ PSIA	$\bar{R}$ PSIA
<u>Injector Data:</u>	=301	=423	=590
1. Injector orifice diameter, $d_o$ (in.)	.035	.042	.052
2. Average propellant density, $\bar{\rho}_p$ (lbs/ft <sup>3</sup> )	62.1	62.0	61.9
3. Average injection velocity, $\bar{V}_{inj}$ (ft/sec)	105	110	101
<u>Drag Coefficient Data:</u>			
1. Mean droplet diameter, $d_d$ (in.)	.0011	.0012	.0013
2. Average combustion gas density, $\bar{\rho}_g$ (lbs/ft <sup>3</sup> )	.1087	.1526	.2109
3. Average gas viscosity, $\bar{\mu}_g$ (micro-poises)	643	648	653
4. Droplet Reynolds' number at inlet, $R_e$	24.2	38.6	52.4
5. Drag coefficient proportionality constant, $C_d R_e$	54.8	66.5	76.7
6. Non-dimensional drag coefficient, $k$	.0289	.0297	.0295
<u>Velocity Distribution Calculations:</u>			
1. Non-dimensional chamber exit gas velocity, $\bar{u}_e$	.0517	.0530	.0540
2. Non-dimensional exit liquid velocity, $\bar{u}_l$	.0348	.0382	.0411
3. Non-dimensional final total time lag, $\bar{\tau}_T$	39.97	34.12	29.92
4. Dimensionless integral $I_1 = \int_0^1 x dx / \bar{u}_e$	18.24	15.52	13.66
5. Dimensionless integral $I_2 = \int_0^1 x \bar{\tau}_T(x) dx / \bar{u}_e$	490.7	359.7	279.3
<u>Calculated Correction Factors:</u>			
1. Effective burned gas residence fraction, $\bar{f}$	0.735	0.835	1.000
2. Gas residence correction factor, $a$	2.42	1.89	1.48
3. Total time lag correction factor, $\Delta_2$	3.755	1.617	0.829
4. Total time lag correction factor, $\Delta_3$	0.480	-0.414	-0.807

TABLE VI - A  
TIME LAG PARAMETER CALCULATIONS - 300 PSIA

RUN NO.	MODU- LATING FREQ. (CPS)	PROCEDURE #1					PROCEDURE #2					
		$\Theta_g$	$\bar{Z}_T$	MILLI- SECS.	MILLI- SECS	REAL $f$	IMAGI- NARY $f$	REAL $Z_T$	IMAGI. $Z_T$	MILLI- SECS	MILLI- SECS	n
A-177	99.2	2.861	0.113	1.589	2.070	-0.53	0.56	1.40	-0.64			
A-187	99.5	2.452	-0.061	2.326	1.377	-0.35	0.32	2.75	-0.28			
A-189	148.8	3.238	-0.063	1.008	1.873	-0.20	0.48	1.60	-0.79			
A-189	148.8	3.409	-0.134	1.003	1.431	-0.16	0.50	1.75	-0.84			
A-201	174.5	1.786	0.312	0.877	0.461	-0.37	0.10	-0.98	0.22			
A-201	174.5	1.719	0.362	0.848	0.115	-0.40	1.00	-1.79	0.17			
A-328	65.5	1.196	0.351	3.164	1.180	-0.23	0.13	1.10	0.32			
A-328	65.5	4.888	-1.384	4.029	2.957	0.06	1.24	6.56	-0.57			
A-330	65.5	4.551	-1.604	4.251	6.308	0.50	1.13	-6.11	-0.66			
A-330	65.5	12.592	-2.293	4.432	5.086	0.50	3.16	---	---			
A-349	162.0	0.435	0.668	1.293	1.727	-0.27	0.50	0.99	0.86			
A-352	156.4	0.203	0.847	0.938	1.496	-0.32	0.53	1.25	0.82			
A-380	211.3	0.914	0.147	0.835	1.196	-0.03	0.24	-0.21	-3.41			
A-380	211.3	0.897	0.155	0.777	1.255	-0.03	0.24	-0.20	-3.77			
A-380	211.3	0.982	0.147	0.734	1.089	-0.03	0.21	-0.29	-2.40			
A-385	219.0	0.813	0.216	0.803	1.124	-0.08	0.28	0.03	---			
A-385	219.0	0.842	0.227	0.751	1.072	-0.10	0.25	0.06	---			
A-385	219.3	0.978	0.228	0.783	1.024	-0.11	0.18	0.00	---			
A-388	242.5	0.865	0.213	0.678	1.019	-0.02	0.24	0.00	---			
A-388	242.5	0.874	0.221	0.696	1.092	-0.11	0.25	0.00	---			
A-388	242.7	0.756	0.234	0.758	1.174	-0.10	0.30	0.04	---			
A-392	243.0	0.987	0.308	0.732	0.862	-0.11	0.16	0.39	1.34			
A-392	242.7	1.011	0.298	0.777	0.955	-0.10	0.16	0.30	1.66			
A-392	242.5	1.061	0.321	0.904	1.027	-0.24	0.13	0.43	1.10			
A-399	241.0	1.048	0.163	0.985	1.043	-0.10	0.19	-0.27	-2.20			
A-399	241.0	0.992	0.180	0.753	1.067	-0.09	0.19	-0.18	-3.47			
A-399	241.0	1.024	0.247	0.784	0.871	-0.14	0.15	0.06	8.18			

TABLE VI - B

## TIME LAG PARAMETER CALCULATIONS - 45° PSIA

RUN NO.	MODU- LATING FREQ. (CPS)	PROCEDURE #1					PROCEDURE #2				
		$\theta_g$	$\bar{Z}_T$	MILLI- SECS.	MILLI- SECS.	REAL $f$	IMAGI- NARY $f$	REAL	$\bar{Z}_T$	MILLI- SECS.	MILLI- SECS.
A-231	236.5	1.330	-0.08	0.843	0.958	0.14	0.12	0.12	-0.85	-1.03	
A-259	154.4	2.046	-0.28	1.144	1.568	0.16	0.22	0.22	-2.19	-0.52	
A-259	154.4	2.358	-0.32	1.104	1.689	0.18	0.31	0.31	-2.52	-0.54	
A-260	150.2	4.643	-0.62	1.117	1.977	0.22	0.82	0.82	2.70	-1.30	
A-260	150.4	4.159	-0.73	1.348	2.032	0.40	0.72	0.72	-3.21	-1.18	
A-263	155.4	3.674	-0.60	1.181	2.057	0.14	0.61	0.61	3.05	-0.92	
A-263	155.4	3.330	-0.52	1.134	1.779	0.10	0.54	0.54	-3.11	-0.75	
A-273	198.7	1.037	0.07	1.418	1.270	0.01	0.23	0.23	-0.36	-1.71	
A-273	199.1	0.742	0.27	0.920	1.181	-0.07	0.26	0.26	0.40	1.76	
A-274	198.9	0.958	0.13	1.110	1.657	0.01	0.24	0.24	-0.15	-3.94	
A-274	198.9	0.800	0.25	0.790	1.628	-0.08	0.24	0.24	0.41	1.57	
A-302	84.7	9.849	-1.78	2.465	2.964	0.58	2.21	2.21	5.38	-1.68	
A-440	244.8	0.947	0.16	0.653	1.244	-0.05	0.21	0.21	0.00	----	
A-440	244.8	0.946	0.17	0.614	1.220	-0.07	0.20	0.20	0.05	9.89	
A-440	244.8	0.952	0.16	0.622	1.135	-0.06	0.20	0.20	0.03	----	
A-442	246.7	0.974	0.20	0.770	1.073	-0.08	0.18	0.18	0.14	3.64	
A-442	246.7	0.995	0.20	0.845	1.053	-0.08	0.17	0.17	0.12	4.44	
A-442	246.7	0.992	0.20	0.847	1.086	-0.08	0.17	0.17	0.13	3.81	
A-449	221.1	0.817	0.37	0.923	0.943	-0.20	0.21	0.21	0.91	0.70	
A-449	221.1	0.873	0.36	1.044	1.050	-0.20	0.21	0.21	0.93	0.63	
A-449	221.1	0.873	0.37	1.025	1.003	-0.20	0.20	0.20	0.96	0.62	
A-469	68.1	----	----	3.184	2.544	-0.29	0.61	0.61	3.83	0.22	
A-469	68.1	----	----	3.431	3.014	-0.21	0.69	0.69	3.57	0.25	
A-469	68.1	0.282	0.88	3.557	2.677	-0.05	0.48	0.48	2.42	0.26	
A-472	121.4	1.035	0.27	1.395	1.444	-0.10	0.19	0.19	0.69	0.69	
A-472	121.4	0.944	0.33	1.612	1.479	-0.15	0.24	0.24	1.04	0.48	
A-474	174.2	1.127	0.09	1.577	1.289	-0.03	0.16	0.16	-0.33	-1.64	
A-474	174.2	1.012	0.13	1.382	1.245	-0.04	0.20	0.20	-0.10	-6.13	
A-474	174.2	1.034	0.15	1.319	1.309	-0.06	0.19	0.19	-0.01	----	
A-475	171.0	0.897	0.28	1.023	1.129	-0.13	0.21	0.21	0.62	0.90	
A-475	171.0	0.888	0.28	0.999	1.105	-0.10	0.24	0.24	0.64	0.87	
A-479	174.6	1.158	0.08	1.749	1.493	0.00	0.17	0.17	-0.47	-1.15	
A-479	174.6	1.116	0.11	1.651	1.472	-0.02	0.18	0.18	-0.30	-1.74	

TABLE VI - C  
TIME LAG PARAMETER CALCULATIONS - 600 PSIA

RUN NO.	MODU- LATING FREQ. (CPS)	PROCEDURE #1					PROCEDURE #2				
		$\theta_g$	$\bar{Z}_T$	REAL $f$	IMAGI- $f$	REAL $Z_T$	IMAGI. $Z_T$	MILLI- SECS.	MILLI- SECS.	MILLI- SECS.	$n$
A-411	76.7	1.727	0.78	2.826	1.090	-0.74	0.04	-3.58	0.28		
A-411	76.7	-----	----	2.718	1.890	-0.84	0.61	5.80	0.24		
A-419	91.5	0.551	0.77	2.655	1.668	-0.38	0.54	3.44	0.21		
A-420	93.2	1.388	0.41	2.021	0	0.28	0	4.77	0.09		
A-420	93.2	1.122	0.52	2.611	2.425	-0.31	0.19	4.58	0.11		
A-420	93.2	1.119	0.62	1.926	2.600	-0.40	0.17	5.26	0.14		
A-432	205.6	1.072	0.32	0.975	0.896	-0.26	0.10	1.47	0.41		
A-432	205.8	1.378	0.27	0.995	0	0.23	0	2.14	0.23		
A-432	205.8	1.114	0.28	1.145	0.718	-0.24	0.10	1.37	0.39		
A-433	221.3	0.631	0.43	1.843	1.280	-0.22	0.26	0.94	0.89		
A-433	221.3	1.434	0.21	1.128	0.518	-0.16	0.04	0.20	8.11		
A-459	246.0	0.954	0.25	0.738	0.907	-0.13	0.17	0.88	0.56		
A-459	246.0	0.897	0.30	0.801	0.818	-0.16	0.17	1.08	0.53		
A-461	247.8	1.236	0.14	1.137	1.147	-0.12	0.09	0.29	1.19		
A-461	247.6	1.300	0.17	1.203	1.518	-0.14	0.07	0.59	0.49		
A-461	247.6	1.199	0.19	1.266	1.392	-0.14	0.11	0.63	0.58		
A-488	68.8	0.534	----	2.968	2.410	-0.38	0.50	4.50	0.20		
A-488	68.8	0.806	0.88	2.645	1.131	-0.57	0.17	6.59	0.12		
A-488	68.8	0.939	0.84	2.416	0	0.57	0	7.01	0.12		
A-489	67.8	-----	----	2.484	2.332	-0.31	0.53	3.99	0.20		
A-489	67.8	0.534	0.83	3.313	1.812	-0.35	0.37	4.47	0.14		
A-489	67.8	0.790	0.59	3.104	1.308	-0.31	0.22	3.83	0.13		

TABLE VII  
SUMMARY OF TIME LAG PARAMETER CALCULATIONS

<u>Parameter:</u>	NOMINAL $\bar{P}_c$ = 301 PSIA	NOMINAL $\bar{P}_c$ = 423 PSIA	NOMINAL $\bar{P}_c$ = 590 PSIA
1. Asymptotic overall gas residence time, $\Theta_g$ (milliseconds)	0.958	0.945	1.063
2. Asymptotic fraction of chamber downstream from position of average space lag, $f$	0.715	0.750	0.980
3. Asymptotic mean total combustion time lag, $\bar{\tau}_T$ (milliseconds)	0.25	0.17	0.11
4. Average sensitive time lag, $\bar{\tau}$ (milliseconds)	0.08	0.05	0.44
5. Average interaction index, $\gamma$	1.04	0.71	0.34

### Time lag schematization

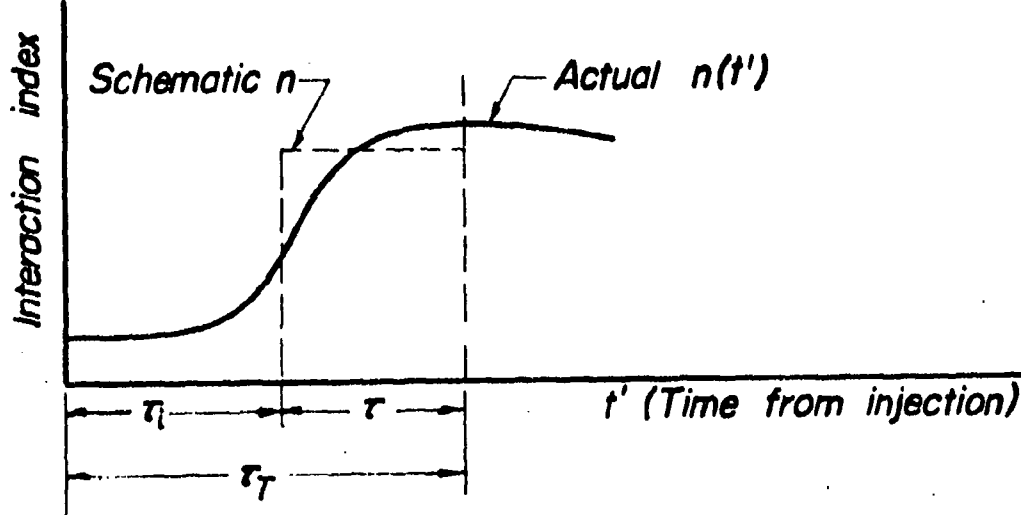
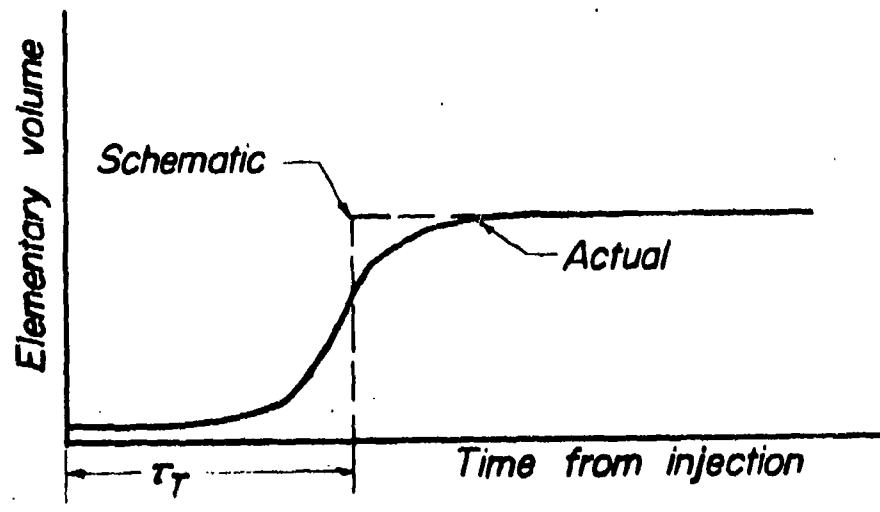
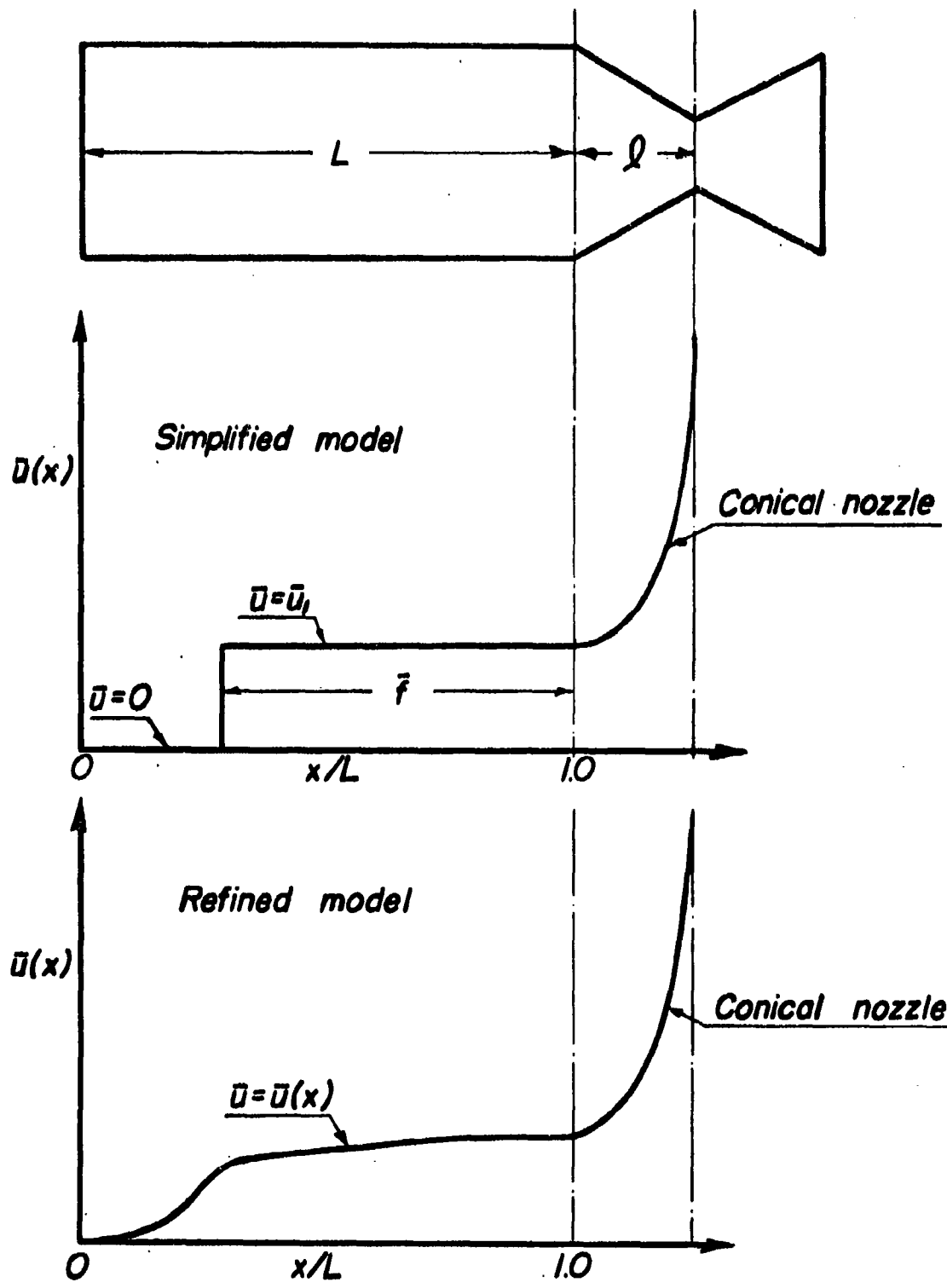


Figure 1

*Comparison of theoretical models*



*Figure 2*

*Typical velocity distributions  
for refined theoretical model*

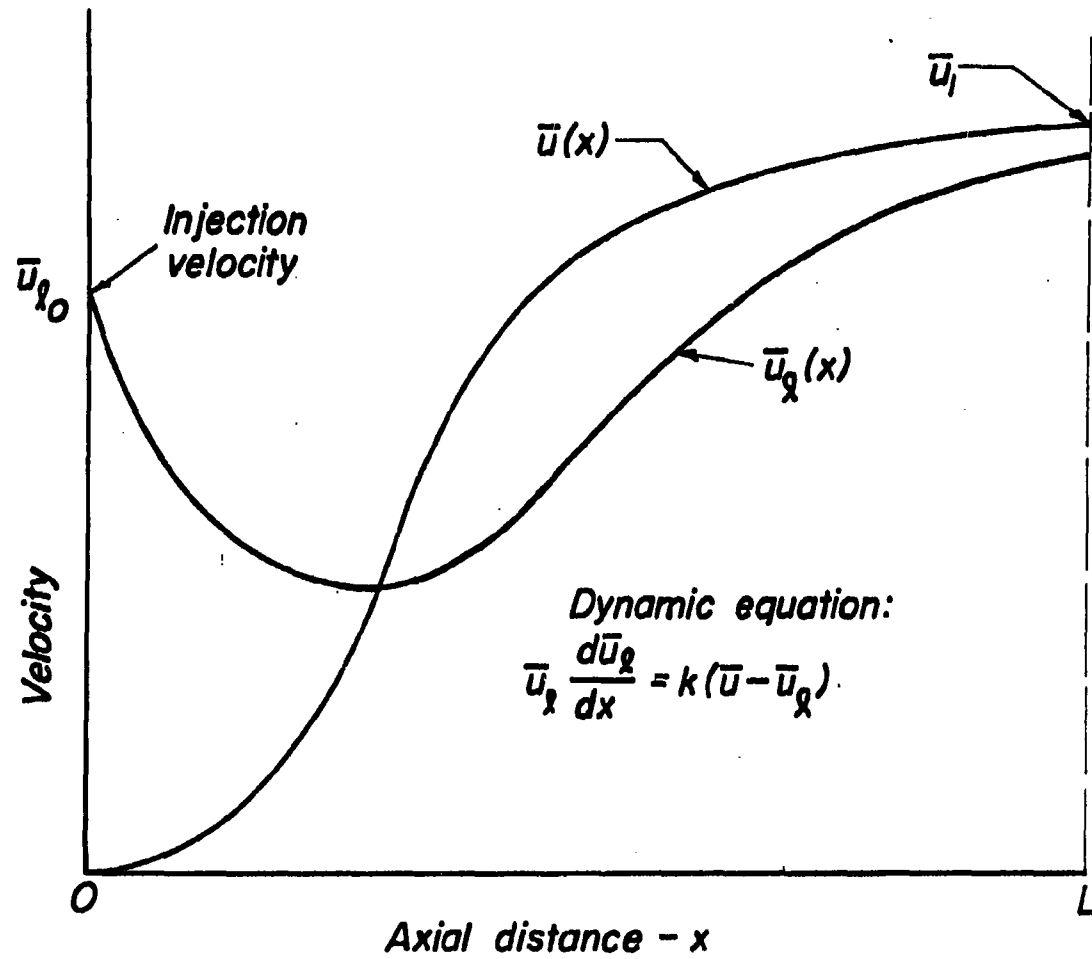


*Figure 3*

*Typical variation of  
velocity perturbation*

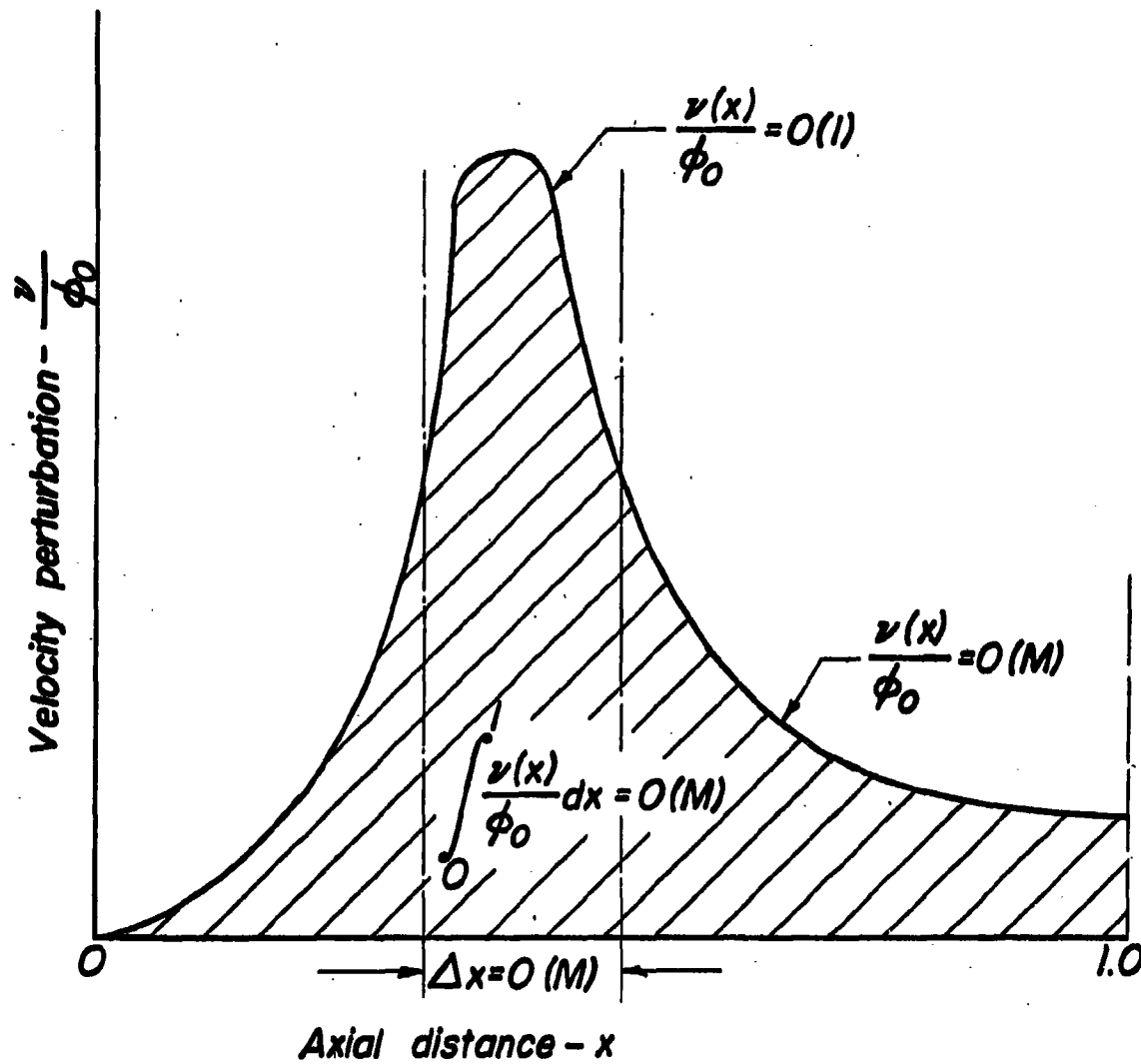


*Figure 4*

**FIGURE 5**  
**COMPARISON OF COMBUSTION CHAMBER EQUATIONS**

**SIMPLIFIED THEORY:**

$$R_F e^{i(\beta_F - \omega \bar{\tau}_T)} = \frac{i\omega \theta_g + \frac{3\gamma - 1}{2\gamma} + \frac{i\omega \theta}{\gamma C^*} (W_1 - \frac{\gamma - 1}{2} W_2) - (\frac{\gamma - 1}{2\gamma}) / (1 - \frac{i\omega \theta_g}{C^* W_1}) e^{-i\omega \theta_g - n(l - e^{-i\omega \theta})}}{1 + \left( \frac{\mu_0}{\mu_F} - n \right) \left[ (n/2 + H + 2K) - K(l - \frac{i\omega \theta}{C^* W_1}) e^{-i\omega \theta_g} \right]}$$

**REFINED THEORY:**

$$R_F e^{i\beta_F} \frac{1}{\bar{u}_l} \int_0^l e^{-i\omega \bar{\tau}_F(x)} \frac{d\bar{u}(x)}{dx} dx = \frac{i\omega + \frac{3\gamma - 1}{2\gamma} + \frac{i\omega}{\gamma} \Gamma(W_1 - \frac{\gamma - 1}{2} W_2) - (\frac{\gamma - 1}{2\gamma}) / (1 - i\omega \bar{\tau} W_1) \frac{1}{\bar{u}_l} \int_0^l e^{-i\omega \theta_g(x)} \frac{d\bar{u}(x)}{dx} dx - n(l - e^{-i\omega \bar{\tau} \bar{u}(x)})}{1 + \left( \frac{\mu_0}{\mu_F} - n \right) (V/2 + H)}$$

**WHERE:**

$R_F e^{i\beta_F}$  = Measured transfer function, based on fuel.

$\mu_0, \mu_F$  = Measured fractional flow rate oscillations.

$\theta_g$  = Gas residence time.

$\bar{\tau}_T$  = Mean total combustion time lag.

$\bar{\tau}$  = Mean sensitive combustion time lag.

$n$  = Interaction index between time lag and chamber pressure.

$\bar{u}_l$  = Gas velocity at end of combustion.

$\ell$  = Length of combustion chamber.

$\bar{\tau}$  = Fraction of chamber length downstream of combustion zone.

$\omega$  = Non-dimensional frequency of oscillations.

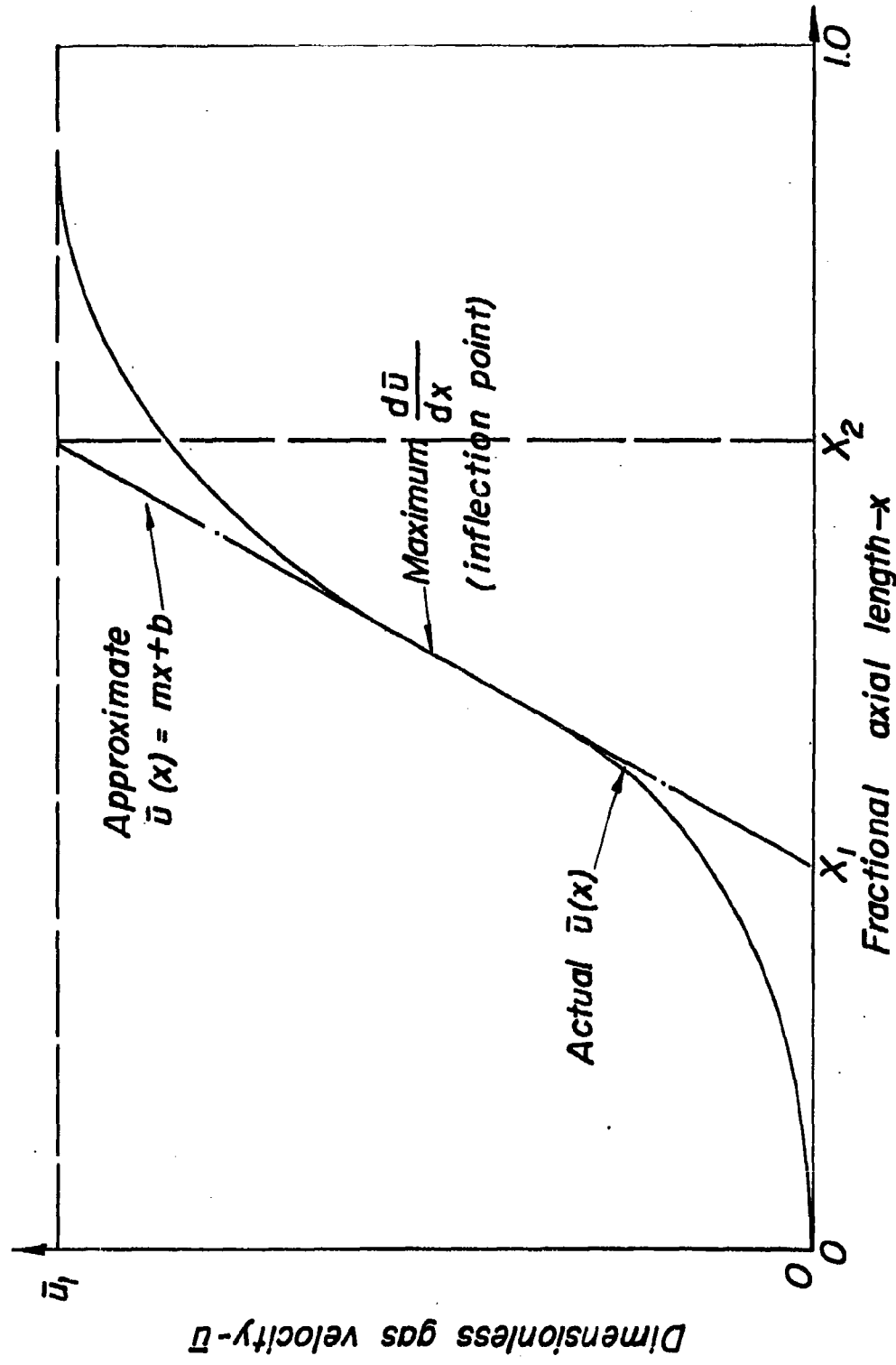
$H, K$  = Mixture ratio parameters.

$C^*$  = Sound velocity at nozzle throat.

$W_1, W_2$  = Integrated velocity parameters for conical nozzle.

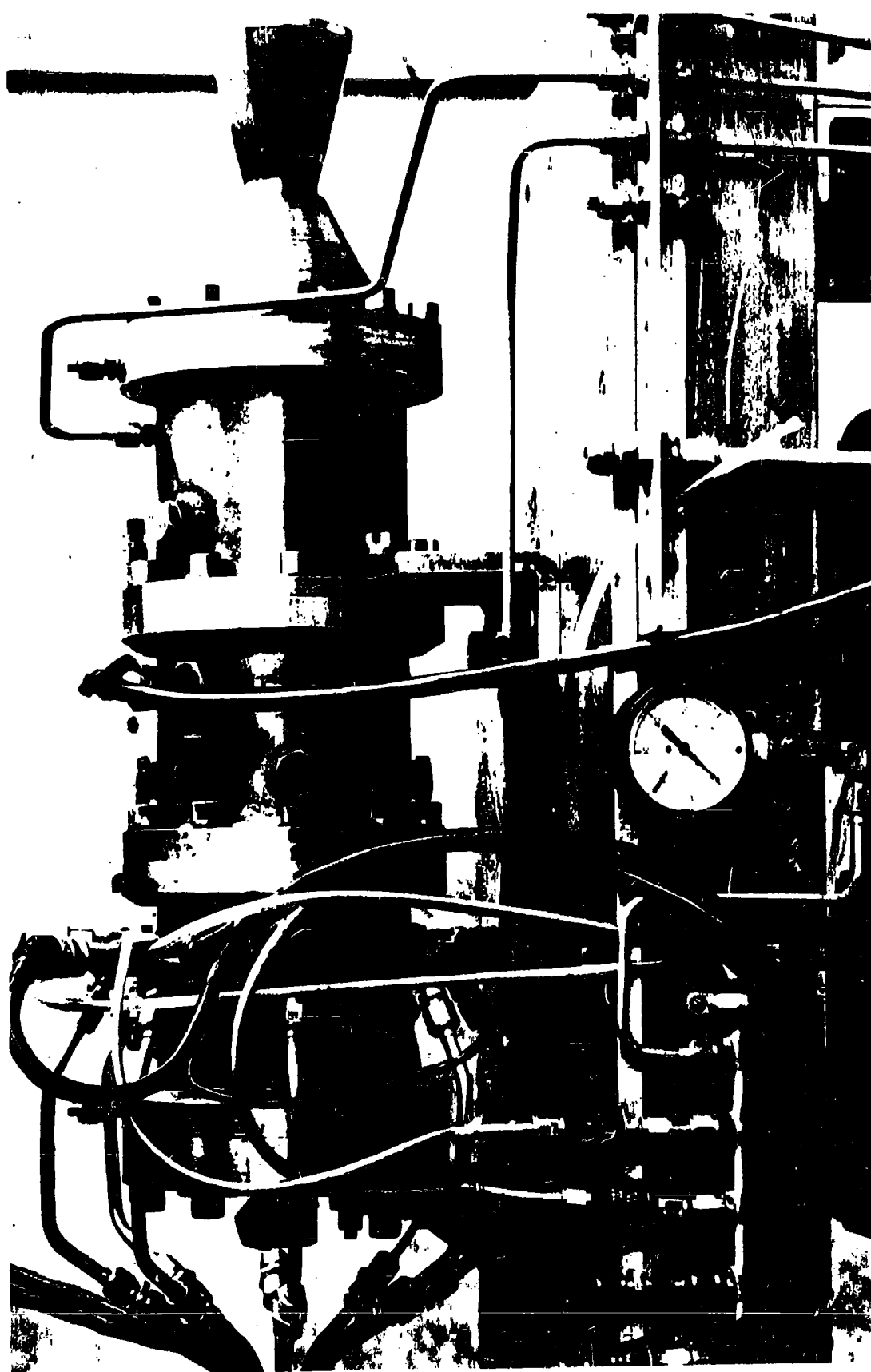
$$\Gamma = \sqrt{\frac{\gamma + 1}{2}} (\rho_{nozzle} / \rho)$$

**Figure 6**  
**VELOCITY DISTRIBUTION APPROXIMATION**  
**FOR**  
**CORRECTION CALCULATIONS**



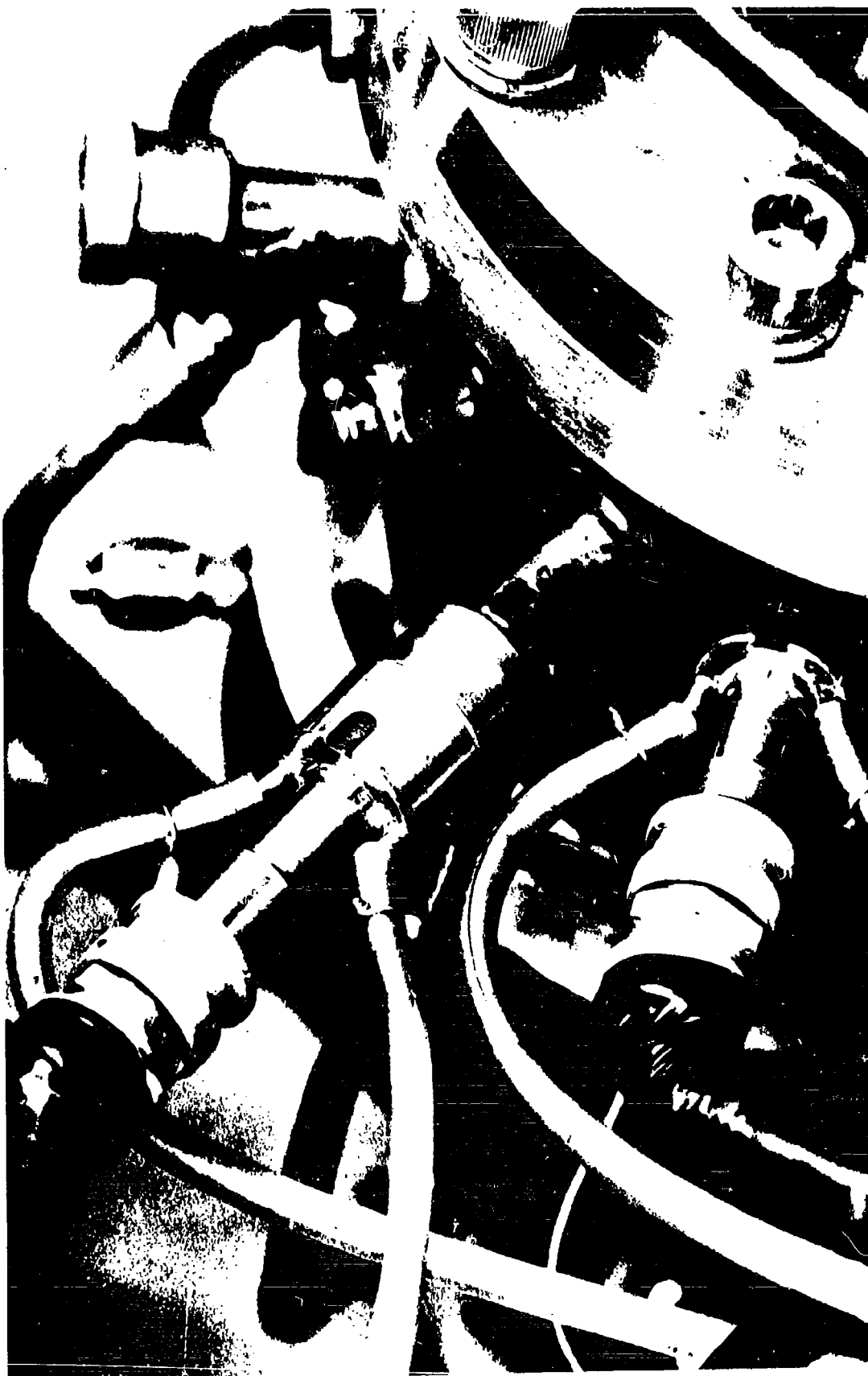
*Figure 7*

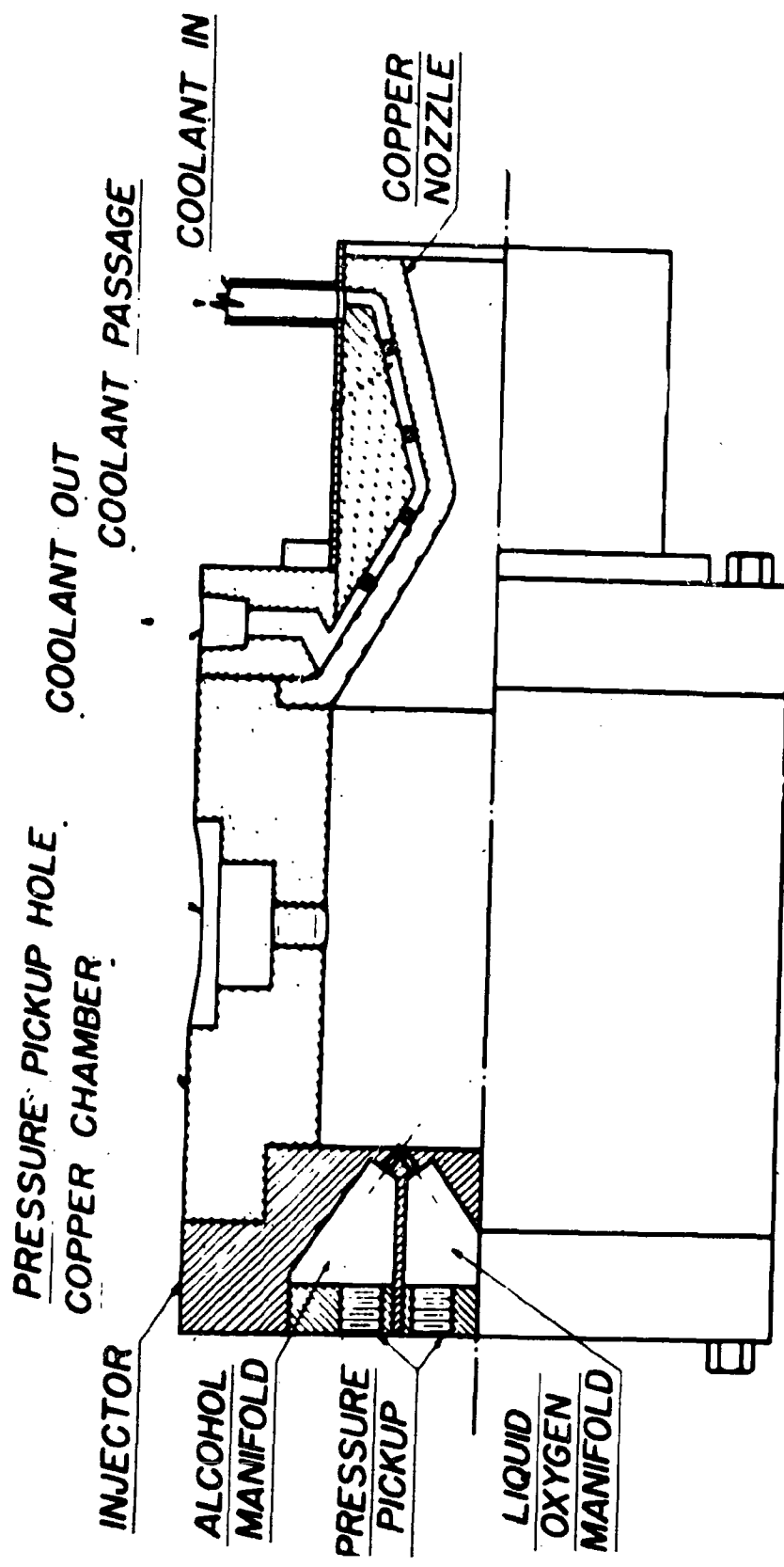
**MONOPROPELLANT ROCKET MOTOR AND TEST STAND**



*Figure 8*

INSTALLATION OF MONOPROPELLANT PRESSURE INSTRUMENTATION

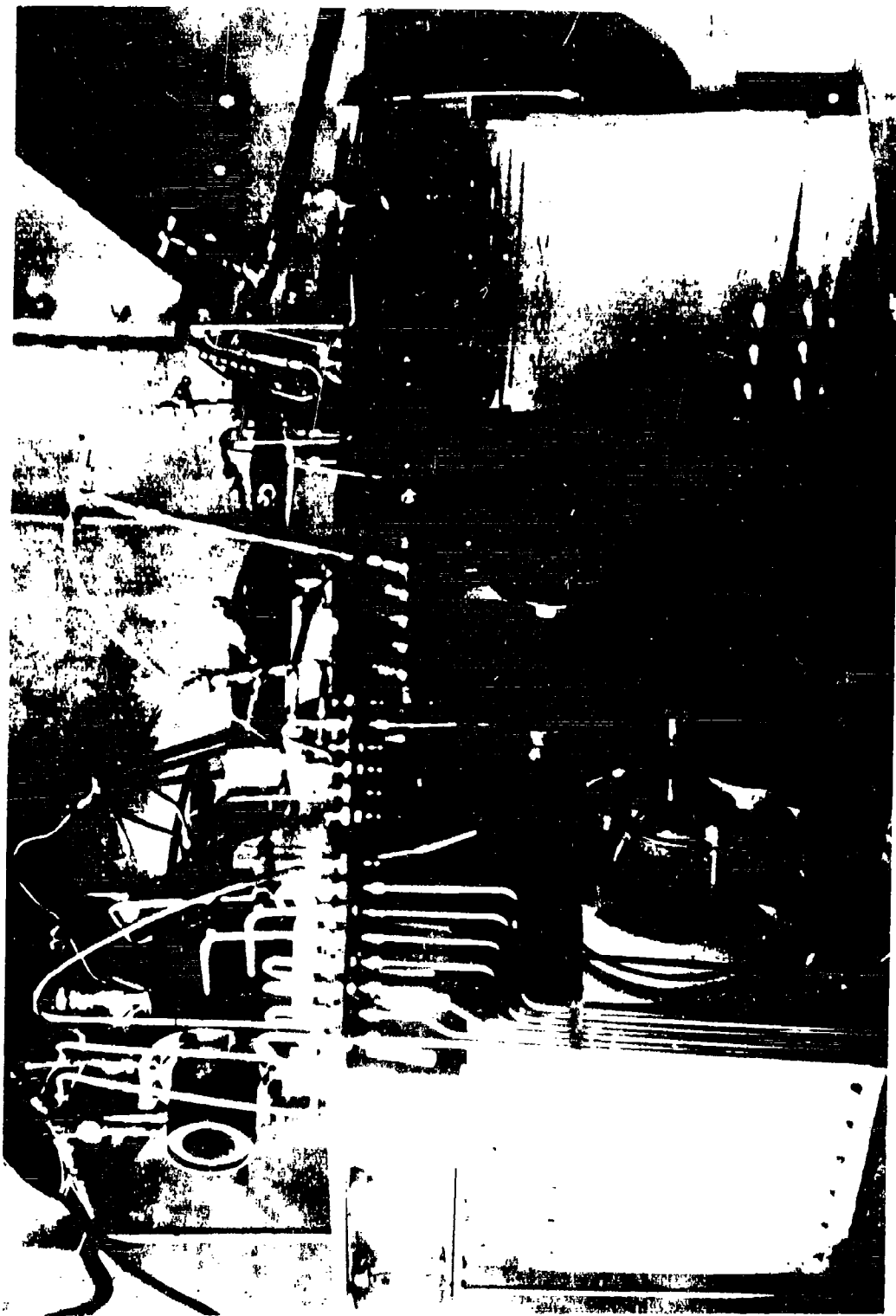




BIPROPELLANT ROCKET MOTOR № 1  
(LIQUID OXYGEN - ALCOHOL)

Figure 9

VIEW OF BIPORELLANT ROCKET TEST STAND  
*Figure 10*



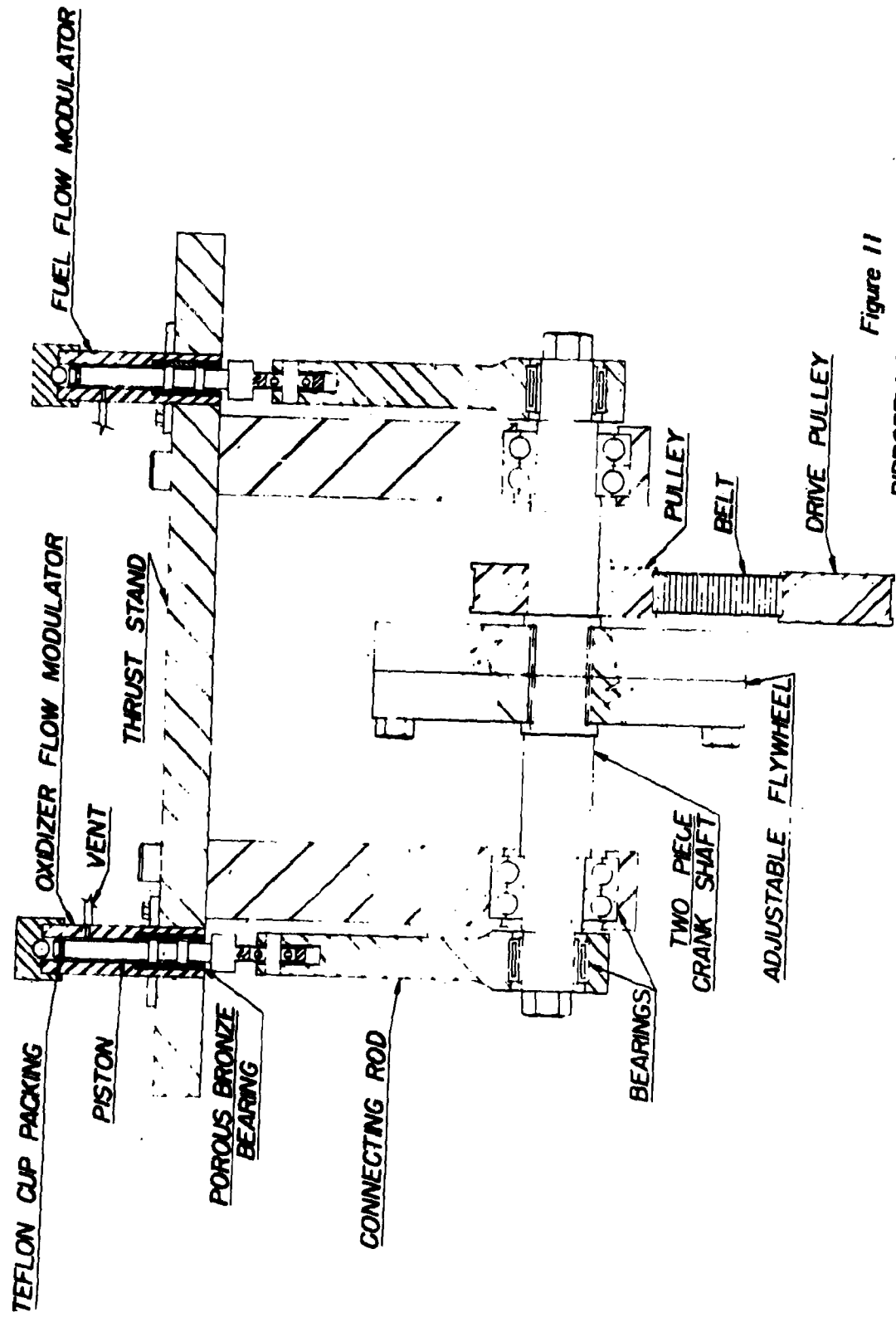


Figure 11  
BIPROPELLANT FLOW MODULATING UNIT

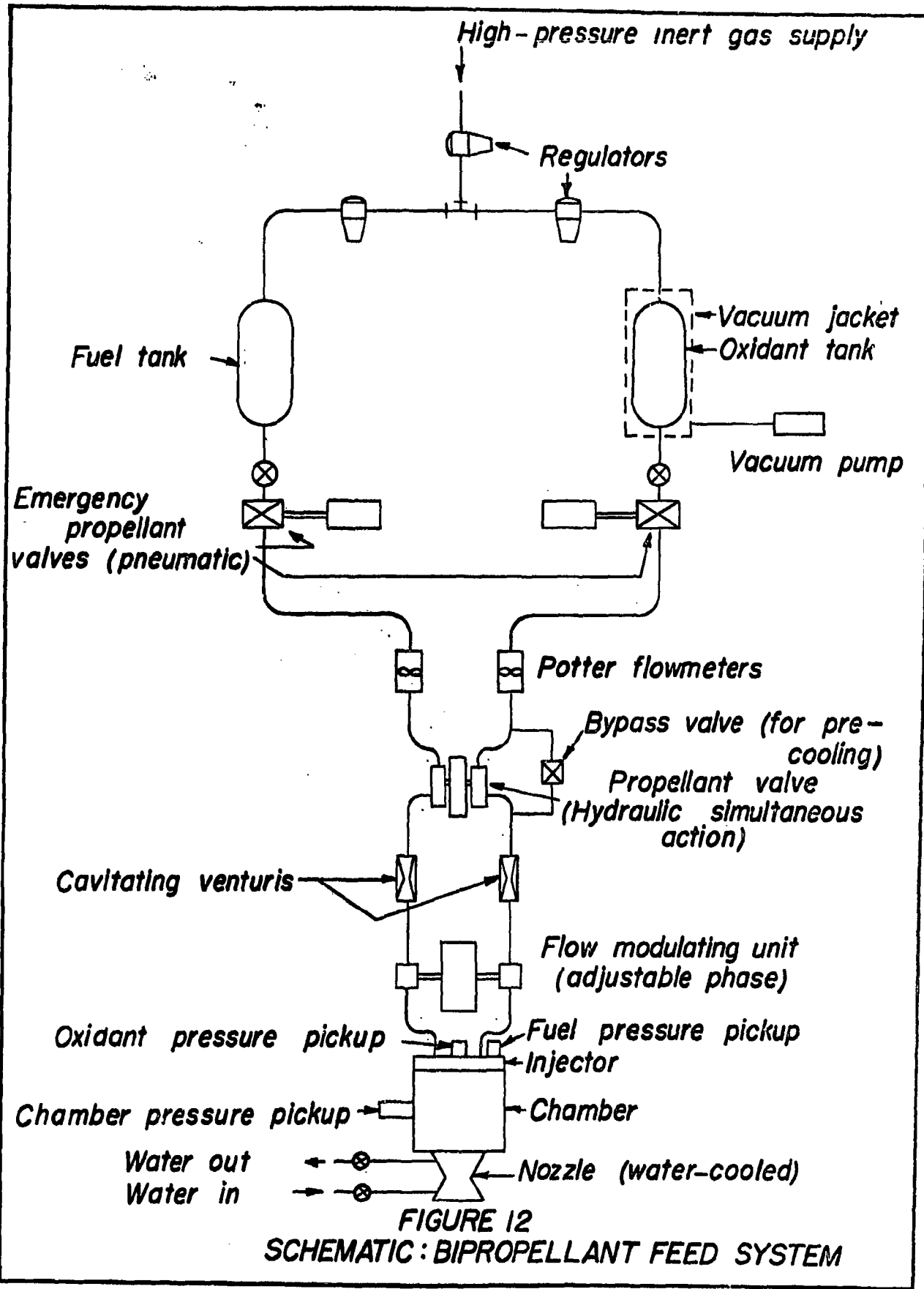
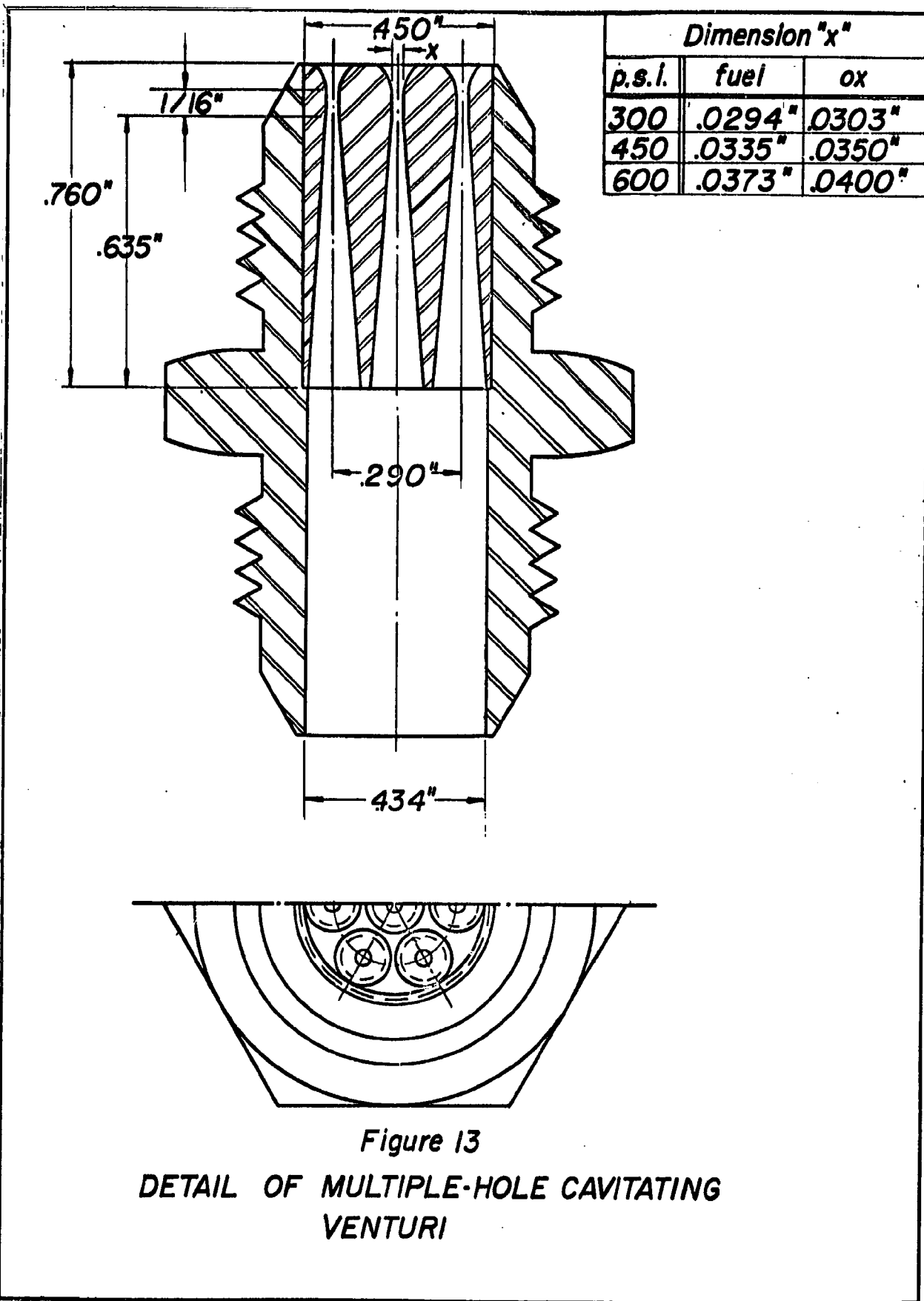
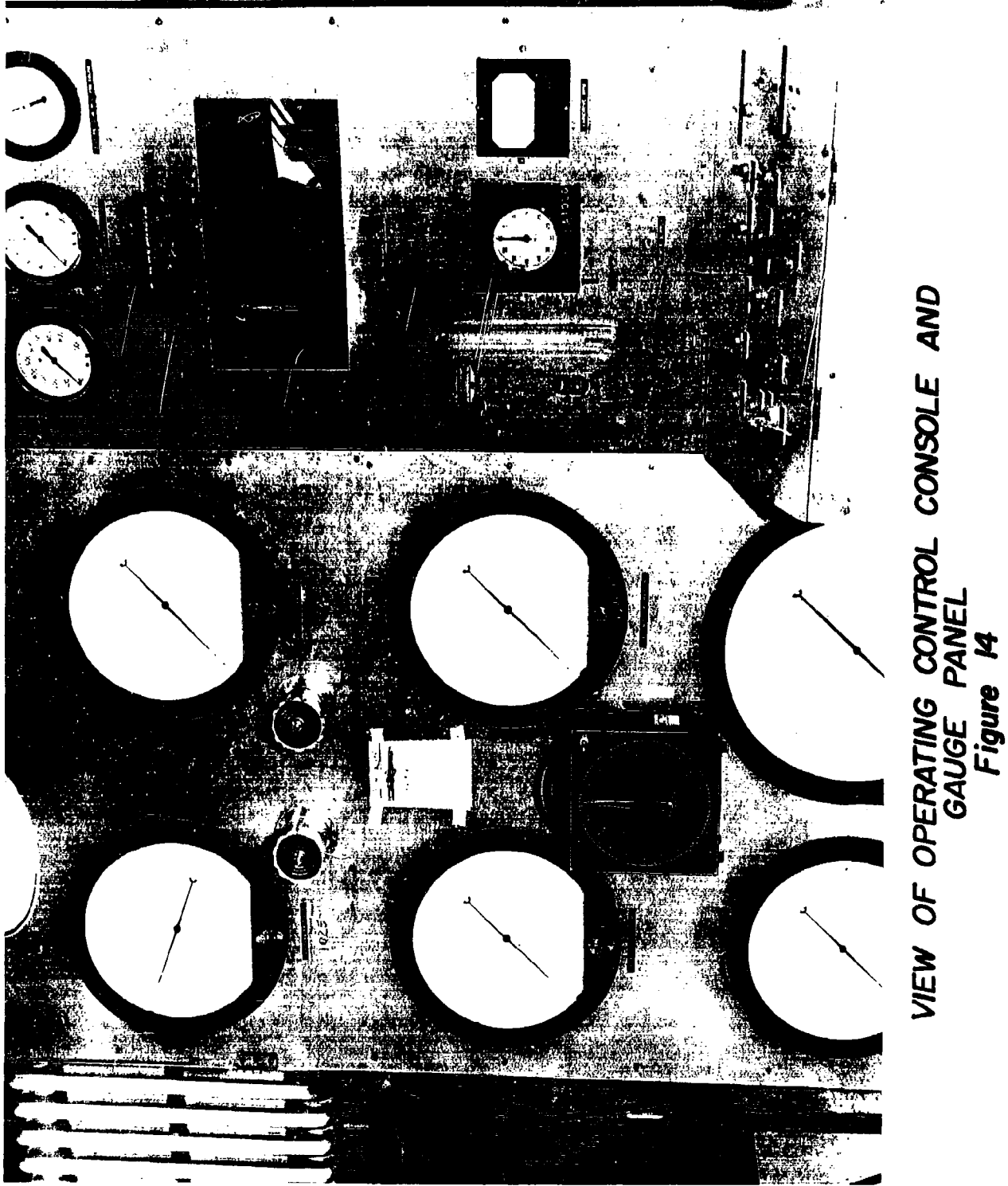


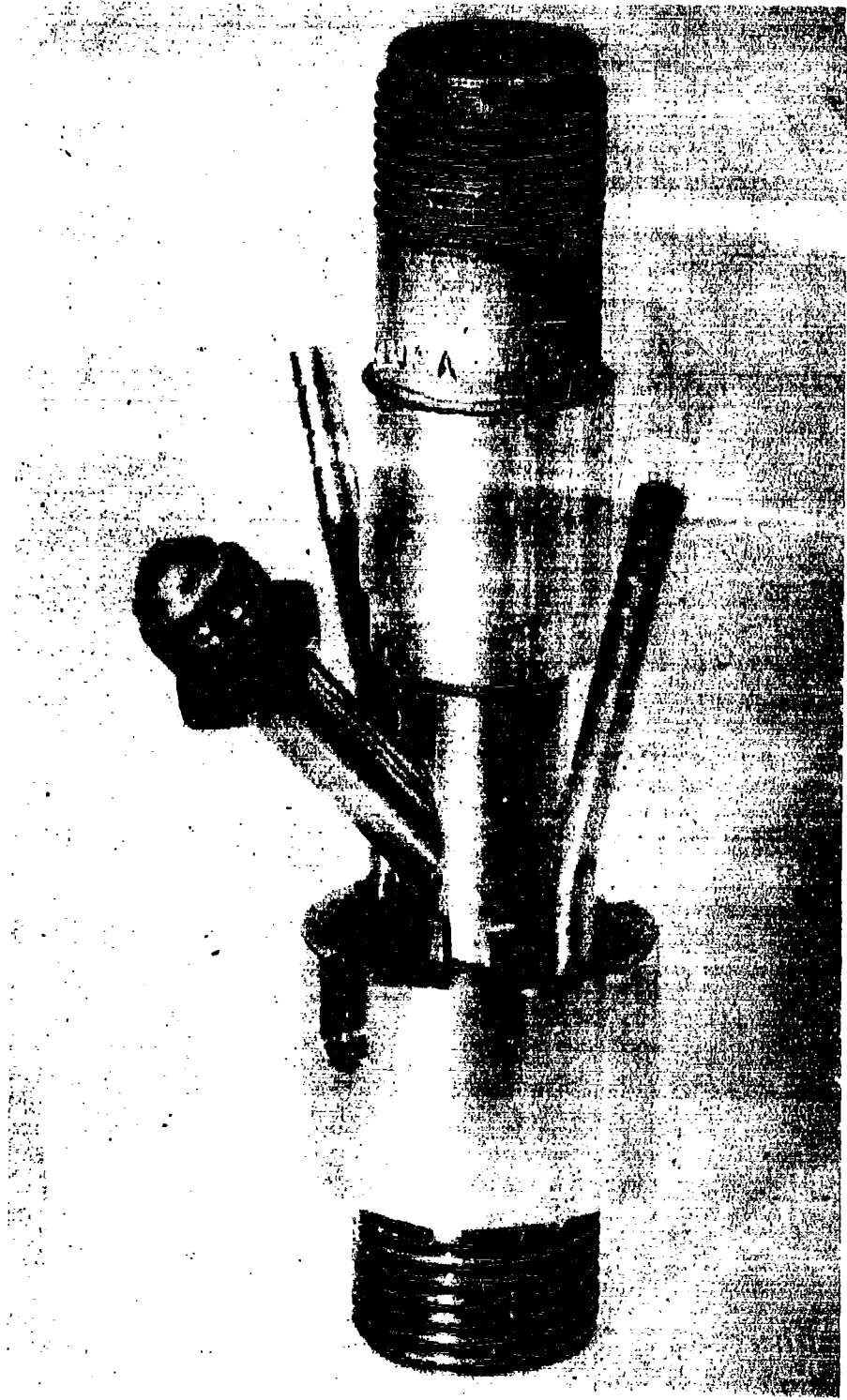
FIGURE 12  
SCHEMATIC: BIPORELLANT FEED SYSTEM





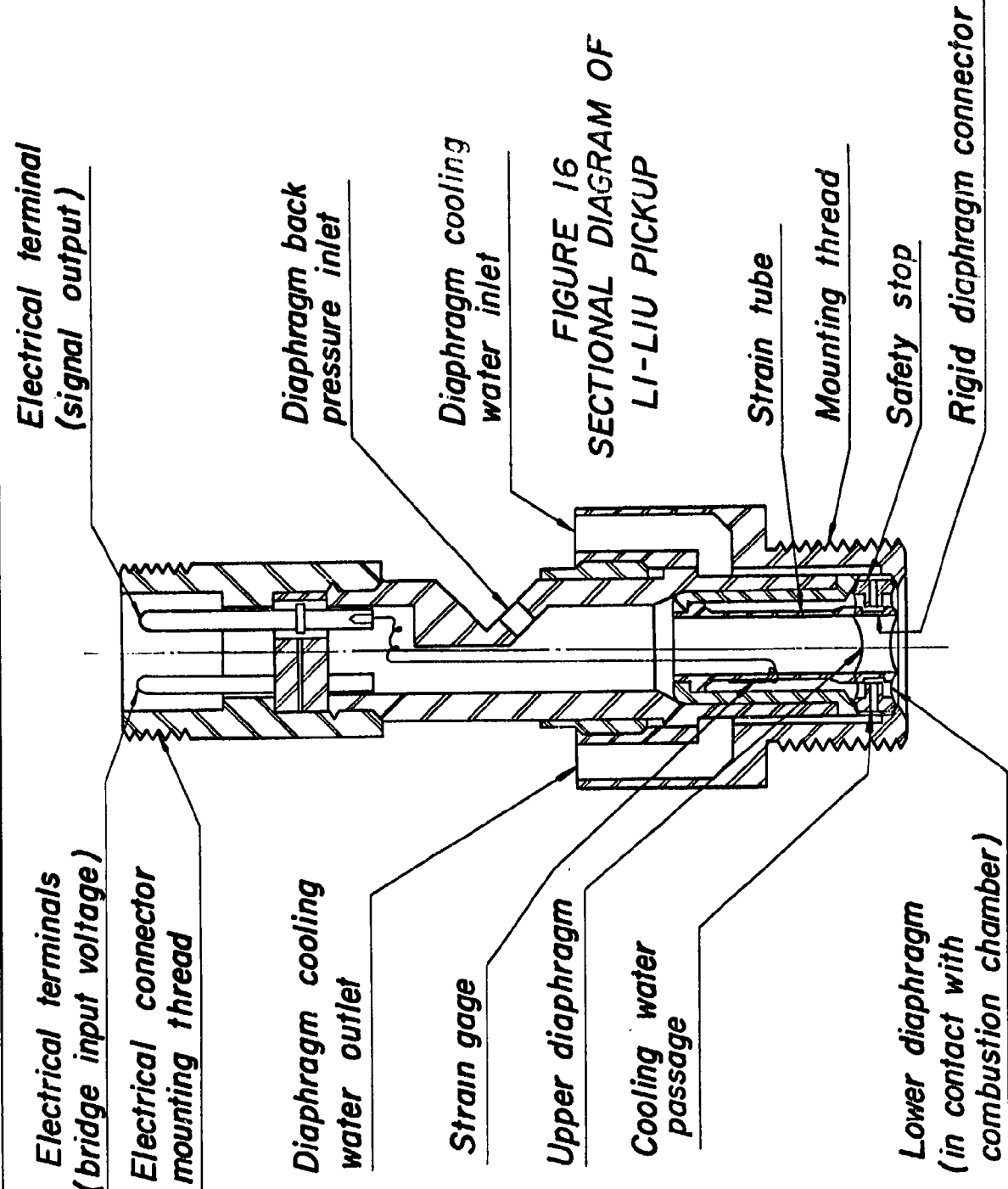
**VIEW OF OPERATING CONTROL CONSOLE AND  
GAUGE PANEL**

**Figure 14**



**EXTERIOR VIEW OF LI-LIU DIFFERENTIAL  
PRESSURE PICKUP**

*Figure 15*



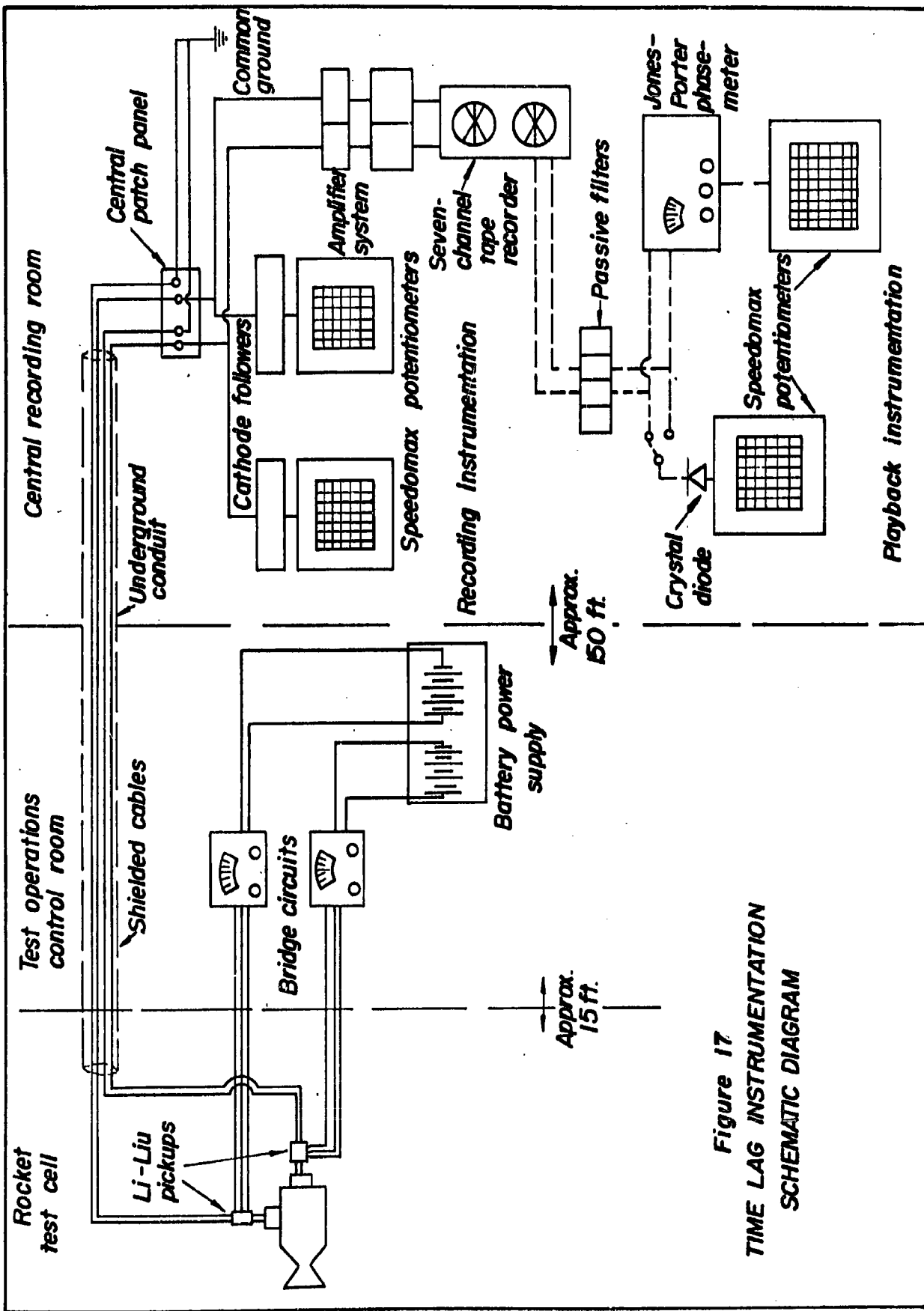
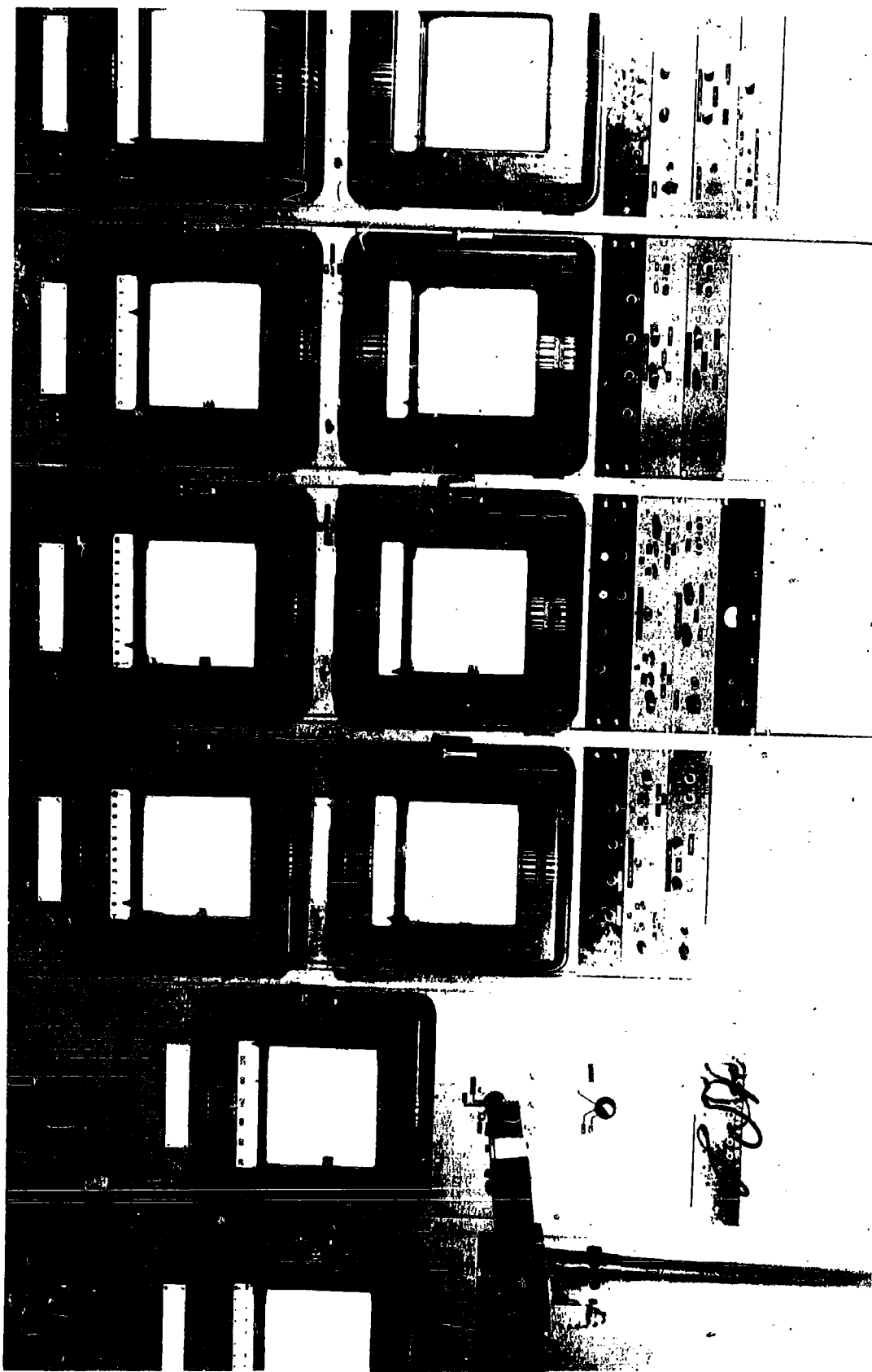


**Figure 17**  
**TIME LAG INSTRUMENTATION**  
**SCHEMATIC DIAGRAM**

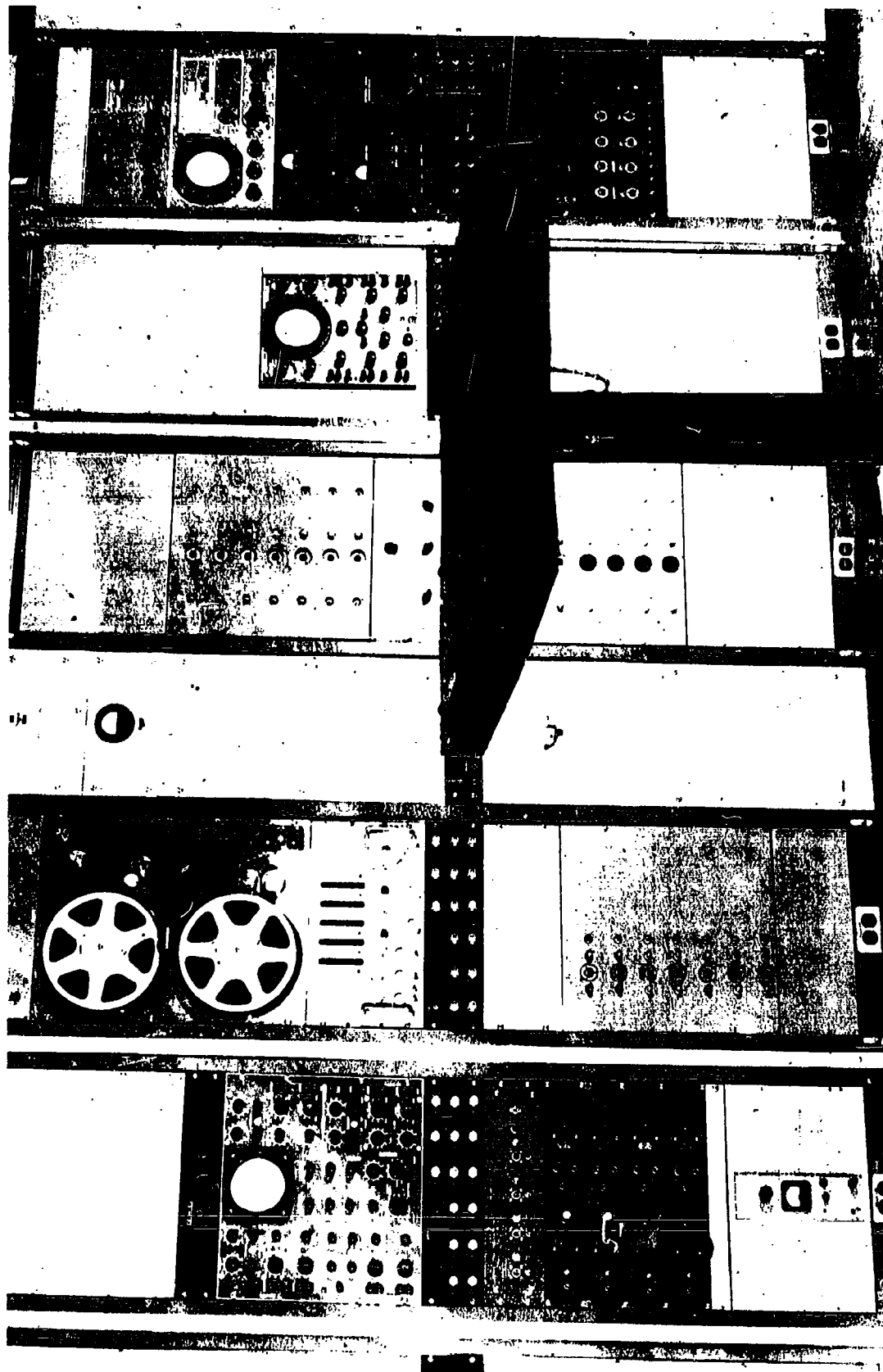
**STEADY STATE RECORDING INSTRUMENTATION**

**Figure 18**

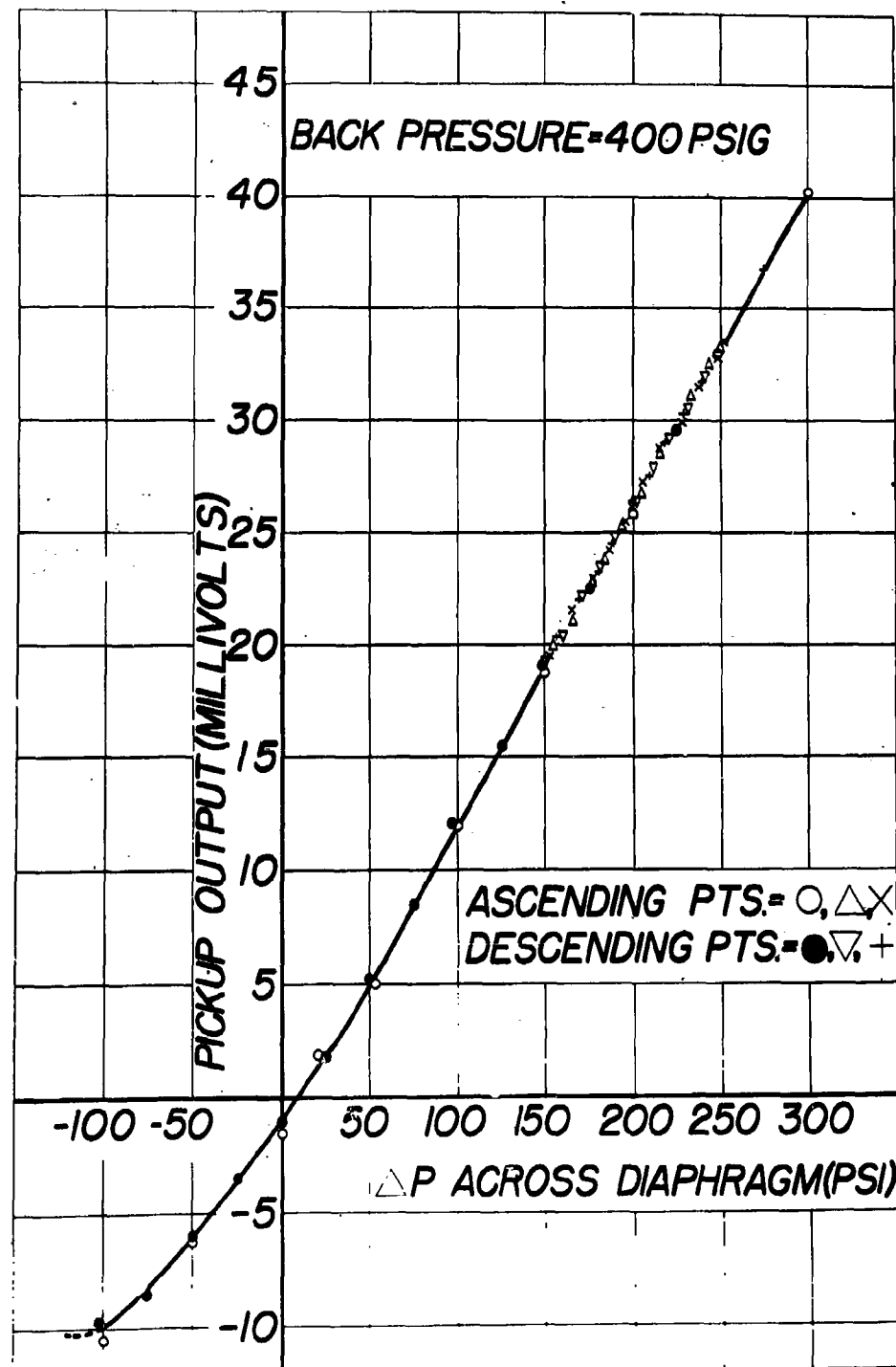


## **TRANSIENT RECORDING INSTRUMENTATION**

**Figure 19**



CYCLING HYSTERESIS CHECK OF LI-LIU  
DIFFERENTIAL PRESSURE PICKUP NO. 12



CYCLING HYSTERESIS CHECK OF LI-LIU  
DIFFERENTIAL PRESSURE PICKUP NO.12

Figure 20

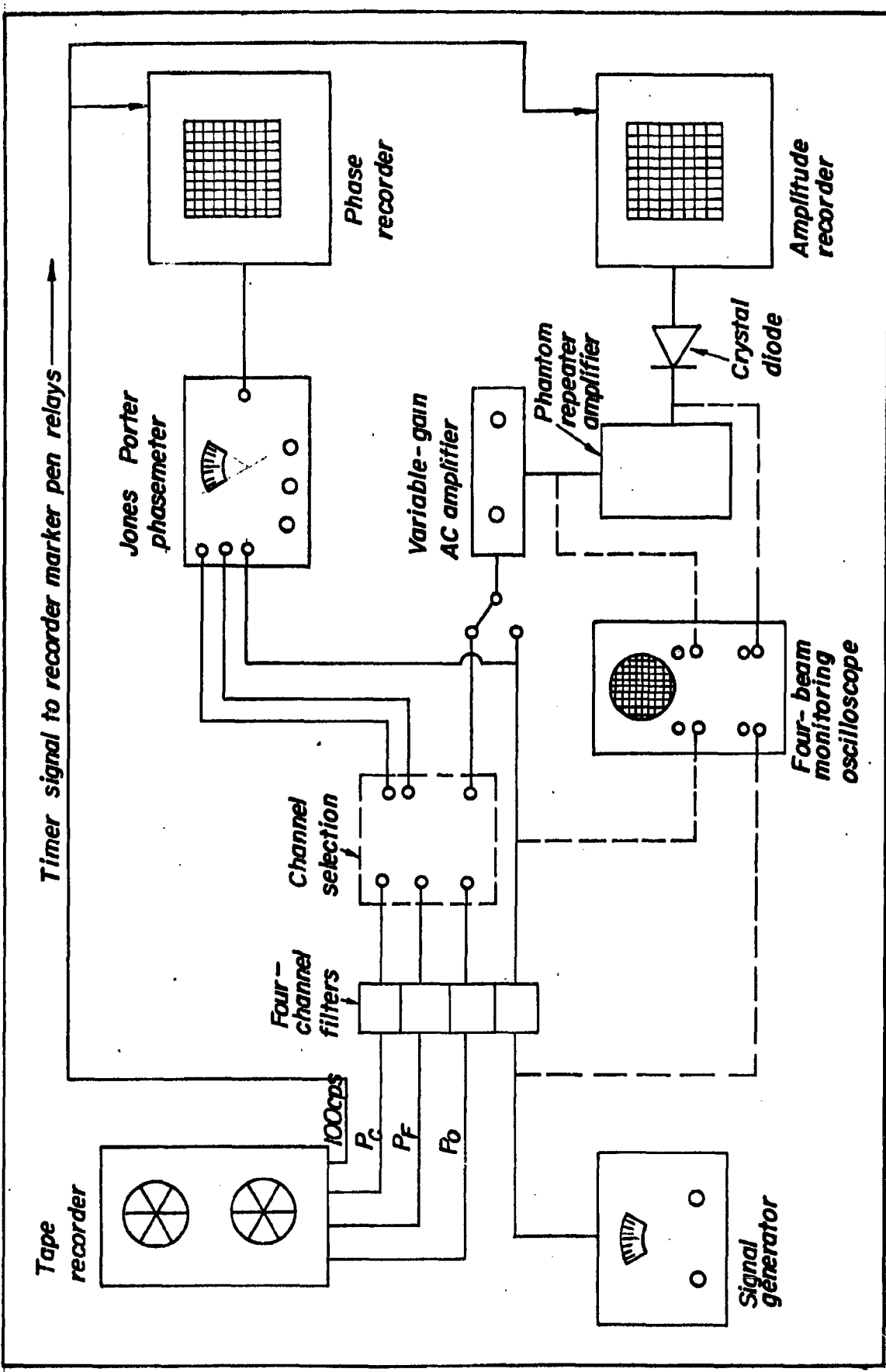


**Figure 21**  
TRANSIENT PLAYBACK INSTRUMENTATION DIAGRAM

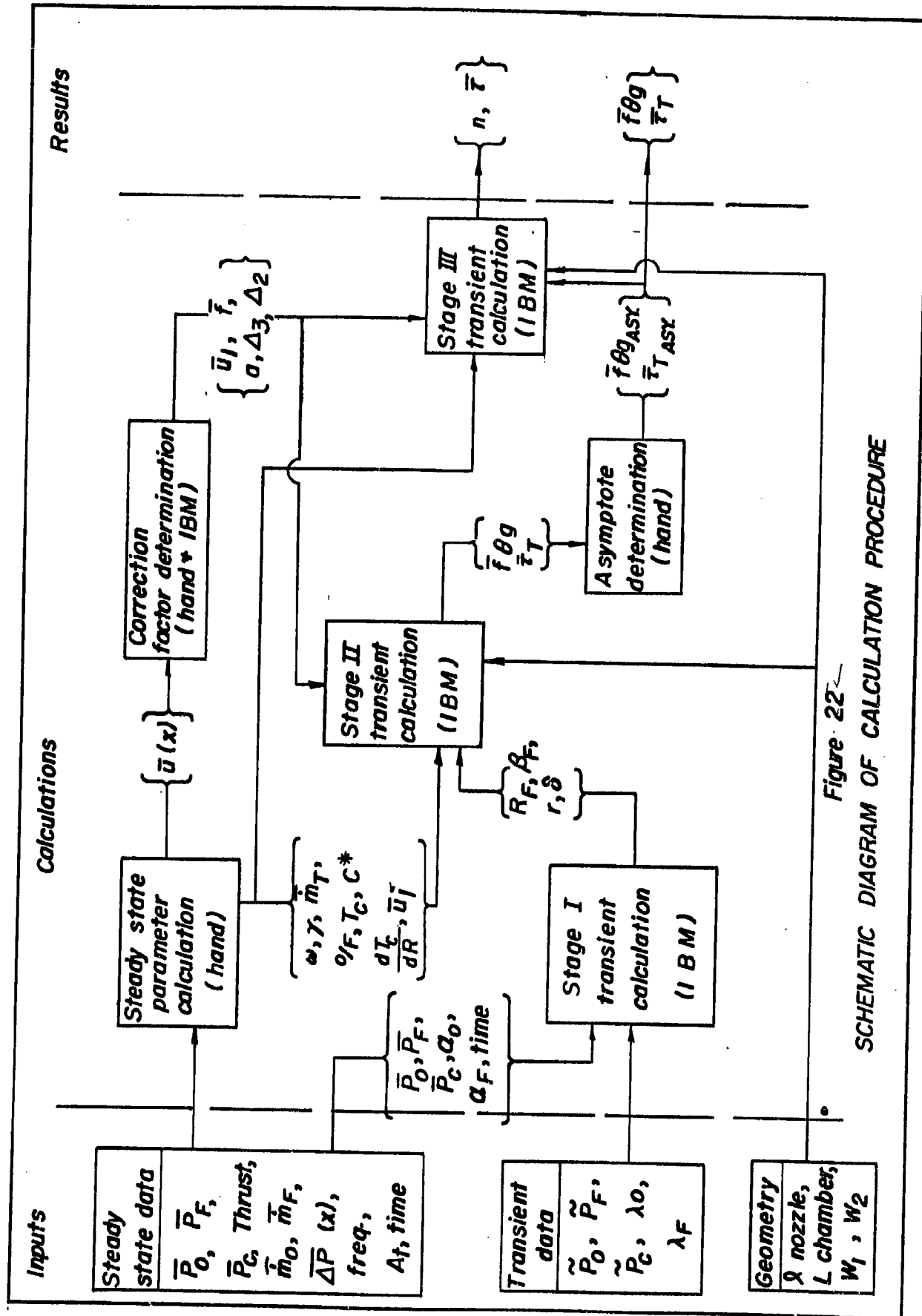
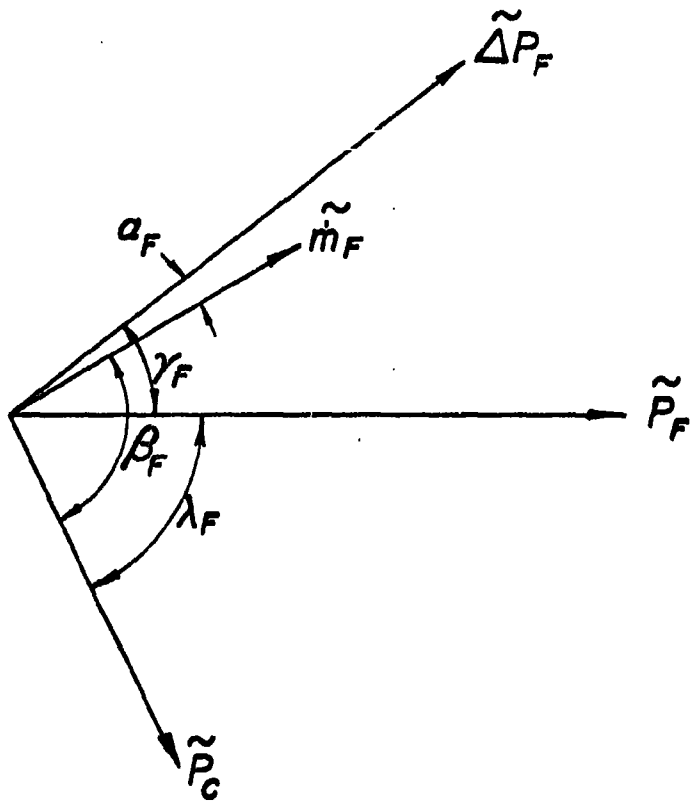


*Figure 22—*  
**SCHEMATIC DIAGRAM OF CALCULATION PROCEDURE**



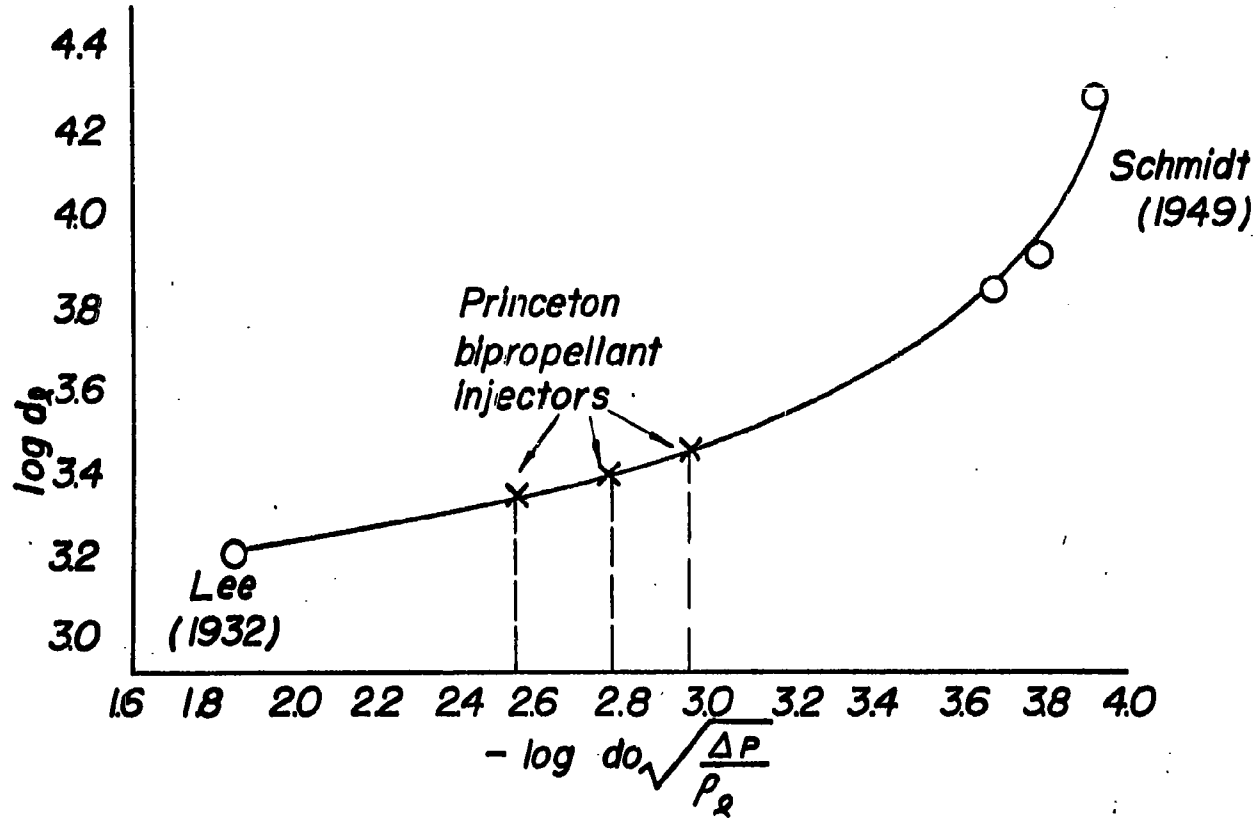
$\tilde{P}_F$  = fuel injector pressure

$\tilde{P}_C$  = chamber pressure

$\tilde{m}_F$  = fuel flow rate

$\tilde{\Delta P}_F$  = fuel injector pressure drop

Figure 23.  
RELATIONSHIPS OF OSCILLATING QUANTITIES  
(BASED ON FUEL)



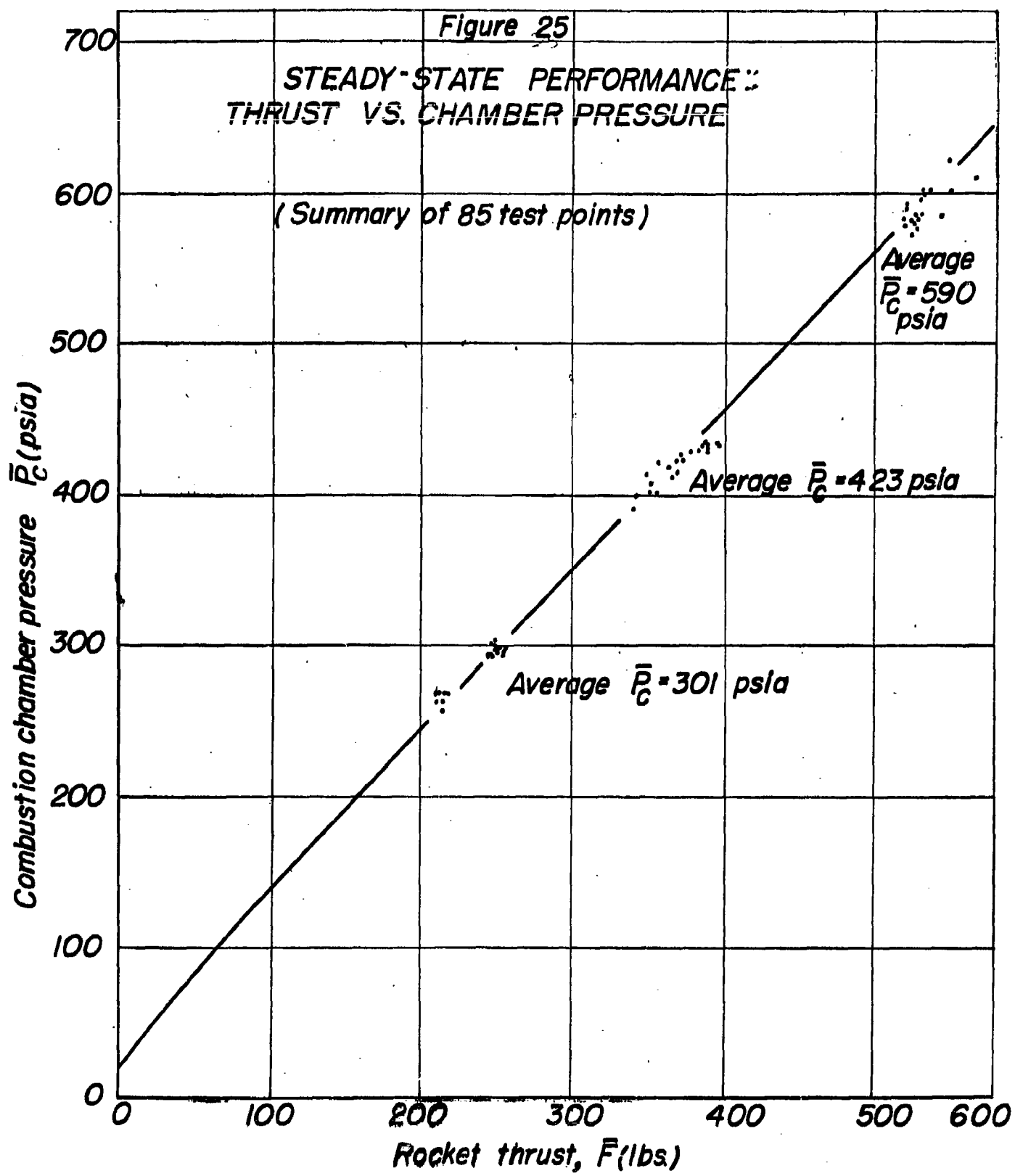
$d_x$  = droplet diameter (microns)

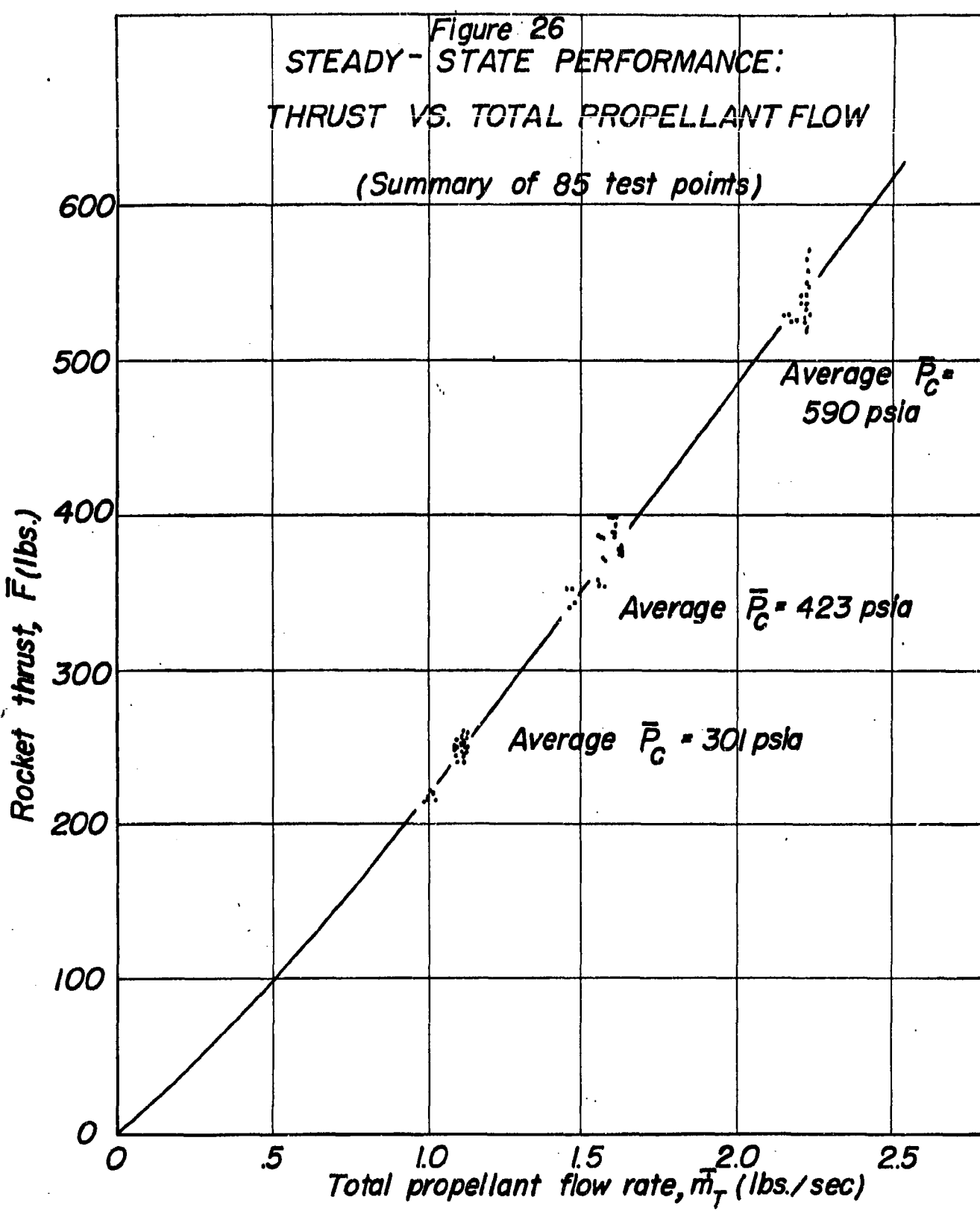
$d_0$  = injector orifice diameter (inches)

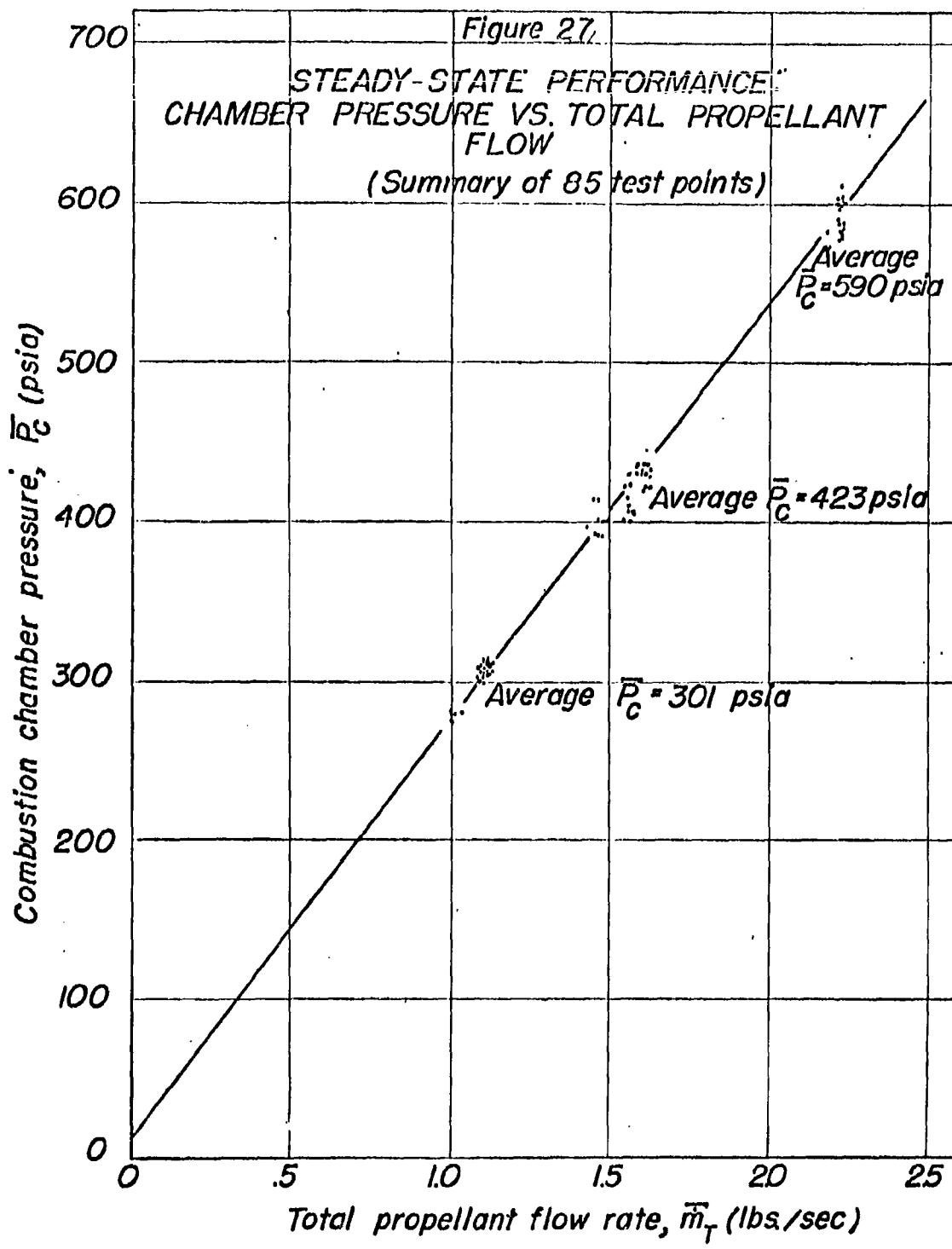
$\Delta P$  = injector pressure drop (psi)

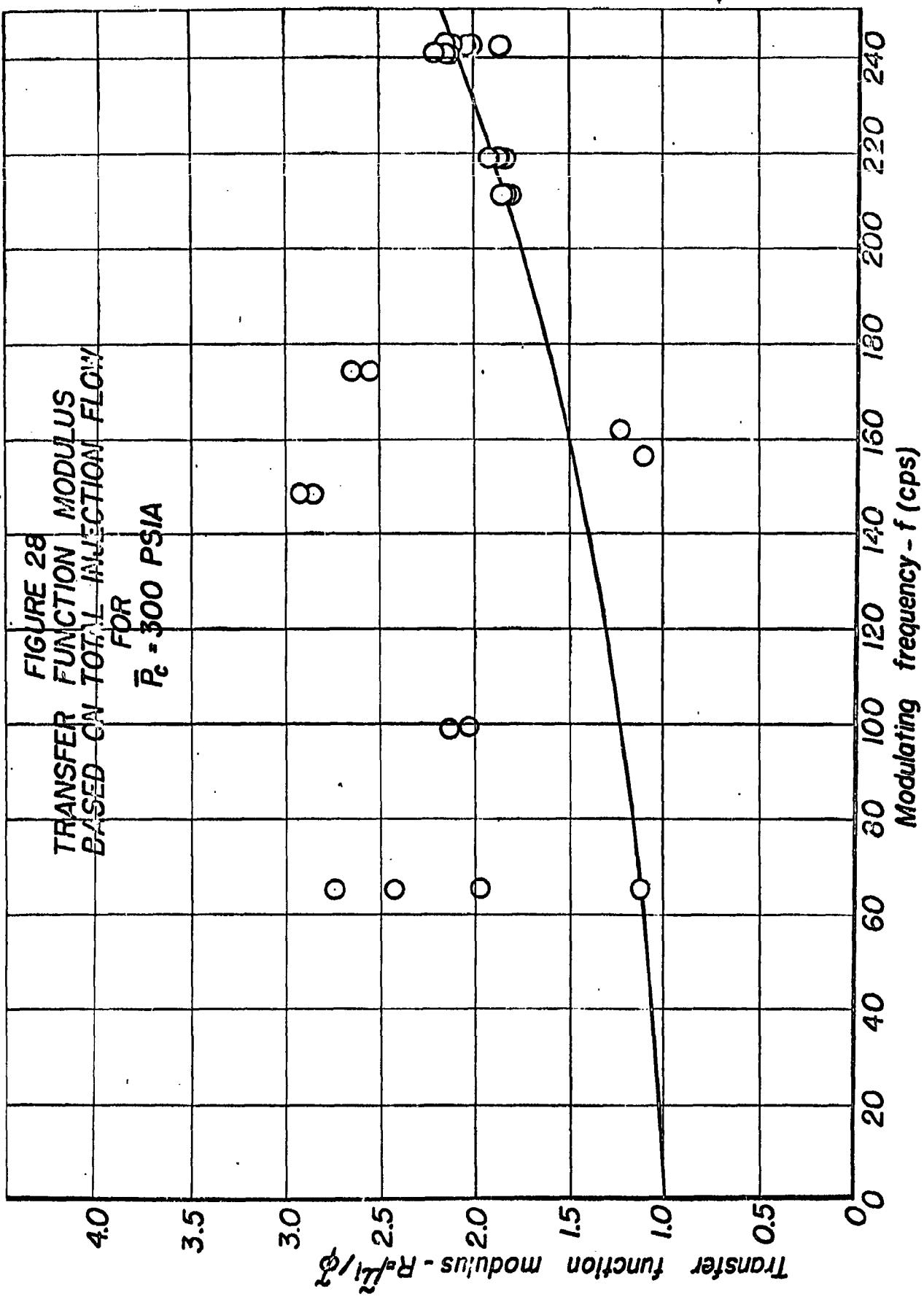
$P_L$  = liquid density (lbs. per ft.<sup>3</sup>)

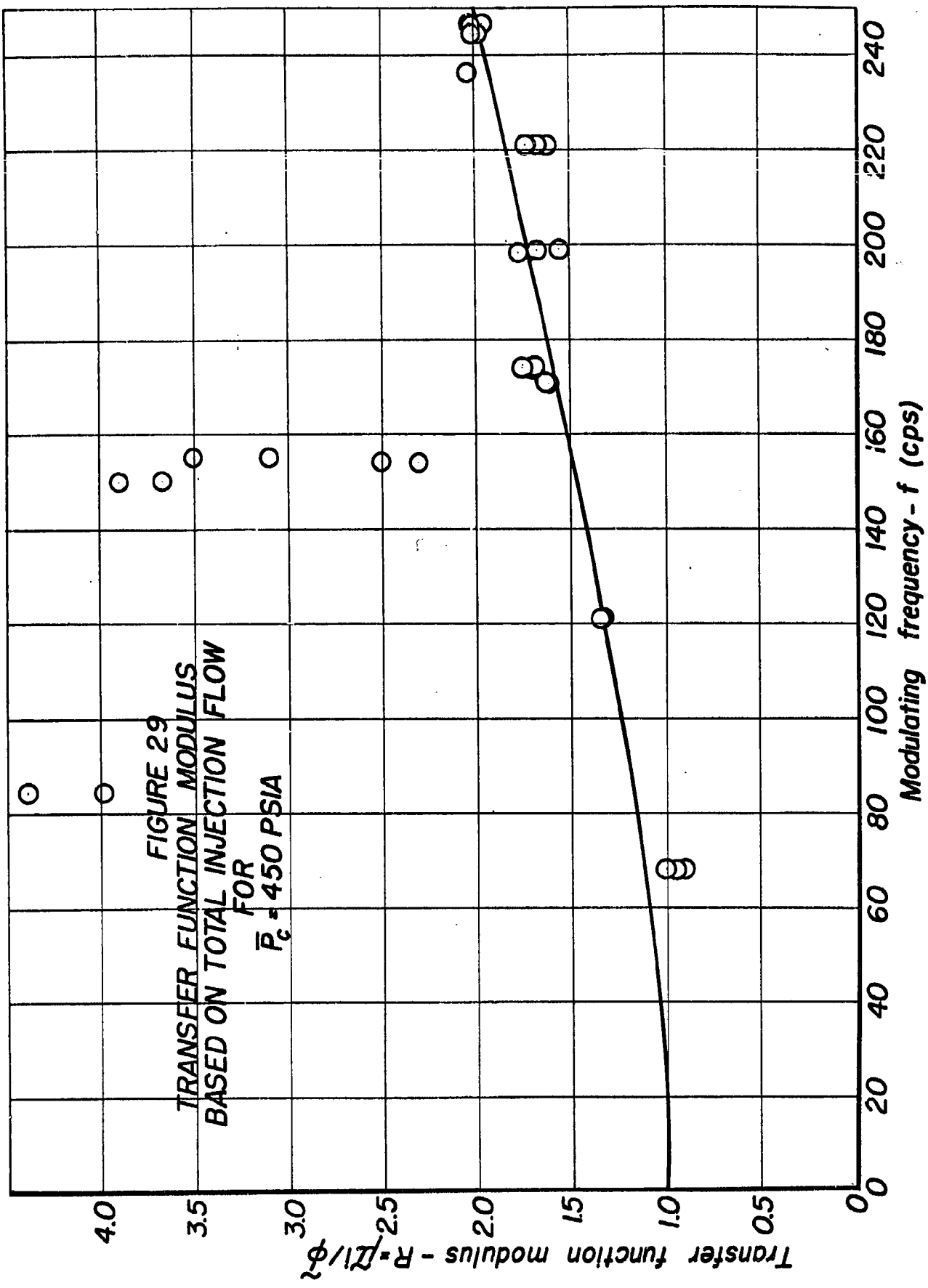
Figure 24  
CORRELATION OF  
DROPLET DIAMETER DATA

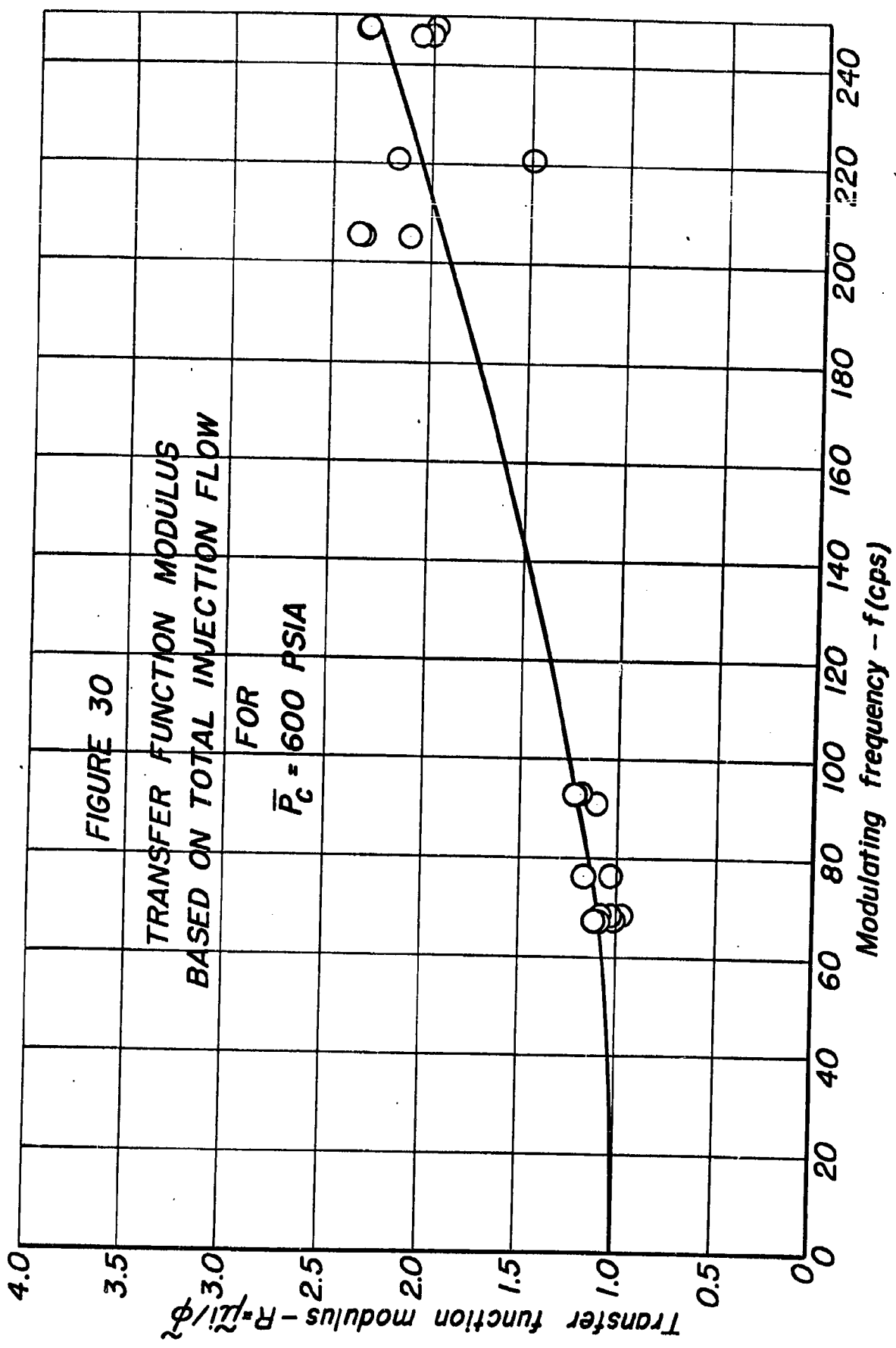


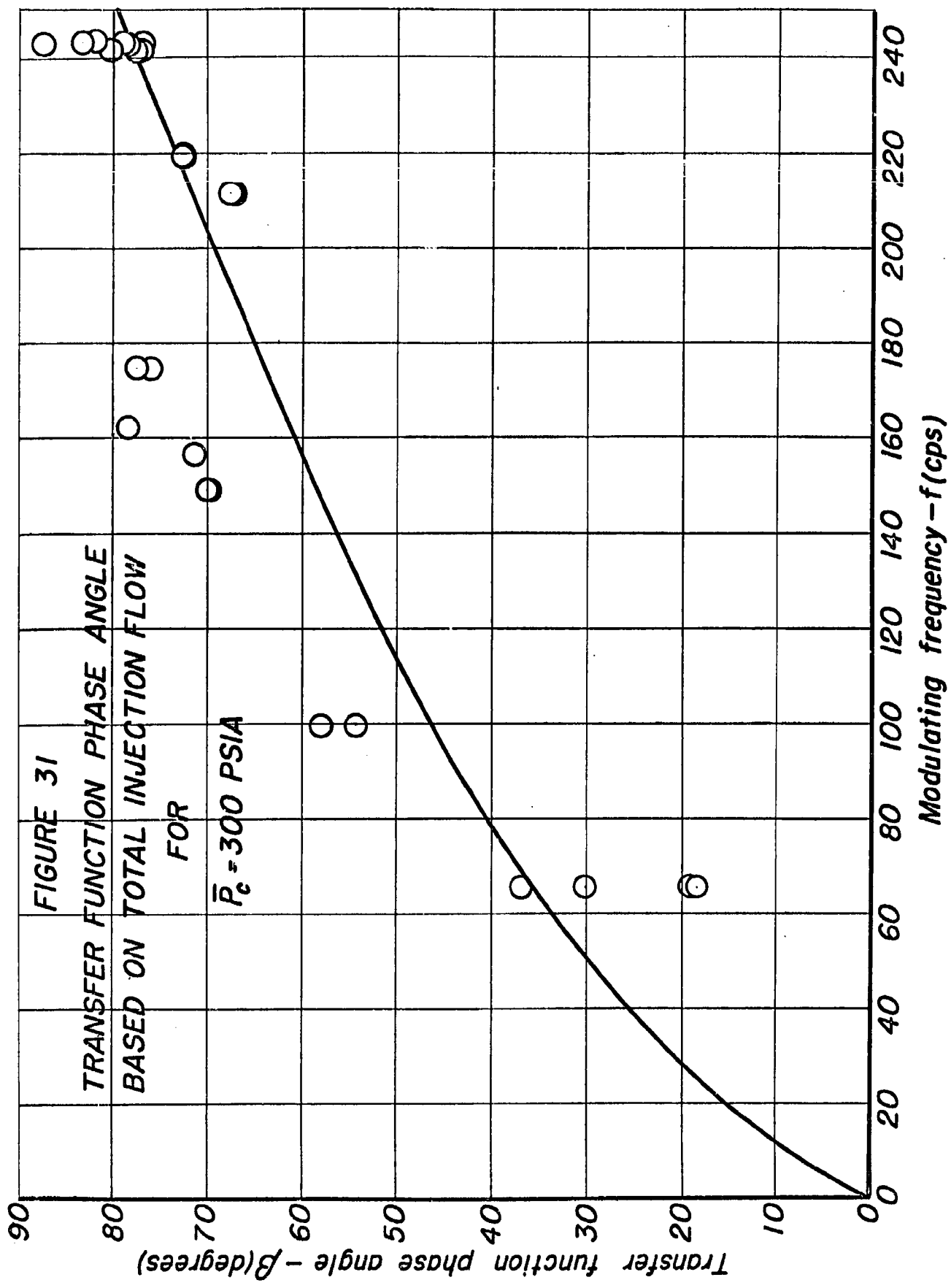


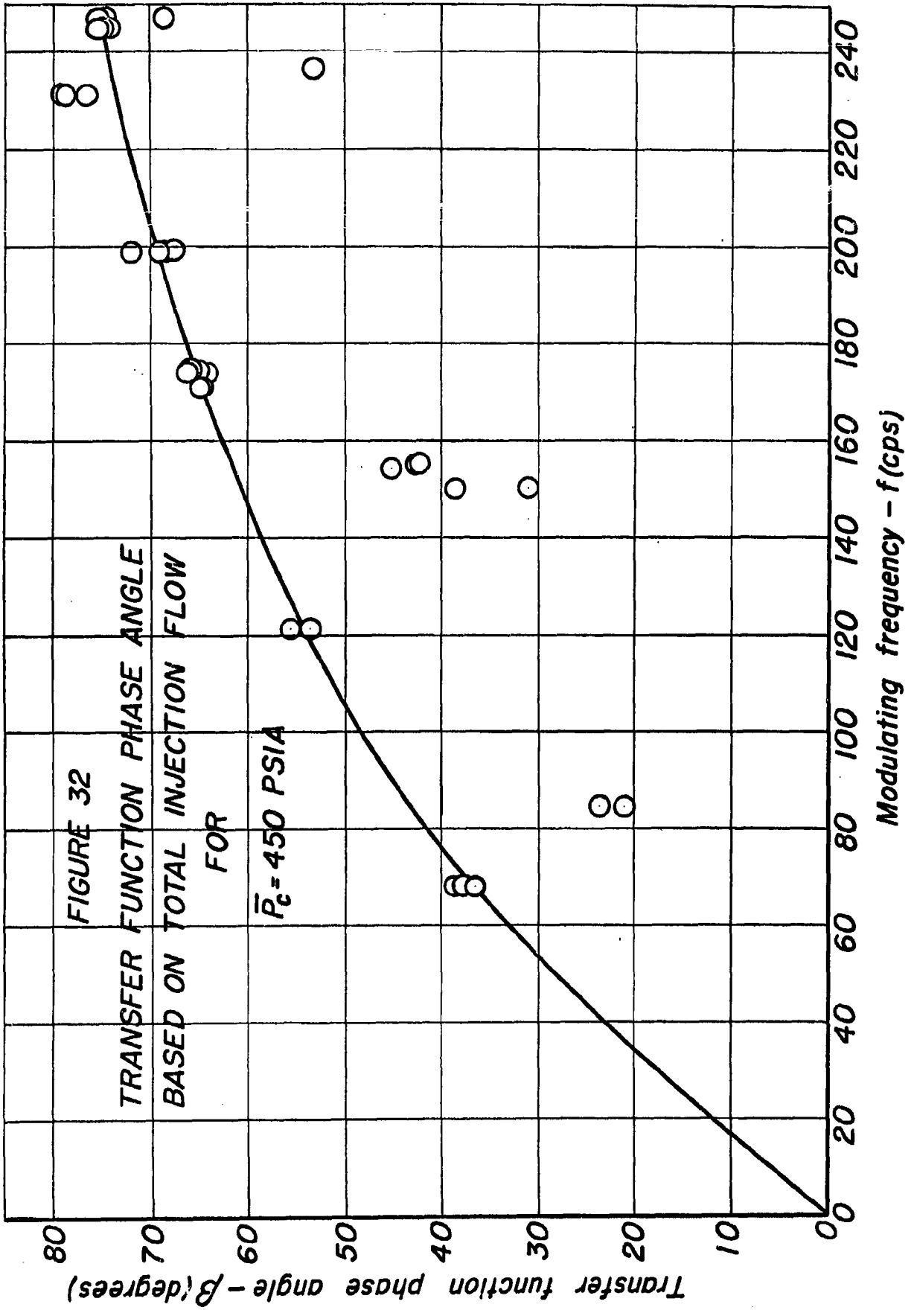


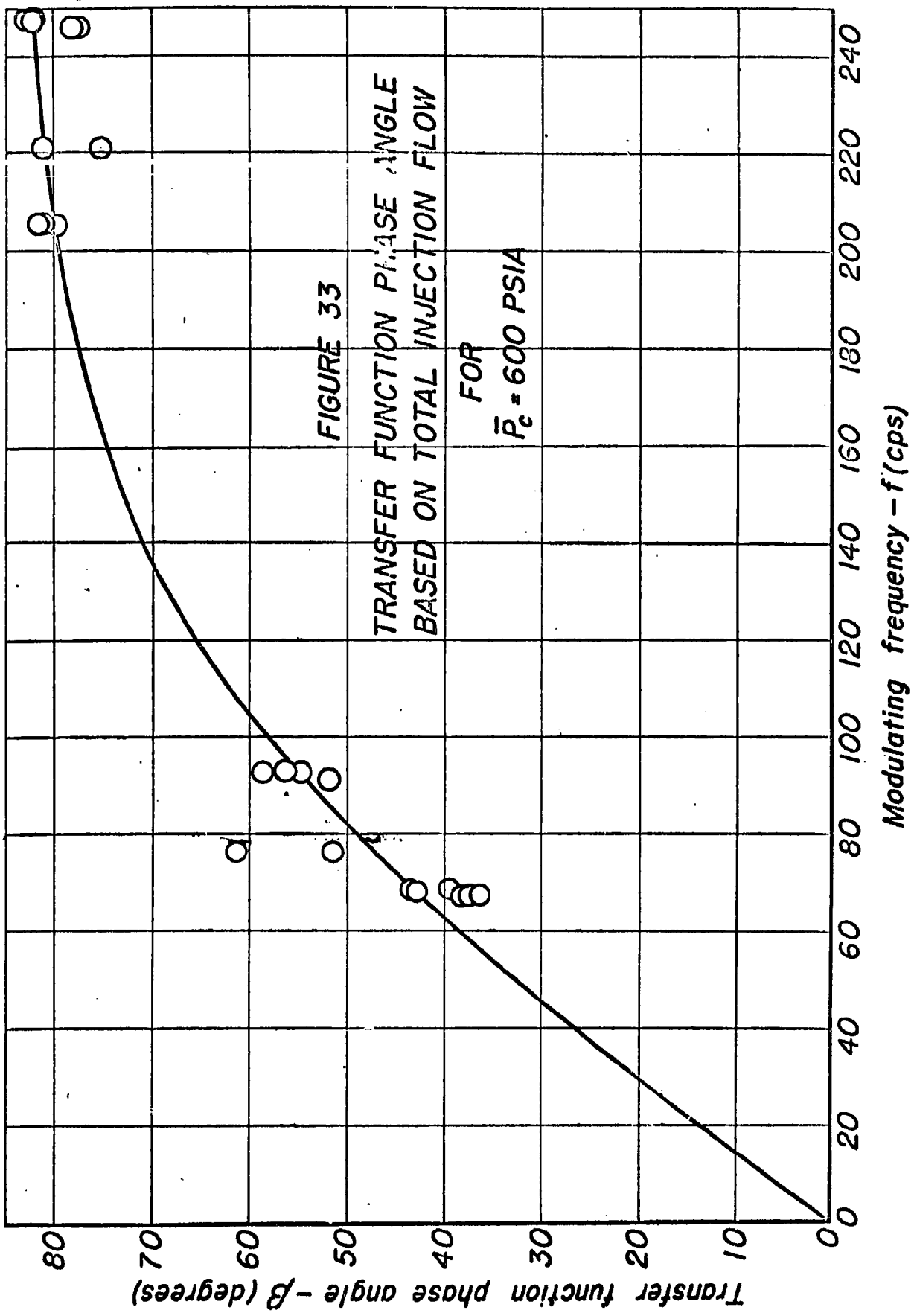




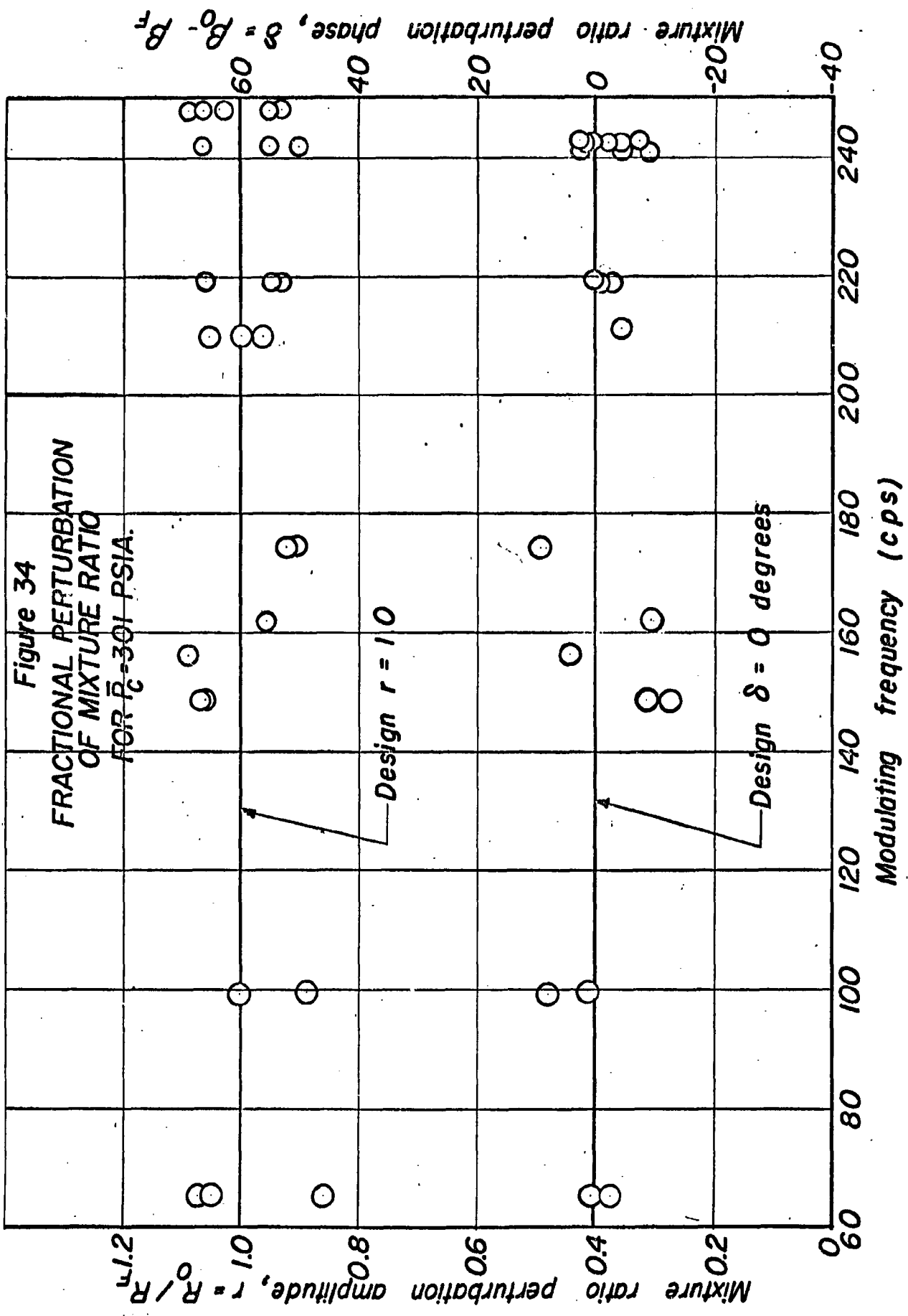


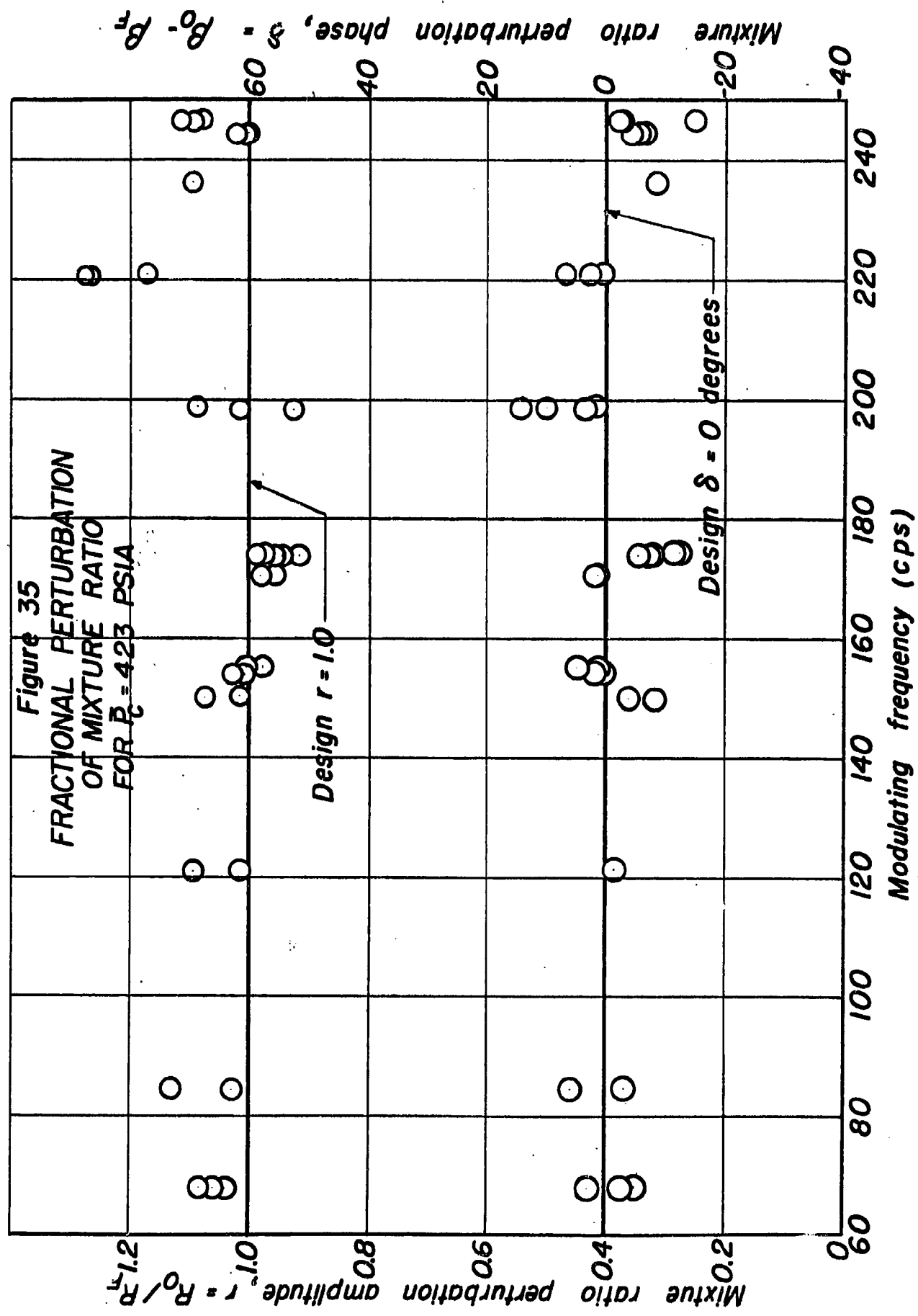


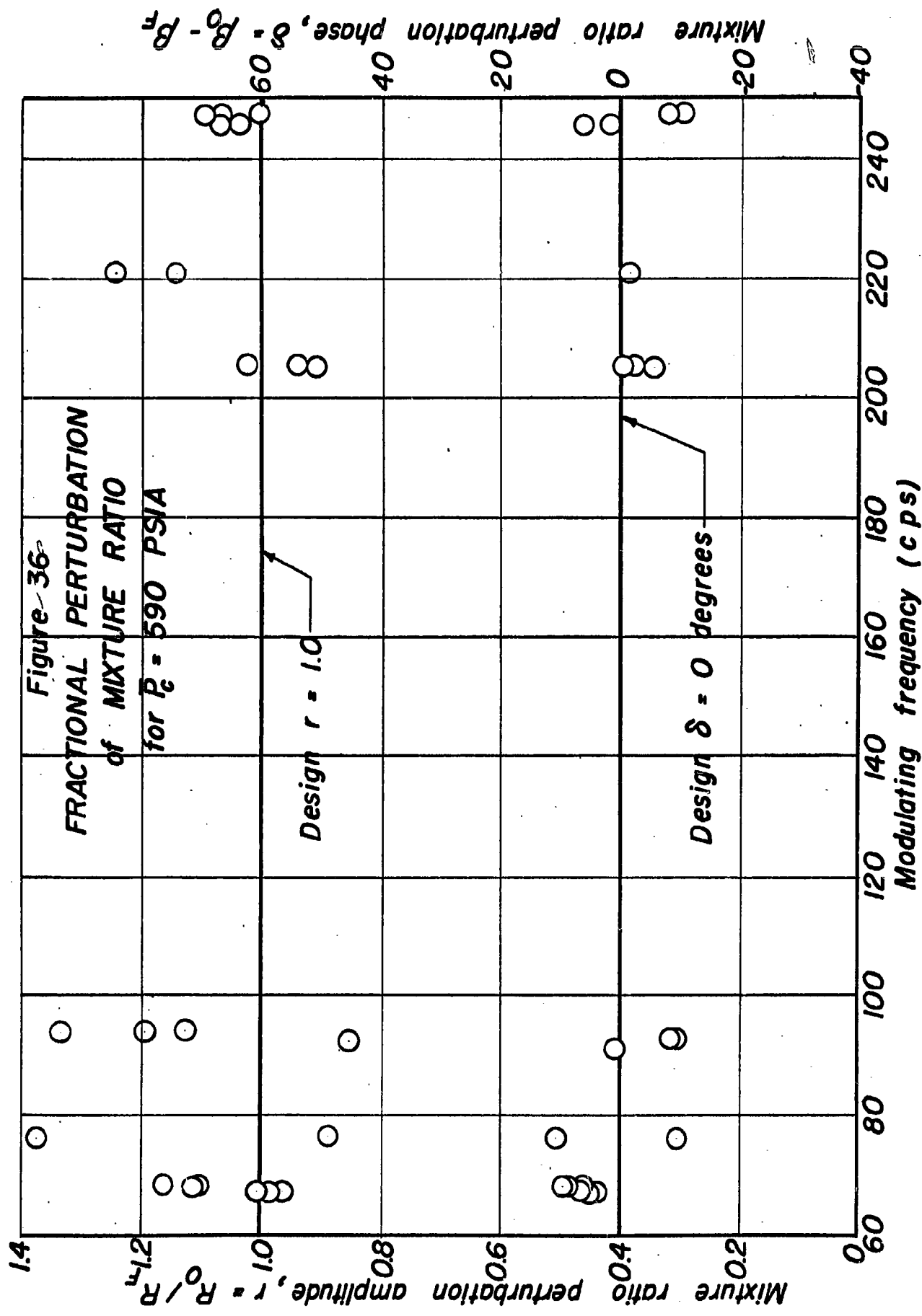


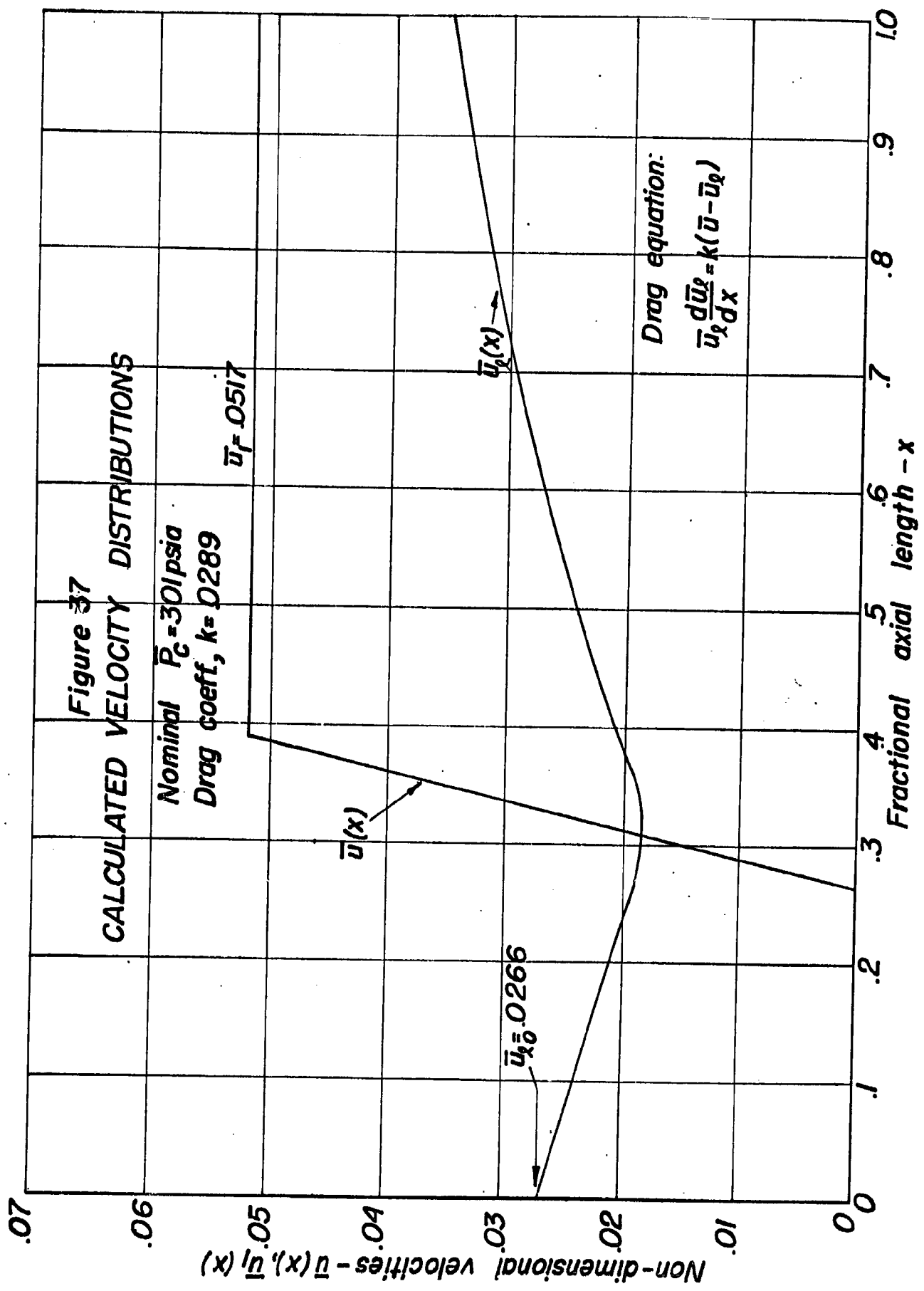


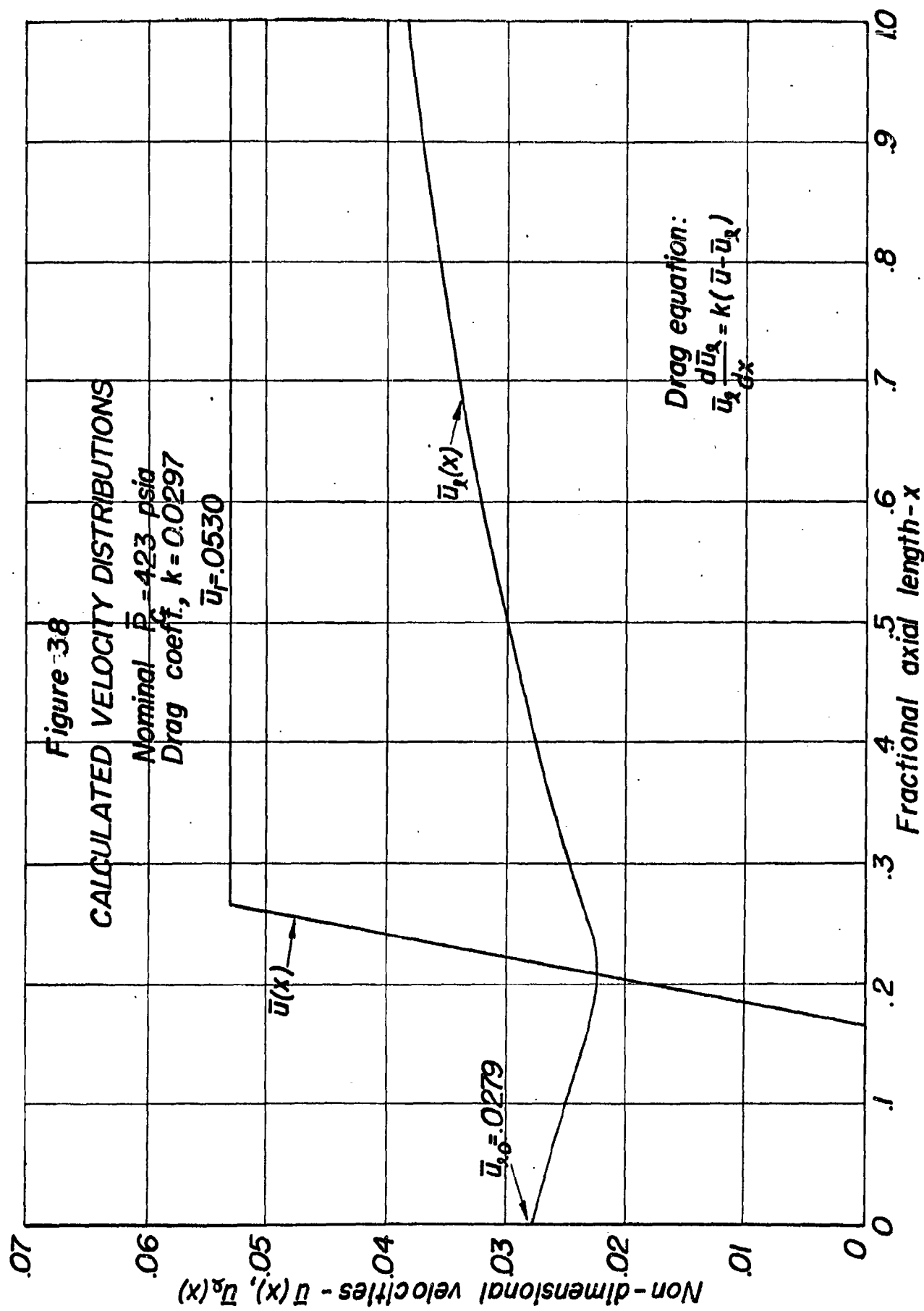
**Figure 34**  
**FRACTIONAL PERTURBATION**  
**OF MIXTURE RATIO**  
**FOR  $\bar{P}_c = 301$  PSIA.**

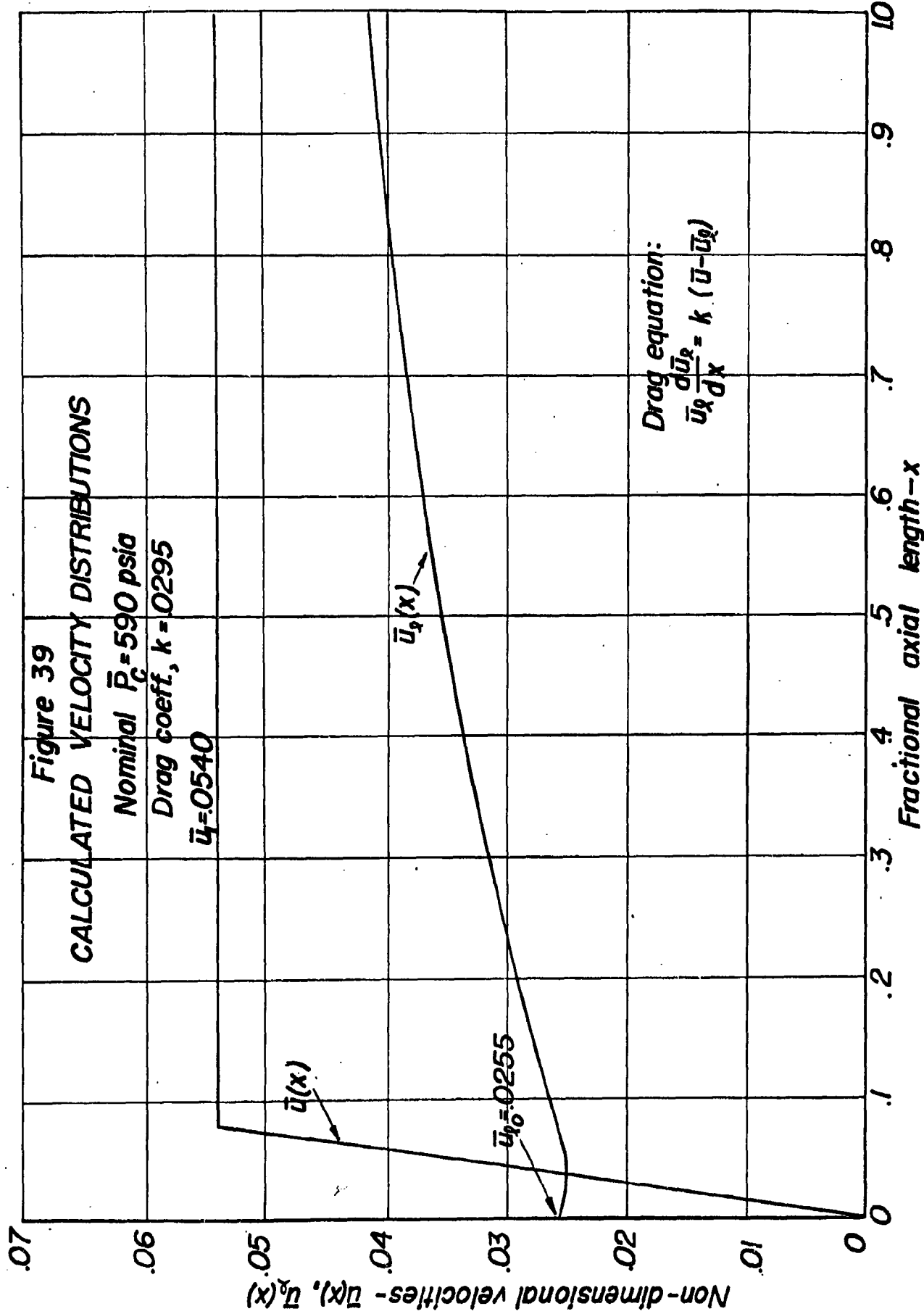


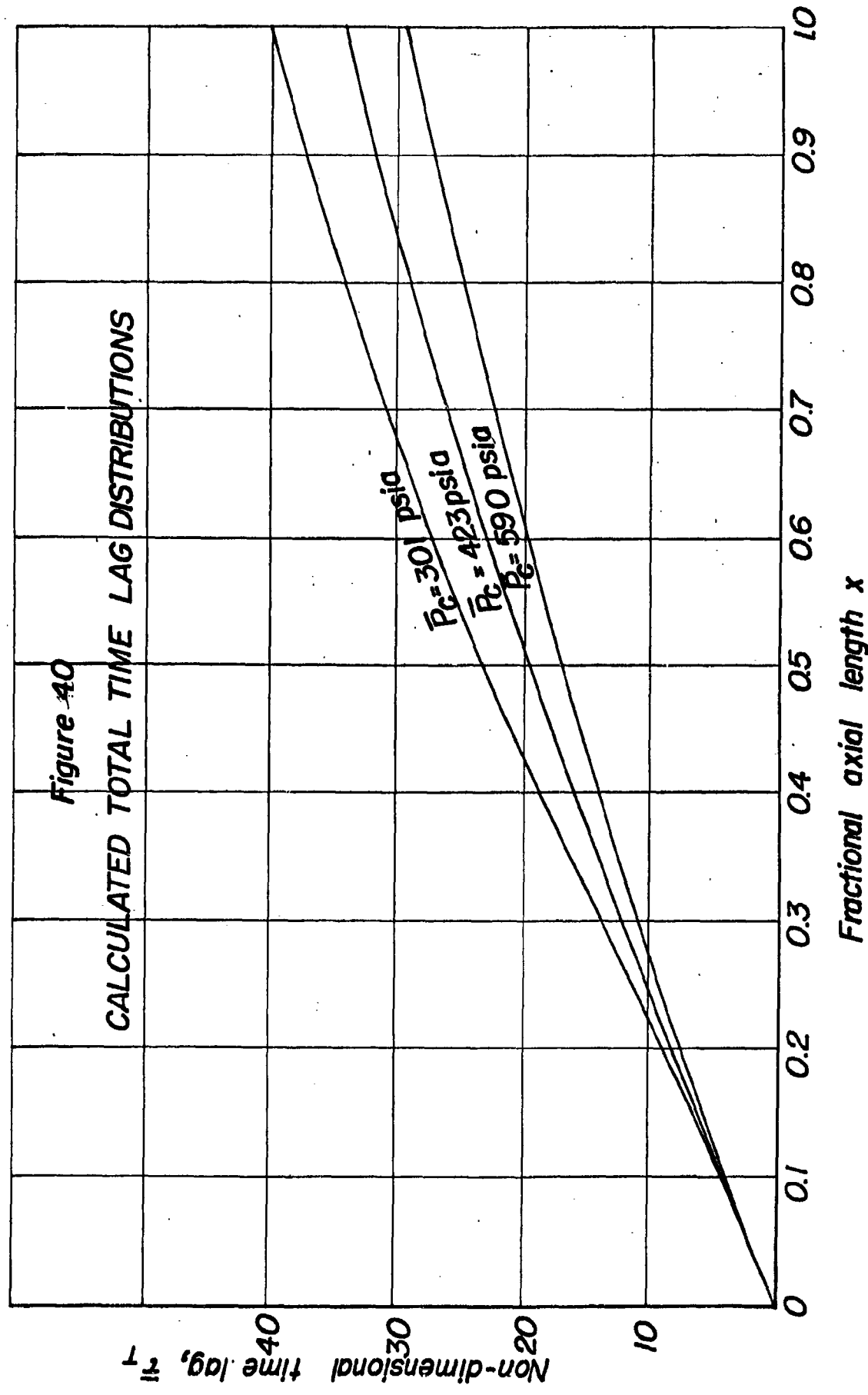


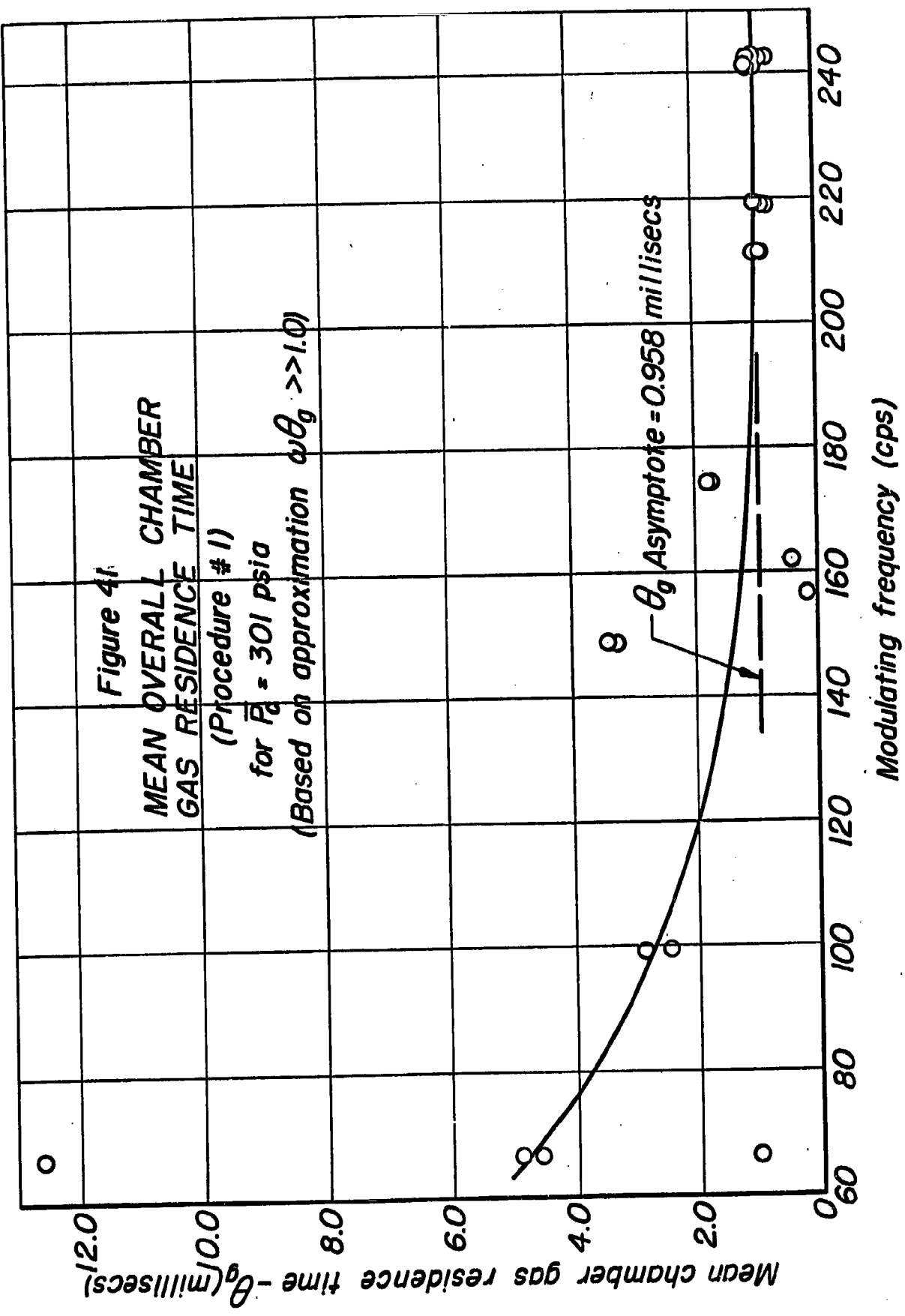


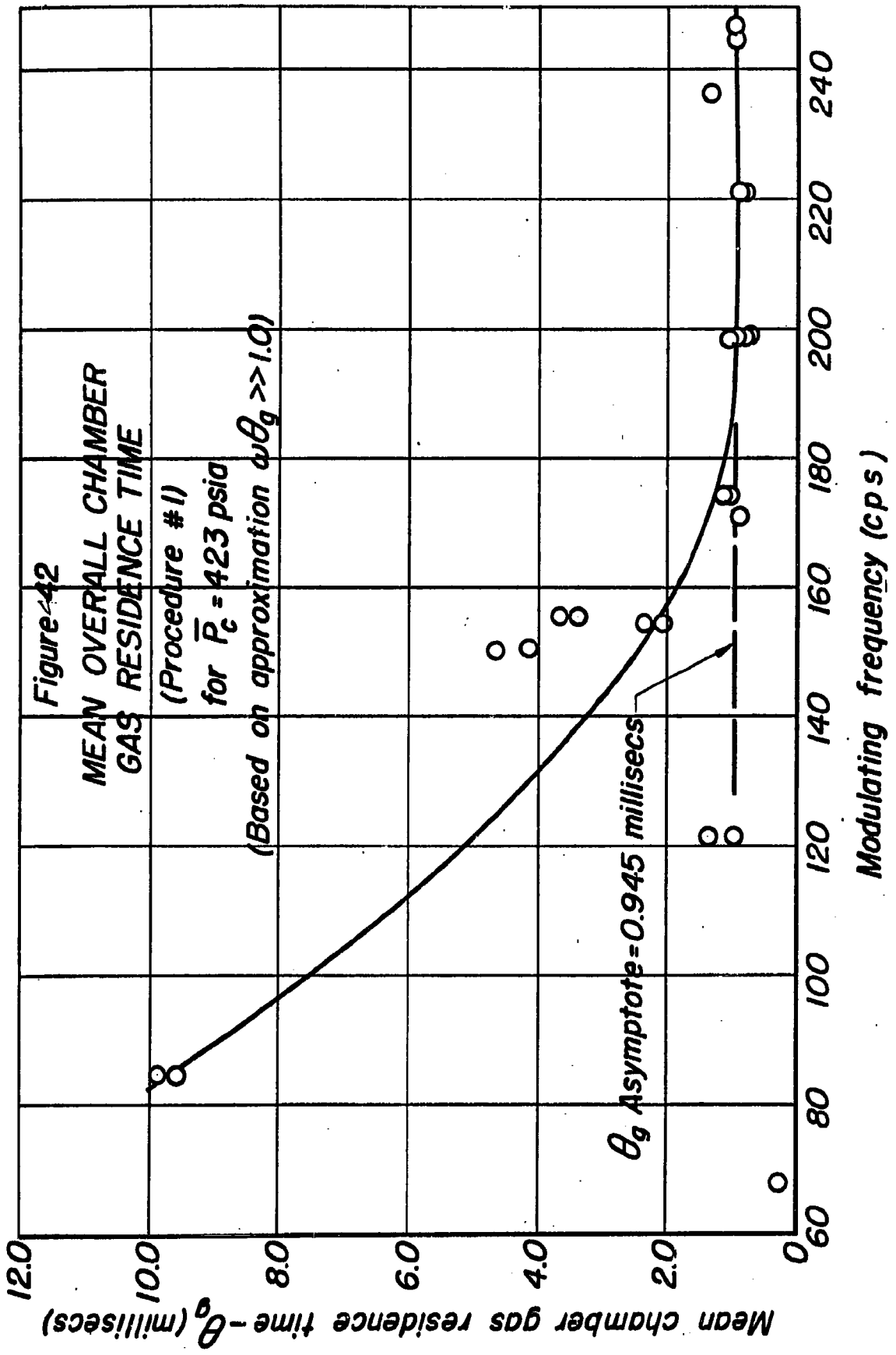


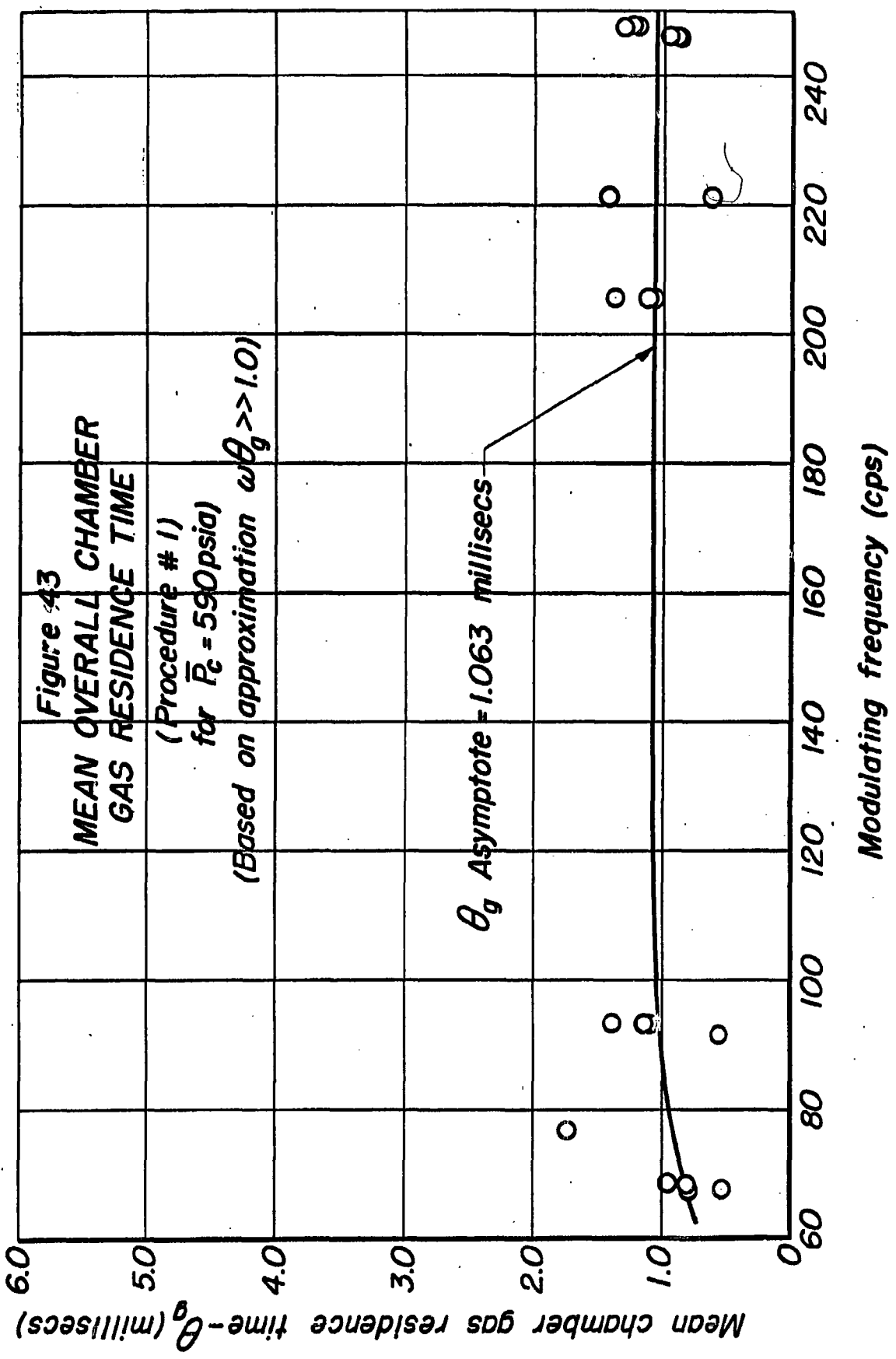


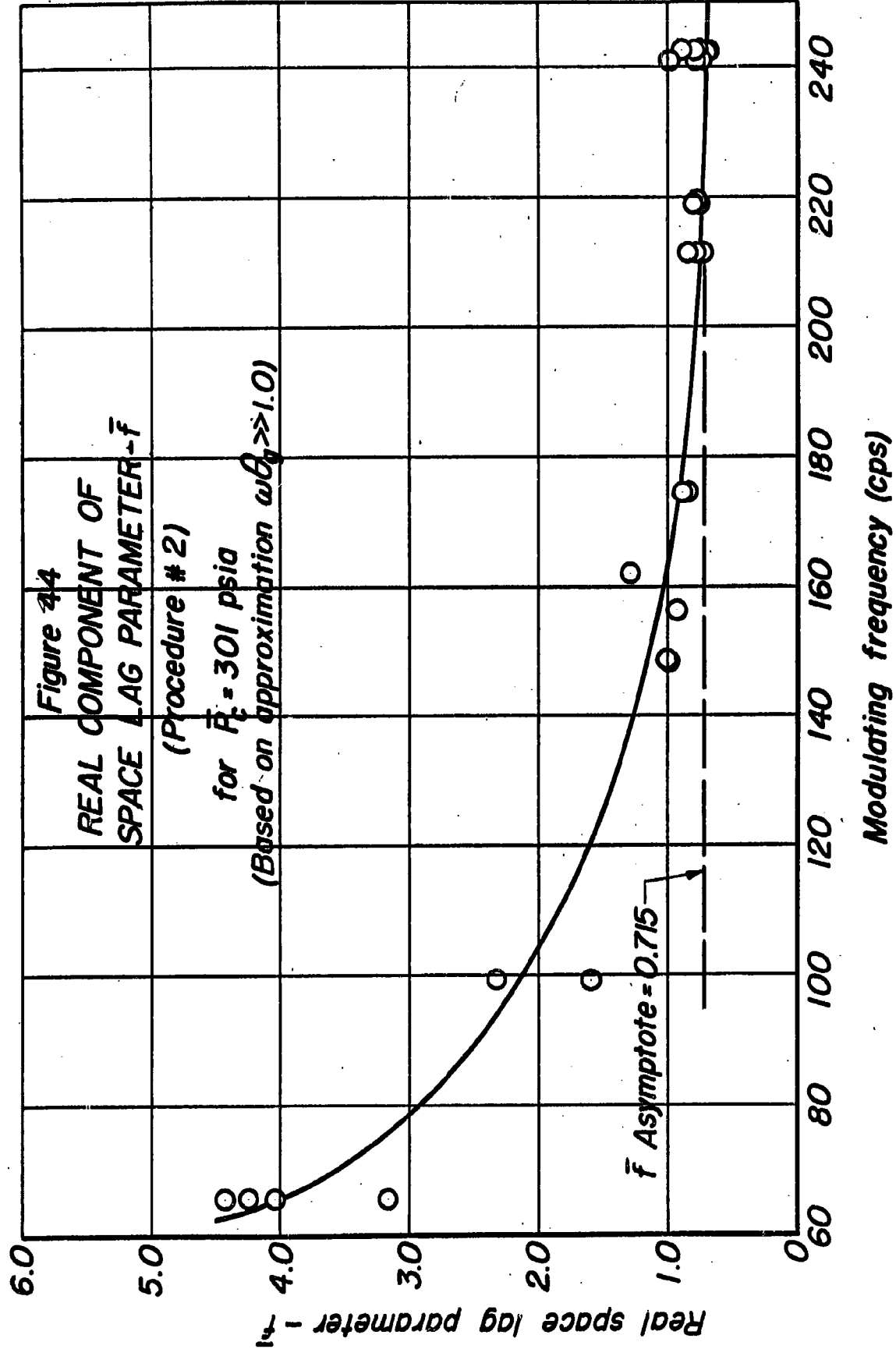


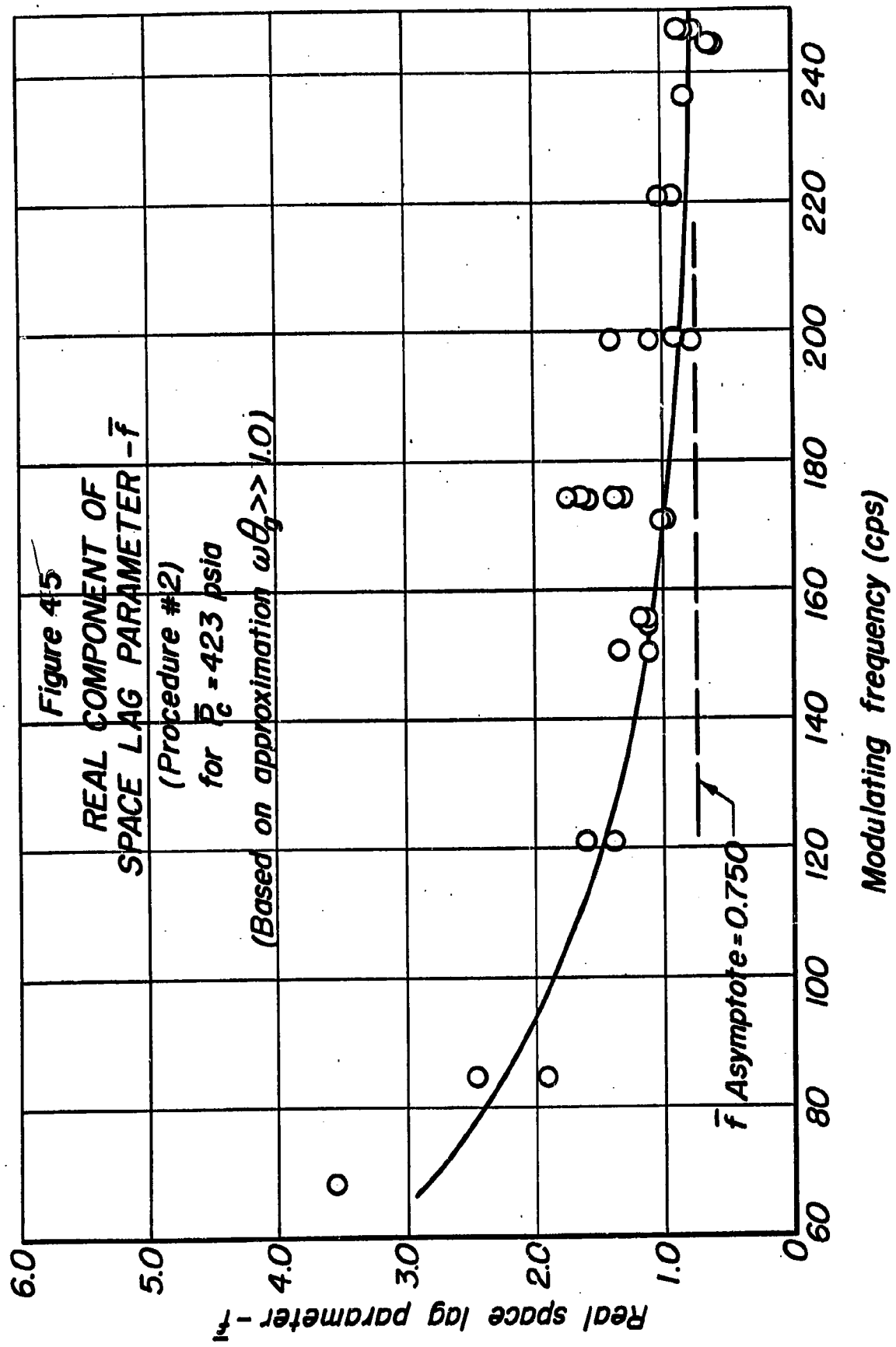


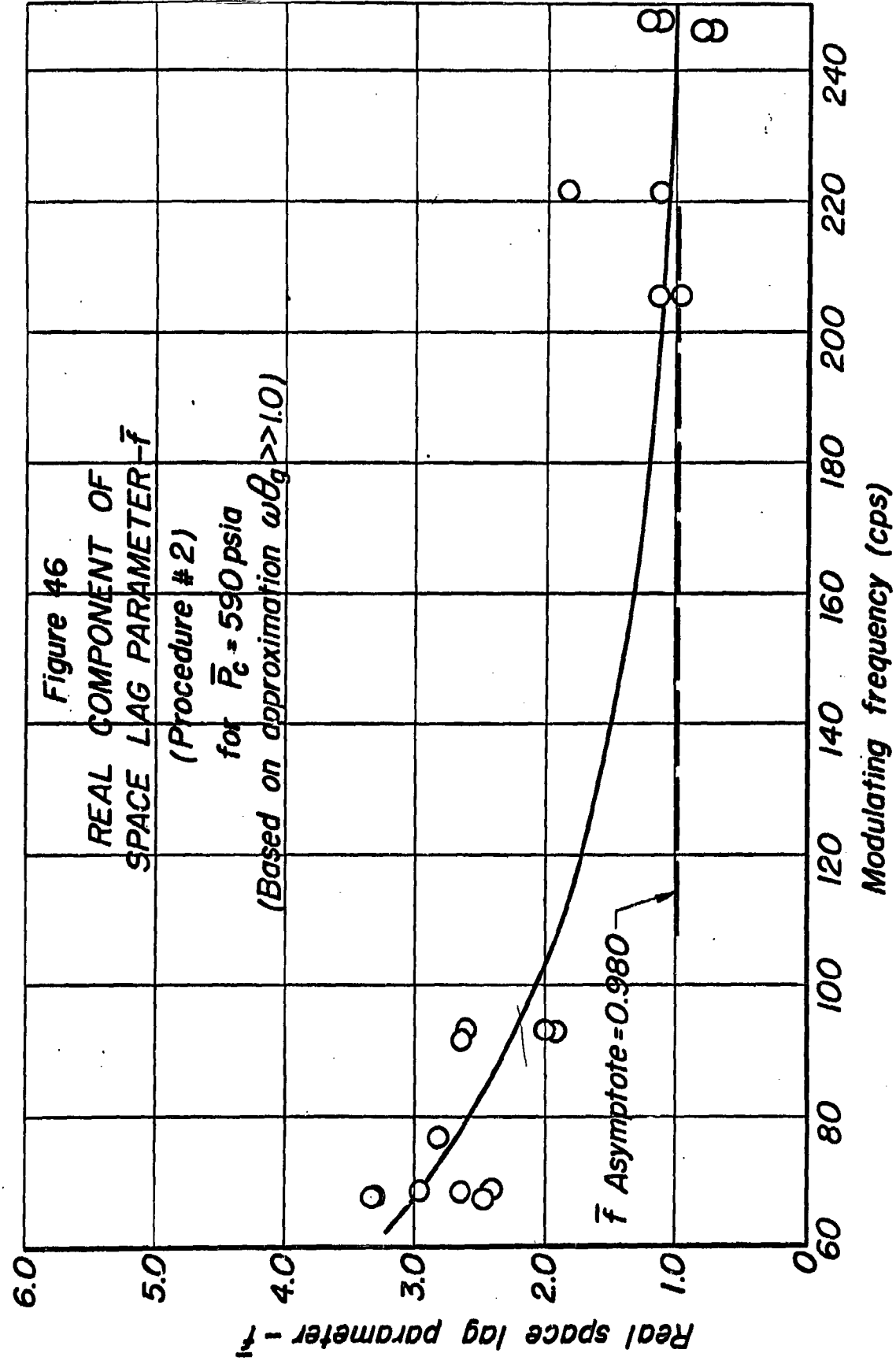


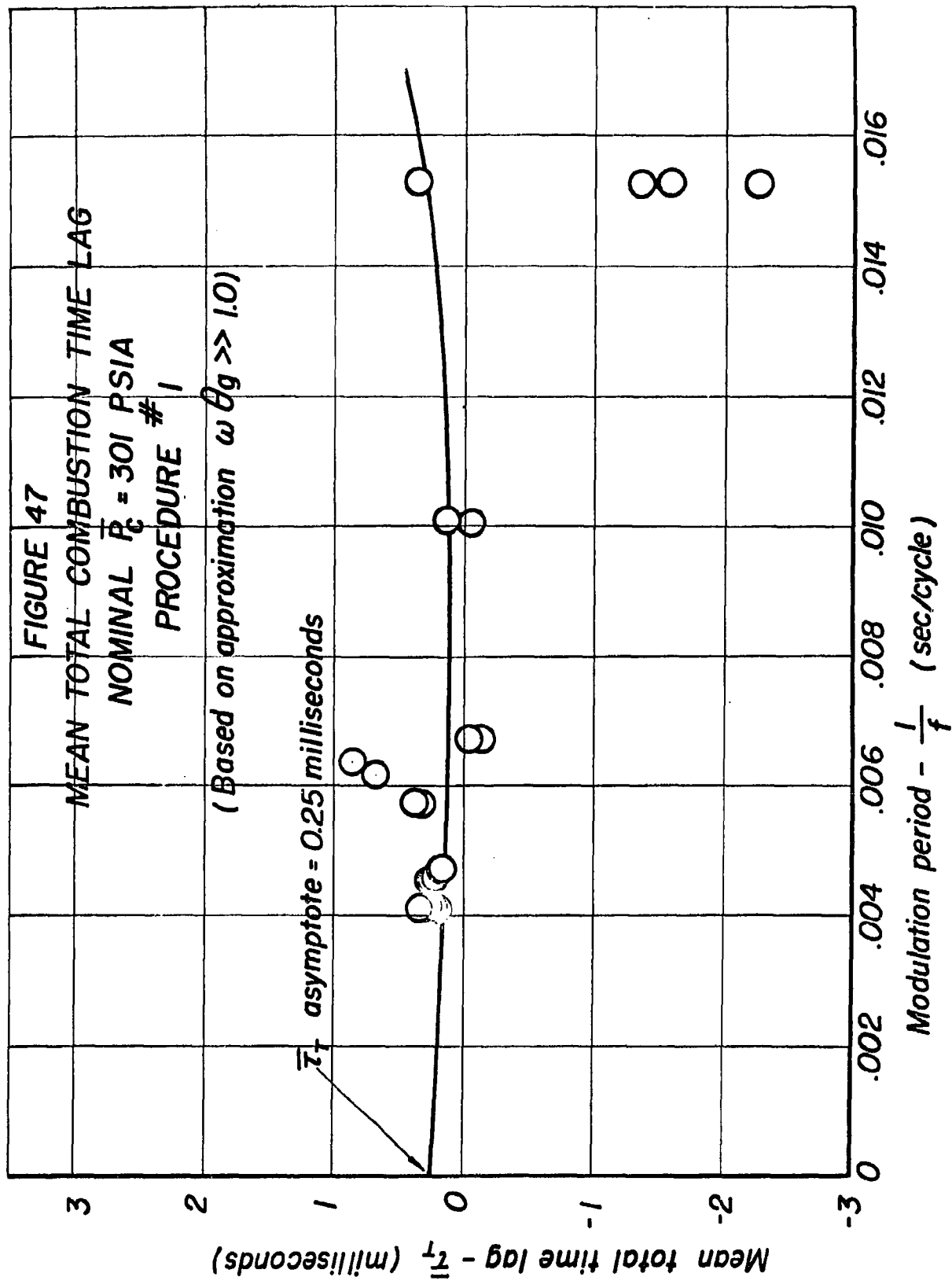


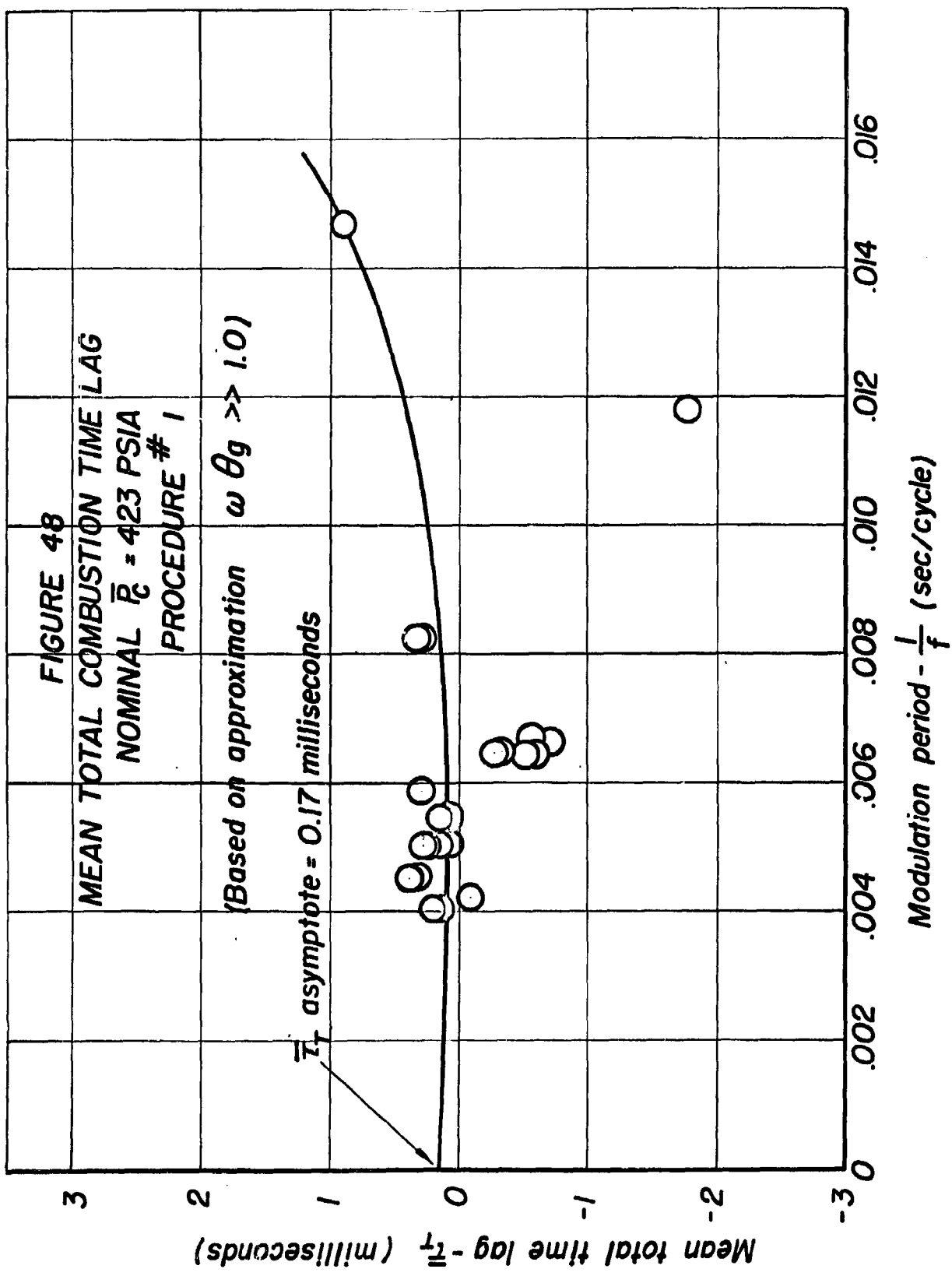


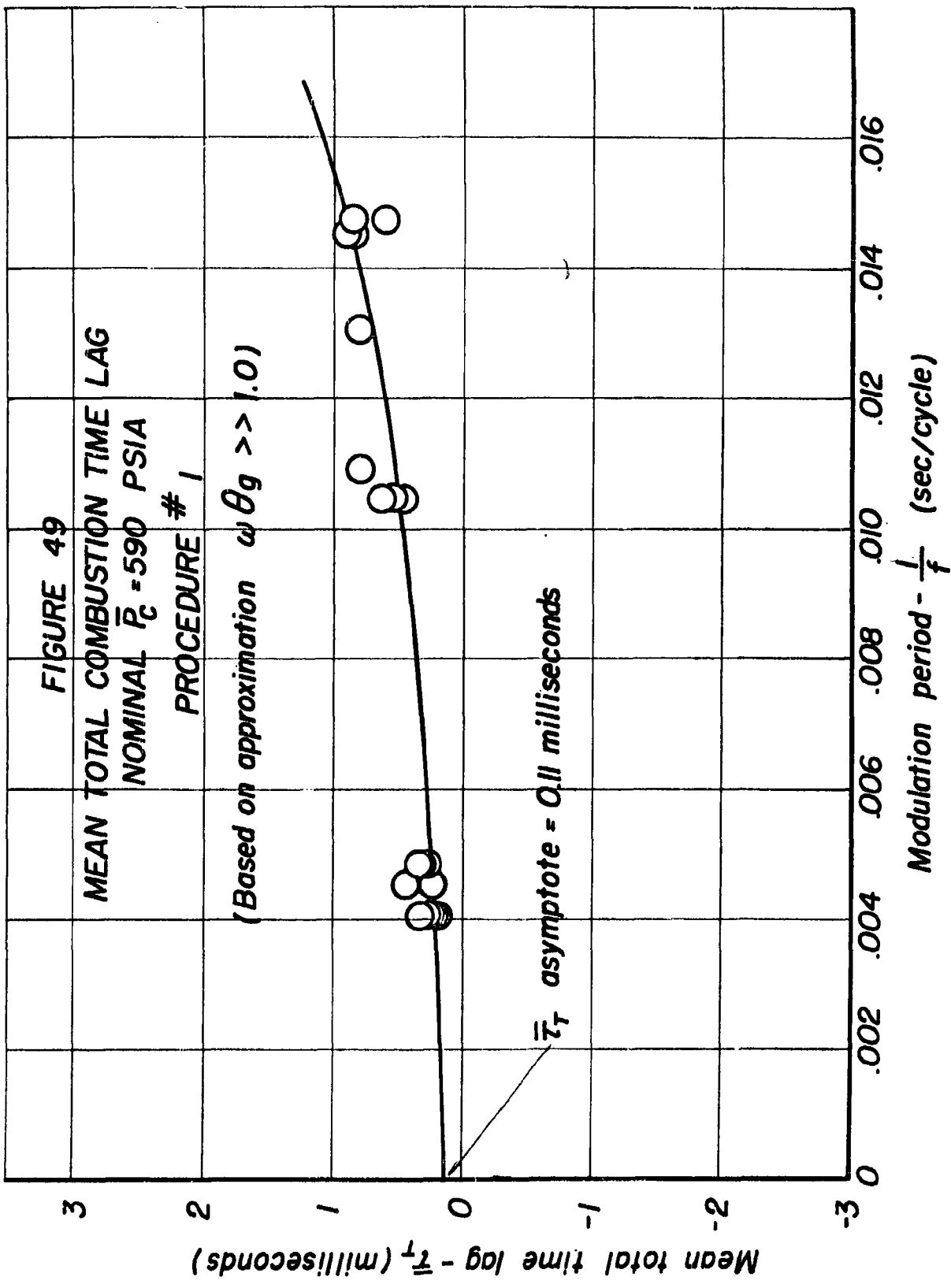


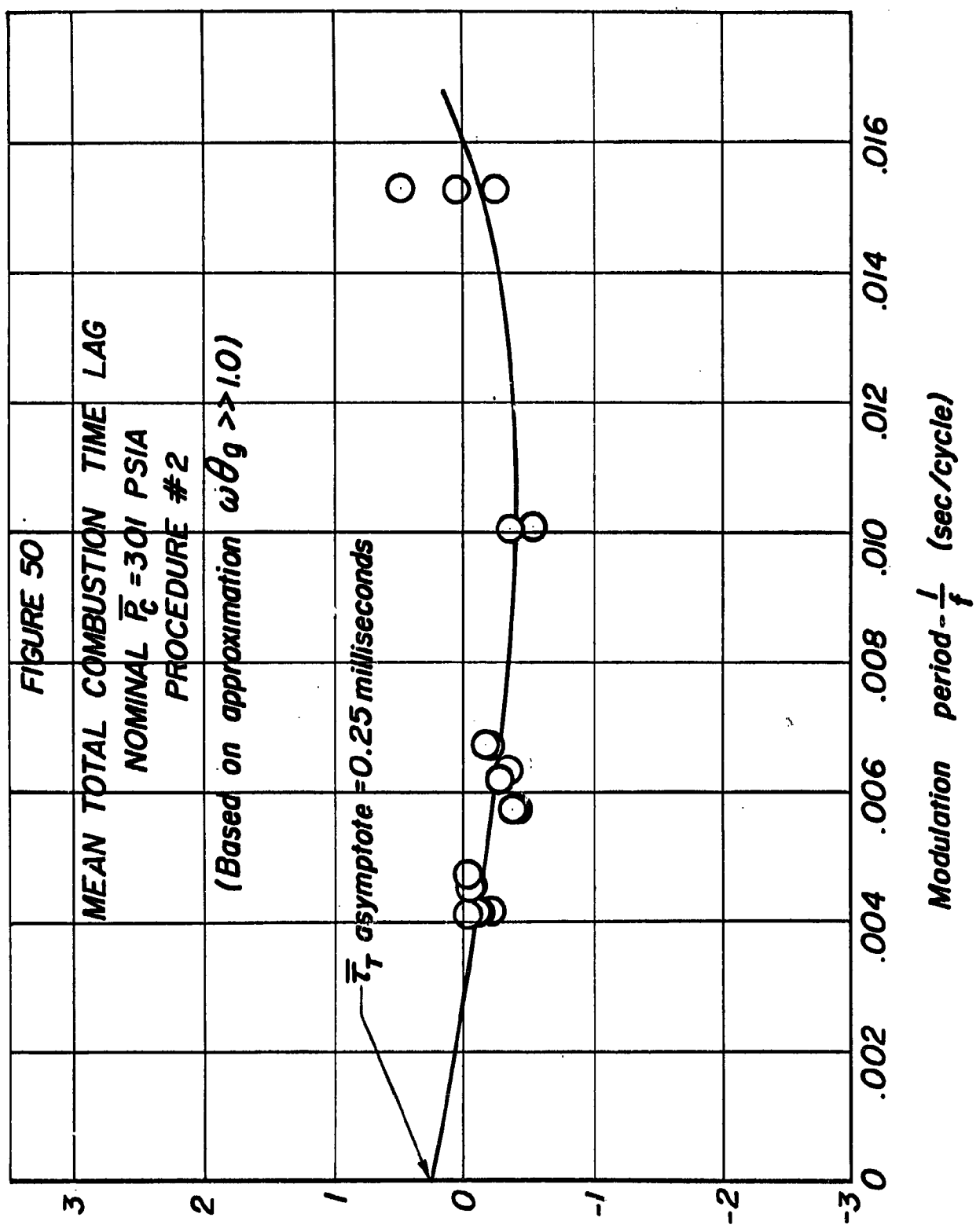


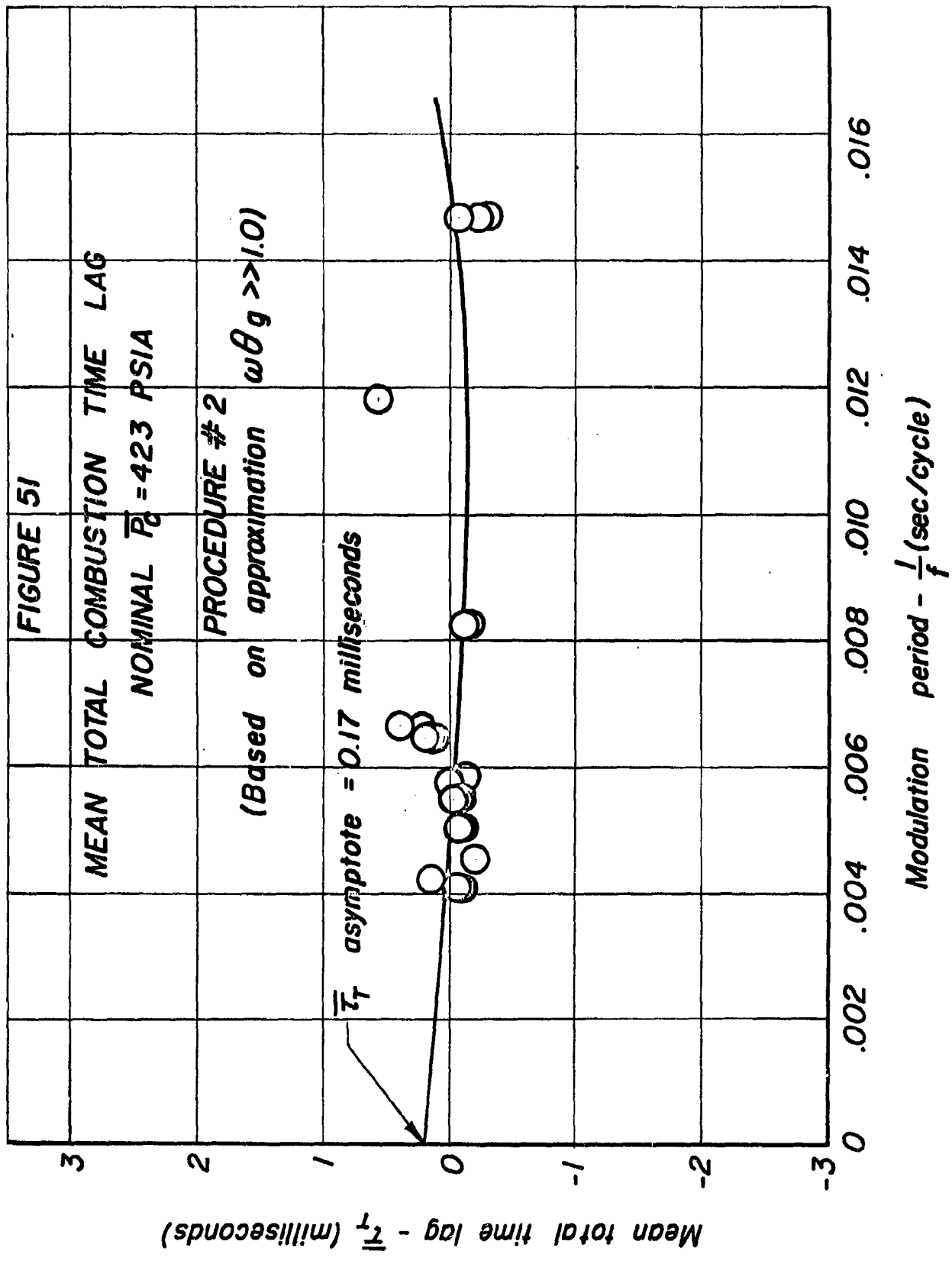


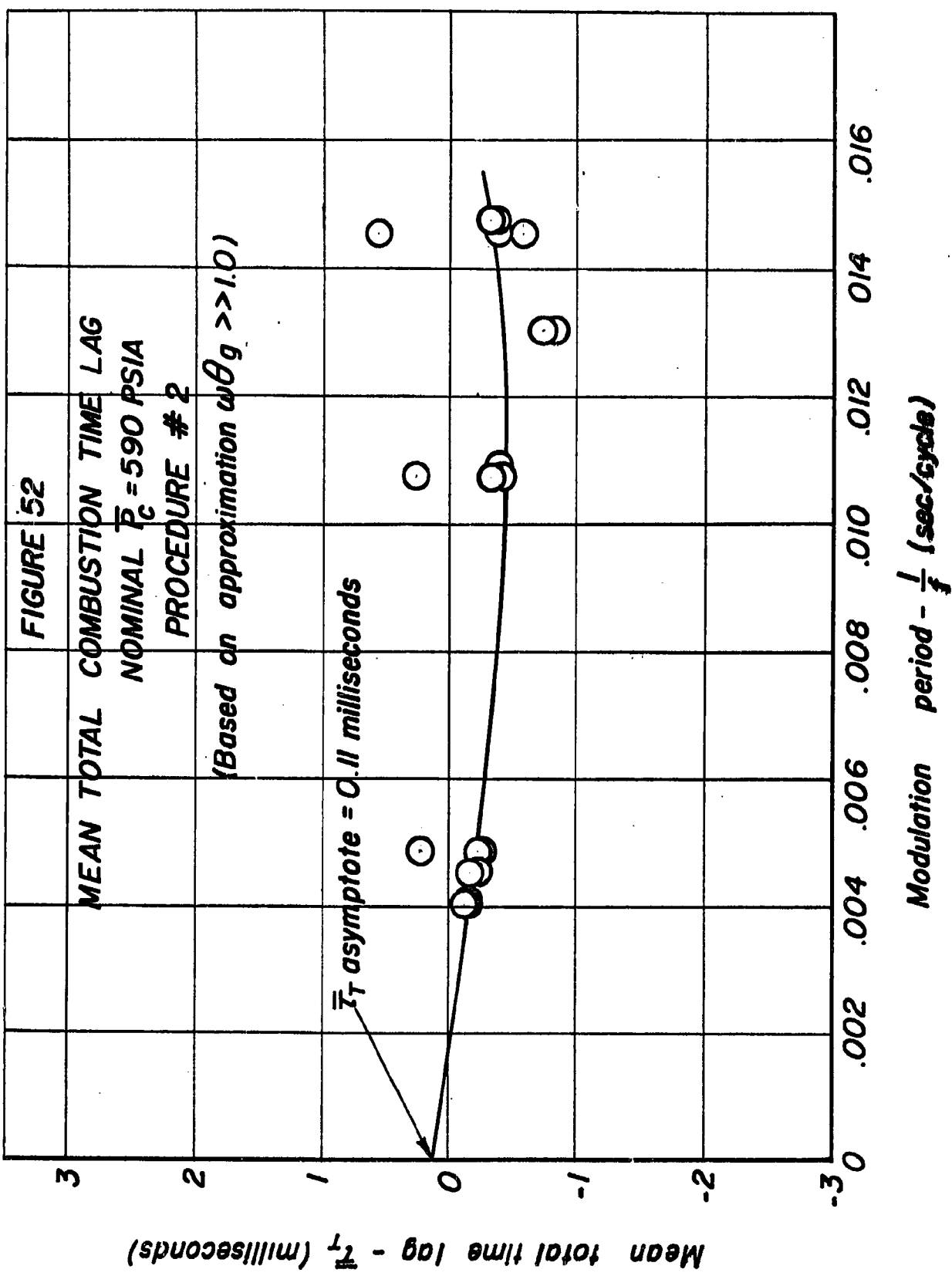












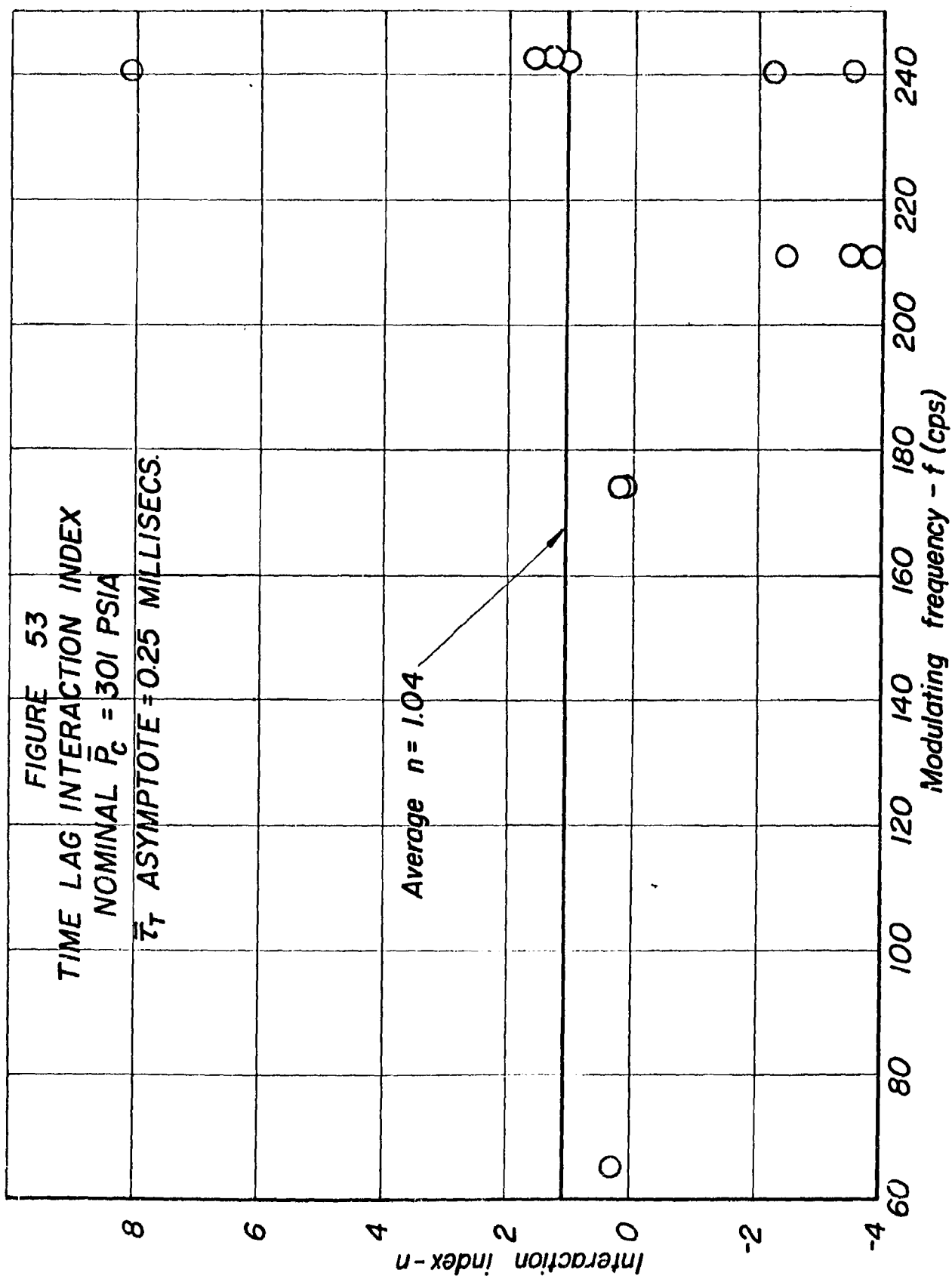


**FIGURE 54**  
**TIME LAG INTERACTION INDEX**  
**NOMINAL  $P_c = 423 \text{ PSIA}$**   
 $\bar{\tau}_f$  ASYMPTOTE = 0.17 millisecs.

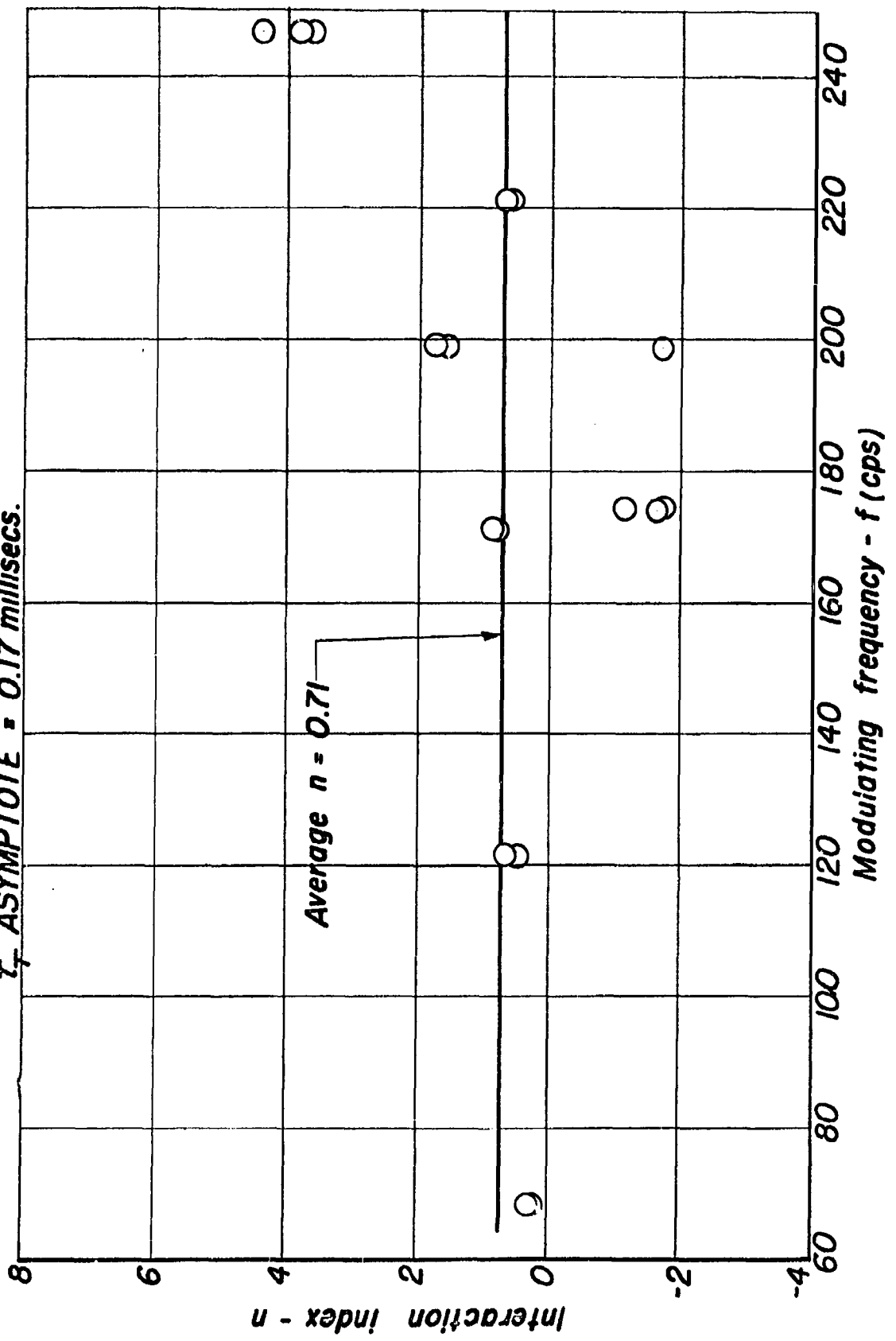
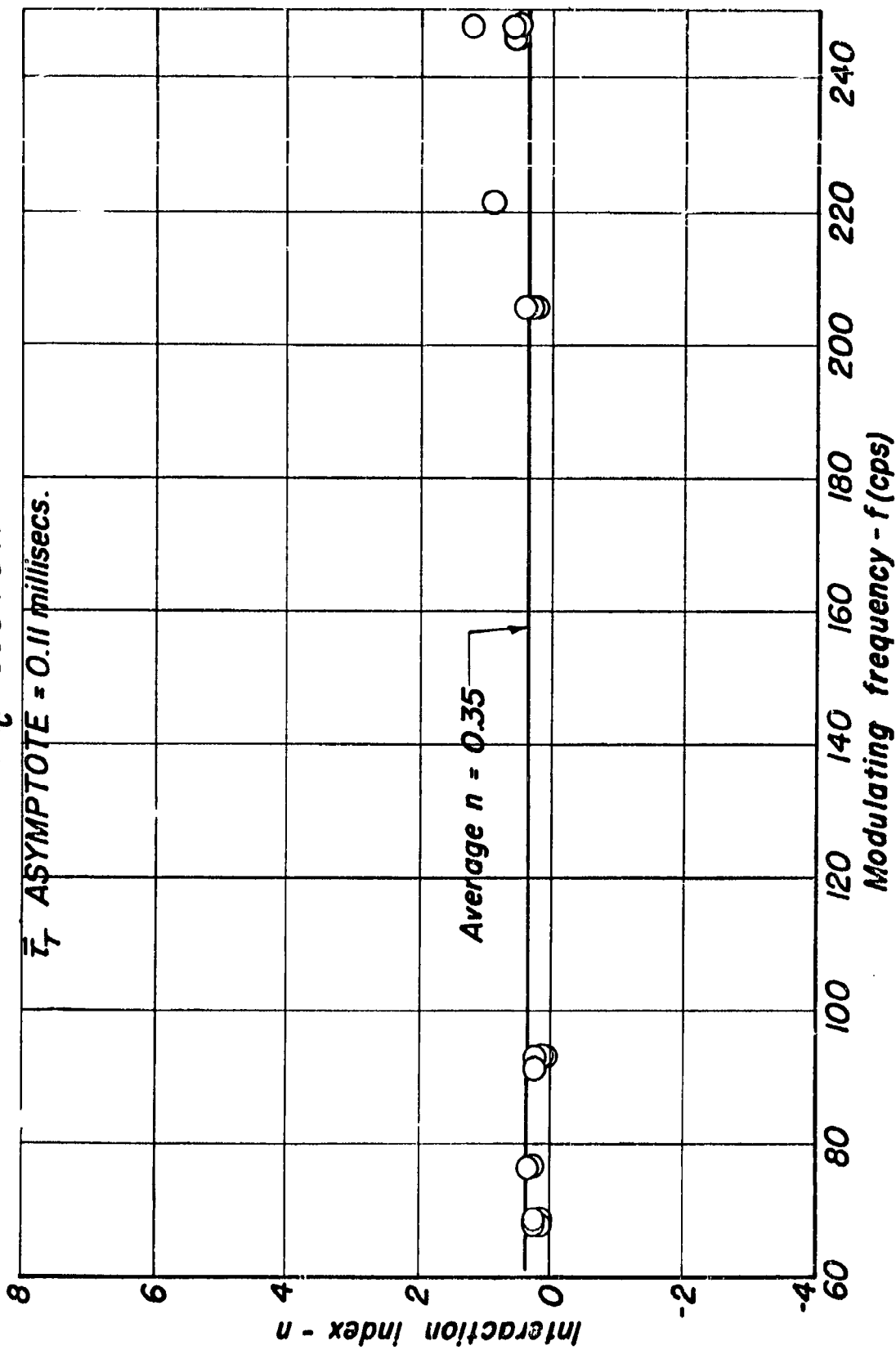


FIGURE 55  
TIME LAG INTERACTION INDEX  
NOMINAL  $P_c = 590$  PSIA



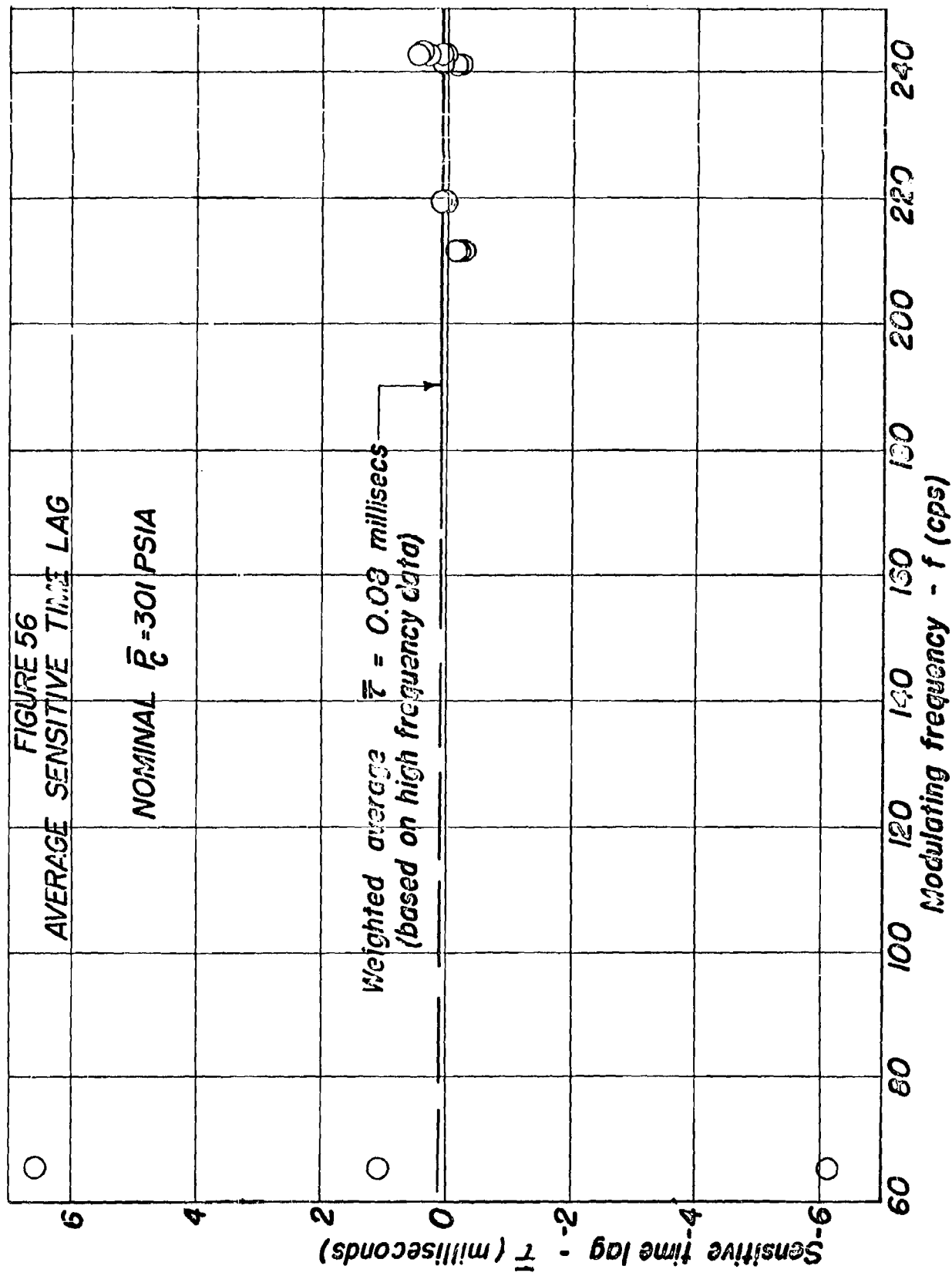


FIGURE 57  
AVERAGE SENSITIVE TIME LAG

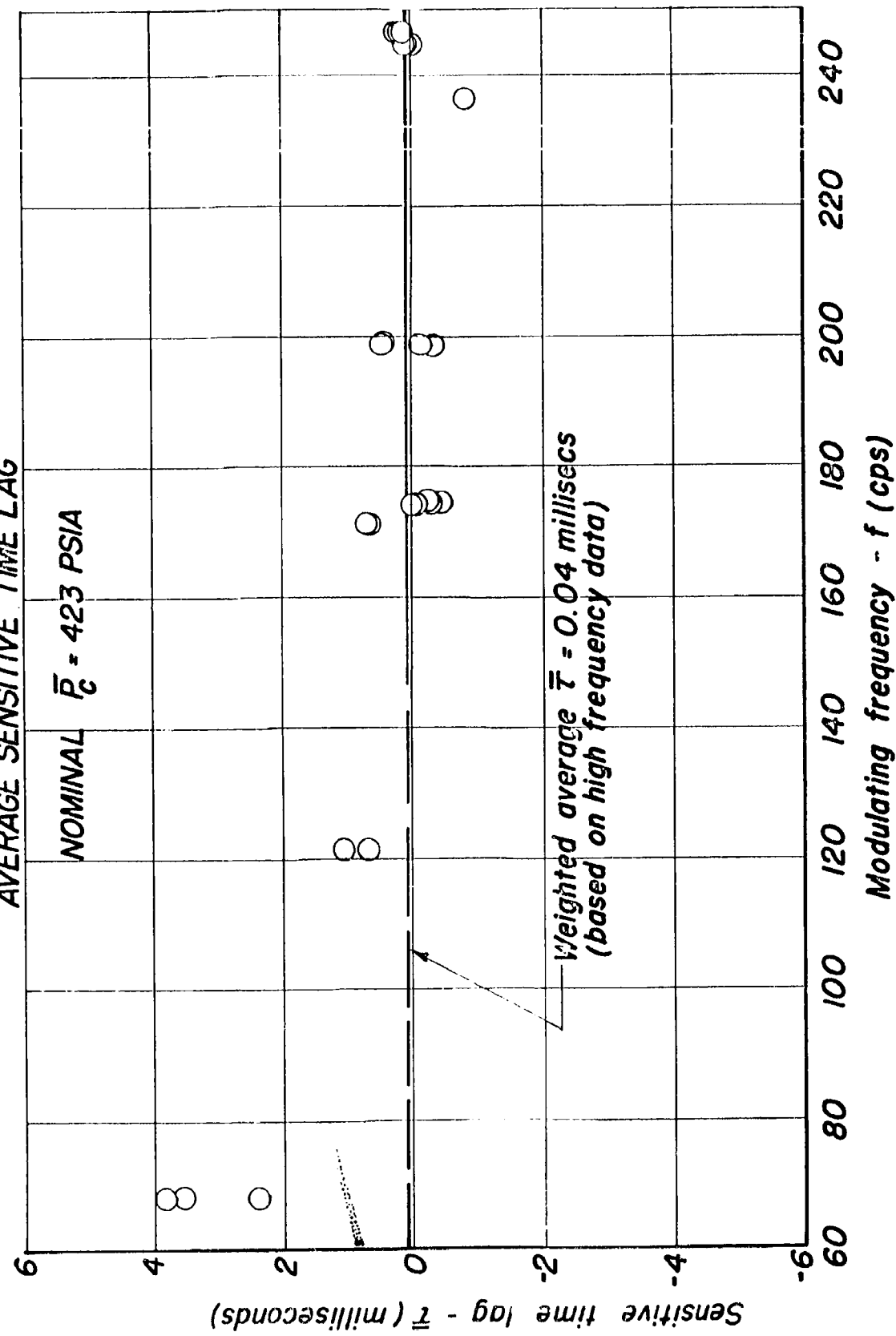


FIGURE 58  
AVERAGE SENSITIVE TIME LAG

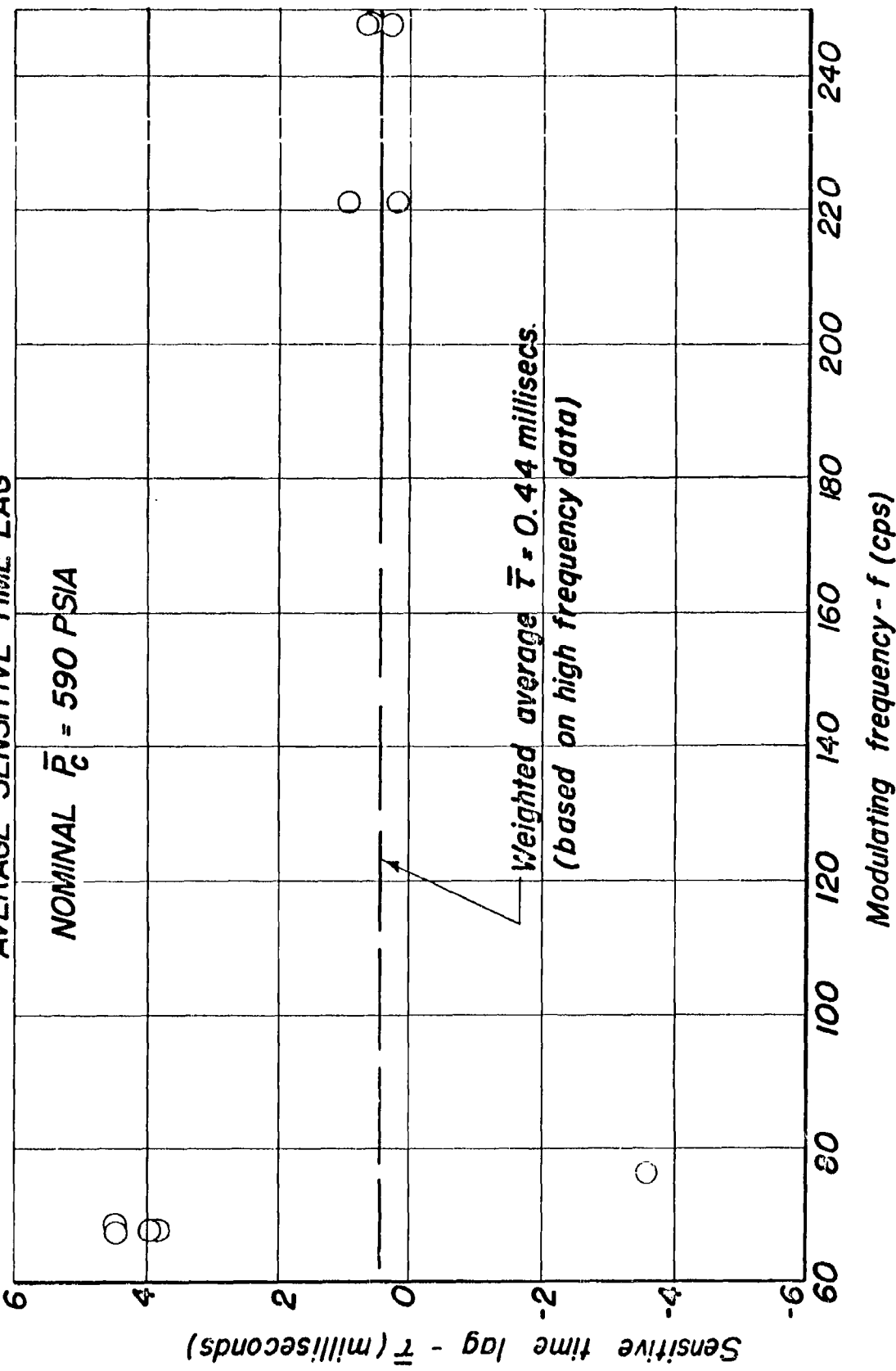
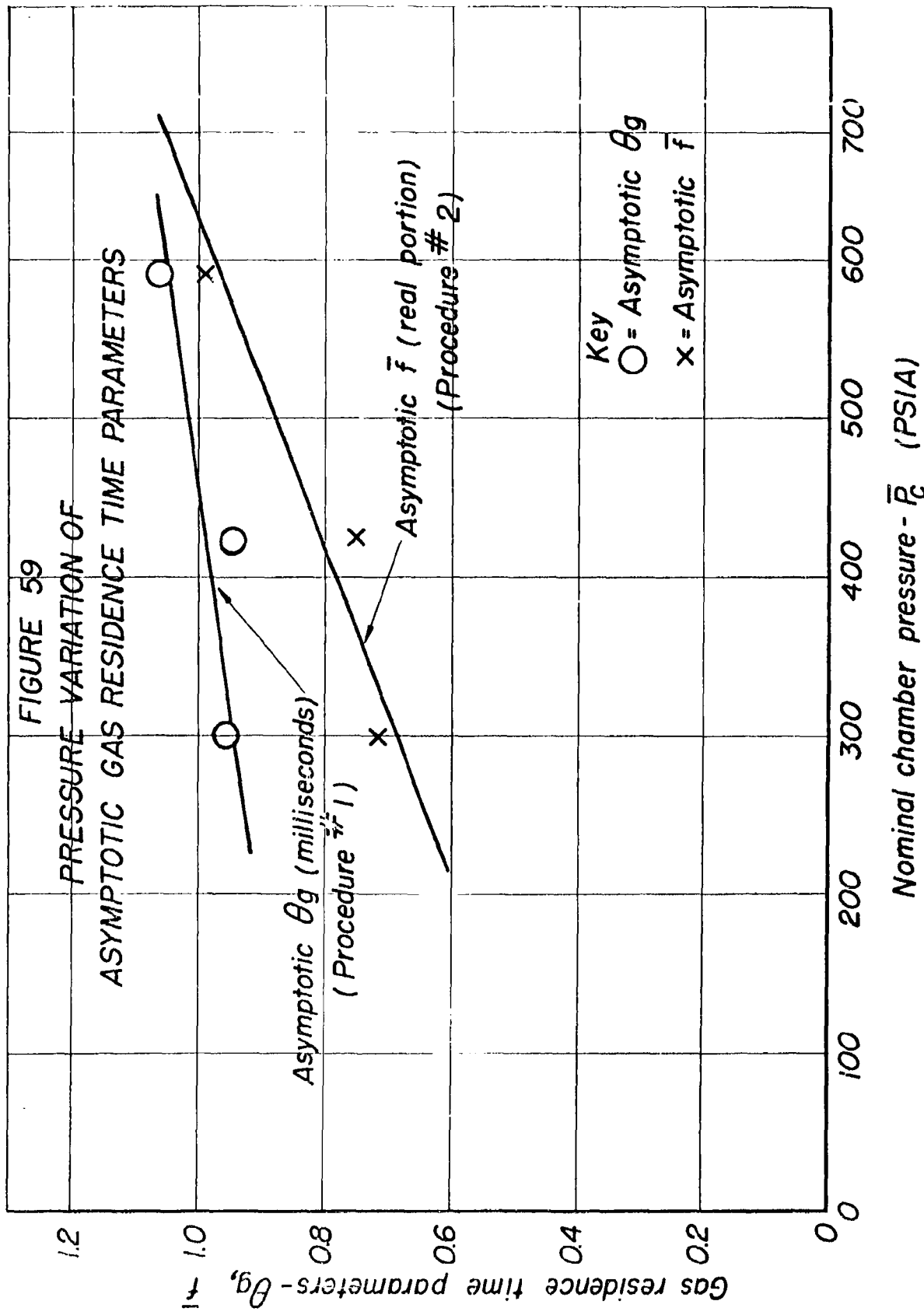


FIGURE 59  
PRESSURE VARIATION OF  
ASYMPTOTIC GAS RESIDENCE TIME PARAMETERS



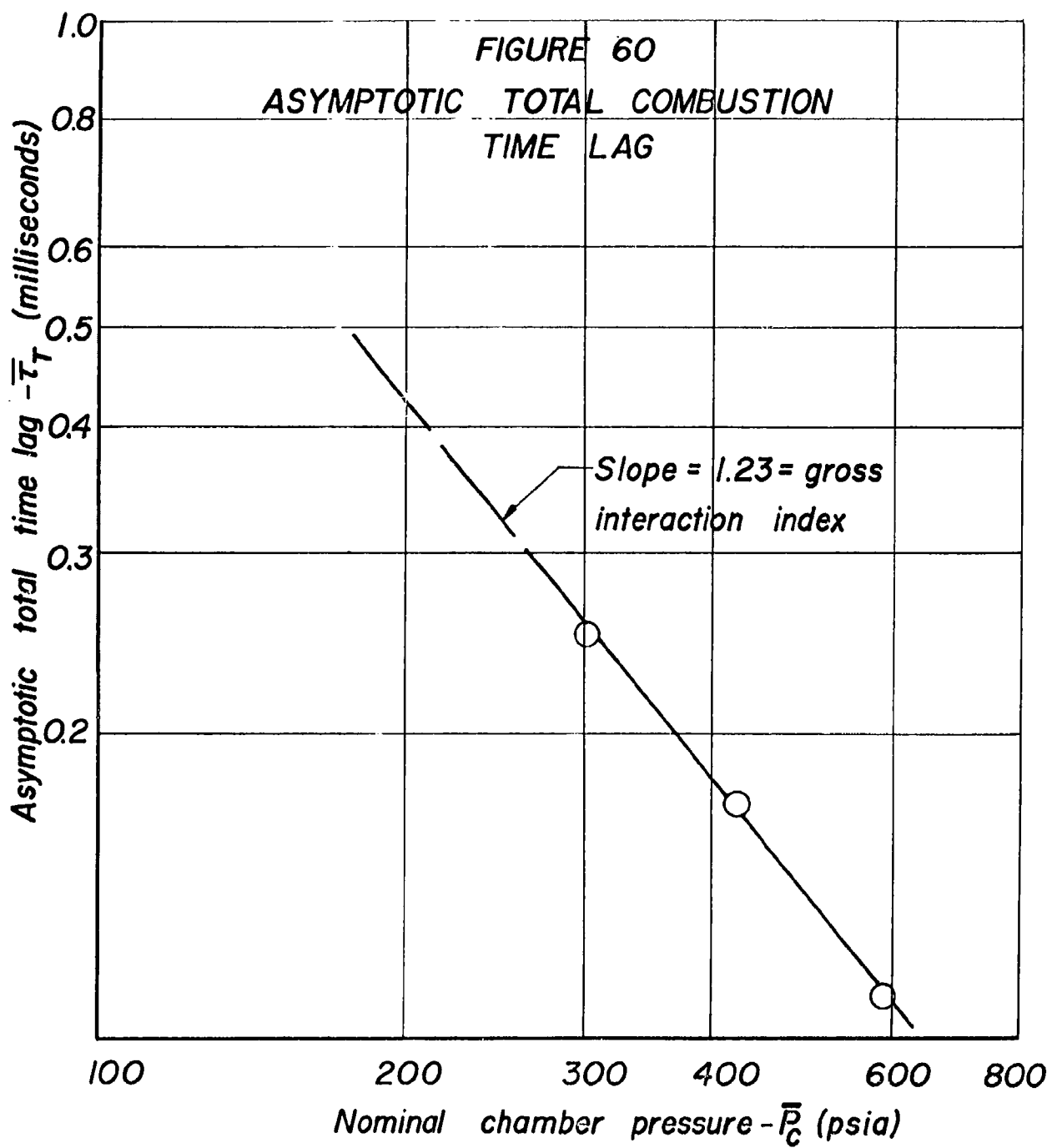
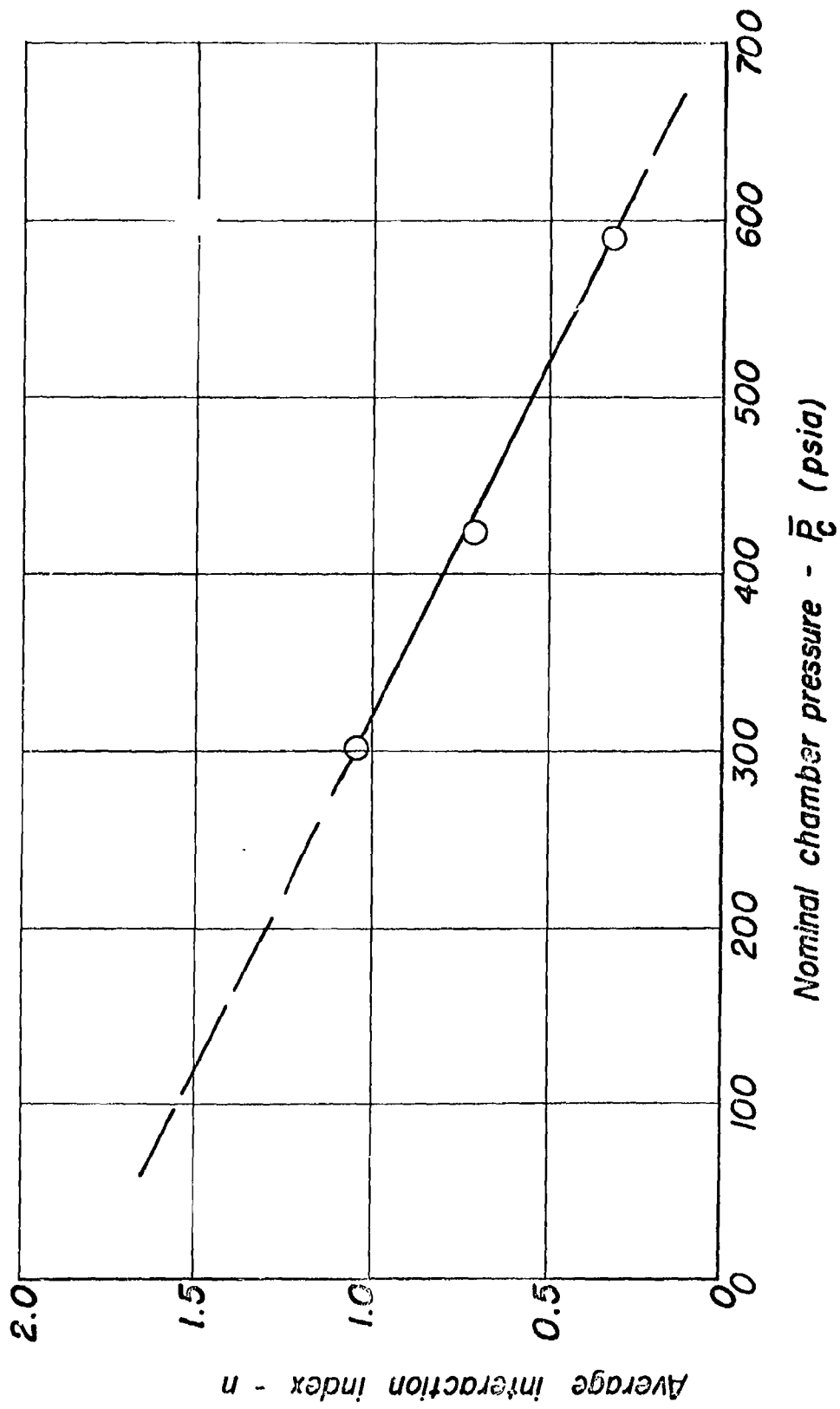
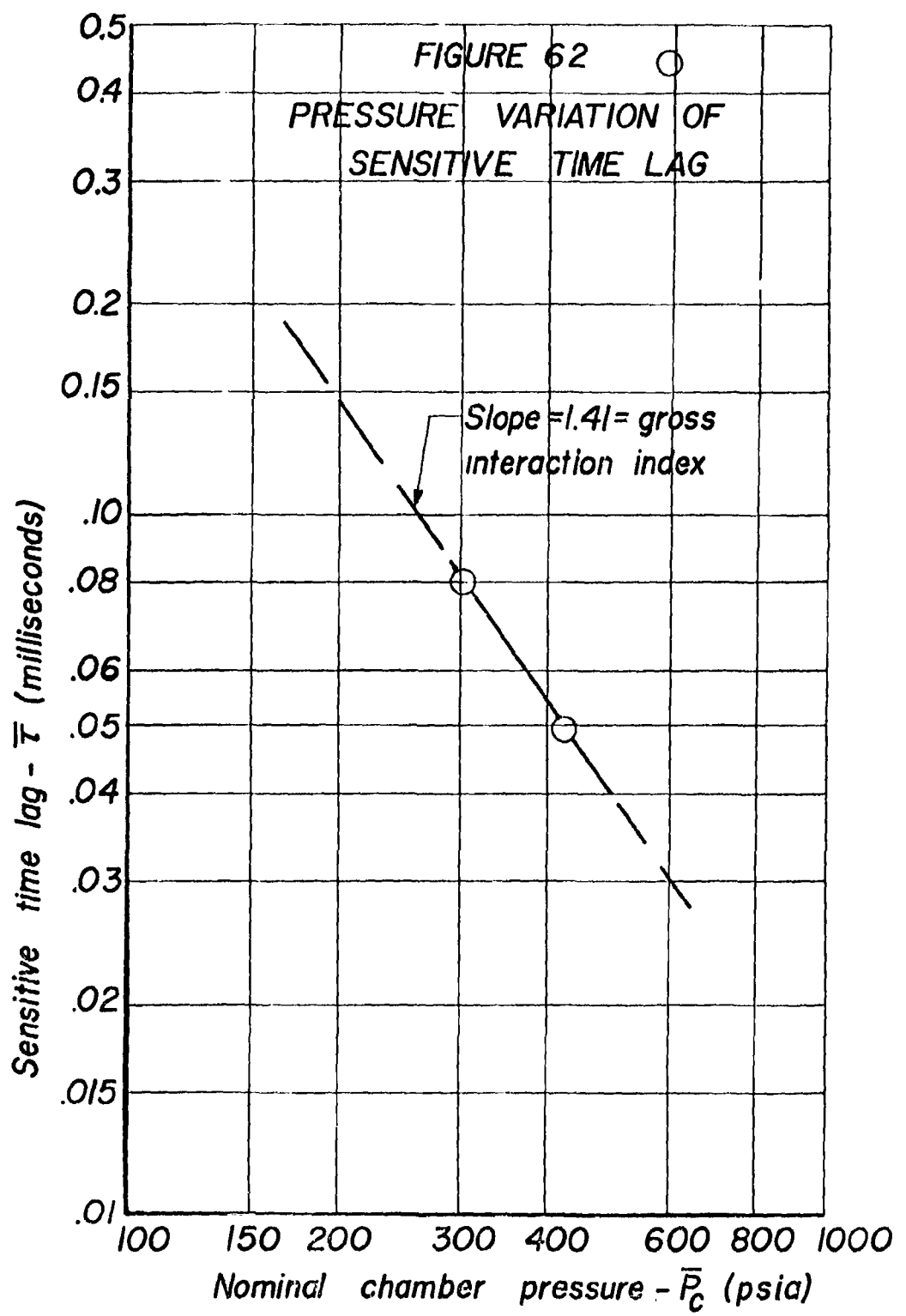


FIGURE 6/  
PRESSURE VARIATION  
of  
AVERAGE INTERACTION INDEX





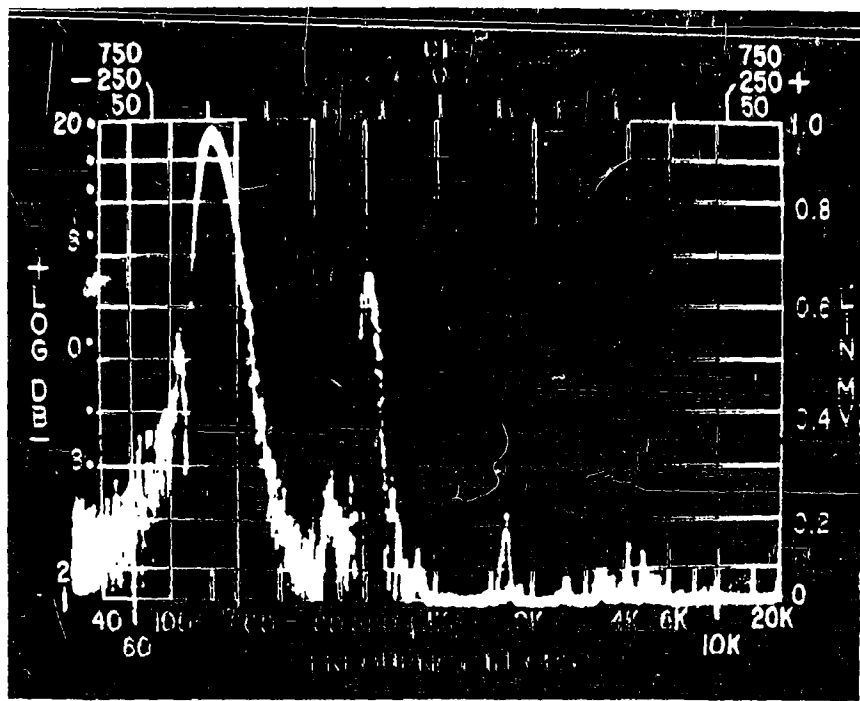


Figure 63  
Sonic analyzer spectrum  
of fuel pressure oscillation

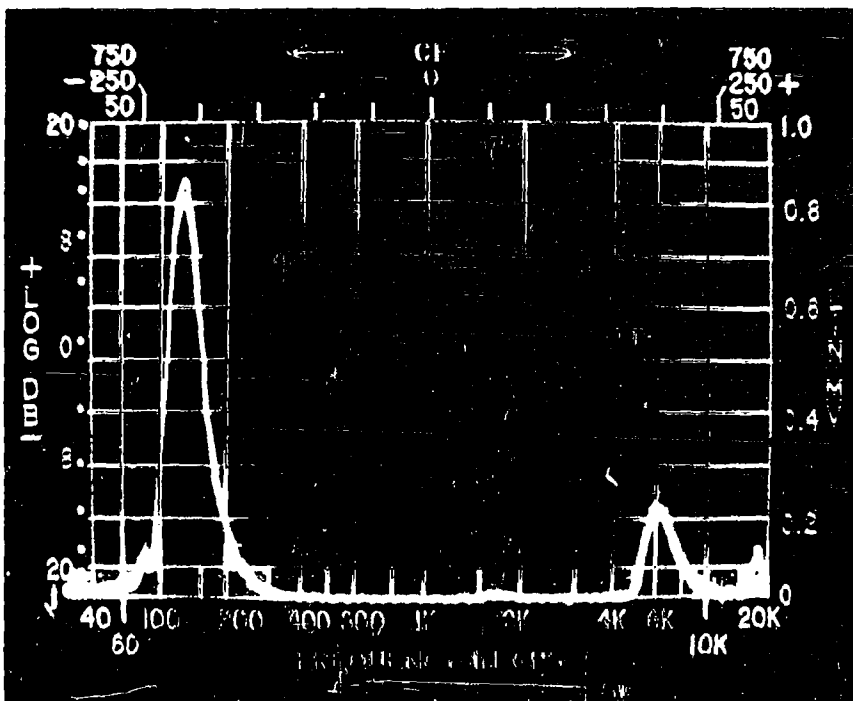
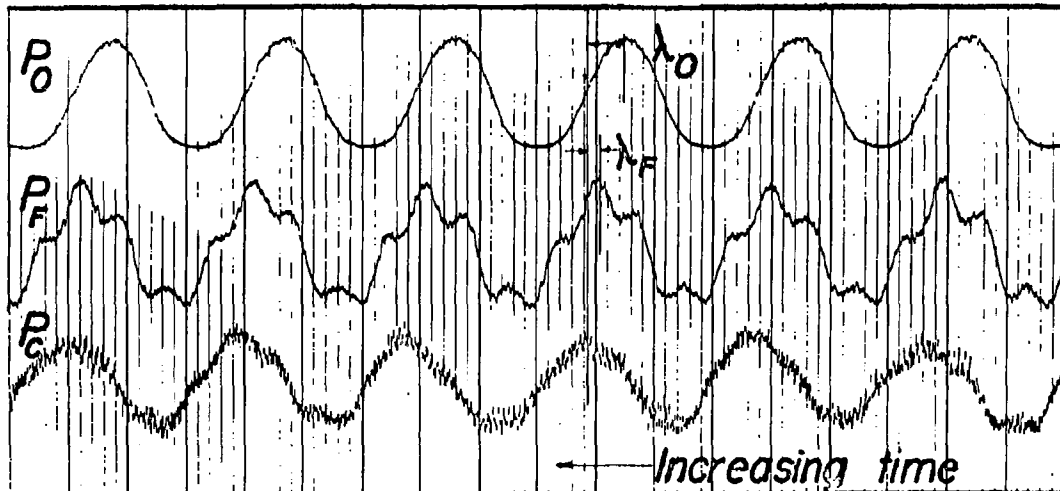
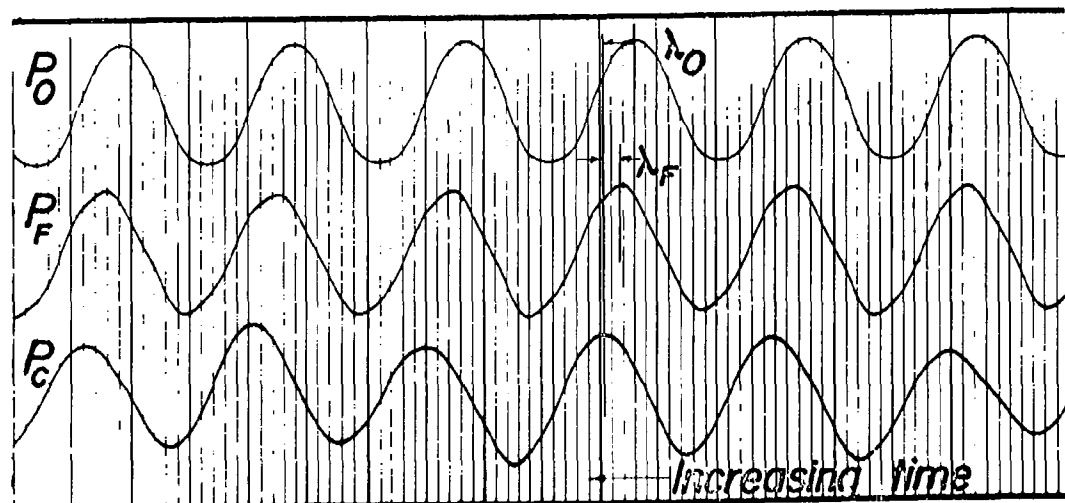


Figure 64  
Determination of  
resonant harmonic

Figure 65  
Typical middle-frequency  
pressure oscillations  
for  
run A-341  
modulating frequency = 136 cps  
nominal  $\bar{P}_C$  = 300 psia

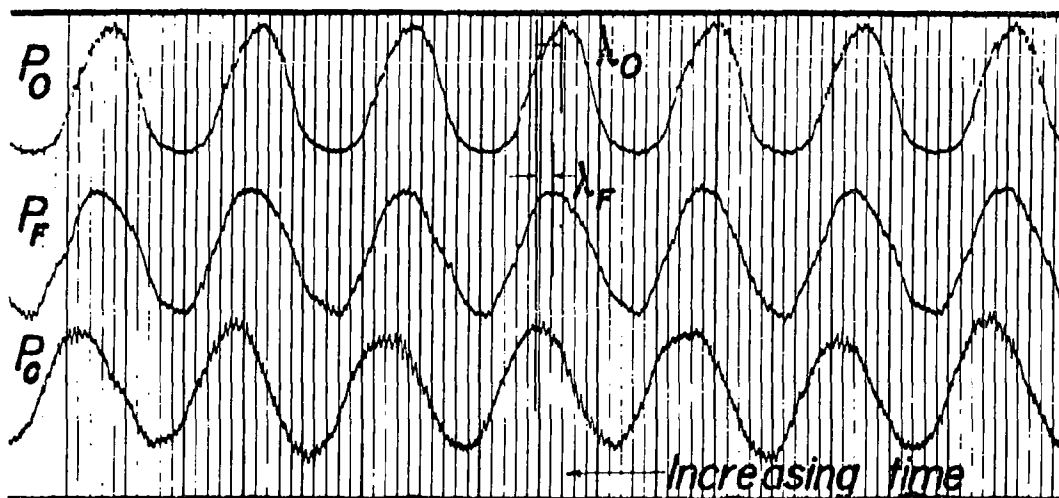


a. Unfiltered pressures

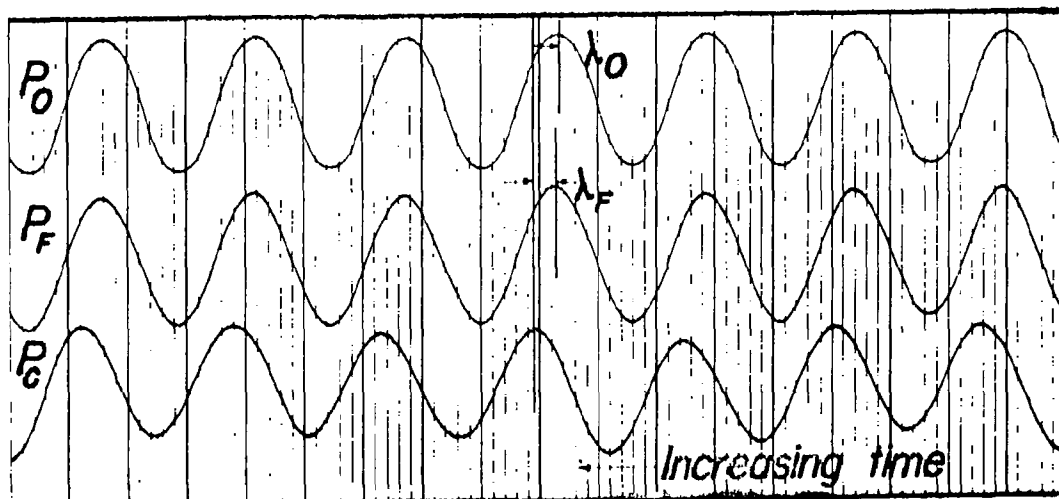


b. Filtered pressures

Figure 66  
Typical border-frequency  
pressure oscillations  
for  
run A-352  
modulating frequency = 162 cps  
nominal  $\bar{P}_C$  = 300 psia

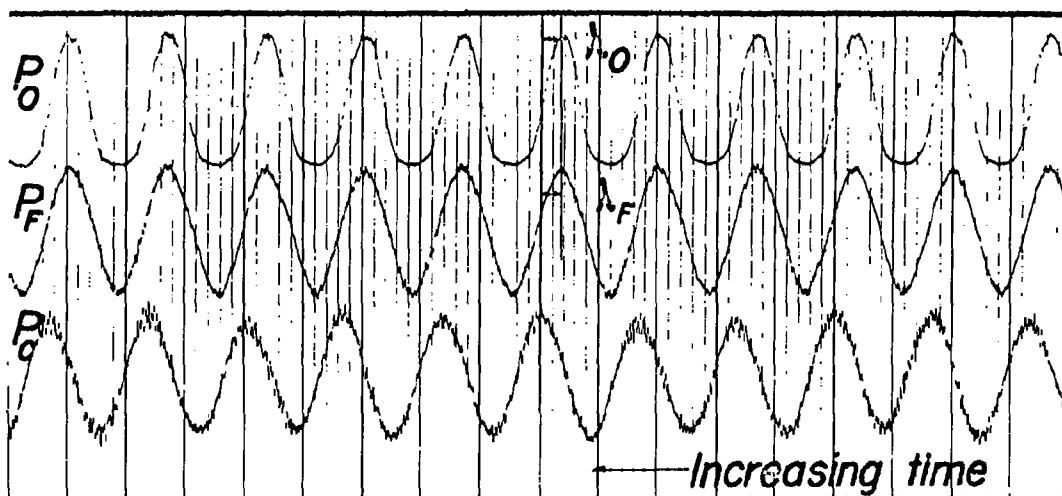


a. Unfiltered pressures

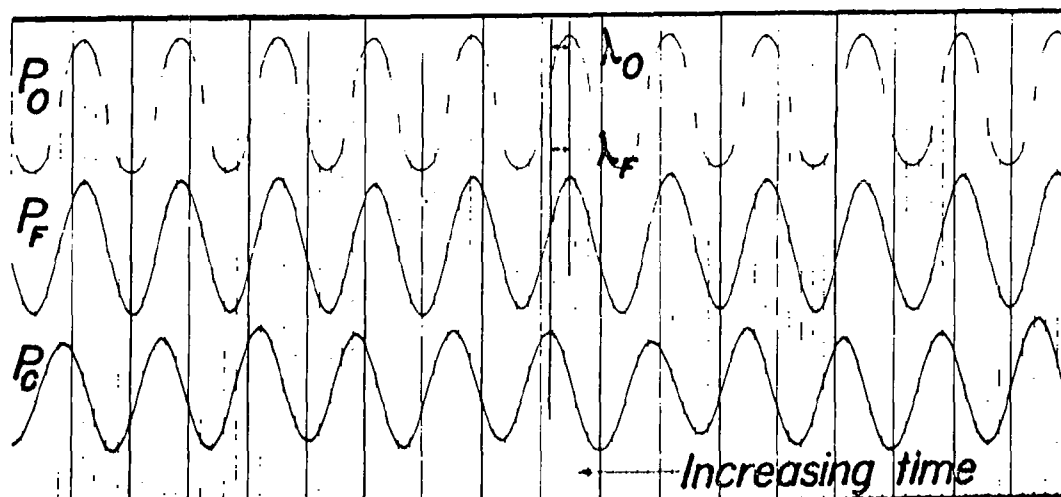


b. Filtered pressures

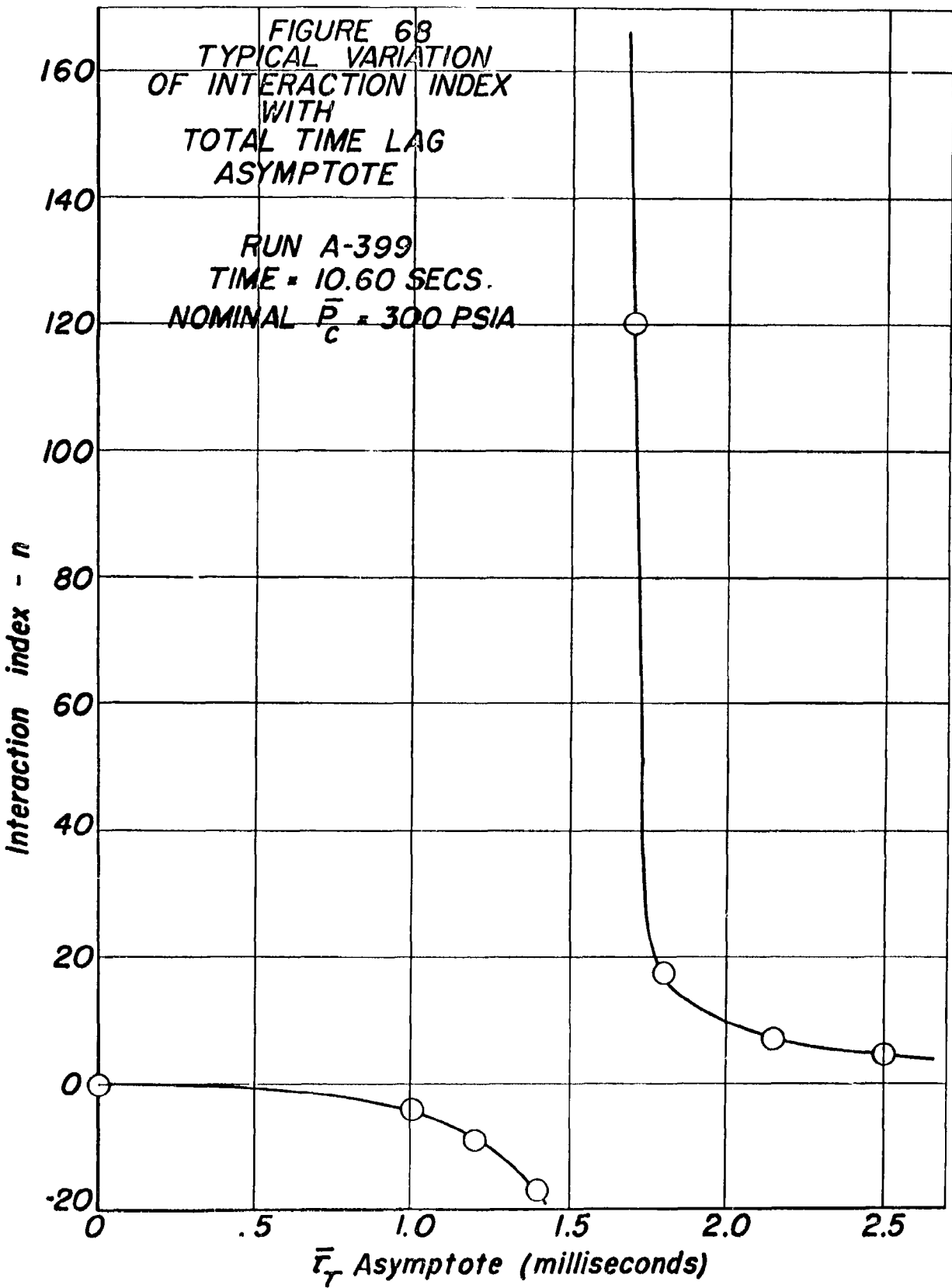
Figure 67  
Typical high-frequency  
pressure oscillations  
for  
run A-399  
modulating frequency = 241 cps  
nominal  $\bar{P}_c$  = 300 psia



a. Unfiltered pressures



b. Filtered pressures



CALCULATED TIME LAG PARAMETERS  
FOR  
AVERAGE TRANSFER FUNCTION VALUES  
(Constant mixture ratio assumed)

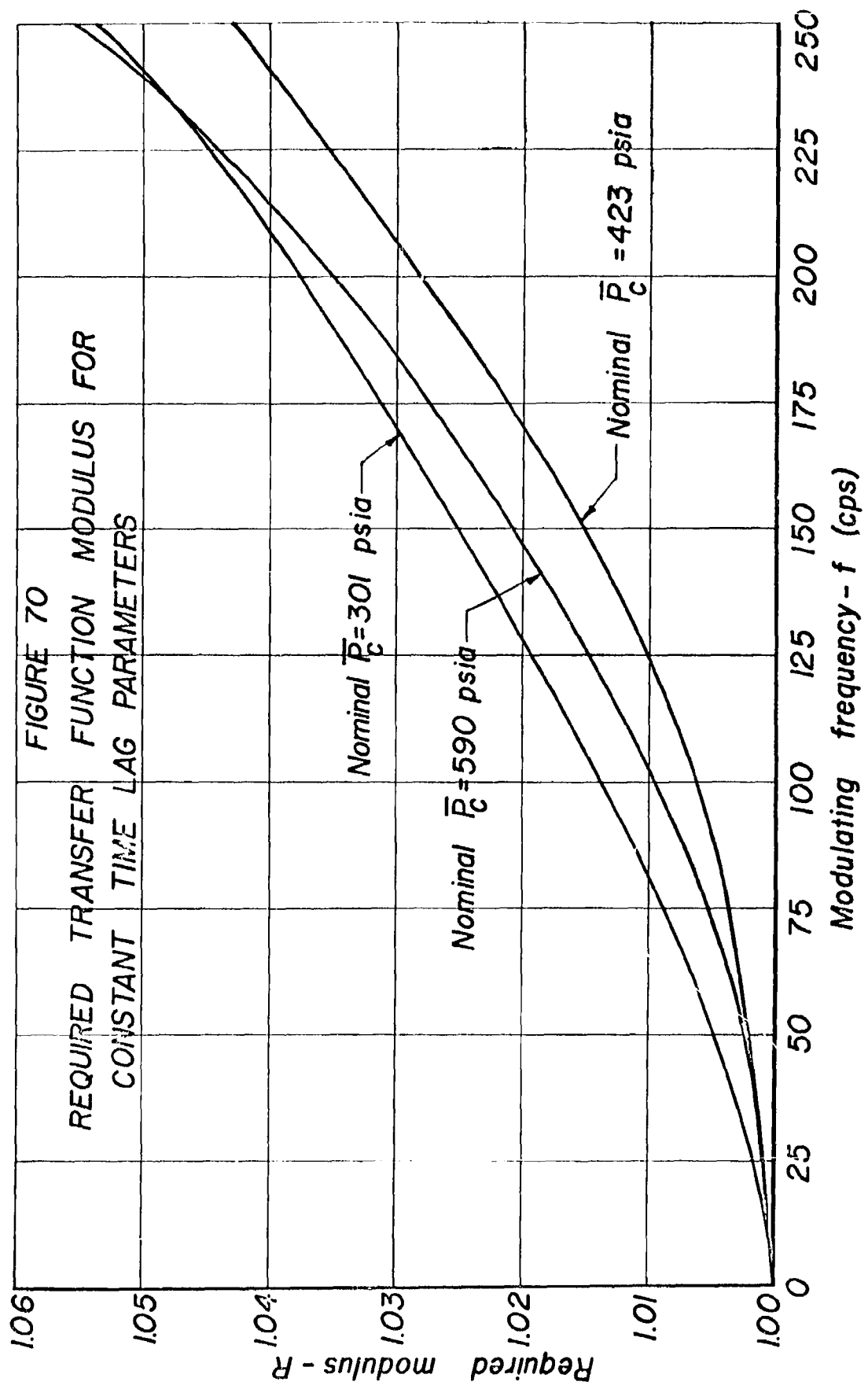
NOMINAL  $\bar{P}_c = 600 \text{ PSIA}$   
 $\bar{\tau}_T$  ASYMPTOTE = 0.2 MILLISECS.

Sensitive time lag -  $\bar{\tau}_T$  (milliseconds)

Interaction index -  $n$

Modulating frequency -  $f$  (cps)





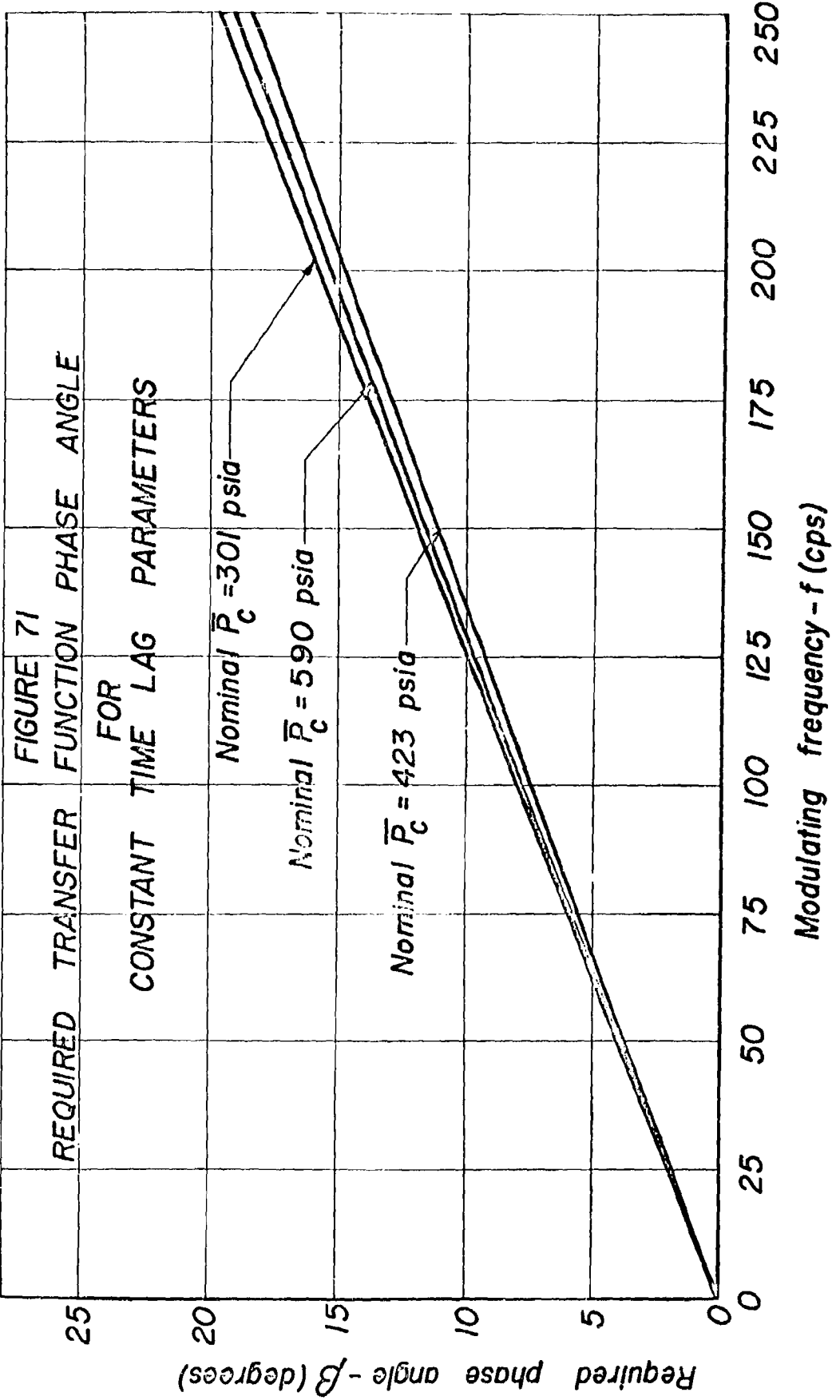


FIGURE 72  
TYPICAL COMPLEX  
RELATIONSHIPS OF  
COMBUSTION CHAMBER  
EQUATION

(Constant mixture  
ratio assumed)

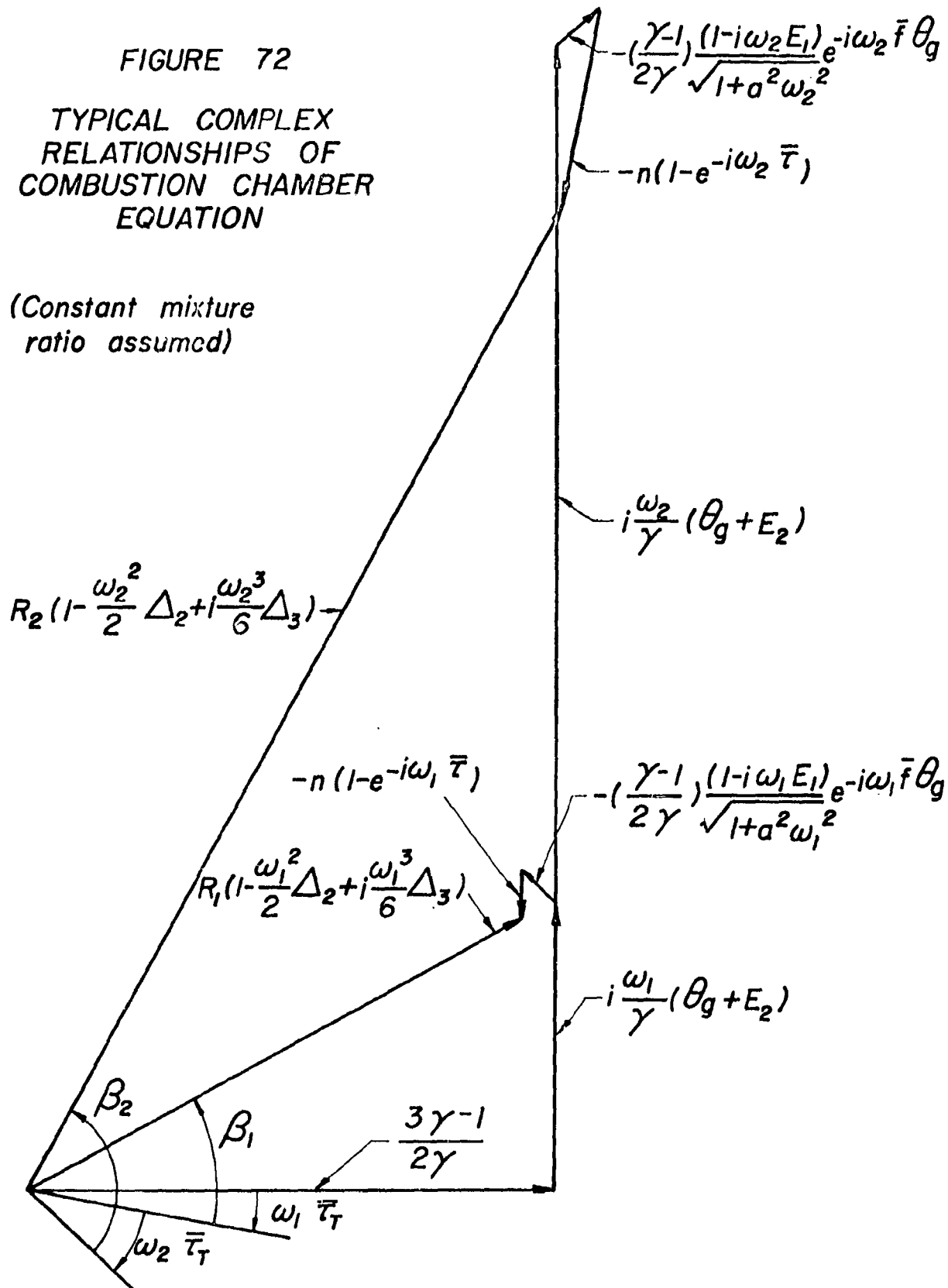


FIGURE 73  
TWO-POINT CALCULATION PROCEDURE:  
FIRST ITERATION

(Non-intersecting case)  
NOMINAL  $\bar{P}_C = 590 \text{ PSIA}$ .

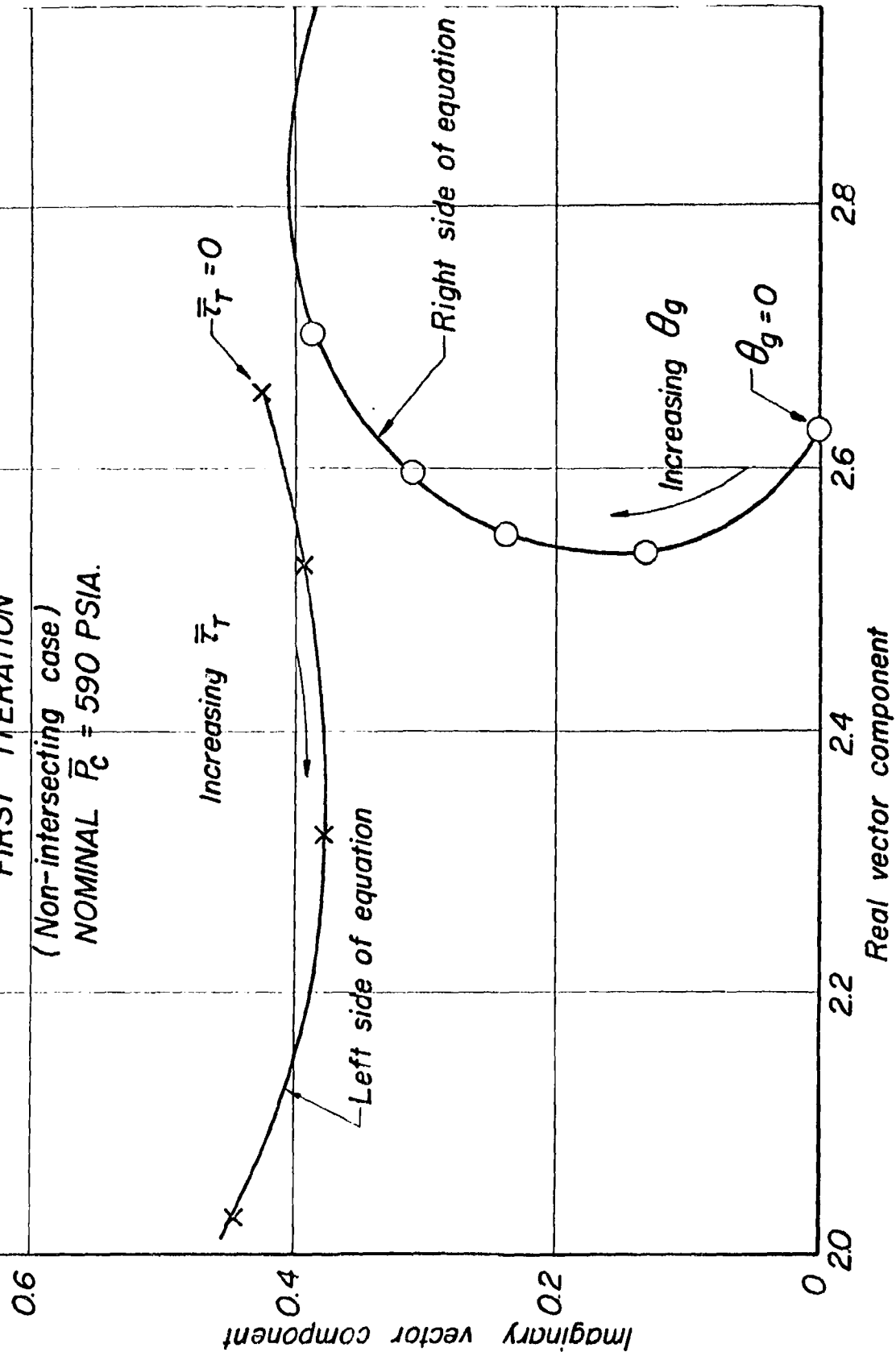
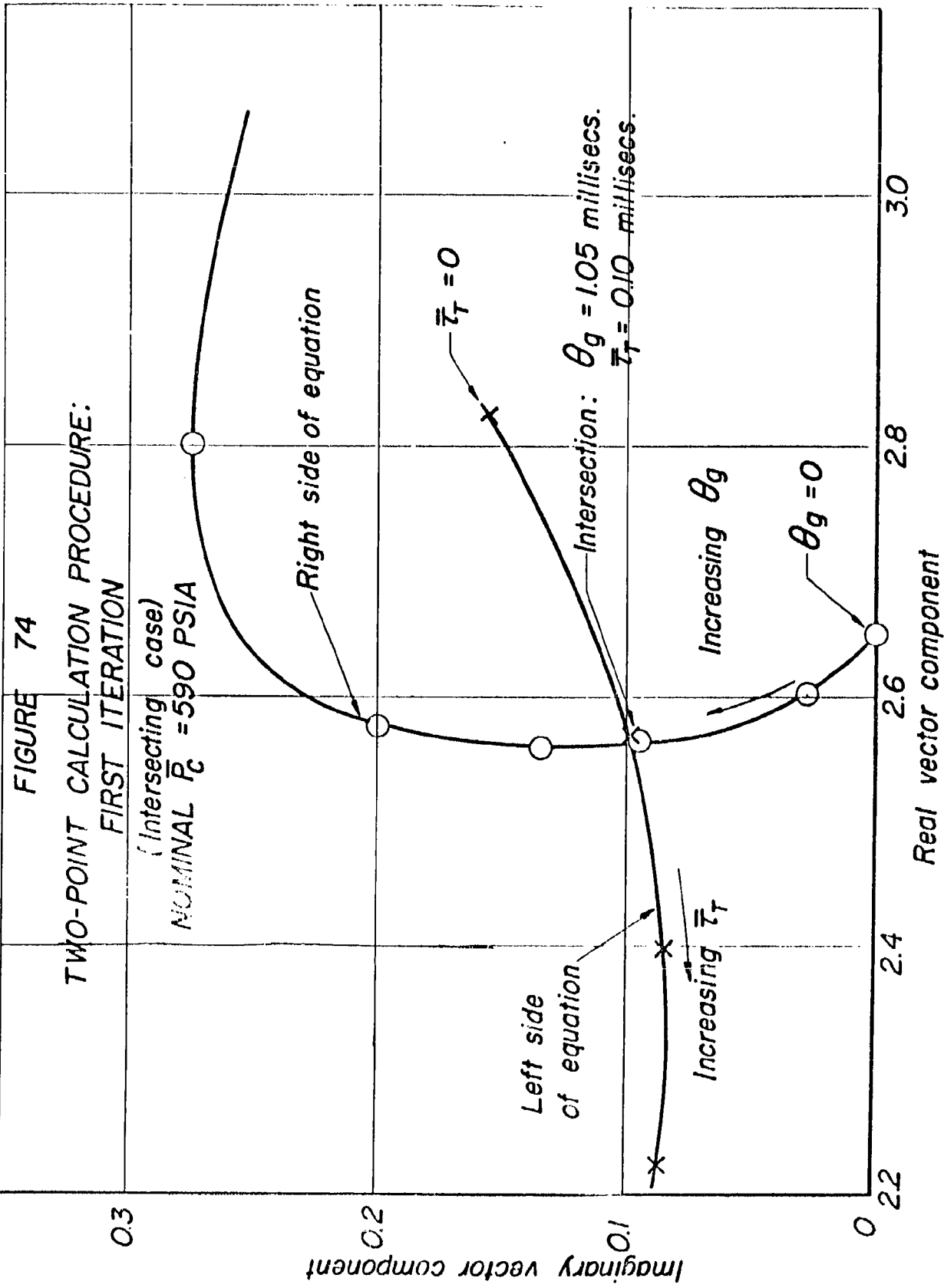


FIGURE 74  
TWO-POINT CALCULATION PROCEDURE:  
FIRST ITERATION

Intersecting case)  
Nominal  $\bar{P}_C = 590 \text{ PSIA}$



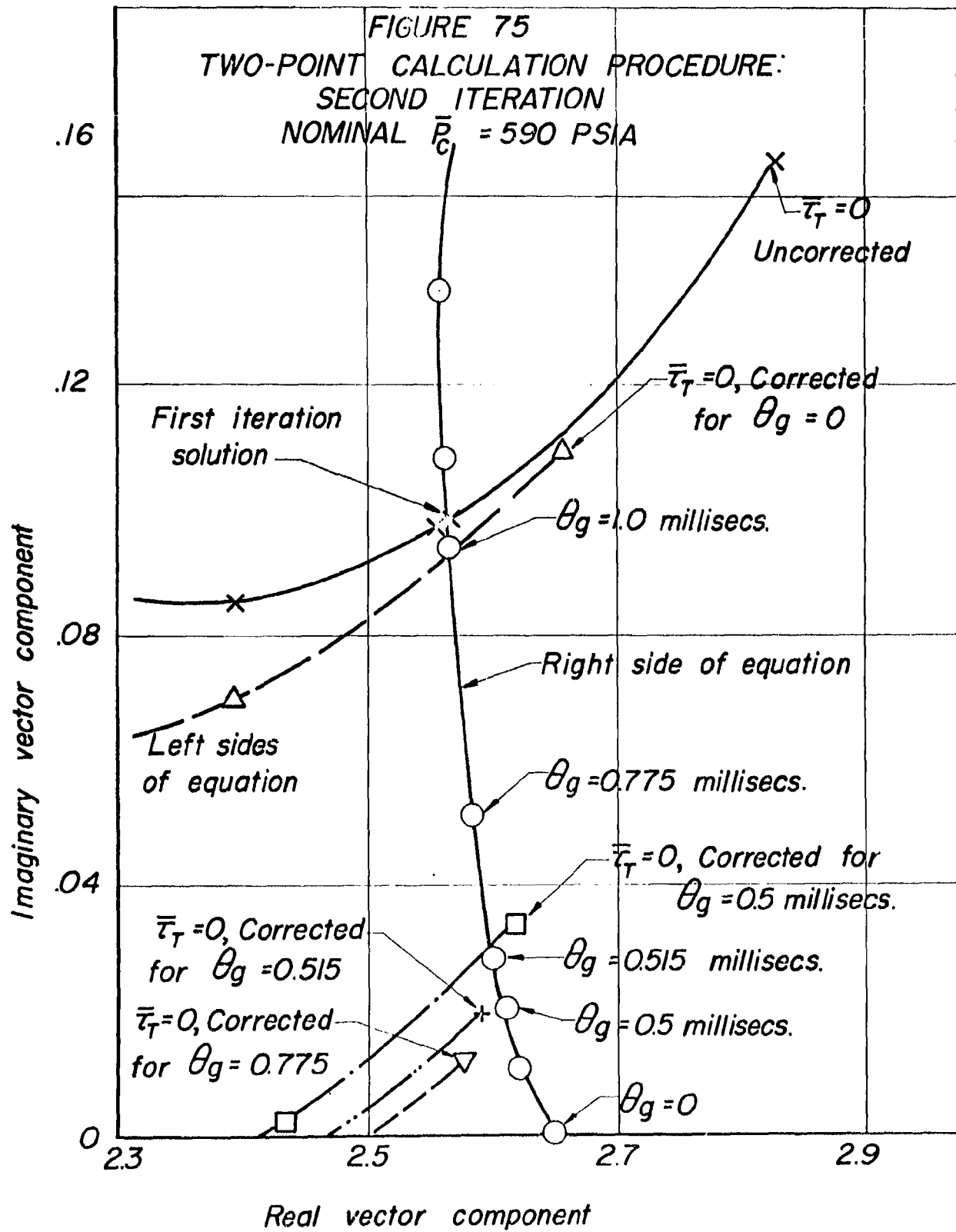


FIGURE 76  
TWO-POINT CALCULATION PROCEDURE:  
THIRD ITERATION

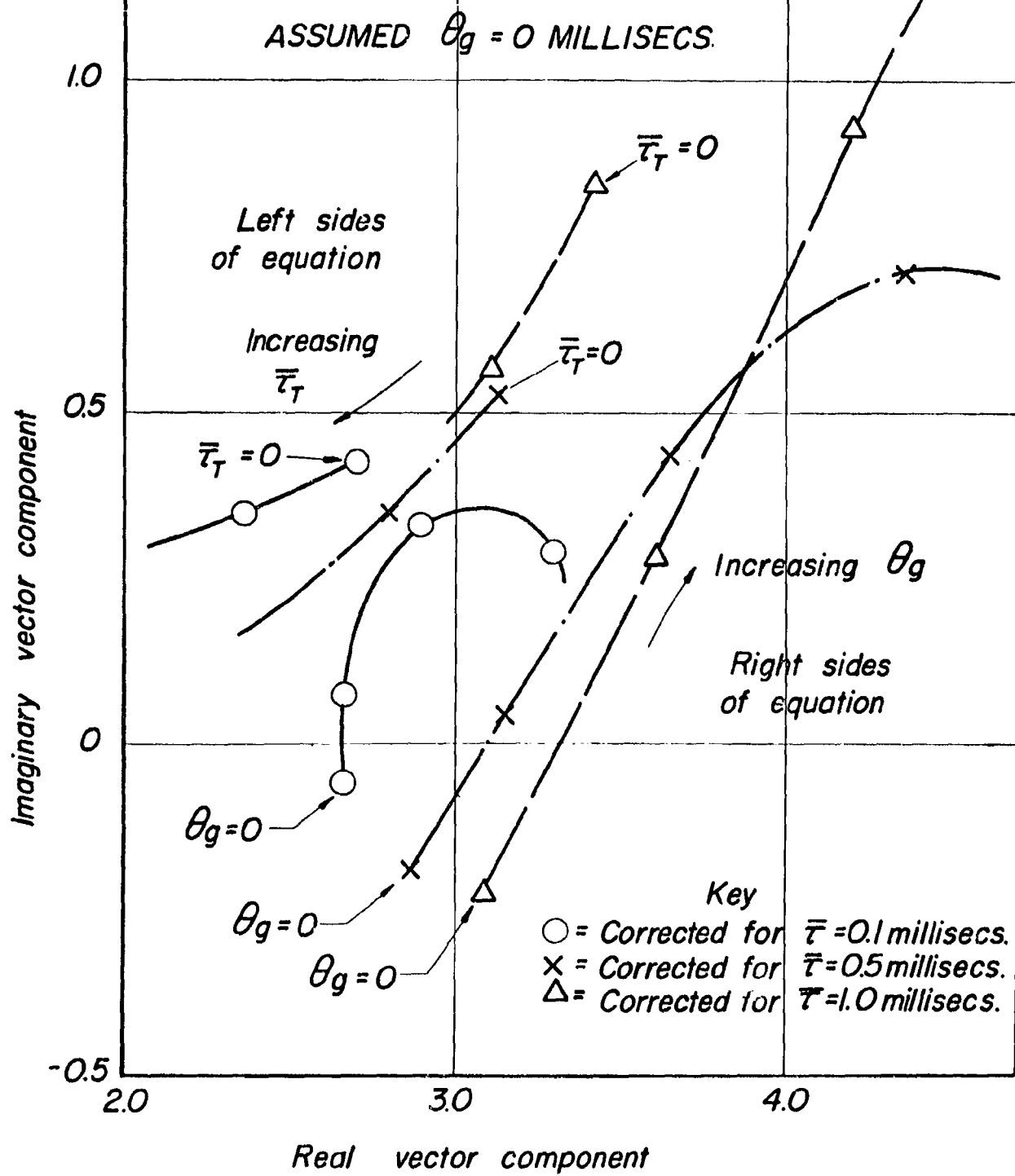
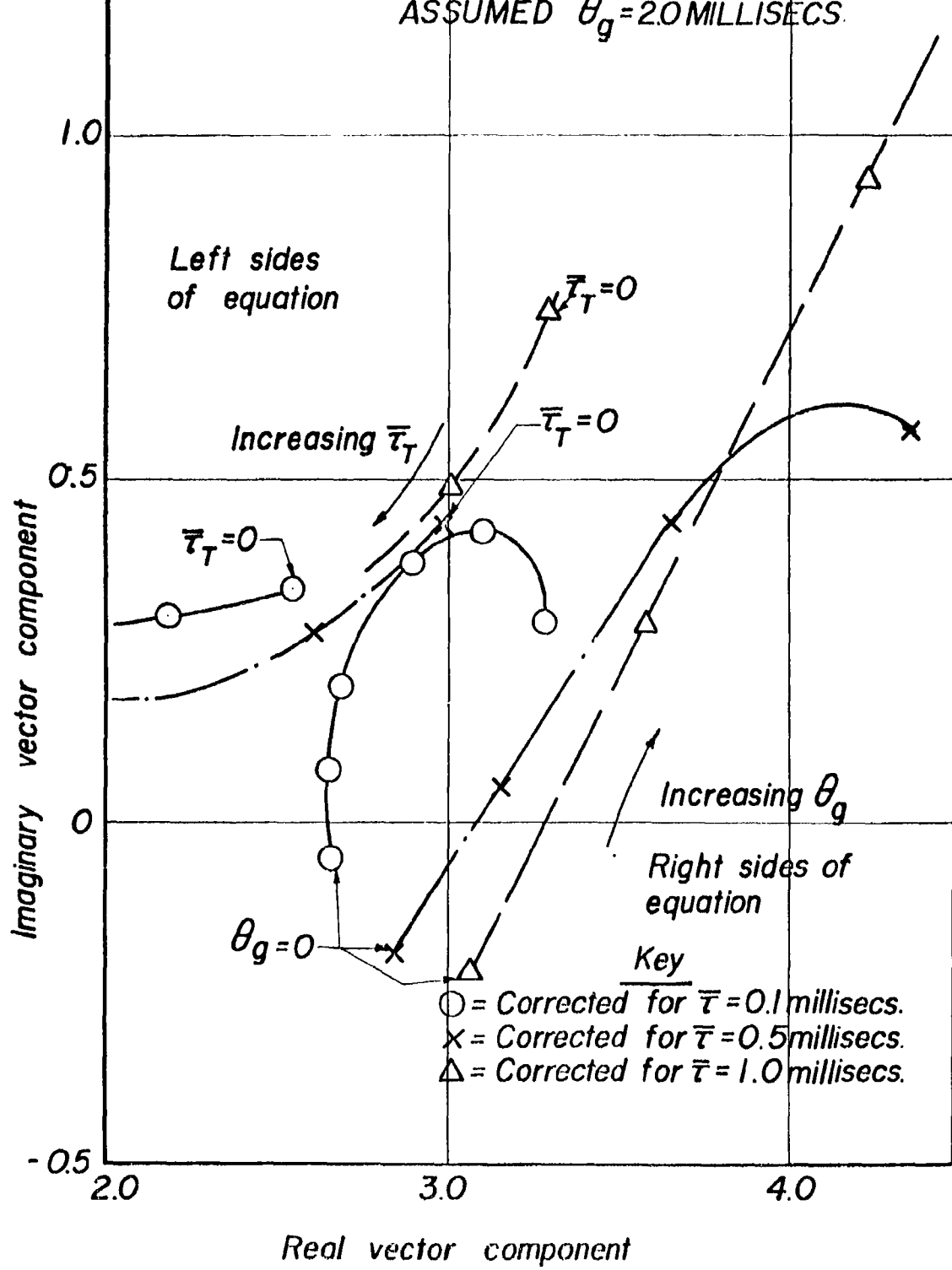


FIGURE 77  
 TWO-POINT CALCULATION PROCEDURE:  
 THIRD ITERATION  
 ASSUMED  $\theta_g = 2.0$  MILLISECS.



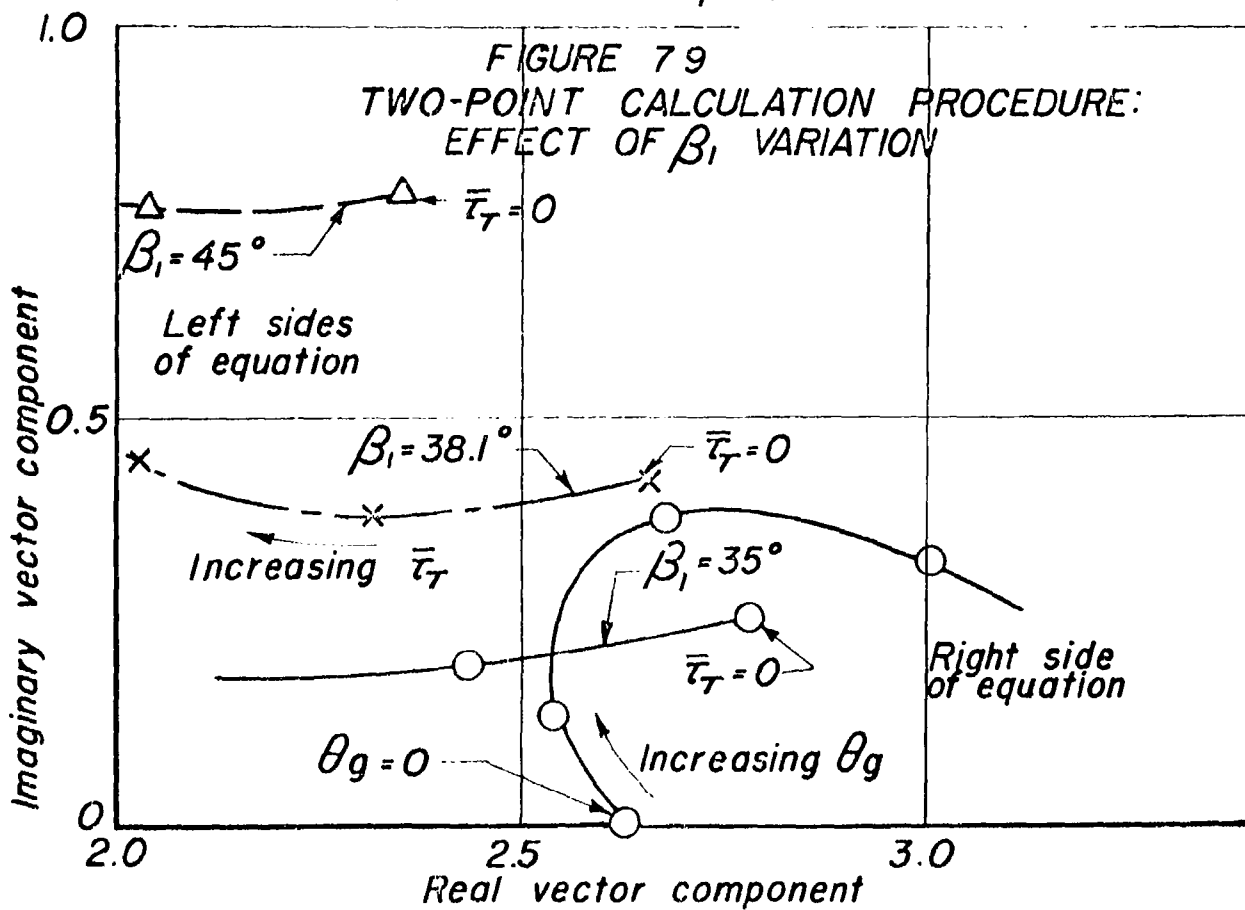
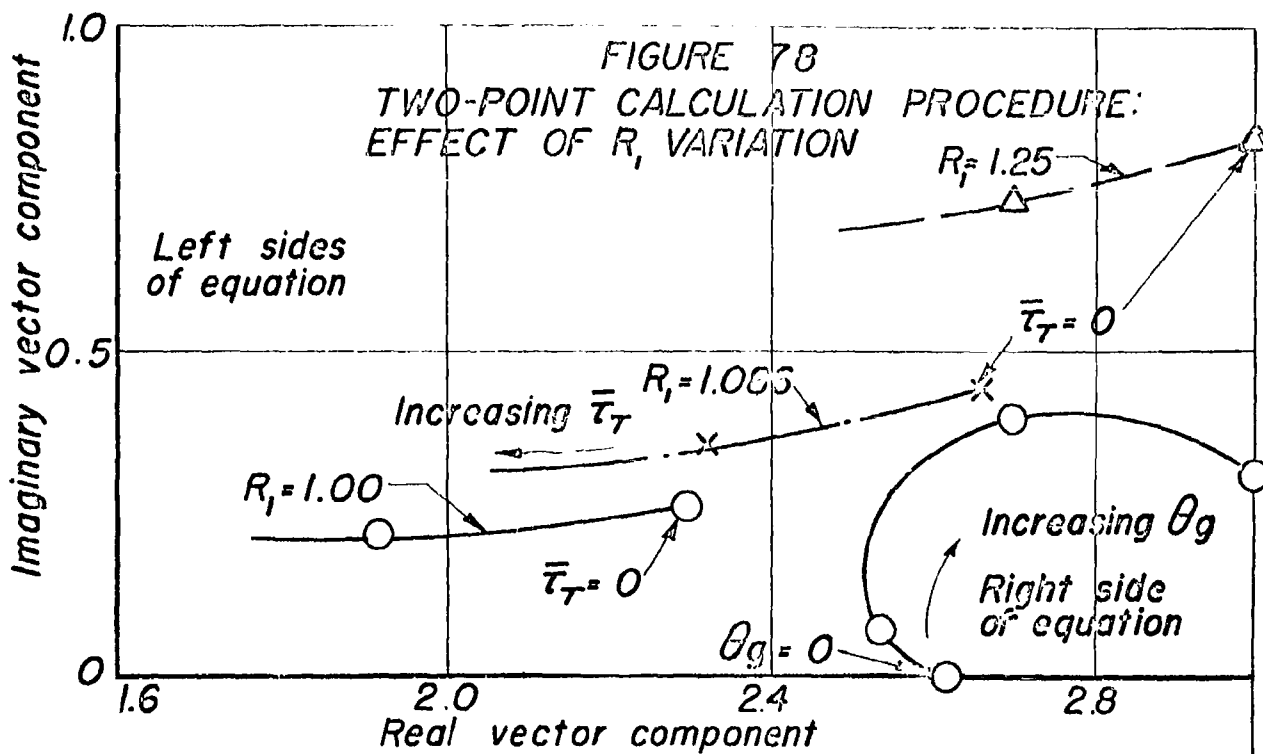
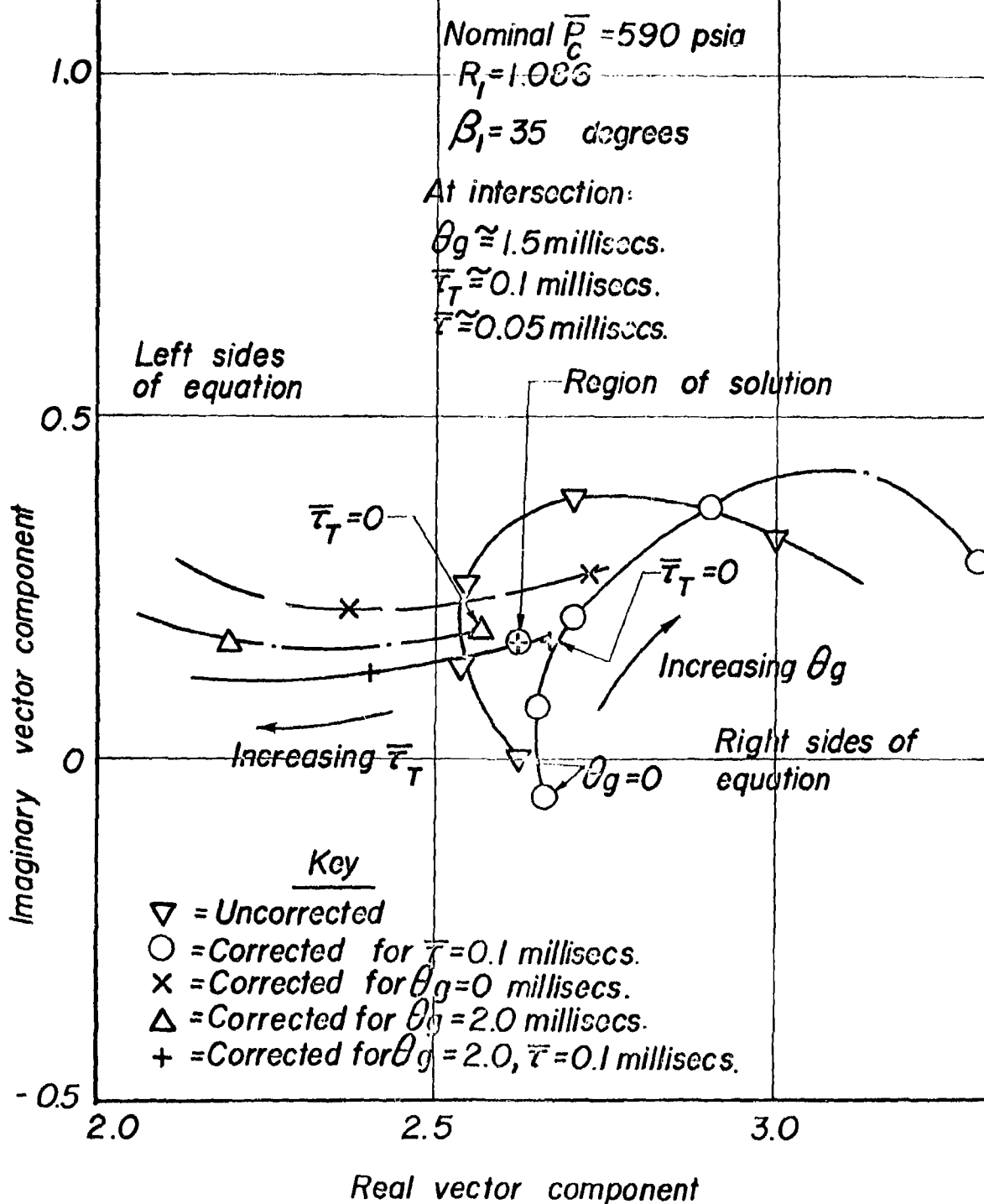


FIGURE 80  
TWO-POINT CALCULATION PROCEDURE:  
SOLUTION WITH MODIFIED  $\beta_i$



## APPENDIX A

DERIVATION OF NOZZLE BOUNDARY EQUATION  
FOR NON-ISENTROPIC OSCILLATIONS AT ENTRANCE

The boundary equation for flow oscillations at the entrance to the subsonic portion of the exhaust nozzle is derived from non-steady, one-dimensional gas dynamics for a number of specific cases in the references previously cited. Tsien (ref. 25) has considered the case of isothermal fluctuations, and Crocco (ref. 26) has extended this to include low and high frequency solutions for arbitrary oscillations as well as a full-frequency solution for the isentropic case. In addition to these treatments, which are based upon a linear velocity gradient along the axis of the subsonic portion of the nozzle, Crocco (ref. 1) has also shown the forms of terms in the low frequency series expansion for isentropic oscillations at the entrance to a nozzle with any general non-linear velocity gradient. It is the purpose of this derivation to extend the low frequency analysis for a non-linear velocity distribution to include the general case of non-isentropic oscillations. The resulting equation in terms of velocity, density, temperature, and entropy perturbations is then transformed through thermodynamic relations and the equation of state into a form suitable for application directly as a boundary condition to the combustion chamber in which the primary variables are velocity or mass flow, pressure and entropy.

Following the notation of Crocco, one may write perturbation equations in the form:

$$\begin{aligned}
 \bar{v} &= \bar{v} + v' \\
 \bar{\rho} &= \bar{\rho} + \rho' \\
 \bar{s}/c_v &= \bar{s}/c_v + s'/c_v \\
 \bar{T} &= \bar{T} + T'
 \end{aligned} \tag{1A}$$

Then, if one considers a length variable,  $x$ , as the distance from the entrance section along the subsonic portions of the nozzle, the equations of motion for the gas (assuming combustion has been completed within the chamber) are written as:

$$\begin{aligned} \frac{\partial}{\partial t} \left( \frac{\rho'}{\rho} \right) + \bar{u} \frac{\partial}{\partial x} \left( \frac{\rho'}{\rho} + \frac{u'}{u} \right) &= 0 \\ \frac{\partial}{\partial t} \left( \frac{u'}{u} \right) + \left( \frac{\rho'}{\rho} + \gamma \frac{u'}{u} \right) \frac{d\bar{u}}{dx} + \bar{u} \frac{\partial}{\partial x} \left( \frac{u'}{u} \right) &= \frac{p'}{p} \frac{d\bar{u}}{dx} - \frac{\bar{p}}{\bar{u}} \frac{\partial}{\partial x} \left( \frac{p'}{p} \right) \quad (2A) \end{aligned}$$

The energy equation, expressing the constancy of entropy following a given fluid mass, becomes:

$$\left( \frac{\partial}{\partial t} + \bar{u} \frac{\partial}{\partial x} \right) \frac{s'}{c_v} = \left( \frac{\partial}{\partial t} + \bar{u} \frac{\partial}{\partial x} \right) \left( \frac{p'}{p} - \gamma \frac{\rho'}{\rho} \right) = 0 \quad (3A)$$

If one postulates an exponential time dependence for the perturbed quantities such that:

$$\begin{aligned} \frac{p'}{p} - \Phi(x)e^{i\omega t} ; \frac{\rho'}{\rho} = \sigma(x)e^{i\omega t} ; \frac{T'}{T} = \Theta(x)e^{i\omega t} \\ \frac{u'}{u} = \nu(x)e^{i\omega t} ; \left( \frac{s'}{c_v} \right)_{\text{entrance}} = \varepsilon, \quad (4A) \end{aligned}$$

then the equations of motion are reduced to the following ordinary differential equations:

$$\begin{aligned} \bar{u} \frac{d\nu}{dx} + \bar{u} \frac{d\sigma}{dx} + i\omega\sigma &= 0 \\ \bar{u} \frac{d\nu}{dx} + \frac{c^2}{\bar{u}} \frac{d\sigma}{dx} + \left( \gamma \frac{d\bar{u}}{dx} + i\omega \right) \nu - (\gamma-1) \frac{d\bar{u}}{dx} \sigma &= \\ - \varepsilon \left( \frac{d\bar{u}}{dx} + i\omega \frac{c^2}{\gamma \bar{u} \varepsilon} \right) e^{-i\omega \int_{x_e}^x \frac{d\bar{u}}{\bar{u}(x')}} & \quad (5A) \end{aligned}$$

Where  $C$  is the local, steady state velocity of sound and where use has been made of the entropy relation from Equation 3A in the form:

$$\frac{s'}{c_v} = \frac{p'}{p} - \gamma \frac{\rho'}{\rho} = f\left(l - \int_{x_e}^x \frac{dx'}{\bar{u}}\right)$$

or:

$$\Phi(x) \cdot \gamma \sigma(x) = e^{-l \omega} \int_{x_e}^x \frac{dx'}{\bar{u}} \quad (6A)$$

If one defines non-dimensional variables as:

$$\xi = \frac{x}{l} \quad (0 \leq \xi \leq 1)$$

$$\omega(\xi) = \bar{u}/c_t \quad (\omega_e \leq \omega \leq 1) \quad (7A)$$

$$\beta = \omega l / c_t$$

where:  $l$  = total length of subsonic portion of nozzle

$c_t$  = velocity of sound at nozzle throat

$e$  = subscript indicating entrance conditions.

then the energy equation in steady state may be written as:

$$\left(\frac{c}{c_t}\right)^2 = \frac{\gamma+1}{\gamma} - \frac{\gamma-1}{\gamma} \omega^2 \quad (8A)$$

and the equations of motion (5A) become:

$$\omega \frac{d\sigma}{d\xi} + \omega \frac{d\omega}{d\xi} + \beta \omega = 0 \quad (9A)$$

$$\begin{aligned} \omega \frac{d\sigma}{d\xi} + \left( \frac{\gamma+1}{\gamma \omega} - \frac{\gamma-1}{\gamma} \omega \right) \frac{d\omega}{d\xi} + \left( \gamma \frac{d\omega}{d\xi} + \beta \omega \right) \omega - (\gamma-1) \frac{d\omega}{d\xi} \sigma = \\ = \xi \left[ \frac{d\omega}{d\xi} + \frac{\beta}{\gamma} \left( \frac{\gamma+1}{\gamma \omega} - \frac{\gamma-1}{\gamma} \right) \right] e^{-\beta \int_{\xi_e}^{\xi} \frac{d\xi}{\omega}} \end{aligned} \quad (10A)$$

Substituting Equation 9A into 10A and defining:

$$\omega' = \frac{d\omega}{d\xi},$$

results in the single equation:

$$\begin{aligned} & \left( \frac{\gamma+1}{2} \right) \left( \frac{1}{\omega} - \omega \right) \frac{d\sigma}{d\xi} + (2\omega' + i\beta) \nu - \left[ (\gamma-1) \omega' + i\beta \right] \sigma = \\ & = \varepsilon \left[ \omega' + \frac{i\beta}{\gamma} \left( \frac{\gamma+1}{2\omega^2} - \frac{\gamma-1}{2} \right) \right] e^{-i\beta \int_0^\xi \frac{d\xi}{\omega}} \end{aligned} \quad (11A)$$

Since no analytical treatment of Equation 11A is possible for general  $\omega(\xi)$ , a solution for the case of low frequency oscillations may be obtained by expanding the unknowns  $\nu$  and  $\sigma$  in a series in  $(i\beta)$ , confining the present analysis to those terms of zeroth and first powers only of the parameter  $(i\beta)$ .

Thus:  $\sigma = \sigma^{(0)} + i\beta \sigma^{(1)} + \dots$

$$\nu = \nu^{(0)} - i\beta \nu^{(1)} + \dots \quad (12A)$$

Before substituting these series expansions, one may reduce Equation 11A to a second order equation in  $\sigma$  only by dividing by the coefficient of the  $\nu$  term, differentiating the entire equation with respect to  $\xi$ , and substituting the relation of 9A. Thus:

$$\begin{aligned} & \frac{d}{d\xi} \left[ \frac{\gamma+1}{2} \left( \frac{1}{\omega} - \omega \right) \frac{d\sigma}{d\xi} \right] - i\beta \sigma - \frac{1}{\omega} \left[ \frac{(\gamma-1)\omega' + i\beta}{2\omega^2 + i\beta} \sigma \right] - \frac{d\sigma}{d\xi} = \\ & = \varepsilon e^{-i\beta \int_0^\xi \frac{d\xi}{\omega}} \left\{ - \frac{i\beta}{\omega} \left[ \omega' + \frac{i\beta}{\gamma} \left( \frac{\gamma+1}{2\omega^2} - \frac{\gamma-1}{2} \right) \right] + \right. \\ & \left. + \frac{d}{d\xi} \left[ \frac{\omega' + \frac{i\beta}{\gamma} \left( \frac{\gamma+1}{2\omega^2} - \frac{\gamma-1}{2} \right)}{2\omega^2 + i\beta} \right] \right\} \end{aligned} \quad (13A)$$

Performing the indicated differentiations, substituting the series expansions of 12A, and neglecting higher order terms, one obtains an equation involving only zeroth and first powers of  $(\xi - \infty)$  as follows:

$$\begin{aligned}
 & \left( \frac{\gamma+1}{\gamma} \right) \left\{ z w' (1-w^2) \frac{d^2 \sigma^{(0)}}{d \xi^2} - \frac{d \sigma^{(0)}}{d \xi} \left[ z w'^2 \left( \frac{1+w^2}{w} \right) + \bar{w} w'' (1-w^2) \right] \right\} + \\
 & + \left( \frac{\gamma+1}{\gamma} \right) i \beta \left\{ z w' (1-w^2) \frac{d^2 \sigma^{(1)}}{d \xi^2} + (1-w^2) \frac{d^2 \sigma^{(0)}}{d \xi^2} - \frac{d \sigma^{(1)}}{d \xi} \left[ z w'^2 \left( \frac{1+w^2}{w} \right) + z w'' (1-w^2) \right] \right\} - \\
 & - \frac{d \sigma^{(0)}}{d \xi} \frac{w'}{w} (1+w^2) \Big\} - 4 w w'^2 \frac{d \sigma^{(0)}}{d \xi} - 4 w w'^2 (i \beta) \frac{d \sigma^{(1)}}{d \xi} - \\
 & - 4 w w' (-\beta) \frac{d \sigma^{(0)}}{d \xi} - 4 w'^2 (-\beta) \sigma^{(0)} - \frac{d \sigma^{(0)}}{d \xi} \left[ z (\gamma-1) w w'^2 \right] - \quad (14A) \\
 & - i \beta \left[ w w' (\gamma+1) \frac{d \sigma^{(0)}}{d \xi} + z (\gamma-1) w w'^2 \frac{d \sigma^{(1)}}{d \xi} + (\gamma-3) w w' \sigma^{(0)} \right] = \\
 & = i \beta \varepsilon \left[ z w'^2 + \left( \frac{\gamma+1}{\gamma} \right) \left( \frac{\partial w'^2}{w^2} + \frac{w''}{w} \right) - w w'' \left( \frac{\partial \gamma-1}{\gamma} \right) \right]
 \end{aligned}$$

Equating the coefficients of terms of like power in  $\varepsilon$  on both sides of the equation produces the two relations:

$$w' (1-w^2) \frac{d^2 \sigma^{(0)}}{d \xi^2} - \frac{d \sigma^{(0)}}{d \xi} \left[ w'^2 \left( \frac{1+w^2}{w} \right) + \bar{w} w'^2 + w'' (1-w^2) \right] = 0 \quad (15A)$$

$$\begin{aligned}
 & w' (1-w^2) \frac{d^2 \sigma^{(1)}}{d \xi^2} + \left( \frac{1-w^2}{z} \right) \frac{d^2 \sigma^{(0)}}{d \xi^2} - \frac{d \sigma^{(1)}}{d \xi} \left[ w'^2 \left( \frac{1+w^2}{w} \right) + \bar{w} w'^2 + w'' (1-w^2) \right] - \\
 & - \frac{d \sigma^{(0)}}{d \xi} \left[ \frac{w'}{z} \left( \frac{1+w^2}{w} \right) + w w' \left( \frac{\gamma+5}{\gamma+1} \right) \right] - \frac{\sigma^{(0)}}{\gamma+1} \left[ 4 w'^2 + (\gamma-3) w w'' \right] = \\
 & = - \frac{\varepsilon}{\gamma+1} \left[ \bar{w} w'^2 + \left( \frac{\gamma+1}{\gamma} \right) \left( \frac{\partial w'^2}{w^2} + \frac{w''}{w} \right) - w w' \left( \frac{\partial \gamma-1}{\gamma} \right) \right] \quad (16A)
 \end{aligned}$$

Equation 15A is a homogeneous linear differential equation of first order in  $\frac{d\sigma^{(0)}}{d\xi}$  and may be solved directly, yielding:

$$\frac{d\sigma^{(0)}}{d\xi} = \frac{C_0 \omega w^1}{(1-w^2)} \xi = -\frac{C_0}{w^2} \left(\frac{1}{1-w^2}\right) \xi \frac{d}{d\xi} (1-w^2),$$

which is integrated again to produce the solution:

$$\sigma^{(0)} = \frac{C_0}{2(1-w^2)} + C_1. \quad (17A)$$

However, the general solution for  $\sigma^{(0)}$  must remain regular as  $w$  approaches 1.0, that is, approaching the sonic throat. Therefore:

$$\begin{aligned} C_0 &= 0 \\ \sigma^{(0)} &= C_1 = \text{CONSTANT} \end{aligned} \quad (18A)$$

Therefore, equating the coefficients of terms of zeroth power in  $(i\beta)$  in Equation 9A,

$$\frac{d\gamma^{(0)}}{d\xi} = -\frac{d\sigma^{(0)}}{d\xi},$$

or:

$$\gamma^{(0)} = \text{CONSTANT} \quad (19A)$$

The constant value of  $\sigma^{(0)}$  must, of course, be equal to the value  $\sigma_e$  at the entrance section, which is determined from thermodynamic relationships (independent of  $\beta$ ) to be:

$$\sigma_e = \frac{\theta_e - \varepsilon}{\gamma - 1} = \sigma^{(0)} \quad (20A)$$

Then, substituting the series expansions for  $\sigma$  and  $\gamma$  into 11A and equating coefficients of zeroth power terms in  $i\beta$ , one obtains:

$$\left(\frac{\gamma+1}{\varepsilon}\right)\left(\frac{1}{\omega} - \omega\right) \frac{d\sigma^{(0)}}{d\xi} + 2\omega^1 \gamma^{(0)} - (\gamma-1) \omega^1 \sigma^{(0)} = \varepsilon \omega^1$$

and, since  $\frac{d\sigma^{(0)}}{d\xi} = 0$ ,

$$\partial w^1 \nu^{(0)} - (\gamma-1) w^1 \sigma^{(0)} = \varepsilon w^1 \quad (21A)$$

Substituting the value of  $\sigma^{(0)} = \sigma_e$  from 20A,

$$\nu^{(0)} = \nu_e^{(0)} - \frac{\varepsilon}{\gamma} + \left(\frac{\gamma-1}{\gamma}\right) \left(\frac{\theta_e - \varepsilon}{\gamma-1}\right)$$

or:

$$\nu^{(0)} = \frac{\theta_e}{\gamma} \quad (22A)$$

Note also that since  $\sigma_e = \text{constant} = \sigma^{(0)}$ , all higher  $\sigma_e^{(k)}$  terms must be zero. Hence,

$$\sigma_e + \sigma_e^{(1)}(\beta) + \sigma_e^{(2)}(\beta) + \dots = \sigma^{(0)}$$

So:

$$\sigma_e^{(1)} = \sigma_e^{(2)} = \dots = \sigma_e^{(r)} = 0 \quad (23A)$$

Returning, now, to Equation 16A and substituting the value of  $\sigma^{(0)}$ , one finds:

$$\begin{aligned} w^1 (1-w^2) \frac{d^2 \sigma^{(1)}}{d\xi^2} &= \left[ w^1 z \left( \frac{1+w^2}{w} \right) + 2w w^1 z + w^2 (1-w^2) \right] \frac{d\sigma^{(1)}}{d\xi} = \\ &= \frac{\theta_e}{\gamma^2-1} \left[ (\gamma-3) w w'' + 4 w^1 z \right] + \frac{\varepsilon}{\gamma} w w'' \left( \frac{\gamma^2+1}{\gamma^2-1} - \frac{1}{w^2} \right) - 2w^1 z \left( \frac{\gamma}{\gamma-1} + \frac{1}{w^2} \right) \end{aligned} \quad (24A)$$

The solution of this equation, which is a first order, non-homogeneous, linear differential equation in  $\frac{d\sigma^{(1)}}{d\xi}$  may be determined in the same manner as that of Equation 15A, giving:

$$\frac{d\sigma^{(1)}}{d\xi} = -\frac{\theta e}{\gamma^2-1} \left[ \frac{(\gamma-3)\omega}{1-\omega^2} + (\gamma-1) \frac{\partial \omega \omega'}{(\gamma-1)(1-\omega^2)^2} \right] \int_{\xi_0}^{\xi} \omega d\xi - \frac{4\omega \omega'}{(\gamma-1)(1-\omega^2)^2} \int_{\xi_0}^{\xi} \frac{d\xi}{\omega} -$$

$$- \frac{\epsilon}{\gamma} \left[ \left( \frac{\omega}{1-\omega^2} \right) \left( \frac{\gamma^2+1}{\gamma^2-1} - \frac{1}{\omega^2} \right) - \frac{\partial}{(\gamma+1)(1-\omega^2)} \right] \int_{\xi_0}^{\xi} \omega d\xi + \frac{\partial}{(\gamma-1)(1-\omega^2)^2} \int_{\xi_0}^{\xi} \frac{d\xi}{\omega} + \frac{C_0 \omega \omega'}{(\gamma-1)(1-\omega^2)^2} \quad (25A)$$

The value of the constant,  $C_0$ , must be chosen such that  $\frac{d\sigma^{(1)}}{d\xi}$  remains finite at  $\xi = 1$ . In order to determine  $C_0$ , one may express 25A in fractional form; thus:

$$\frac{d\sigma^{(1)}}{d\xi} = \left\{ -\frac{\theta e}{\gamma^2-1} \left[ \omega(1-\omega^2)(\gamma-3) + \partial(\gamma-3)\omega \omega' \int_{\xi_0}^{\xi} \omega d\xi - 4\omega \omega' \int_{\xi_0}^{\xi} \frac{d\xi}{\omega} \right] - \right.$$

$$\left. - \frac{\epsilon}{\gamma} \left[ \omega(1-\omega^2) \left( \frac{\gamma^2+1}{\gamma^2-1} - \frac{1}{\omega^2} \right) - \frac{\partial \omega \omega'}{(\gamma+1)} \int_{\xi_0}^{\xi} \omega d\xi + \frac{\partial \omega \omega'}{(\gamma-1)} \int_{\xi_0}^{\xi} \frac{d\xi}{\omega} + C_0 \omega \omega' \right] \right\} \div (1-\omega^2)^2$$

Since the denominator becomes zero at  $\xi = 1$  ( $\omega = 1$ ),  $C_0$  must equal zero in order that the numerator be zero. This leaves  $\left[ \frac{d\sigma^{(1)}}{d\xi} \right]_{\xi=1}$  in the indeterminate form  $0/0$ . Successive applications of L'Hospital's rule

produce:

$$\left( \frac{d\sigma^{(1)}}{d\xi} \right)_{\xi=1} = \left\{ \frac{\theta e}{\gamma^2-1} \left[ 1 \partial \omega \omega'^2 + (\gamma-1)\omega'' + 3(\gamma-3)\omega^2 \omega'' + \partial(3\omega' \omega' + \omega \omega''') \right] \right.$$

$$\left. \left[ (\gamma-1) \int_{\xi_0}^{\xi} \omega d\xi - \epsilon \int_{\xi_0}^{\xi} \frac{d\xi}{\omega} \right] - \frac{\epsilon}{\gamma} \left[ \frac{\partial \omega'^2}{\omega} \left( \frac{1}{\gamma-1} - \frac{1}{\omega^2} \right) + \frac{4\omega'}{\omega^3} + \omega'' \left( 1 - \frac{1}{\omega^2} \right) + \right. \right.$$

$$\left. \left. + \omega'' \left( \frac{3\gamma^2 + \partial\gamma + 1}{\gamma^2-1} \right) - \frac{6\gamma}{\gamma-1} \omega \omega'^2 - \omega^2 \omega''' \left( \frac{3\gamma^2 + 4\gamma - 1}{\gamma^2-1} \right) - \partial(3\omega' \omega'' + \omega \omega''') \right] \right\} \div \left[ 8\omega^2 \omega'^2 - 4(\omega'^2 + \omega \omega'') (1 - \omega^2) \right]_{\xi=1}$$

In this last expression the denominator is no longer zero, and the value of  $\left(\frac{d\sigma^{(1)}}{d\xi}\right)_{\xi=1}$  may be evaluated, yielding:

$$\left(\frac{d\sigma^{(1)}}{d\xi}\right)_{\xi=1} = -\frac{\Theta e}{\gamma^2-1} \left[ 1 + \left(\frac{\gamma-1}{3}\right) \frac{w_t''}{w_t'} \right] - \frac{\epsilon}{3\gamma(\gamma-1)} \left[ \frac{w_t''}{w_t'} + \frac{4}{\gamma-1} - 2\gamma + \gamma+1 \right] \quad (27A)$$

For monotonically increasing  $w_t$  (and hence  $w_t' \neq 0$ ), and the expression is regular.

Having determined the value of  $C_0$  and satisfied the non-singularity of  $\frac{d\sigma^{(1)}}{d\xi}$  at  $\xi = 1$  for this value, one may now return to Equation 25A and integrate directly (integration by parts on the right-hand side) to obtain

$$\sigma^{(1)} = \frac{\Theta e}{\gamma^2-1} \left[ 2 \int_0^\xi \frac{wd\xi}{1-w^2} - 2 \int_0^\xi \frac{d\xi}{w(1-w^2)} + \frac{1}{(1-w^2)} \int_0^\xi \frac{d\xi}{w} - \frac{(\gamma-1)}{(1-w^2)} \int_0^\xi wd\xi \right] -$$

$$- \frac{\epsilon}{\gamma} \left[ \left( \frac{\gamma}{\gamma-1} \right) \left( \int_0^\xi \frac{wd\xi}{1-w^2} - \int_0^\xi \frac{d\xi}{w(1-w^2)} \right) + \frac{1}{(1-w^2)} \left( \frac{1}{\gamma-1} \int_0^\xi \frac{d\xi}{w} - \frac{1}{\gamma+1} \int_0^\xi wd\xi \right) \right] + C_1 \quad (28A)$$

The value of  $C_1$  is determined by the boundary condition at the entrance, namely that  $C_1 = -C_0 e^{(\gamma-1)}$ . Hence, from Equation 23A,

$$C_0 e^{(\gamma-1)} = 0$$

Thus:

$$C_1 = \frac{\Theta e}{\gamma^2-1} \left[ 2 \left( \int_0^\xi \frac{wd\xi}{1-w^2} - \int_0^\xi \frac{d\xi}{w(1-w^2)} \right) + \frac{1}{1-w^2} \left( \int_0^\xi \frac{d\xi}{w} - (\gamma-1) \int_0^\xi wd\xi \right) \right] - \frac{\epsilon}{\gamma} \left[ \frac{\gamma}{\gamma-1} \left( \int_0^\xi \frac{wd\xi}{1-w^2} - \int_0^\xi \frac{d\xi}{w(1-w^2)} \right) + \frac{1}{1-w^2} \left( \frac{1}{\gamma-1} \int_0^\xi \frac{d\xi}{w} - \frac{1}{\gamma+1} \int_0^\xi wd\xi \right) \right] \quad (29A)$$

Substituting this value of  $\zeta$  into the expression for  $\sigma^{(1)}$  in 28A gives:

$$\begin{aligned}\sigma^{(1)} = & \frac{2\theta_e}{\gamma^2 - 1} \left\{ \frac{1}{(1-w^2)} \left[ w^2 \int_1^\xi \frac{d\xi}{w} - \left(\frac{\gamma-1}{2}\right) \int_1^\xi w d\xi \right] + \right. \\ & + \frac{1}{1-w_e^2} \left[ w_e^2 \int_0^1 \frac{d\xi}{w} - \left(\frac{\gamma-1}{2}\right) \int_0^1 w d\xi \right] \left. \right\} - \frac{\epsilon}{(\gamma-1)(1-w^2)} \left[ (w^2 - \frac{\gamma-1}{\gamma}) \int_1^\xi \frac{d\xi}{w} - (30A) \right. \\ & \left. - \left(\frac{\gamma-1}{\gamma+1}\right) \int_1^\xi w d\xi \right] + \frac{1}{(1-w_e^2)} \left[ (w_e^2 - \frac{\gamma-1}{\gamma}) \int_0^1 \frac{d\xi}{w} - \left(\frac{\gamma-1}{\gamma+1}\right) \int_0^1 w d\xi \right]\end{aligned}$$

The solution for  $\gamma^{(1)}$  now becomes merely a matter of substitution of derived quantities. Referring to Equation 11A and rewriting gives (for terms of first order in  $i\beta$ ):

$$\begin{aligned}\left(\frac{\gamma+1}{2}\right)\left(\frac{1-w^2}{w}\right) \frac{d\sigma^{(1)}}{d\xi} + 2w\gamma^{(1)} - (\gamma-1)w\sigma^{(1)} = \\ = \sigma^{(0)} - \gamma^{(0)} + \frac{\epsilon}{\gamma} \left( \frac{\gamma+1}{2w^2} - \frac{\gamma-1}{2} \right) - \epsilon w^2 \int_0^\xi \frac{d\xi}{w}\end{aligned}$$

Dividing by the coefficient of  $\gamma^{(1)}$  and solving for  $\gamma^{(1)}$  gives:

$$\begin{aligned}\gamma^{(1)} = & \frac{\sigma^{(0)} - \gamma^{(0)}}{2w^2} + \frac{(\gamma-1)\sigma^{(1)}}{2} - \left(\frac{\gamma+1}{2}\right) \left(\frac{1-w^2}{2w^2}\right) \frac{d\sigma^{(1)}}{d\xi} + \\ & + \frac{\epsilon}{4\gamma} \left( \frac{\gamma+1}{w^2 w^2} - \frac{\gamma-1}{w^2} \right) - \frac{\epsilon}{2} \int_0^\xi \frac{d\xi}{w}\end{aligned}\quad (31A)$$

Substituting Equations 30A, 25A, 22A, and 20A for  $\sigma^{(1)}$ ,  $\frac{d\sigma^{(1)}}{d\xi}$ ,  $\gamma^{(0)}$ , and  $\sigma^{(0)}$ , respectively, gives:

$$\gamma^{(1)} = \frac{\theta_e}{\gamma+1} \left[ \left( \frac{w^2 - \frac{\gamma+1}{\gamma-1}}{1-w^2} \right) \int_1^\xi \frac{d\xi}{w} + \left( \frac{1}{1-w^2} \right) \int_1^\xi w d\xi + \left( \frac{w_e^2}{1-w_e^2} \right) \int_0^1 \frac{d\xi}{w} - \left( \frac{\gamma-1}{2} \right) \frac{1}{1-w_e^2} \int_0^1 w d\xi \right] + \quad (32A)$$

$$+ \frac{\epsilon}{2\gamma} \left[ \left( \frac{2}{\gamma-1} \right) \frac{1}{1-w^2} \int_1^\xi \frac{d\xi}{w} + \left( \frac{\gamma^2 - 2\gamma - 1}{\gamma+1} \right) \frac{1}{1-w^2} \int_1^\xi w d\xi - \left( \frac{1}{1-w_e^2} \right) \int_0^1 \frac{d\xi}{w} + \frac{\gamma(\gamma-1)}{\gamma+1} \left( \frac{1}{1-w_e^2} \right) \int_0^1 w d\xi \right]$$

The complete solutions for  $\sigma$  and  $\gamma'$  are then (up to terms of first order

in  $i\beta$ ):

$$\begin{aligned} \sigma(\xi) = & \frac{\theta e}{\gamma-1} \left\{ 1 - \frac{2i\beta}{\gamma+1} \left[ \left( \frac{w^2}{1-w^2} \right) \int_0^\xi \frac{d\xi}{w} - \left( \frac{\gamma-1}{\gamma} \right) \frac{1}{1-w^2} \int_0^\xi w d\xi + \right. \right. \\ & \left. \left. + \frac{we^\xi}{1-w^2} \int_0^\xi \frac{d\xi}{w} - \left( \frac{\gamma-1}{\gamma} \right) \frac{1}{1-w^2} \int_0^\xi w d\xi \right] \right\} - \left( \frac{\xi}{\gamma-1} \right) \left\{ 1 + i\beta \left[ \left( \frac{w^2 - \frac{\gamma-1}{\gamma}}{1-w^2} \right) \int_0^\xi \frac{d\xi}{w} - \right. \right. \\ & \left. \left. - \left( \frac{\gamma-1}{\gamma+1} \right) \frac{1}{1-w^2} \int_0^\xi w d\xi + \left( \frac{w^2 - \frac{\gamma-1}{\gamma}}{1-w^2} \right) \int_0^\xi \frac{d\xi}{w} - \left( \frac{\gamma-1}{\gamma+1} \right) \frac{1}{1-w^2} \int_0^\xi w d\xi \right] \right\} \right\} \end{aligned} \quad (33A)$$

and:

$$\begin{aligned} \gamma'(\xi) = & \theta e \left\{ \frac{1}{2} + \frac{i\beta}{\gamma+1} \left[ \left( \frac{w^2 - \frac{\gamma+1}{\gamma-1}}{1-w^2} \right) \int_0^\xi \frac{d\xi}{w} + \left( \frac{1}{1-w^2} \right) \int_0^\xi w d\xi + \left( \frac{we^\xi}{1-w^2} \right) \int_0^\xi \frac{d\xi}{w} - \right. \right. \\ & \left. \left. - \left( \frac{\gamma-1}{\gamma} \right) \frac{1}{1-w^2} \int_0^\xi w d\xi \right] \right\} + \frac{e i \beta}{\gamma} \left[ \left( \frac{\partial}{\partial \gamma} \right) \frac{1}{1-w^2} \int_0^\xi \frac{d\xi}{w} + \right. \\ & \left. + \left( \frac{\gamma^2 - 2\gamma - 1}{\gamma+1} \right) \frac{1}{1-w^2} \int_0^\xi w d\xi - \left( \frac{1}{1-w^2} \right) \int_0^\xi \frac{d\xi}{w} + \frac{\gamma(\gamma-1)}{(\gamma+1)} \frac{1}{1-w^2} \int_0^\xi w d\xi \right] \end{aligned} \quad (34A)$$

Since the entrance conditions at the nozzle form a boundary condition for the combustion chamber, it is necessary to determine  $\sigma_e$  and  $\gamma'_e$ , which are the values of  $\sigma(\xi)$  and  $\gamma'(\xi)$  for  $\xi = 0$ .

Substituting  $\xi = 0$  into Equation 33A produces the result previously determined, e.g.,

$$\sigma_e^{(1)} = 0, \text{ and } \sigma_e^{(0)} - \sigma_e = \frac{\theta e - \xi}{\gamma-1}$$

From Equation 34A, when  $\xi = 0$ , one obtains:

$$\gamma'_e = \frac{\theta e}{\xi} \left[ 1 + \frac{i\beta}{(1-w_e^2)(\gamma-1)} \left( \int_0^\xi \frac{d\xi}{w} - \int_0^\xi w d\xi \right) \right] - \frac{\xi}{\gamma} \left( \frac{i\beta}{1-w_e^2} \right) \left( \frac{\gamma+1}{\gamma-1} \right) \left( \int_0^\xi \frac{d\xi}{w} - \int_0^\xi w d\xi \right) \quad (35A)$$

It is convenient to apply this boundary condition in terms of  $\phi_e$  and  $\epsilon$  rather than  $\sigma_e$ ,  $\theta_e$ , and  $\epsilon$ . The relating equations are those of the perfect gas law and the previous equation for  $\sigma_e$ :

$$\frac{P}{P_0} = \frac{\rho}{\rho_0} \frac{T}{T_0}$$

$$\phi_e = \sigma_e - \theta_e \quad (\text{for small perturbations})$$

or:

$$\theta_e = \phi_e - \sigma_e$$

and:

$$\sigma_e = \frac{\theta_e - \epsilon}{\gamma - 1}$$

Combining these gives:

$$\theta_e = \phi_e + \frac{\epsilon - \theta_e}{\gamma - 1}$$

$$\theta_e = \left( \frac{\gamma - 1}{\gamma} \right) \phi_e + \frac{\epsilon}{\gamma} \quad (36A)$$

Substituting this value for  $\theta_e$  into 35A produces:

$$\gamma_e = \frac{\phi_e}{\gamma} \left[ \frac{\gamma - 1}{\gamma} + \frac{i\beta}{(1 - \omega_e^2)} \left( \int_0^1 \frac{d\xi}{w} - \frac{\gamma - 1}{2} \int_0^1 w d\xi \right) \right] + \frac{\epsilon}{\gamma} \left[ 1 - \frac{i\beta}{(1 - \omega_e^2)} \int_0^1 \frac{d\xi}{w} \right] \quad (37A)$$

In terms of exit mass flow from the chamber, this relation is slightly modified;

thus:

$$1 + \mu_e = \frac{m}{\dot{m}} = \frac{\rho u A}{\bar{\rho} \bar{u} A} = (1 + \sigma_e)(1 + \gamma_e) = 1 + \gamma_e + \sigma_e$$

$$\mu_e = \gamma_e + \sigma_e = \gamma_e + \frac{\theta_e - \epsilon}{\gamma - 1} \quad (38A)$$

$$\mu_e = \gamma_e + \phi_e/\gamma - \epsilon/\gamma$$

Employing the value of  $\nu_e$  from Equation 37A, the expression for mass flow fluctuation at the nozzle entrance becomes:

$$\mu_e = \frac{\Phi e}{\gamma} \left[ \frac{r+1}{2} + \frac{i\beta}{(1-w_e^2)} \left( \int_0^1 \frac{d\xi}{w} - \frac{r-1}{2} \int_0^1 w d\xi \right) \right] - \frac{\xi}{2\gamma} \left[ 1 + \frac{i\beta}{(1-w_e^2)} \int_0^1 \frac{d\xi}{w} \right] \quad (39A)$$

The two integrals,  $\int \frac{d\xi}{w}$  and  $\int w d\xi$ , appearing in Equations 37A and 39A are completely determined by the geometry of the exhaust nozzle and the specific heat ratio of the combustion gases within the nozzle, since flow through the subsonic portion of this nozzle is assumed isentropic following a fluid particle. For application in the combustion chamber equation, these integrals are combined with their multiplying constant to form two non-dimensional velocity parameters,  $w_1$  and  $w_2$ , defined by:

$$w_1 = \frac{1}{(1-w_e^2)} \int_0^1 \frac{d\xi}{w} \quad (40A)$$

$$w_2 = \frac{1}{(1-w_e^2)} \int_0^1 w d\xi$$

The order of magnitude of these quantities is illustrated by the numerical example carried out for the particular exhaust nozzle employed in the bipropellant rocket motor tests described previously in the text. This is a double-conical nozzle with a circular arc contour at the throat section, and has the following dimensions:

Entrance diameter = 3.00 inches

Throat diameter = 0.875 inch

Length of subsonic portion = 1.974 inches

Half-angle of entrance cone =  $30^\circ$

Circular arc radius at throat = 0.50 inch

With this geometry, for combustion gases with an average specific heat ratio in the subsonic portion of the nozzle of 1.20, the velocity parameters have the values:

$$W_1 = 8.078$$

$$W_2 = 0.240$$

APPENDIX BMETHOD OF SOLUTION OF VELOCITY  
PERTURBATION INTEGRAL EQUATION

The zeroth iteration of the perturbation equation for axial distribution of the amplitude of disturbances in gas velocity has been derived in the refined theoretical analysis and appears as Equation 135 in the following form:

$$\frac{\gamma \bar{v}^{(0)}(x)}{\Phi_0} = -\gamma k \bar{u}_L(x) \frac{d \bar{u}(x)}{dx} e^{-s \bar{\tau}_T(x)} \int_0^x \frac{d D(x')}{dx'} dx' \int_0^{x'} \frac{\bar{v}^{(0)}(x'')}{\Phi_0} e^{(s+k) \bar{\tau}_T(x'')} dx'' - \frac{\gamma \eta_0 \bar{u}_{L0}}{\Phi_0} \bar{u}_L(x) \frac{d \bar{u}(x)}{dx} e^{-s \bar{\tau}_T(x)} D(x), \quad (135)$$

where the quantity  $D(x)$  is defined by:

$$D(x) = \int_0^x \frac{e^{-k \bar{\tau}_T(x')}}{\bar{u}_L^{(3)}(x')} dx'$$

and:

$$\bar{\tau}_T(x) = \int_0^x \frac{dx'}{\bar{u}_L(x')}$$

Here the velocity perturbation,  $\frac{\bar{v}^{(0)}(x)}{\Phi_0}$ , appears as the unknown on the left side of the equation as well as within the interior integral on the right side of the equation. A solution to this integral equation by the introduction of new variables in an integrated form was suggested by Crocco and is presented in detail herein. The judicious choice of these new variables transforms Equation 135 into a second order, linear, ordinary differential equation in one of the unknowns which is amenable to straightforward solution.

This solution is then transformed back into the original variables, resulting in a simple expression for the zeroth iteration of gas velocity perturbations.

If two integral variables are defined as:

$$I_{\gamma}(x) = \int_0^x \frac{z^{(0)}(x')}{\phi_0} e^{-(s+k)\bar{\tau}_T(x')} dx', \quad (1B)$$

and:

$$J_{\gamma}(x) = \int_0^x \frac{e^{-k\bar{\tau}_T(x')}}{\bar{u}_L^3(x')} I_{\gamma}(x') dx',$$

Then the gas velocity perturbation may be expressed as:

$$\frac{v^{(0)}(x)}{\phi_0} = e^{-(s+k)\bar{\tau}_T(x)} \frac{dI_{\gamma}(x)}{dx},$$

and Equation 135 takes the form:

$$e^{-k\bar{\tau}_T(x)} \frac{dI_{\gamma}(x)}{dx} = -k\bar{u}_L(x) \frac{d\bar{u}}{dx} J_{\gamma}(x) - \frac{\gamma_0 \bar{u}_{L0}}{\phi_0} \bar{u}_L(x) \frac{d\bar{u}(x)}{dx} D(x), \quad (2B)$$

However, from the definition of  $J_{\gamma}(x)$ ,

$$J_{\gamma}(x) = \bar{u}_L^2(x) e^{k\bar{\tau}_T(x)} \frac{dJ_{\gamma}(x)}{dx},$$

so that:

$$e^{-k\bar{\tau}_T(x)} \frac{dI_{\gamma}(x)}{dx} = \bar{u}_L^2(x) \frac{dJ_{\gamma}(x)}{dx} \left( k + \frac{d\bar{u}_L}{dx} \right) + \bar{u}_L^3(x) \frac{d^2 J_{\gamma}(x)}{dx^2}.$$

Substitution of this relation into Equation 2B produces the following second order differential equation in  $J_V(x)$  :

$$\bar{u}_L^2(x) \frac{d^2 J_V(x)}{dx^2} + \left( K + 3 \frac{d\bar{u}_L}{dx} \right) \bar{u}_L(x) \frac{d J_V(x)}{dx} + K \frac{d\bar{u}(x)}{dx} J_V(x) = - \frac{\eta_0 \bar{u}_{L0}}{\phi_0} D(x) \frac{d\bar{u}(x)}{dx}$$

which may be arranged in the form:

$$\frac{d}{dx} \left[ \bar{u}_L^2(x) \frac{d J_V(x)}{dx} \right] + \left( K + \frac{d\bar{u}_L}{dx} \right) \bar{u}_L(x) \frac{d J_V(x)}{dx} + K \frac{d\bar{u}(x)}{dx} J_V(x) = \frac{\eta_0 \bar{u}_{L0}}{\phi_0} D(x) \frac{d\bar{u}(x)}{dx} \quad (3B)$$

This equation is considerably simplified by noting from the steady state droplet dynamics relation (Equation 57) that:

$$K + \frac{d\bar{u}_L(x)}{dx} = K \frac{\bar{u}(x)}{\bar{u}_L(x)}$$

Substitution of this expression into Equation 3B yields:

$$\frac{d}{dx} \left[ \bar{u}_L^2(x) \frac{d J_V(x)}{dx} + K \bar{u}(x) J_V(x) \right] = - \frac{\eta_0 \bar{u}_{L0}}{\phi_0} D(x) \frac{d\bar{u}(x)}{dx} \quad (4B)$$

The boundary conditions at the injector face,  $x=0$ , show that  $J_V(0)=0$ ;  $\bar{u}(0)=0$ ;  $I_V(0)=0$ ;  $J_V'(0)=0$  and  $D(0)=0$ . With these in mind, Equation 138 may be integrated twice to give:

$$J_V(x) = - \frac{\eta_0 \bar{u}_{L0}}{\phi_0} \int_0^x \frac{e^{K \int_{x'}^x \frac{\bar{u}(x'')}{\bar{u}_L^2(x'')} dx''}}{\bar{u}_L^2(x')} dx' \int_0^{x'} D(x'') \frac{d\bar{u}(x'')}{dx''} dx'' \quad (5B)$$

Substituting this result into Equation 135 gives:

$$\frac{Y_V(x)}{\phi_0} = \frac{\gamma \eta_0 \bar{u}_{L0}}{\phi_0} \bar{u}_L(x) \frac{d\bar{u}(x)}{dx} e^{-K \int_x^0 \frac{\bar{u}(x'')}{\bar{u}_L^2(x'')} dx''} \left[ K \int_0^x \frac{e^{K \int_{x'}^x \frac{\bar{u}(x'')}{\bar{u}_L^2(x'')} dx''}}{\bar{u}_L^2(x')} dx' \int_0^{x'} D(x'') \frac{d\bar{u}(x'')}{dx''} dx'' \right] \quad (6B)$$

One may simplify the quantity within brackets on the right side of Equation 6B. Thus, defining this quantity as  $K(x)$  and integrating by parts, one obtains:

$$K(x) = - \int_0^x e^{-\int_x^{x''} \frac{\bar{U}_L(x'')}{\bar{U}_{L0}(x'')} dx''} \frac{dD(x')}{dx'} dx' - \int_0^x \frac{Ke^{-\int_x^{x''} \frac{\bar{U}_L(x'')}{\bar{U}_{L0}(x'')} dx''}}{\bar{U}_{L0}(x')} dx' \int_0^x \bar{U}(x'') \frac{dD(x'')}{dx''} dx'' \quad (7B)$$

The steady state droplet dynamics equation again furnishes a useful relation, e.g.,

$$\frac{K \bar{U}(x)}{\bar{U}_{L0}^2(x)} = \frac{K}{\bar{U}_{L0}(x)} + \frac{1}{\bar{U}_{L0}(x)} \frac{d\bar{U}_L(x)}{dx}$$

so that:

$$e^{-K \int_x^{x''} \frac{\bar{U}_L(x'')}{\bar{U}_{L0}(x'')} dx''} = e^{-\int_x^{x''} \frac{d \ln \bar{U}_L(x'')}{\bar{U}_{L0}(x'')} dx''} = \frac{\bar{U}_L(x'')}{\bar{U}_{L0}(x)} e^{-K [\bar{\epsilon}_T(x'') - \bar{\epsilon}_T(x)]},$$

and Equation 7B reduces to:

$$K(x) = - \frac{e^{-K \bar{\epsilon}_T(x)}}{\bar{U}_{L0}(x)} \left\{ \int_0^x \frac{dx'}{\bar{U}_{L0}^2(x')} + \int_0^x \frac{e^{-K \bar{\epsilon}_T(x')}}{\bar{U}_{L0}(x')} dx' \int_0^{x'} \left[ \frac{K}{\bar{U}_{L0}(x'')} + \frac{1}{\bar{U}_{L0}(x'')} \frac{d\bar{U}_L(x'')}{dx''} \right] e^{-K \bar{\epsilon}_T(x'')} dx'' \right\} \quad (8B)$$

Inspection of the interior integral in the second term within the brackets shows it to be an exact differential of the quantity  $- \frac{e^{-K \bar{\epsilon}_T(x'')}}{\bar{U}_{L0}(x'')}$ ,

so that Equation 8B becomes:

$$K(x) = - \frac{e^{-K \bar{\epsilon}_T(x)}}{\bar{U}_{L0}(x)} \left\{ \int_0^x \frac{dx'}{\bar{U}_{L0}^2(x')} + \int_0^x \frac{e^{-K \bar{\epsilon}_T(x')}}{\bar{U}_{L0}(x')} \left[ \frac{1}{\bar{U}_{L0}} - \frac{e^{-K \bar{\epsilon}_T(x'')}}{\bar{U}_{L0}(x')} \right] dx' \right\}$$

or:

$$K(x) = -\frac{e^{-K\bar{\tau}_T(x)}}{\bar{u}_L(x)} \left\{ \int_0^x \frac{dx'}{\bar{u}_L(x')} + \frac{1}{K\bar{u}_{L0}} \int_0^x \frac{K}{\bar{u}_L(x')} e^{K\bar{\tau}_T(x')} dx' - \int_0^x \frac{dx'}{\bar{u}_L^2(x')} \right\}$$

$$= \frac{e^{-K\bar{\tau}_T(x)}}{K\bar{u}_{L0}\bar{u}_L(x)} \int_0^x \frac{d}{dx'} \left[ e^{K\bar{\tau}_T(x')} \right] dx'$$

which is integrated directly to produce the simple result:

$$K(x) = \frac{e^{-K\bar{\tau}_T(x)-1}}{K\bar{u}_{L0}\bar{u}_L(x)} \quad (9B)$$

Finally, substituting this value of  $K(x)$  into its proper place within the brackets of Equation 6B, one obtains the desired expression for the gas velocity perturbation (in the zeroth iteration) as given in Eq. 136. Thus

$$\frac{\gamma v^{(0)}(x)}{\phi_0} = \frac{\gamma \eta_0}{K\phi_0} \frac{du(x)}{dx} e^{-S\bar{\tau}_T(x)} \left[ e^{-K\bar{\tau}_T(x)-1} \right]. \quad (136)$$

APPENDIX CTHEORETICAL CALCULATION OF PRESSURE-FLOW PHASE LAG IN THE BIFROPELLANT ROCKET MOTOR INJECTORS

The energy equation for one-dimensional, incompressible flow may be expressed in the form:

$$\frac{\partial E_K}{\partial t} + \dot{m} (\epsilon_2 - \epsilon_1) = \frac{\dot{m}}{\rho} (P_1 - P_2)$$

between two stations (1) and (2), where

$E_K$  = total kinetic energy enclosed between Stations (1) and (2).

$\epsilon$  = kinetic energy per unit mass at any one station.

$\dot{m}$  = mass flow rate.

$\rho$  = fluid density.

$P$  = pressure at any one station.

Expressing these quantities in terms of velocity, area, density, etc., gives:

$$E_K = \int_{1}^{2} \rho A \frac{u^2}{2} dx$$

and:

$$\epsilon = \frac{u^2}{2}$$

Since the fluid is incompressible,

$$u_2 A_2 = u_1 A_1 = u A$$

So:

$$E_K = \int_{1}^{2} \rho A \frac{u_2^2}{2} \left( \frac{A_2}{A} \right)^2 dx = \frac{u_2^2}{2} \left[ \rho A_2^2 \int_{1}^{2} \frac{dx}{A} \right]$$

$$\text{But: } \rho A_2^2 \int_{1}^{2} \frac{dx}{A}$$

is a factor which is constant for the system and dependent upon geometry only.

$$E_K = K \frac{u_2^2}{2}$$

We may define it by  $K$ , giving:

$$\text{Also: } \dot{E}_2 - \dot{E}_1 = \frac{\dot{U}_2^2}{\rho} - \frac{\dot{U}_1^2}{\rho} = \frac{\dot{U}_2^2}{\rho} \left( 1 - A_2^2/A_1^2 \right)$$

Substituting these into the original energy equation gives:

$$\frac{\partial}{\partial t} \left( K \frac{\dot{U}_2^2}{\rho} \right) + \dot{m} \frac{\dot{U}_2^2}{\rho} \left( 1 - A_2^2/A_1^2 \right) = \frac{\dot{m}}{\rho} (P_1 - P_2)$$

or:

$$\frac{K}{\dot{m}} \frac{\partial}{\partial t} \left( \frac{\dot{U}_2^2}{\rho} \right) + \frac{\dot{U}_2^2}{\rho} \left( 1 - A_2^2/A_1^2 \right) = \frac{\Delta P}{\rho}$$

Now, let:  $\Delta P = \bar{\Delta P} (1 + \psi)$

$$\psi = \bar{\psi} (1 + \mu)$$

$$\dot{m} = \bar{m} (1 + \mu)$$

where  $\mu$ ,  $\psi$  are time-dependent and superscript bar indicates steady-state.

Then:

$$\frac{K}{\bar{m}(1+\mu)} \left( \frac{\bar{U}_2^2}{\rho} \right) \frac{\partial}{\partial t} (1+\mu)^2 + \frac{\bar{U}_2^2}{\rho} (1+\mu)^2 \left( 1 - A_2^2/A_1^2 \right) = \frac{\bar{\Delta P}}{\rho} (1 + \psi)$$

For steady-state operation,  $\mu$  and  $\psi = 0$ , and:

$$\frac{\bar{\Delta P}}{\rho} = \frac{\bar{U}_2^2}{\rho} \left( 1 - A_2^2/A_1^2 \right)$$

Thus, dividing through by  $\bar{\Delta P}/\rho$  gives:

$$1 + \psi = (1 + \mu)^2 + \left[ K / \bar{m} \left( 1 - A_2^2/A_1^2 \right) \right] \frac{1}{(1 + \mu)} \frac{\partial}{\partial t} (1 + \mu)^2$$

Since  $\mu$  and  $\psi$  are small quantities, their squares and products may be neglected, giving:

$$1 + \psi = 1 + 2\mu + \left[ \frac{K}{\bar{m} (1 - A_2^2/A_1^2)} \right] \approx \frac{\partial \mu}{\partial t}$$

Now, let  $\mu$  vary sinusoidally =  $\tilde{\mu} e^{i\omega t}$

$$\text{Then: } \frac{\partial \mu}{\partial t} = i\omega \tilde{\mu} e^{i\omega t} = i\omega \mu$$

$$\text{So: } 1 + \psi = 1 + \bar{c}\mu + i\omega \frac{R\mu K}{\bar{m}(1 - A_2^2/A_1^2)}$$

$$\text{or: } \psi = \bar{c}\mu \left[ 1 + i\omega K/\bar{m}(1 - A_2^2/A_1^2) \right]$$

An equivalent length,  $l_{eq.}$ , may be defined from steady-state kinetic energy. Thus:

$$\rho A_2 l_{eq} \frac{\bar{u}_2^2}{2} = \bar{E}_k = K \frac{\bar{u}_2^2}{2}$$

$$\text{So: } l_{eq.} = K/\rho A_2$$

$$\text{and: } K/\bar{m} = K/\rho A_2 \bar{u}_2 = l_{eq.}/\bar{u}_2$$

$$\text{Hence: } \psi = \bar{c}\mu \left[ 1 + i\omega \frac{l_{eq.}}{\bar{u}_2} (1 - A_2^2/A_1^2) \right]$$

The flow pattern in each bipropellant injector orifice is assumed as follows (see Fig. C-1)

- a) Spherical sink flow from  $R = \infty$  to  $R = R_0$  with center at (A).
- b) Spherical sink flow from  $R = R_1$  to  $R = R_2$  with center at (B).
- c) Uniform rectilinear flow from (3) to (4) through a circular duct of radius  $R = R_3 = R_4$ .

The previous equation for  $\mu$  and  $\psi$  may be applied between station (4) and  $R = \infty$ .

In this case  $A_2/A_1 = 0$ , since  $A_1 \rightarrow \infty$ , and the equation becomes:

$$\psi = \bar{c}\mu \left( 1 + i\omega \frac{l_{eq.}}{\bar{u}_3} \right) \quad (\text{since } \bar{u}_3 = \bar{u}_4)$$

where:  $\psi$  is now the fractional oscillation in the pressure drop between  $R = \infty$  and station (4).

In order to determine  $\text{leq.}$ , one may first evaluate the kinetic energy in the various regions of flow. Thus:

Region I ( $R = \infty$  to  $R = R_0$ ):

$$\bar{E}_{K_I} = \int_{R_0}^{\infty} \rho A \frac{\bar{u}^2}{2} dR = \int_{R_0}^{\infty} \rho \frac{(2\pi R^2)}{2} \left( \frac{\bar{m}}{\rho 2\pi R^2} \right)^2 dR$$

$$\bar{E}_{K_I} = \int_{R_0}^{\infty} \frac{\bar{m}^2}{4\rho 2\pi R^2} dR = \frac{\bar{m}^2}{4\pi\rho} \int_{R_0}^{\infty} \frac{dR}{R^2} = \frac{\bar{m}^2}{4\pi\rho R_0}$$

Region II  $R = R_1$  to  $R = R_2$

$$A = \int_0^{\theta_w} (2\pi R \sin \phi) (R d\phi) = 2\pi R^2 \int_0^{\theta_w} \sin \phi d\phi$$

$$A = 2\pi R^2 (1 - \cos \theta_w)$$

and:

$$\bar{E}_{K_{II}} = \int_{R_2}^{R_1} \rho A \frac{\bar{u}^2}{2} dR = \int_{R_2}^{R_1} \frac{\rho 2\pi R^2 (1 - \cos \theta_w)}{2} \left( \frac{\bar{m}}{\rho 2\pi R^2 (1 - \cos \theta_w)} \right)^2 dR$$

$$\bar{E}_{K_{II}} = \int_{R_2}^{R_1} \frac{\bar{m}^2 dR}{\rho 4\pi R^2 (1 - \cos \theta_w)} = \frac{\bar{m}^2}{4\pi\rho (1 - \cos \theta_w)} \int_{R_2}^{R_1} \frac{dR}{R^2}$$

$$\bar{E}_{K_{II}} = \frac{\bar{m}^2}{4\pi\rho (1 - \cos \theta_w)} \left( \frac{1}{R_2} - \frac{1}{R_1} \right)$$

Region III  $(R=R_3)$  Section 3  $\rightarrow$  4

$$\bar{E}_{kIII} = \int_0^L \rho A \frac{\bar{u}^2}{2} dx = \int_0^L \left( \frac{\rho \pi R_3^2}{2} \right) \left( \frac{\bar{m}}{\rho \pi R_3^2} \right)^2 dx$$

$$\bar{E}_{kIII} = \frac{\bar{m}^2}{2\pi\rho R_3^2} \int_0^L dx = \frac{\bar{m}^2 L}{2\pi\rho R_3^2}$$

For the transition regions between I and II and between II and II<sub>1</sub>, it will suffice to find the average kinetic energy per unit mass and multiply it by the mass contained in the region. Thus, in

Region IV (Between I and II)

$$\left( \frac{\bar{u}^2}{2} \right)_{AVG} = \frac{1}{4} (\bar{u}_0^2 + \bar{u}_1^2) = \frac{1}{4} \left[ \left( \frac{\bar{m}}{\rho 2\pi R_0^2} \right)^2 + \left( \frac{\bar{m}}{\rho 2\pi R_1^2 (1-\cos \theta_w)} \right)^2 \right]$$

$$\left( \frac{\bar{u}^2}{2} \right)_{AVG} = \frac{\bar{m}^2}{16\pi^2 \rho^2} \left[ \left( 1/R_0 \right)^4 + \frac{1}{R_1^4 (1-\cos \theta_w)^2} \right]$$

The volume contained in this region is the difference between a hemisphere of radius  $R_0$  and a spherical cap of radius  $R_1$  of depth equal to the distance from section (l) to (A).

This cap has a volume given by:

$$V_{cap} = \frac{2}{3} \pi R_1^3 (1 - \cos \theta_w) - \frac{1}{3} \pi h (R_1 \sin \theta_w)^2$$

But,  $h = R_1 \cos \theta_w$  = distance from (A) to (B)

$$\text{So: } V_{cap} = \frac{2}{3} \pi R_1^3 (1 - \cos \theta_w) - \frac{1}{3} \pi R_1^3 \cos \theta_w \sin^2 \theta_w$$

$$= \frac{2}{3} \pi R_1^3 (1 - \cos \theta_w - \cos \theta_w \sin^2 \theta_w / 2)$$

$$V_{cap} = \frac{2}{3} \pi R_1^3 \left[ 1 - \cos \theta_w \left( 1 + \frac{\sin^2 \theta_w}{2} \right) \right]$$

Then  $V_{IV}$  = volume in region IV =  $\sqrt{\text{hemisphere}} - \sqrt{\text{cap}}$

$$= \frac{\pi}{3} R_0^3 - \frac{\pi}{3} R_1^3 \left[ 1 - \cos \theta_w \left( 1 + \frac{\sin^2 \theta_w}{\kappa} \right) \right]$$

$$V_{IV} = \frac{\pi}{3} R_0^3 \left\{ 1 - \frac{R_1^3}{R_0^3} \left[ 1 - \cos \theta_w \left( 1 + \frac{\sin^2 \theta_w}{\kappa} \right) \right] \right\}$$

Then:

$$\bar{E}_{K_{IV}} = \rho V_{IV} \left( \frac{4}{3} \right)_{AVG} = \frac{2}{3} \pi \rho R_0^3 \left\{ 1 - \left( \frac{R_1}{R_0} \right)^3 \left[ 1 - \cos \theta_w \left( 1 + \frac{\sin^2 \theta_w}{\kappa} \right) \right] \right\} \times$$

$$\times \frac{\bar{m}^2}{16 \pi^2 \rho^2 R_0^4} \left[ 1 + \left( \frac{R_0}{R_1} \right)^4 \frac{1}{(1 - \cos \theta_w)^2} \right]$$

$$E_{K_{IV}} = \frac{\bar{m}^2}{24 \pi \rho R_0} \left\{ 1 - \left( \frac{R_1}{R_0} \right)^3 \left[ 1 - \cos \theta_w \left( 1 + \frac{\sin^2 \theta_w}{\kappa} \right) \right] \right\} \left[ 1 + \left( \frac{R_0}{R_1} \right)^4 \frac{1}{(1 - \cos \theta_w)^2} \right]$$

A similar procedure may be applied to a fifth region, that between sections (2) and (3). Here the volume is that of a spherical cap. For this

region:

$$\left( \frac{4}{3} \right)_{AVG} = \frac{1}{4} \left( \frac{4}{2} + \frac{4}{3} \right) = \frac{1}{4} \left\{ \left[ \frac{\bar{m}}{16 \pi^2 \rho^2 R_2^2 (1 - \cos \theta_w)} \right]^2 + \left( \frac{\bar{m}}{16 \pi^2 \rho^2 R_3^2} \right)^2 \right\}$$

$$\left( \frac{4}{3} \right)_{AVG} = \frac{\bar{m}}{16 \pi^2 \rho^2 R_2^4} \left[ 4 \left( \frac{R_2}{R_3} \right)^4 + \left( \frac{1}{1 - \cos \theta_w} \right)^2 \right]$$

and:  $V_{V} = \frac{\pi}{3} R_2^3 (1 - \cos \theta_w) - \frac{1}{3} \pi R_2 \cos \theta_w (R_2 \sin \theta_w)^2$

$$= \frac{\pi}{3} R_2^3 \left[ (1 - \cos \theta_w) - \frac{1}{2} \cos \theta_w \sin^2 \theta_w \right]$$

$$V_{V} = \frac{\pi}{3} \left[ 1 - \cos \theta_w \left( 1 + \frac{\sin^2 \theta_w}{\kappa} \right) \right]$$

Then:

$$\bar{E}_{K_V} = \rho \left( \frac{\pi}{3} R_2^3 \right) \left[ 1 - \cos \theta_w \left( 1 + \frac{\sin^2 \theta_w}{\kappa} \right) \right] \left( \frac{\bar{m}^2}{16 \pi^2 \rho^2 R_2^4} \right) \left[ 4 \left( \frac{R_2}{R_3} \right)^4 + \left( \frac{1}{1 - \cos \theta_w} \right)^2 \right]$$

$$\bar{E}_{K_V} = \frac{\bar{m}^2}{24 \pi \rho R_2} \left[ 1 - \cos \theta_w \left( 1 + \frac{\sin^2 \theta_w}{\kappa} \right) \right] \left[ 4 \left( \frac{R_2}{R_3} \right)^4 + \frac{1}{(1 - \cos \theta_w)^2} \right]$$

The total kinetic energy is then given by:

$$\begin{aligned}\bar{E}_K &= \bar{E}_{K_I} + \bar{E}_{K_{II}} + \bar{E}_{K_{III}} + \bar{E}_{K_{IV}} + \bar{E}_{K_{V}} \\ \bar{E}_K &= \frac{\bar{m}}{4\pi/\rho R_0} + \frac{\bar{m}^2}{4\pi/\rho} \left( \frac{1}{1-\cos\theta_w} \right) \left( \frac{1}{R_2} - \frac{1}{R_1} \right) + \frac{\bar{m}^2 L}{2\pi/\rho R_3} + \\ &+ \frac{\bar{m}^2}{24\pi/\rho R_0} \left\{ 1 - \left( \frac{R_1}{R_0} \right)^3 \left[ 1 - \cos\theta_w \left( 1 + \frac{\sin^2\theta_w}{\pi} \right) \right] \right\} \left[ 1 + \left( \frac{R_0}{R_1} \right)^4 \left( \frac{1}{1-\cos\theta_w} \right)^2 \right] + \\ &+ \frac{\bar{m}^2}{24\pi/\rho R_2} \left\{ 1 - \cos\theta_w \left( 1 + \frac{\sin^2\theta_w}{\pi} \right) \right\} \left[ 4 \left( \frac{R_2}{R_3} \right)^4 + \left( \frac{1}{1-\cos\theta_w} \right)^2 \right] \\ \bar{E}_K &= \frac{\bar{m}^2}{2\pi/\rho} \left\{ \frac{1}{2R_0} + \frac{1}{2} \left( \frac{1}{1-\cos\theta_w} \right) \left( \frac{1}{R_2} - \frac{1}{R_1} \right) + \frac{L}{R_3^2} + \frac{1}{12R_0} \left[ 1 - \left( \frac{R_1}{R_0} \right)^3 \times \right. \right. \\ &\times \left. \left( 1 - \cos\theta_w \left( 1 + \frac{\sin^2\theta_w}{\pi} \right) \right) \right] + \frac{1}{12R_2} \left[ 1 - \cos\theta_w \left( 1 + \frac{\sin^2\theta_w}{\pi} \right) \right] \left[ 4 \left( \frac{R_2}{R_3} \right)^4 + \right. \\ &\left. \left. \left( \frac{1}{1-\cos\theta_w} \right)^2 \right] \right\}\end{aligned}$$

Now, the equivalent length is defined by:

$$l_{eq} = K/\rho A_3 \Rightarrow K = \frac{\rho \bar{E}_K}{\bar{q}_3^2}$$

$$\text{so that } l_{eq.} = \frac{\rho \bar{E}_K}{\rho A_3 \bar{q}_3^2} = \frac{2\pi/\rho R_3^2 \bar{E}_K}{\bar{m}^2}$$

$$\begin{aligned}\text{Thus: } l_{eq.} &= R_3^2 \left\{ \frac{1}{2R_0} + \frac{1}{2} \left( \frac{1}{1-\cos\theta_w} \right) \left( \frac{1}{R_2} - \frac{1}{R_1} \right) \right\} + L + \\ &+ \frac{R_2^2}{12R_0} \left\{ 1 - \left( \frac{R_1}{R_0} \right)^3 \left[ 1 - \cos\theta_w \left( 1 + \frac{\sin^2\theta_w}{\pi} \right) \right] \right\} \left[ 1 + \left( \frac{R_0}{R_1} \right)^4 \left( \frac{1}{1-\cos\theta_w} \right)^2 \right] + \\ &+ \frac{R_2^2}{12R_2} \left[ 1 - \cos\theta_w \left( 1 + \frac{\sin^2\theta_w}{\pi} \right) \right] \left[ 4 \left( \frac{R_2}{R_3} \right)^4 + \left( \frac{1}{1-\cos\theta_w} \right)^2 \right]\end{aligned}$$

and, finally:

$$\begin{aligned}l_{eq} &= \frac{R_3^2}{2\bar{q}_3} \left[ \frac{1}{R_0} + \left( \frac{1}{1-\cos\theta_w} \right) \left( \frac{1}{R_2} - \frac{1}{R_1} \right) \right] + \frac{L}{\bar{q}_3} + \frac{R_3^2}{12R_0\bar{q}_3} \left\{ 1 - \right. \\ &\left. - \left( \frac{R_1}{R_0} \right)^3 \left[ 1 - \cos\theta_w \left( 1 + \frac{\sin^2\theta_w}{\pi} \right) \right] \right\} \left[ 1 + \left( \frac{R_0}{R_1} \right)^4 \left( \frac{1}{1-\cos\theta_w} \right)^2 \right] + \\ &+ \frac{R_2^2}{12R_2\bar{q}_3} \left[ 1 - \cos\theta_w \left( 1 + \frac{\sin^2\theta_w}{\pi} \right) \right] \left[ 4 \left( \frac{R_2}{R_3} \right)^4 + \left( \frac{1}{1-\cos\theta_w} \right)^2 \right]\end{aligned}$$

From this expression,  $\text{leg.}$  may be evaluated for all flow rates (chamber pressures), from which the phase lag  $\alpha$  may be computed by:

$$\alpha = \tan^{-1} \left( \frac{\omega \text{leg}}{U_3} \right)$$

For the bipropellant injector now in use, these geometric variables are:  $R_0 = R_3 + 1/3Z''$

$$R_1 = R_0 \sqrt{Z}$$

$$R_2 = R_3 \sqrt{Z}$$

$$\theta_w = 45^\circ$$

$$\cos \theta_w = \sqrt{Z}/Z$$

$$1 - \cos \theta_w = 1 - \sqrt{Z}/Z = 0.293$$

$$\sin \theta_w = \sqrt{Z}/Z$$

$$\frac{1}{1 - \cos \theta_w} = 3.412$$

$$\sin^2 \theta_w = 1/Z$$

$$\sin^2 \theta_w \cos \theta_w / Z = \sqrt{Z}/8 = 0.1768$$

Then:

$$(1 - \cos \theta_w)^2 = 0.0858$$

$$(1/(1 - \cos \theta_w))^2 = 11.655$$

$$(1 - \cos \theta_w - \frac{\sin^2 \theta_w \cos \theta_w}{Z}) = 0.116$$

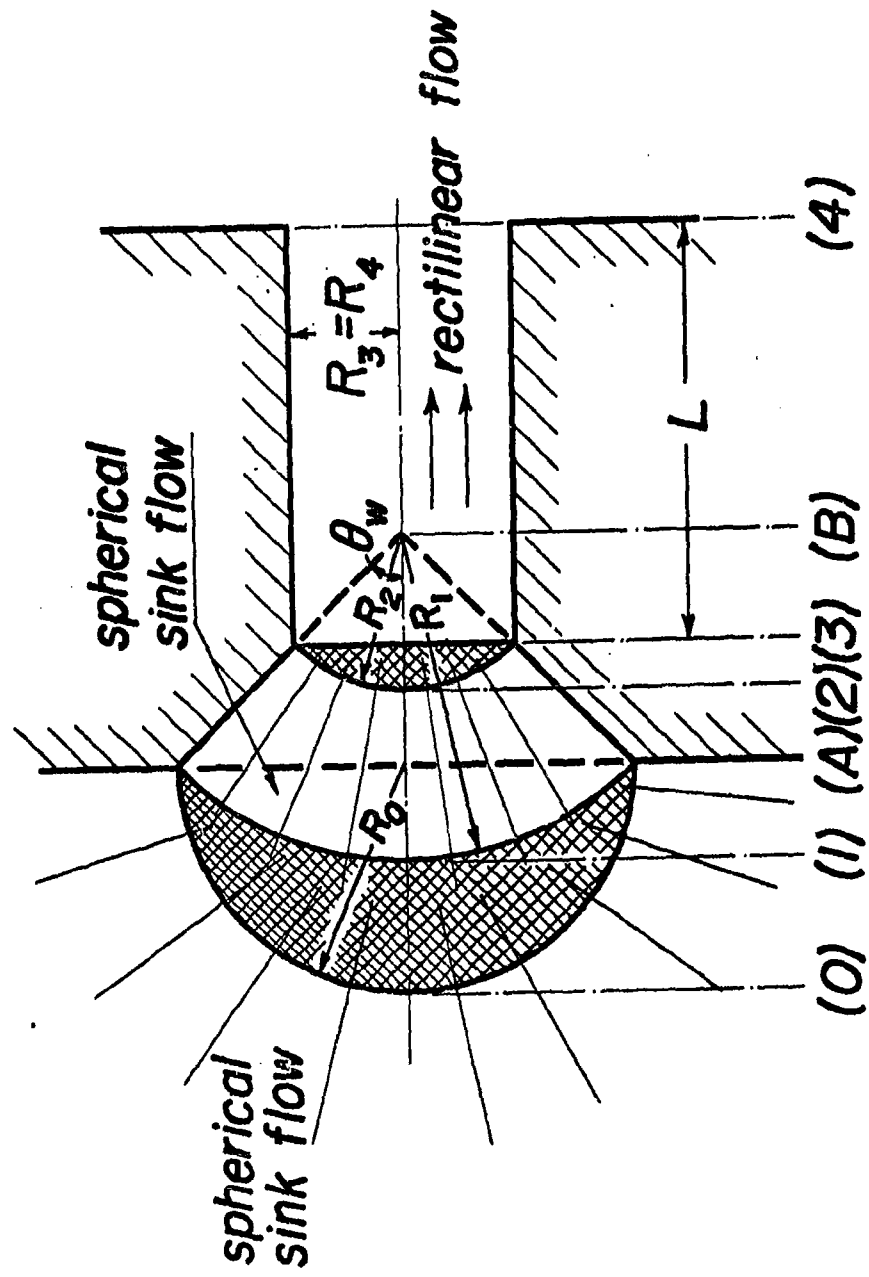
Therefore:

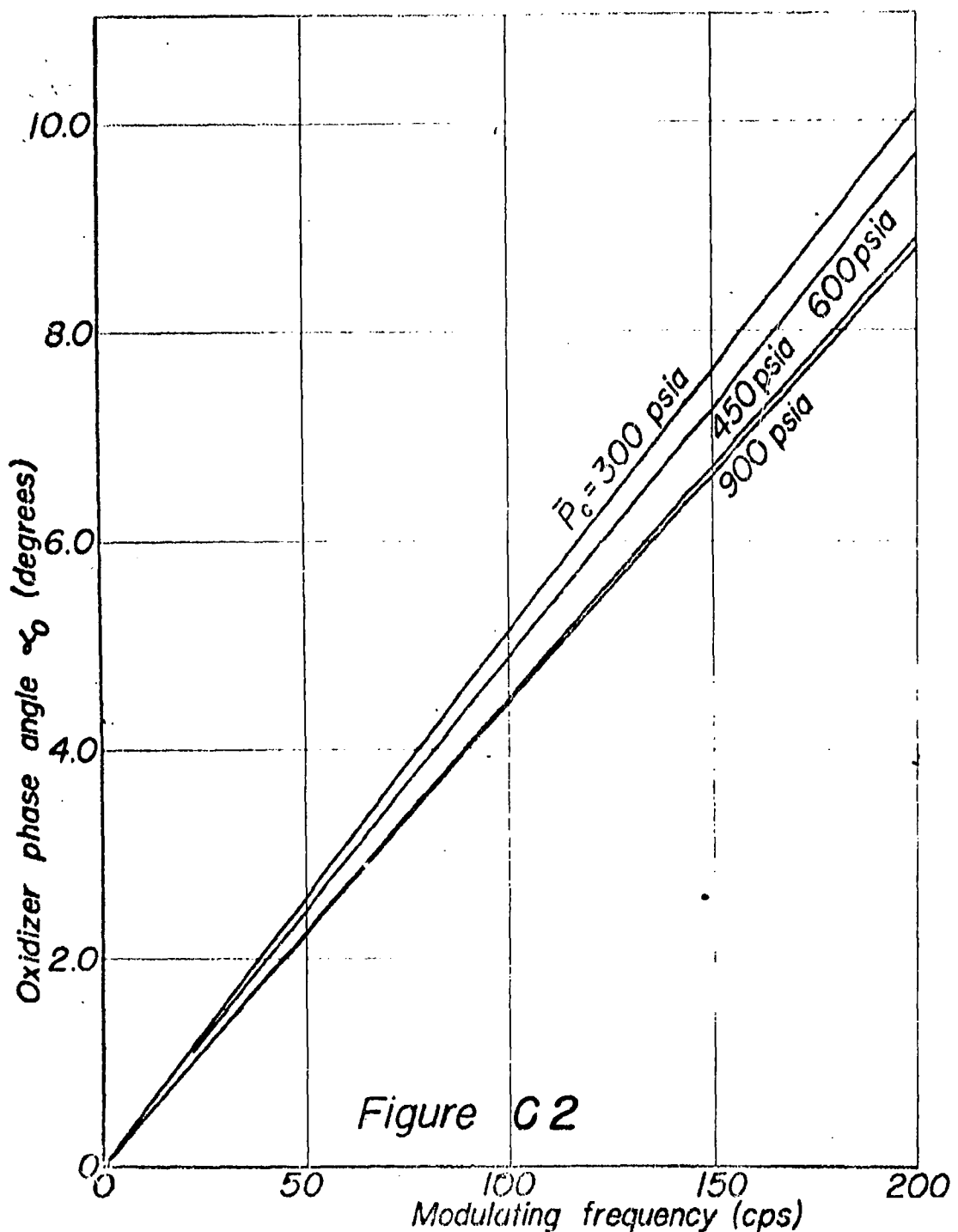
$$\begin{aligned} \frac{\text{leg}}{U_3} &= \frac{R_3^2}{Z U_3} \left[ \frac{1}{R_0} + 3.412 \left( \frac{1}{R_2} - \frac{1}{R_1} \right) \right] + \frac{L}{U_3} + \\ &+ \frac{R_3^2}{12 R_0 U_3} \left[ 1 - 0.116 \left( \frac{R_1}{R_0} \right)^3 \right] \left[ 1 + 11.655 \left( \frac{R_0}{R_1} \right)^4 \right] + \\ &+ \frac{R_3^2}{12 R_2 U_3} (0.116) \left[ 11.655 + 4 \left( \frac{R_2}{R_3} \right)^4 \right] \end{aligned}$$

These data are employed to find the equivalent lengths of the five regions from the individual terms of the final equation. Values of the phase lag  $\alpha$  are plotted for the different injectors as a function of frequency in Figs. C-2 and C-3, where  $\alpha$  is defined by

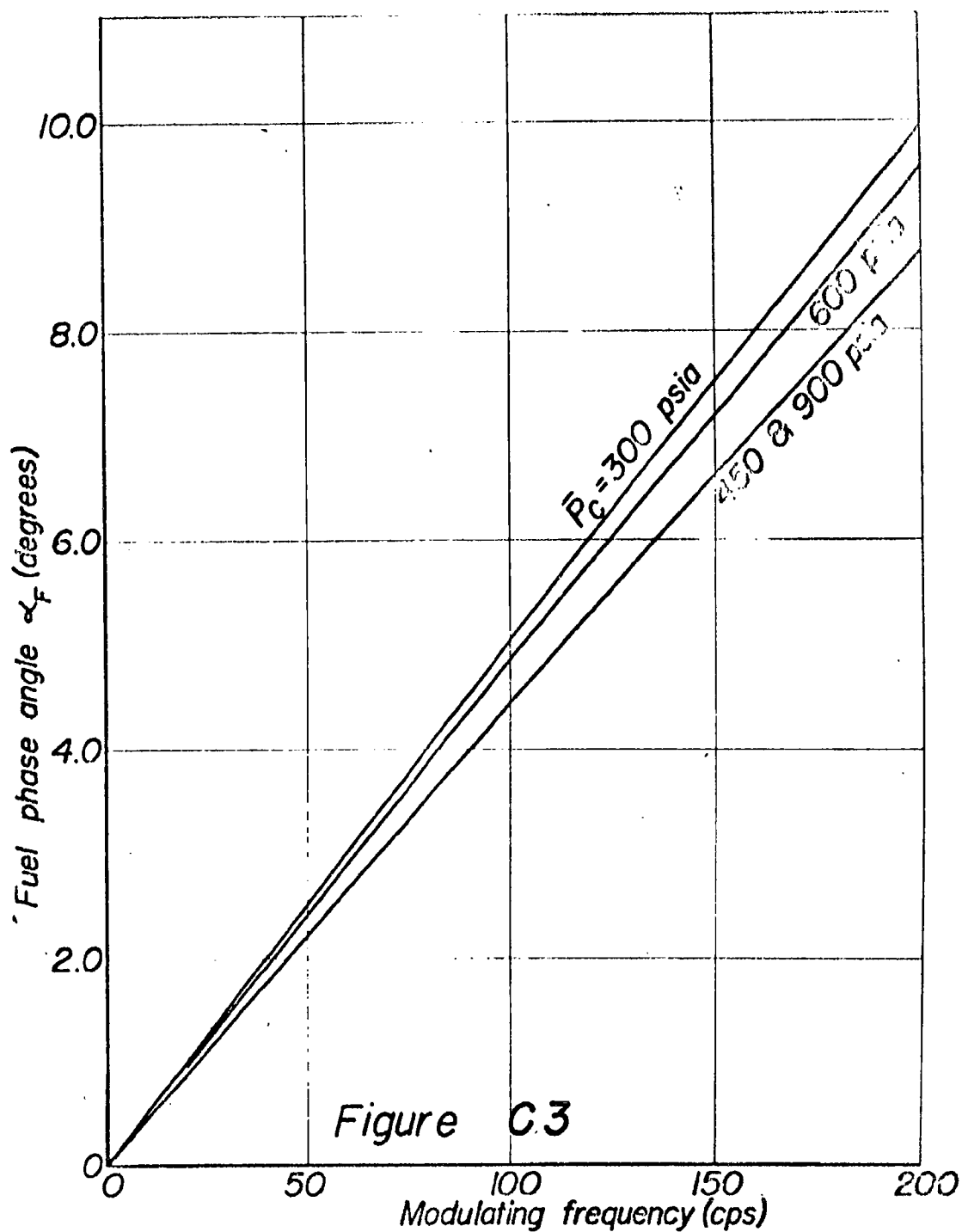
$$\frac{\psi}{\mu} = \frac{Z}{\cos \alpha} e^{i\alpha}$$

**Figure C1**  
**Representation of Bipropellant**  
**Injector Orifice**





Inertial Phase Lag Between Pressure Drop  
And Flow Rate in Bipropellant Oxidizer  
Injector  
(Medium: liquid oxygen)



*Inertial Phase Lag Between Pressure Drop  
And Flow Rate in Bipropellant Fuel  
Injector  
(Medium: ethyl alcohol)*

APPENDIX D: SAMPLE CALCULATIONS

The computation processes and magnitudes of numerical quantities involved are illustrated by the following sample calculation. A typical data point is selected with primary measurements given, and successive steps in the complete procedure for determining time lag parameters are listed. In each step the detailed computation process is explained; this is followed immediately by the numerical example from the chosen data point. Steps are broken into major groups as described in a previous section.

Run No.: A-461

Run Date: 6-17-56

Nominal  $\bar{P}_c$ : 600 psia

Nominal Frequency: 248 cps

### I. Stage I Calculations

#### A. Steady-state parameters

1. Read all photographed values, including time.

Example: Time = 7.00 secs.       $\bar{P}_c$  = 602 psig

$\bar{P}_o$  = 730 psig      Thrust =  $\bar{F}$  = 530 lts.

$\bar{P}_f$  = 710 psig      Pref. = 440 psig

2. Correct all photo pressure values by most recent dead-weight-test gauge calibration curves.

Ex.  $\bar{P}_o$  = 752 psia      Pref. = 455 psia

$\bar{P}_f$  = 714 psia

$\bar{P}_c$  = 581 psia

3. Correct photo thrust value from thrust calibration curve.

Ex.  $\bar{F}$  = 530 lbs.

4. Mark all Speedomax recorder charts at time of reading, using cessation of fuel flow to determine end of run and marker pen indications to locate start.

5. Record all net chart readings, subtracting the indicated chart zeros.

Ex.  $\bar{F} = 7.77$  divs.

$$\bar{P}_O = 4.26 - 0.83 = 3.43 \text{ divs.}$$

$$\bar{P}_f = 5.60 - 1.68 = 3.92 \text{ divs.}$$

$$\bar{P}_C = 4.72 - 0.70 = 4.02 \text{ divs.}$$

$$\bar{m}_{OX} = .6.72 \text{ divs.}$$

$$\bar{m}_f = 6.76 \text{ divs.}$$

$$\text{freq.} = 9.88 \text{ divs.}$$

6. Determine actual pickup value of thrust from calibration curve of chart reading vs. actual load.

Ex.  $\bar{F} = 527.1$  lbs.

7. Determine oxygen and fuel flow calibration factors from known line frequency indications.

Ex. Ox factor =  $(60.0/4.99) = 12.01$  cps/div.

Fuel factor =  $(60.0/5.00) = 12.00$  cps/div.

8. Determine net frequency outputs of oxygen and fuel Potter flowmeters from calibration factors and measured net flow indications.

Ex. Ox Potter freq. =  $(12.01) (6.72) = 80.77$  cps

Fuel Potter freq. =  $(12.00) (6.76) = 81.12$  cps

9. Obtain oxygen and uncorrected fuel flow rates from Potter calibrations, with density factors based on standard ethyl alcohol (sp. gr. = 0.783) and liquid oxygen and thermal correction for 5% area contraction at liquid oxygen temperature.

Ex. Ox flow =  $\bar{m}_{OX} = 1.284$  lbs./sec.

Fuel flow =  $\bar{m}_f$  (uncorr.) = 0.947 lbs./sec.

10. From measured fuel temperature and empirical hydrometer calibration curve, obtain actual fuel specific gravity.

Ex. Fuel Temp. = 86°F.

$$\text{Sp. Gr.} = 0.794 - .000496 (T_{\text{fuel}} - 64.4^{\circ}\text{F})$$

$$\text{Actual fuel sp. gr.} = 0.7843$$

11. Correct fuel flow rate for actual specific gravity.

$$\underline{\text{Ex.}} \quad \bar{m}_f = \bar{m}_f (\text{uncorr.}) \times \frac{\text{sp. gr.}}{0.783} = 0.947 \frac{0.784}{0.783} = 0.947 \frac{\text{lbs.}}{\text{sec.}}$$

12. Add fuel and oxygen flows to get total propellant flow rate.

$$\underline{\text{Ex.}} \quad \bar{m}_{\text{total}} = 1.284 + 0.947 = 2.231 \text{ lbs/sec.}$$

13. Divide oxygen flow by fuel flow to obtain weight mixture ratio.

$$\underline{\text{Ex.}} \quad \bar{r} = \bar{O}/\bar{F} = 1.284/0.947 = 1.356$$

14. Determine run frequency calibration factor from line frequency chart reading.

$$\underline{\text{Ex.}} \quad \text{Freq. Cal. factor} = (120/4.79) = 25.05 \text{ cps/div.}$$

15. Obtain actual run freq. from net chart reading and calibration factor.

$$\underline{\text{Ex.}} \quad \text{Freq.} = (25.05) (9.88) = 247.6 \text{ cps}$$

16. Select most recent pressure pickup-to-Speedomax calibration curve at reference pressure observed during run. With this curve, determine net across pickups during run from net chart readings.

$$\underline{\text{Ex.}} \quad \Delta(\bar{P}_o) = 3.43/.0127 = 270 \text{ psi}$$

$$\Delta(\bar{P}_f) = 3.53/.0133 = 265 \text{ psi}$$

$$\Delta(\bar{P}_c) = 4.02/.0730 = 551 \text{ psi}$$

17. Add corrected Pref. to these values (for differential pickups) to obtain absolute pressures.

Ex.  $\bar{P}_o = 455 + 270 = 725 \text{ psia}$

$\bar{P}_f = 455 + 265 = 720 \text{ psia}$

$\bar{P}_c = 15 + 551 = 566 \text{ psia}$  (absolute pickup employed)

18. Subtract photo  $\bar{P}_c$  from  $\bar{P}_o$  and  $\bar{P}_f$  to determine injector pressure drops.

Ex.:  $\bar{\Delta P}_o = 171 \text{ psi}$

$\bar{\Delta P}_f = 133 \text{ psi}$

19. At run frequency measured, consult inertial phase lag curves for particular injector employed to determine standard phase lags.

Ex.:  $\alpha_o \text{ at } 247.6 \text{ cps} = 12.00^\circ$

$\alpha_f \text{ at } 247.6 \text{ cps} = 11.85^\circ$

20. From ratio of standard to actual flow rates, correct standard injector phase lags.

Ex.:  $\alpha_o = (1.083) (12.00) = 12.99^\circ$

$\alpha_f = (1.050) (11.85) = 12.44^\circ$

## B. Transient Data

- Play back pre-run amplitude calibrations and run signals through network described into Speedomax recorders. Simultaneously record 100-cps taped timing trace with recorder marker pens. Mark all charts at time of reading.

- Read net values of all amplitudes, including calibrations, as R.M.S. values from charts.

Ex.  $\tilde{P}_o \text{ (Cal)} = 8.47 \text{ divs.}$

$\tilde{P}_o = 8.84 \text{ divs.}$

$\tilde{P}_f \text{ (Cal)} = 8.45 \text{ divs.}$

$\tilde{P}_f = 7.10 \text{ divs.}$

$\tilde{P}_c \text{ (Cal)} = 8.46 \text{ divs.}$

$\tilde{P}_c = 7.40 \text{ divs.}$

3. Form ratio of run-to-calibration signals and multiply by known calibration input amplitude to obtain actual electrical signal amplitudes of pressure pickup outputs.

Ex.:

$$\tilde{P}_o = (8.84/8.47) \cdot 5.656 = 5.905 \text{ mv}$$

$$\tilde{P}_f = (7.10/8.47) \cdot 5.656 = 4.751 \text{ mv}$$

$$\tilde{P}_c = (7.40/8.46) \cdot 2.262 = 1.979 \text{ mv}$$

4. Noting pressure pickups employed and corrected  $P_{ref}$  applied during run, select most recent sensitivity calibration curve for each pickup. By interpolation between calibration reference pressures, determine pickup sensitivity at actual run value of  $P_{ref}$ .

Ex.:  $\tilde{P}_o$  sens. (Pickup #2) = 0.1261 mv/psi

$$\tilde{P}_f$$
 sens. (Pickup #14) = 0.1319 mv/psi

$$\tilde{P}_c$$
 sens. (Pickup #25A) = 0.0728 mv/psi

5. Divide electrical amplitudes of each signal by calibration sensitivity to obtain pressure amplitudes during run.

Ex.:  $\tilde{P}_o = 5.905/.1261 = 46.83 \text{ psi}$

$$\tilde{P}_f = 4.751/.1319 = 36.02 \text{ psi}$$

$$\tilde{P}_c = 1.979/.0728 = 27.18 \text{ psi}$$

6. Play back three pressure signals in pairs:  $(P_o - P_c)$ ,  $(P_f - P_c)$ ,  $(P_o - P_f)$  through phase measuring networks into Speedomax with timing trace. Mark recorded phase difference charts at proper reading time.

7. Read gross phase angles from charts, subtracting chart zeros.

Ex.:  $\lambda_o = (P_o - P_c) = 56.4^\circ$

$$\lambda_f = (P_f - P_c) = 51.8^\circ$$

$$\delta' = (P_o - P_f) = 5.5^\circ$$

D-6

8. Playback taped, post-run calibrations through same network and record instrument phase shifts. Read these chart values for the pairs indicated.

Ex.:  $(P_o - P_c)$  Cal. =  $-0.4^\circ$   
 $(P_f - P_c)$  Cal. =  $0.5^\circ$   
 $(P_o - P_f)$  Cal. =  $-0.9^\circ$

9. Subtract calibration angles from gross phases to obtain net phase angles during run. Compare net  $\delta'$  with difference between net  $\lambda_o$  and  $\lambda_f$  as check on proper phasemeter settings.

~~$\lambda_o = 56.0^\circ$~~        ~~$\delta' = 6.40^\circ$~~   
 $\lambda_f = 51.3^\circ$        $\lambda_o - \lambda_f = 5.5^\circ$

#### C. Digital Computer Calculations

1. Tabulate punch on input cards, and verify inputs of run number, reading time,  $P_o$ ,  $P_f$ ,  $P_c$ ,  $\alpha_o$ ,  $\alpha_f$ ,  $\tilde{P}_o$ ,  $\tilde{P}_f$ ,  $\tilde{P}_c$ ,  $\lambda_o$ ,  $\lambda_f$ , on two cards.
2. On fixed-decimal control panel perform Stage I calculations to obtain outputs of transfer function parameters and instantaneous fractional mixture ratio. Tabulate these values.

Ex.: Output values are:

$$\begin{array}{ll} R_o = 2.388 & \lambda = 1.068 \\ R_f = 2.236 & \delta = -7.7^\circ \\ \beta_o = 79.3^\circ & \beta_f = 87.0^\circ \end{array}$$

3. From same calculation, intermediate quantities  $Y_o$ ,  $Y_f$ ,  $\tilde{\Delta P}_o$ ,  $\tilde{\Delta P}_f$  are obtained and tabulated.

Ex.: Intermediate values are:

$$\begin{array}{ll} Y_o = 35.45^\circ & \tilde{\Delta P}_o = 39.21 \text{ psi} \\ Y_f = 48.11^\circ & \tilde{\Delta P}_f = 28.49 \text{ psi} \end{array}$$

## II. Stage II Calculations

### A. Steady State chamber properties

- With nozzle insert plug, measure throat diameter and calculate throat area.

Ex. Diameter = 0.885 in.

$$A_t = 0.6151$$

- From  $\bar{P}_c$ ,  $\dot{m}$  total, and  $A_t$ , calculate experimental value of  $c^*$

$$\text{Ex.: } c^* = \frac{\bar{P}_c A_t g}{\dot{m}_{\text{total}}} = \frac{(581) (.6151) (32.2)}{(2.231)} = 5158 \text{ ft/sec.}$$

- From  $\bar{P}_c$  and  $\bar{r}$ , consult theoretical equilibrium calculations and curves to obtain values for  $T_c$ ,  $\gamma$ ,  $\gamma_{\text{nozzle}}$ ,  $dT_c/dr$ , and molecular weight ( $m_c$ )

$$\begin{aligned} \text{Ex.: } T_c (\text{theor.}) &= 5606^\circ R & \frac{dT_c}{dr} &= 2370^\circ R \\ \gamma &= 1.2099 & m_c &= 21.55 \text{ lb/lb-mol} \\ \gamma_N &= 1.2382 \end{aligned}$$

- Using theoretical combustion gas composition and properties, compute

$$\Gamma = f(\gamma) = c_0/c^*, \quad c^* (\text{theor.}), M_1.$$

$$\text{Ex. } \Gamma = 0.7152$$

$$c^* (\text{theor.}) = 5529 \text{ ft/sec.}$$

$$M_1 (\text{for } A_c/A_t = 11.49) = .0515$$

- Form the ratio  $c^* (\text{actual}) / c^*(\text{theor.})$  and calculate  $T_c$  (act.) from this ratio multiplied by  $T_c$  (theor.)

$$\text{Ex.: } T_c (\text{act.}) = T_c (\text{th.}) \left( \frac{c^* \text{act.}}{c^* \text{th.}} \right)^{\frac{1}{k}} = 5605 (.8705) = 4879^\circ R$$

6. Employing the perfect gas law and theoretical value of molecular weight, calculate gas density from  $\bar{\rho}_c$  and  $T_c$  (act.)

$$\text{Ex.: } \bar{\rho}_c = \frac{\bar{P}_c m_c}{R T_c} = \frac{(581) (144) (21.55)}{(1544) (4879)} = 0.2083 \text{ lbs./ft}^3$$

7. From gas density, known chamber area, and total propellant flow, calculate chamber exit velocity,  $\bar{u}_1^*$ :

$$\text{Ex.: } \bar{u}_1^* = \frac{\dot{m}_{\text{total}}}{\bar{\rho}_c A_c} = \frac{(2.231) (144)}{(0.2083) (7.065)} = 218.2 \text{ ft/sec.}$$

8. From  $c_0^*$  (act.) and  $\Gamma^*(Y)$ , calculate  $C_o$  (act.) and non-dimensionalize  $\bar{u}_1^*$  to form  $\bar{u}_1^* = M_1$ .

$$\text{Ex.: } \bar{u}_1^* = \frac{\bar{u}_1^*}{c_0 \text{ (act.)}} = \frac{(218.2)}{(3689)} = 0.0591$$

### B. Transient

1. Collect and retain output punched cards from Stage III digital computer results.

### C. Determination of correction factors.

1. From measured pressure distributions, assuming one-dimensional, incompressible flow, calculate axial velocity distribution. Correct for two-dimensional effects by extending final velocity to non-dimensional value  $\bar{u}_1$  averaged from steady state computations.

Ex.: (See Figure 39 for this distribution)

2. Determine arithmetic average of steady state parameters  $\bar{P}_c$ ,  $\bar{r}$ ,  $\bar{\rho}_c$ ,  $\bar{m}_t$ ,  $T_c$ , (Sp. Gr.) fuel,  $C_o$ ,  $\Delta P_{\text{exit}}$ , mol fractions ( $x_i$ ).

$$\text{Ex.: } \bar{P}_c = 590 \text{ psia} \quad X_{CO_2} = 0.1224$$

$$\bar{r} = 1.36 \quad X_{CO} = 0.2666$$

$$\bar{\rho}_c = 0.2109 \text{ lbs/ft}^3 \quad X_{H_2O} = 0.4494$$

$$\bar{m}_t = 2.215 \text{ lbs/sec} \quad X_{H_2} = 0.1304$$

$$(S.G.)_F = 0.788$$

$$c_0 = 3965 \text{ ft/sec.}$$

$$\Delta P_{INT} = 137 \text{ psi}$$

3. From mixture ratio,  $\bar{r}$ , and (Sp. Gr.)<sub>F</sub>, calculate average liquid density at injection,  $\bar{\rho}_{l_0}$ .

$$\text{Ex.: } \bar{\rho}_{l_0} = 62.4 \frac{(S.G.)_{ox}(\bar{r}) + (S.G.)_F}{\bar{r} + 1}$$

$$= 62.4 \frac{(1.142)(1.36) + 0.788}{2.36} = 61.9 \text{ lbs./ft}^3$$

4. Using known injector orifice area,  $\bar{m}_t$ , and  $\bar{\rho}_{l_0}$ , compute average injector entrance velocity,  $\bar{u}_{l_0}^*$

$$\text{Ex.: } \bar{u}_{l_0}^* = \frac{\bar{m}_t}{\bar{\rho}_{l_0} A_i} = 101 \text{ ft/sec.}$$

5. Calculate correlation parameter

$$\text{Ex.: } d_0 \sqrt{\frac{\Delta P_{INT}}{\bar{\rho}_{l_0}}} = 0.0795$$

$$d_0 \sqrt{\frac{\Delta P_{INT}}{\bar{\rho}_{l_0}}}$$

6. From empirical droplet diameter correlation curve (Figure 24) estimate mean inlet droplet diameter,  $d_i$ .

$$\text{Ex.: } d_i = .0013 \text{ in.}$$

7. Using data and empirical equations of N.B.S. circular, calculate viscosity at temperature  $T_c$  for each of major constituent combustion gases.

$$\text{Ex.: } \text{CO}_2: \frac{\mu_{T_c}}{\mu_{T_0}} = 6.03$$

$$\mu_{T_0} \text{ (from N.B.S.)} = 137 \text{ micropoises}$$

$$\mu_{T_c} = (6.03)(137) = 826 \text{ micropoises}$$

$$\text{CO: } \frac{\mu_{T_c}}{\mu_{T_0}} = 5.10; \mu_{T_0} = 165.7 \text{ micropoises}$$

$$\mu_{T_c} = (5.10)(165.7) = 847 \text{ micropoises}$$

$$\text{H}_2\text{O: } \mu_{T_c} \text{ (direct from N.B.S. data)} = 605 \text{ micropoises}$$

$$\text{H}_2: \frac{\mu_{T_c}}{\mu_{T_0}} = 4.97; \mu_{T_0} = 84.11 \text{ micropoises}$$

$$\mu_{T_c} = 418 \text{ micropoises}$$

8. Compute the weighted sum  $\sum_i \mu_i x_i$  as the average mixture viscosity.

$$\text{Ex.: } \sum_i \mu_i x_i = \bar{\mu}_c = (826(.1224) + (847)(.2666) + (605)(.4494) + (84.11)(.1304)) = 653 \text{ micropoises.}$$

9. Calculate Reynolds' number of injected liquid,  $R_{e_0}$ .

$$\text{Ex.: } R_{e_0} = \frac{\bar{\rho}_c \bar{u}_{g_0} d_e}{\bar{\mu}_c} = 52.4$$

10. From drag coefficient curves for spherical particles estimate the proportionality constant ( $C_D R_{e_0}$ ) at the calculated  $R_{e_0}$

$$\text{Ex.: } (C_D R_{e_0}) (\text{at } R_{e_0} = 52.4) = 76.7$$

11. Using known  $\bar{\rho}_c$  and ( $C_D R_{e_0}$ ), calculate dimensional value of droplet drag coefficient,  $k^*$ .

$$\text{Ex.: } k^* = \frac{(C_D R_{e_0})}{3\bar{\rho}_c d_e^2} = 350 \text{ sec}^{-1}$$

12. Non-dimensionalize  $k^*$  by  $c_o$  and known chamber length.

$$\text{Ex.: } k = k^* \frac{l}{c_o} = (350) \frac{(4.016)/12}{3965} = 0.0295$$

13. Apply droplet drag coefficient,  $k$ , to gas velocity distribution,  $\bar{u}(x)$  and integrate droplet dynamics equation:

$$\bar{u}_d \frac{du_d}{dx} = k (\bar{u} - \bar{u}_d) \quad \text{numerically on digital com-}$$

puter to find liquid velocity distribution,  $\bar{u}_l(x)$ . Note value of  $\bar{u}_l$ . (See Figure 39 for resultant  $\bar{u}_l(x)$  curve.)

$$\text{Ex.: } \bar{u}_l = 0.0411$$

14. Numerically integrate  $1/\bar{u}_d(x)$  to obtain distributed total time lag,  $\bar{\tau}_d(x)$ . Note value of  $\bar{\tau}_d$ .

$$\text{Ex.: } (\text{See Figure 40 for resultant } \bar{\tau}_d(x) \text{ curve}). \quad \bar{\tau}_d = 29.92$$

15. Compute two values of correction integrals,  $I_1$  and  $I_2$  on digital calculator.

$$\text{Ex.: } I_1 = \int_0^1 \frac{x dx}{\bar{u}_1(x)} = 13.66$$

$$I_2 = \int_0^1 \frac{x \bar{Z}_T(x) dx}{\bar{u}_1(x)} = 279.3$$

16. Calculate two time lag distribution correction factors,  $\Delta_2$  and  $\Delta_3$  from equations:

$$\Delta_2 = \frac{2}{k \bar{u}_1} \left( 1 + k I_1 - \bar{u}_{x_0} \bar{Z}_T \right) - \frac{1}{\bar{u}_1} \left( 1 + \frac{\bar{u}_{x_1} - \bar{u}_{x_0}}{k} \right)^2 = 0.829$$

$$\Delta_3 = \frac{6}{k \bar{u}_1} \left[ \frac{\bar{u}_{x_0} \bar{Z}_T^2}{2} + \frac{1}{\bar{u}_1} \left( 1 + \frac{\bar{u}_{x_1} - \bar{u}_{x_0}}{k} \right) \left( 1 + k I_1 - \bar{u}_{x_0} \bar{Z}_T \right) - \right. \\ \left. - I_1 \left( 1 + k \bar{Z}_T \right) \right] + \frac{6 I_2}{\bar{u}_1} - \frac{2}{\bar{u}_1} \left( 1 + \frac{\bar{u}_{x_1} - \bar{u}_{x_0}}{k} \right)^3 = -0.807$$

17. Consult original gas velocity distribution curve in straight-line segmented form to calculate two gas residence time correction factors,  $\bar{f}$  and  $a$ .

$$\text{Ex.: } \bar{f} = (1-x_2) + \frac{\bar{u}_1}{\omega} \tan^{-1} \left[ \frac{\omega(x_2 - x_1)}{\bar{u}_1} \right] \approx (1-x_1) = 1.00$$

$$a = \left( \frac{x_2 - x_1}{\bar{u}_1} \right) = 1.48$$

#### D. Calculation of time lag parameters - Procedure #I.

- Assuming known value of  $\bar{f}$  (see above), tabulate, punch input cards, and check values of Run no., reading time,  $c_0$ ,  $\bar{r}$ ,  $T_c$ ,  $\frac{dT_c}{dr}$ ,  $\gamma$ ,  $\gamma_N$ , freq.,  $a$ ,  $\Delta_2$ ,  $\Delta_3$ , and  $\bar{f}$ , on two cards. Collate these cards with output

cards from Stage I into running procedure for digital computation of Newton-Rabson iteration on fixed-decimal control panel.

- Obtain solutions for  $(\omega \bar{f} \theta_g)$  and reduce to  $\theta_g$ .

$$\text{Ex.: } \theta_g = 1.300 \text{ milliseconds.}$$

3. By same procedure, obtain values for  $\sin \omega \bar{Z}_T$ ,  $\cos \omega \bar{Z}_T$ , choose proper quadrant for  $\omega \bar{Z}_T$ , and reduce to  $\bar{Z}_T$ .

Ex.:  $\omega \bar{Z}_T = 0.264$  rad.

$$\bar{Z}_T = 0.17 \text{ millisecs.}$$

4. Plot  $\Theta_g$  and  $\bar{Z}_T$  as functions of reciprocal frequency at each chamber pressure level and select asymptotic values for both parameters.

Ex.:  $\Theta_g$  Asymptotic = 1.063 millisconds (See Figure 43)

$\bar{Z}_T$  Asymptotic = 0.11 millisconds (See Figure 49)

E. Calculation of time lag parameters - Procedure #2

1. Assuming known value of  $\bar{u}_1$ , tabulate and punch input cards identical to those of procedure #1 with substitution of  $\bar{u}_1$ , for  $\bar{f}$ . Collating these inputs into running procedure for complex analytical solution, perform calculations on fixed decimal control panel of digital computer.

2. Obtain solutions for real and imaginary parts of  $\sin(\omega \bar{f} \Theta_g) = \sin(\frac{\omega \bar{f} L}{\bar{u}_1 C_0})$  listing constant outputs  $C_1, C_2, C_3$ .

Ex.: Real part of  $\sin(\omega \bar{f} \Theta_g) = 3.6128$

Imag. part of  $\sin(\omega \bar{f} \Theta_g) = 21.81$

$$C_1 = 0.2913$$

$$C_3 = -0.002150$$

$$C_2 = 0.01299$$

3. Substituting  $\bar{f} = c + id$  into equation for  $\omega \bar{f} \Theta_g$ , calculate  $\tan(\omega c \Theta_g)$  and  $\tanh(\omega d \Theta_g)$ .

Ex.:  $\tan(\omega c \Theta_g) = -C_3/C_2 = 0.1655$

$$\tanh(\omega d \Theta_g) = \pm \sqrt{1 - \left( \frac{C_2^2 + C_3^2}{C_1^2} \right)} = \pm 0.9990$$

4. Choosing appropriate quadrant for  $(\omega C \theta_g)$  and appropriate sign for  $(\omega d \theta_g)$ , reduce these values to real and imaginary parts of  $\bar{f}$ , c and d.

Ex.:  $c = 1.203$

$$d = + 1.518$$

5. Plot c and d as functions of frequency. Verify that d asymptote = 0 and determine c asymptote.

Ex.: C asymptote =  $\bar{f}$  asymptote = 0.980

(See Figure 46)

6. Carry out similar digital computer calculation to obtain real and imaginary parts of  $\sin \omega \bar{Z}_T$  and  $\bar{Z}_T = y + i z$ .

Ex.: Real part of  $\sin \omega \bar{Z}_T = 0.21029$

Imag. part of  $\sin \omega \bar{Z}_T = -0.11096$

$y = -0.11$  millisecs.  $z = + 0.07$  millisecs.

7. Plot y and z as functions of frequency. Verify that z asymptote = 0; determine y asymptote =  $\bar{Z}_T$  asymptote.

Ex.: y asymptote = 0.11 millisecs (See Figure 52)

8. Compare  $(\bar{f} \theta_g)$  asy. and  $\bar{Z}_T$  asy. from two procedures.

Ex.: Procedure #1:

$(\bar{f} \theta_g)$  asy. = 1.063 milliseconds

$(\bar{Z}_T)$  asy. = 0.11 milliseconds

Procedure #2:

$(\bar{f} \theta_g)$  asy. = 1.530 millisecs.

$(\bar{Z}_T)$  asy. = 0.11 milliseconds

### III. Stage III Calculations

#### A. Sensitive time lag and interaction index calculations.

1. Punch input cards similar to those of Stage II, omitting  $\bar{f}$  or  $\bar{u}_1$  and adding ( $\bar{f}\theta_g$ ) asymptote and ( $\bar{\tau}_T$ ) asymptote. Collate with Stage I output cards into running procedure for exact Stage III equation on fixed-decimal control panel of digital computer.
2. Obtain output values for interaction index, n and  $\sin \omega \bar{\tau}$ , and  $\cos \omega \bar{\tau}$ .

Ex.: n = 0.49

$$\sin \omega \bar{\tau} = 0.7981$$

$$\cos \omega \bar{\tau} = 0.6025$$

3. Choosing appropriate quadrant for ( $\omega \bar{\tau}$ ), reduce to sensitive time lag,  $\bar{\tau}$ .

Ex.:  $\bar{\tau} = 0.59$  milliseconds

#### B. Gross variation of time lag parameters with pressure.

1. Determine gross value of n from slope of log-log plot of  $\bar{\tau}_{avg}$  vs.  $\bar{P}$ .

Ex.: n (gross) = 1.41